



The  
University  
Of  
Sheffield.

# **The Application of Additive Manufacturing to Nickel-base Superalloys for Turbocharger Applications**

**Charlotte Amelia Boig**

A thesis submitted in partial fulfilment of the requirements for the degree of  
Doctor of Engineering (EngD)

The University of Sheffield

Department of Materials Science and Engineering

Submission Date: 2<sup>nd</sup> October 2018

## **Abstract**

Metal additive manufacturing (AM) is a disruptive technology which has the potential to deliver numerous benefits over conventional manufacturing including design freedom, increased innovation and shorter lead times. However, adoption of the technology by the automotive industry is currently restricted by the cost, limited availability of suitable engineering alloys and the lack of robust process control. These issues are all relevant in the present discussion on the application of laser powder bed fusion (LPBF) to the nickel-base superalloy IN713C. This alloy, along with other precipitation strengthened nickel-base superalloys, is considered to be “un-weldable” due to its susceptibility to cracking; an issue which makes it similarly challenging to process via LPBF. This thesis addresses both the business case for LPBF in terms of turbocharger componentry, and the behaviour of IN713C under LPBF in terms of understanding the defect response.

Statistical design of experiments (DOE), advanced material characterisation and analysis techniques, analytical melt pool modelling, thought experiments and the application of literature models have all been employed, facilitating the development of a process map for LPBF of IN713C. The process map illustrates the thresholds for the onset of defect formation and can be used to direct future work on the design of processing strategies for complex components. Use of the process map alongside statistical response surface methodology enabled the identification of process settings for which porosity in test cube specimens was minimised. The application of literature models for solidification cracking provided insight into the relationships between process settings, solidification conditions and crack susceptibility.

## Preface

This EngD project was a collaboration between the University of Sheffield and Cummins Turbo Technologies, conducted within the scope of assessing the feasibility of laser powder bed fusion (LPBF) for additive manufacturing of turbocharger components, such as the turbine wheel, from nickel-base superalloy IN713C. At present, the potential benefits of LPBF such as novel geometrical design and short lead times are inaccessible for precipitation strengthened superalloys like IN713C because their “un-weldable” chemistries leave them susceptible to forming defects during processing. This thesis contributes to the understanding of the relationships between material, process and output using statistically designed experiments and advanced characterisation techniques to classify types, predict the onset of, and mitigate against defects.

The thesis is split into two parts. Part 1, the “Business case and rationale”, introduces AM technologies, outlines their benefits and limitations and discusses the business cases for LPBF for turbocharger components. Part 2 is a scientific study on the behaviour of IN713C processed using LPBF.

The main scientific outputs of this work fall into two categories: process mapping and material response (cracking). Process maps, based on LPBF processing parameters and related derived quantities, illustrate the competitive nature of the defect formation mechanisms and the sensitivity of IN713C to slight changes in solidification conditions. Identification and quantification of the various void types through sequential designed experiments led to the identification of a narrow processing window in which porosity was reduced to  $0.05 \pm 0.02\%$ . Melt pool modelling and dimensional analysis methods were used to successfully predict the onset of lack-of-fusion and keyhole type defects. Electron microscopy and x-ray tomography were employed in the creation of an extensive “taxonomy of defects” which is useful as a classification tool and as a guide in the parameter optimisation process for a new material.

The cracks present in LPBF IN713C were identified as belonging to one of two types; solidification cracking and stress relief cracking. Solidification cracking occurs in the mushy zone during the final stages of solidification whereas stress

relief cracking is a solid state phenomenon related to thermomechanical effects. The solidification crack tendency was investigated through the application of various literature models, as well as through Thermo-calc simulations of the solidification path and transmission electron microscopy (TEM). It was shown that the probability of initiating solidification cracking can be deduced using the Rappaz, Drezet and Gremaud model for “hot crack susceptibility”. Changes in the distribution of the dislocation network according to input energy of the laser were observed and correlated to the time available for recovery. Since the microstructure is dependent on the solidification and cooling conditions, sample geometry and cross section can affect a deviation from the expected defect response.

The thesis concludes by taking a hypothetical stroll around the process map, considering the effect on material robustness of moving outside of the boundaries of the optimal processing window. This highlights the sensitivity of the material to deviations from optimal conditions and instructs the direction of further work required to design processing strategies for components with complex geometries.

All the work presented in this thesis was carried out by the author, except for some aspects of selected experiments, for which the person or persons responsible are explicitly credited.

## Layout

Nomenclature and abbreviations.....	4
Acknowledgements.....	10
PART 1: Business case and rationale.....	11
PART 2: Scientific studies.....	40
References.....	196
Appendices.....	211



## Nomenclature and abbreviations

Symbol	Description	Units
*	Normalised quantity	-
$A$	Fraction of beam power absorbed	-
$A$	Surface area of casting	$\text{m}^2$
$a_0$	Interatomic distance	m
AM	Additive manufacturing	-
ANOVA	Analysis of variance	-
APT	Atom probe tomography	-
$\underline{b}$	Burgess vector	-
BBD	Box Behnken Design	-
$C_0$	Nominal solute concentration	wt %
CAD	Computer aided design	-
CCD	Central composite design	-
CCM	Crack compliance method	-
CET	Columnar to equiaxed transition	-
CFD	Computational fluid dynamics	-
$C_L$	Composition of liquid	-
$C_l^*$	Liquid concentration ahead of solid front	wt %
CMI	Cummins Inc.	-
$C_p$	Specific heat capacity at constant pressure	$\text{J}\cdot\text{kg}^{-1}\cdot\text{K}^{-1}$
$C_s$	Composition of solid	-
CSC	Crack susceptibility coefficient	-
CTT	Cummins Turbo Technologies	-
$d$	Characteristic length scale	m
$D$	Diffusion coefficient	$\text{m}^2\cdot\text{s}^{-1}$
$D_0$	Diffusion pre-factor	$\text{m}^2\cdot\text{s}^{-1}$
DAS	Dendrite arm spacing	m

## The Application of AM to Ni-base Superalloys

DDC	Ductility dip cracking	-
DED	Directed energy deposition	-
$D_i$	Interface diffusion coefficient	$\text{m}^2 \cdot \text{s}^{-1}$
DMLS	Direct metal laser sintering	-
DOE	Design of experiments	-
$E_0$	Energy density	$\text{J} \cdot \text{m}^{-3}$
EDM	(Wire) Electrical discharge machining	-
EDX	Energy dispersive x-ray (spectroscopy)	-
$E(T)$	Cumulated deformation rate	$\text{s}^{-1}$
$F_0$	Statistical parameter	-
fcc	Face centred cubic	-
FEM	Finite element modelling	-
FIB	Focussed ion beam	-
$f_L$	Fraction liquid	-
$f_s$	Fraction solid	-
$G$	Thermal gradient	$\text{K} \cdot \text{m}^{-1}$
GB	Grain boundary	-
$h$	Hatch spacing	m
HAZ	Heat affected zone	-
HCS	Hot crack susceptibility	-
$h_s$	Enthalpy at melting	$\text{J} \cdot \text{kg}^{-1}$
$Iv()$	Ivantsov function	-
$k_0$	Equilibrium partition coefficient	-
$k$	Velocity dependent partition coefficient	-
$k$	Number of terms in regression model	-
KGT	Kurz, Giovanola and Trivedi	-
$l$	Layer thickness	m
$L$	Harmonic of perturbation constant	-
LPBF	Laser powder bed fusion	-

LEAP <sup>®</sup>	Local electrode atom probe	-
LCI	Life cycle inventory	-
LMK	Langer and Muller-Krumbhaar	-
LOF	Lack of fusion	-
$M$	Ripening parameter	-
$n$	Number of observations	-
$n_c$	Number of CCD centre points	-
OEM	Original equipment manufacturer	-
$P$	Peclet number ( $=Vd/2D$ )	-
PBF	Powder bed fusion	-
PDAS	Primary dendrite arm spacing	m
PMZ	Partially melted zone	-
PSD	Particle size distribution	-
$q$	Attenuated laser power	W
$Q$	Activation energy for diffusion	J
$q'$	Input laser power	W
$q_e$	Heat flux away from melt	-
$R$	Melt pool radius	m
$R$	Gas constant	J·mol·K <sup>-1</sup>
$r_B$	Laser beam radius	m
RDG	Rappaz, Drezet and Gremaud	-
RS	Rapid solidification	m
RSM	Response surface methodology	-
SAC	Strain age cracking	-
SDAS	Secondary dendrite arm spacing	m
SEBM	Selective electron beam melting	-
SEM	Scanning electron microscopy	-
SLM	Selective laser melting	-
$SS_E$	Error sum of squares	-

## The Application of AM to Ni-base Superalloys

$SS_R$	Regression sum of squares	-
$\dot{T}$	Cooling rate	$K \cdot s^{-1}$
$T_0$	Initial temperature of powder bed	K
tcp	Topologically close packed	-
$T_D$	Dendrite formation temperature	K
$T_E$	Eutectic temperature	K
TEM	Transmission electron microscopy	-
$t_f$	Local solidification time	s
TGM	Temperature gradient mechanism	-
$T_L$	Liquidus temperature	K
$T_M$	Melting temperature	K
$T_P$	Planar growth temperature	K
$t_R$	Time in stress relaxation region	s
$t_v$	Time in vulnerable region	s
$u$	Casting volume	$m^3$
UTS	Ultimate tensile strength	-
$v$	Laser velocity	$m \cdot s^{-1}$
$V$	Growth rate of solid	$m \cdot s^{-1}$
$V_a$	Limit of absolute stability	$m \cdot s^{-1}$
$V_C$	Velocity of sound	$m \cdot s^{-1}$
$v_s$	Shrinkage velocity	$m \cdot s^{-1}$
$V_{Tmax}$	Velocity limit before planar front re-established	$m \cdot s^{-1}$
XCT	X-ray computer tomography	-
$Y$	Melt pool overlap depth	m
$\alpha$	Thermal diffusivity ( $= \lambda/\rho C_p$ )	$m^2 \cdot s^{-1}$
$\alpha$	Axial point distance from centre of CCD	-
$\beta$	Shrinkage factor ( $=(\rho_l/\rho_s)-1$ )	-
$\beta_k$	Regression coefficients	-
$\delta$	Interface width	m

$\dot{\varepsilon}_p$	Strain rate	$s^{-1}$
$\Delta H$	Specific enthalpy	$J \cdot kg^{-1}$
$\Delta H_f$	Latent heat of fusion	$J \cdot kg^{-1}$
$\Delta P_C$	Cavitation pressure drop	Pa
$\Delta T_0$	Equilibrium temperature range	K
$\Gamma$	Gibbs-Thompson coefficient	-
$\lambda$	Thermal conductivity	$W \cdot m^{-1} \cdot K^{-1}$
$\lambda_1$	Primary dendrite arm spacing	m
$\lambda_2$	Secondary dendrite arm spacing	m
$\rho$	Density	$kg \cdot m^{-3}$
$\rho_l$	Density of liquid	$kg \cdot m^{-3}$
$\rho_s$	Density of solid	$kg \cdot m^{-3}$
$\tau$	Laser exposure time	s
$\mu$	Dynamic viscosity	$kg \cdot m^{-1} \cdot s^{-1}$
$x_k$	Coded variables	-

## Acknowledgements

I would like to acknowledge the financial support of the EPSRC and Cummins Turbo Technologies (CTT), who jointly funded this work and CTT for making the excellent facilities in their materials laboratory available to me throughout.

I would like to thank everyone who has supported me during the last four years. I am grateful to Prof Iain Todd for providing academic supervision, stimulating discussions and keeping an eye on me. Also to Dr Michael Burkinshaw for his support through his role as industrial supervisor, for his unwavering belief in my ability and for creating so many opportunities for me. Thank you to all project stakeholders at Cummins who have shown such interest in the project, kept me motivated and welcomed me to the company.

The technical staff at the University of Sheffield and CTT deserve a special thanks, as without them this work would not have been possible. I would also like to acknowledge Dr Andrew London (University of Oxford) for his work using atom probe tomography, Dr Julia Behnsen (MXIF) and Dr Sam Tammas-Williams (University of Sheffield) for their contributions to the work using XCT, Dr Jo Sharp (University of Sheffield) for obtaining TEM data, Dr Le Ma for preparing TEM samples using FIB and Felicity Freeman (University of Sheffield) for providing the melt pool model used extensively throughout this work.

I can't even begin to thank my friends enough for preserving my sanity through the most challenging period of my life. Especially Felicity, Emily, Alistair, Lova, Tom and Yevgeni, who have really borne the brunt of it - see you all in the pub. I will be forever grateful to Mum, Dad, Timmi and the rest of my gorgeous family for everything they have done and continue to do to support me.

To my ever loyal shadow Ruben, thanks for taking me out for walks and for keeping my feet (and my heart) warm.

# PART 1

## Business case and rationale

### Contents

1. Scope.....	12
2. Aims and objectives.....	12
3. Metal additive manufacturing technologies.....	13
3.1. Powder bed fusion .....	13
3.2. Direct energy deposition .....	17
3.3. Binder jet printing .....	19
3.4. LPBF Hardware.....	21
4. Benefits, challenges and opportunities .....	23
5. Efficiency of AM.....	27
6. Business case for AM within CMI .....	31
6.1. Use of “Factory Physics” .....	31
6.2. Applications.....	33
6.3. Business case for LPBF within Cummins: The turbine wheel.....	36
7. Impact of the project .....	38
8. Summary of Part 1 .....	39

## 1. Scope

The requirements of Cummins Inc. (CMI) of gaining understanding in the AM sector and the output of the VOC questionnaire (Appendix 1) allowed the development of the following scope:

**The scope of this EngD project includes aspects of investigation relating to assessing the feasibility of laser powder bed fusion of IN713C from a technical and commercial perspective, evaluating the applicability of the process to prototyping and volume production. Alloy design, topology optimisation, component testing and the use of AM technologies other than LPBF was outside the scope of this project.**

## 2. Aims and objectives

- Assess the business case for AM of turbocharger components.
  - Consider the views of key stakeholders to guide the direction of the project.
  - Critically assess the applicability of LPBF technology to turbocharger componentry for prototyping or volume production.
  - Define the state of the art technology and how it is predicted to develop.
  - Discuss the advantages and limitations of AM in the context of the automotive industry.
- Investigate the material response of IN713C to LPBF processing.
  - Identify and characterise possible defect types resulting from LPBF and correlate these with the process settings.
  - Investigate cracking behaviour in LPBF IN713C using solidification cracking models to assess crack susceptibility in terms of process setting.
- Produce a process map for LPBF of IN713C.
  - Use sophisticated characterisation techniques to identify defects occurring in LPBF IN713C test cube specimens.
  - Correlate observed defect formation with process settings using statistical methods.



- Recommend a suitable method of process strategy development and optimisation.
  - Identify a processing window for LPBF IN713C.
- Understand the importance of achieving good process control on the mitigation of defect formation in LPBF IN713C and the implications of a loss of control.
  - Understand how the various defect formation mechanisms can influence the design of a processing strategy for a component.

### **3. Metal additive manufacturing technologies**

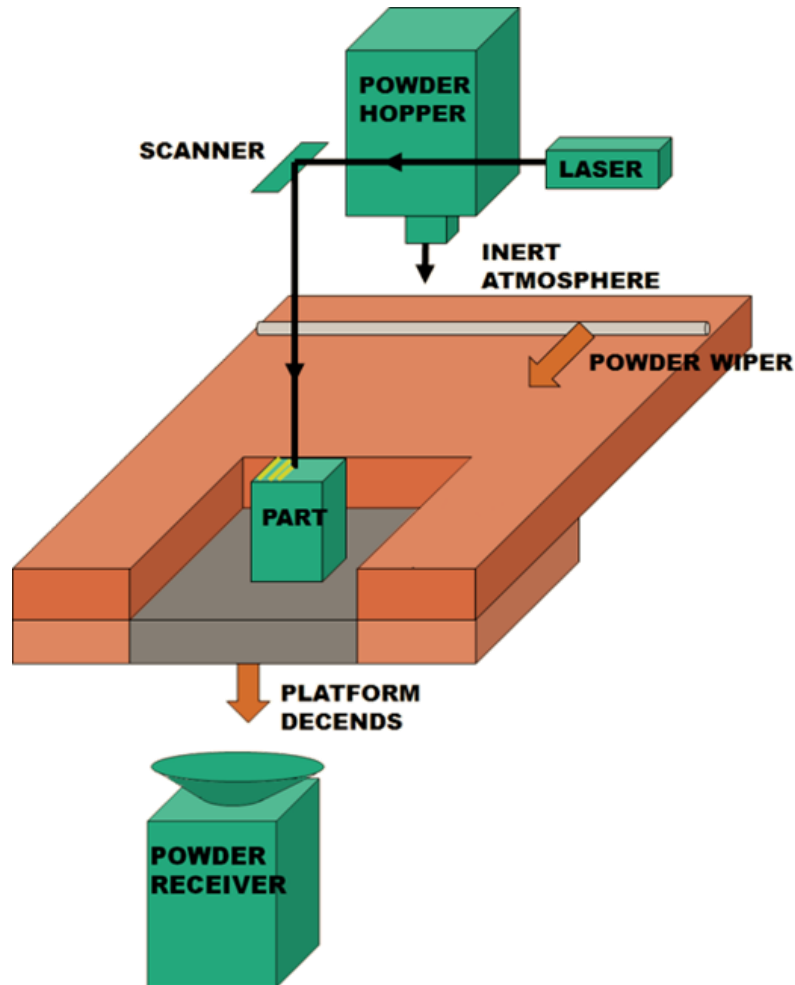
#### **3.1. Powder bed fusion**

Powder bed fusion (PBF) AM is used for the fabrication of net shape or near net shape components. The benefits are most effectively realised for small components with complex geometries which cannot be produced via conventional manufacturing techniques. The heat source options for PBF are a laser or electron beam. Laser powder bed fusion (LPBF) is the main focus of this work and was used to investigate the applicability of AM to nickel-base superalloy IN713C. Although the design of LPBF machines varies between machine suppliers, the basic theory for operation and machine architecture remains the same (Figure 3.1).

Powdered metal feedstock, held in a hopper is deposited onto the base of the build chamber either through gravity (e.g. Renishaw (Figure 3.2)) or by raising an adjacent hopper (e.g. Concept laser, Aconity). A wiper/re-coater blade sweeps a thin layer of powder over the build platform which is selectively melted by a focussed heat source according to a .stl file of the component. The platform then descends a distance equal to the layer thickness and the process repeats until the component has built to its full height. Processing occurs in an inert atmosphere. Excess powder is collected and processed ready for re-use. Literature is available on the effect of powder re-use in LPBF [1], [2].

Electron beam powder bed fusion (Figure 3.3), also known as selective electron beam melting (SEBM), is a similar process to LPBF, the main differences being the electron beam heat source and processing occurs under vacuum. Arcam are the sole suppliers of SEBM systems. A pre-heat scan is used to heat and partially sinter the

powder bed prior to melting. This “warm processing” means that the powder bed is held at a temperature specific to the material throughout the build, reducing residual stress in the part [3]. SEBM build rates are faster than LPBF but the surface roughness and accuracy of fine features are compromised. Since SEBM is predominantly suited to titanium alloys, it was not used in this study.



**Figure 3.1. Schematic diagram of the LPBF process in a Renishaw SLM 125 system.**

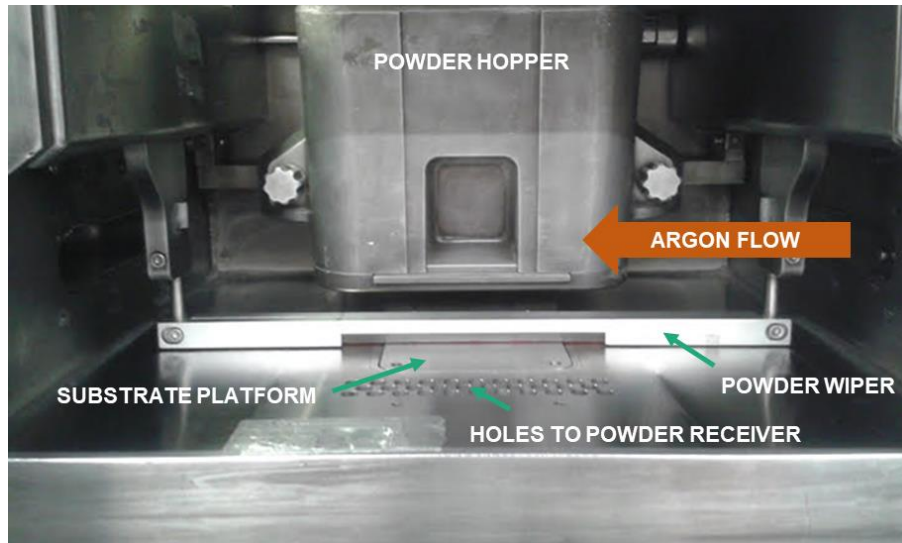


Figure 3.2. Inside the build chamber of the Renishaw SLM125.

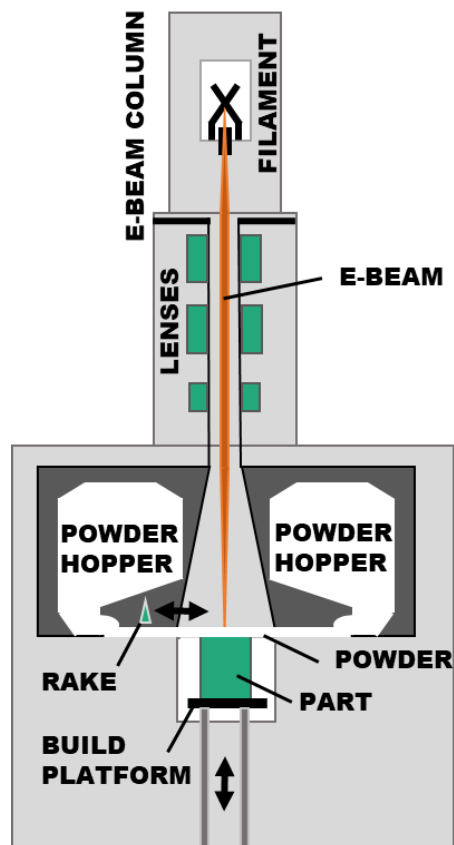


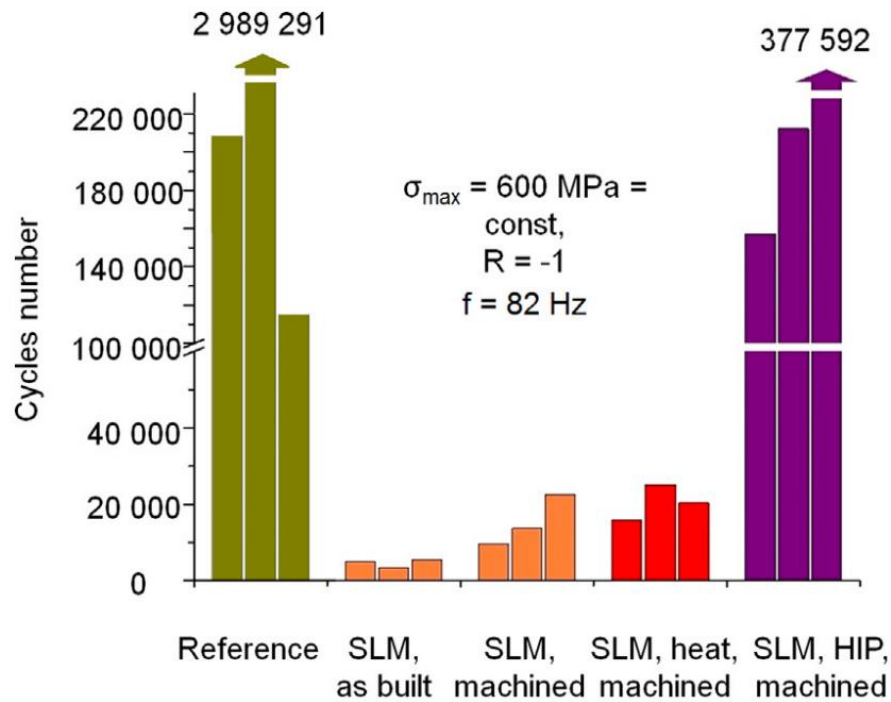
Figure 3.3. Schematic architecture of an Arcam SEBM system, after [3].

## The Application of AM to Ni-base Superalloys

LPBF processing regimes for a limited collection of engineering alloys have been developed and are established for use in various engineering applications. Popular engineering alloys which have received the most research attention and are acknowledged to be suitable for processing via SLM include Ti-6Al-4V [4]–[7], stainless steel, tool steel, cobalt chrome, AlSi10Mg [8], [9], IN625 [10], [11] and IN718 [1], [12]. Complex geometrical features can be produced including enclosed structures, thin walls and lattices.

Although processing routes are established for these materials, it is usually necessary to perform some post processing techniques on PBF components. Excess material and support structures are routinely machined off post-build. It is common for material to be added to a certain important face or feature such that it can be precision milled to create the final required geometry.

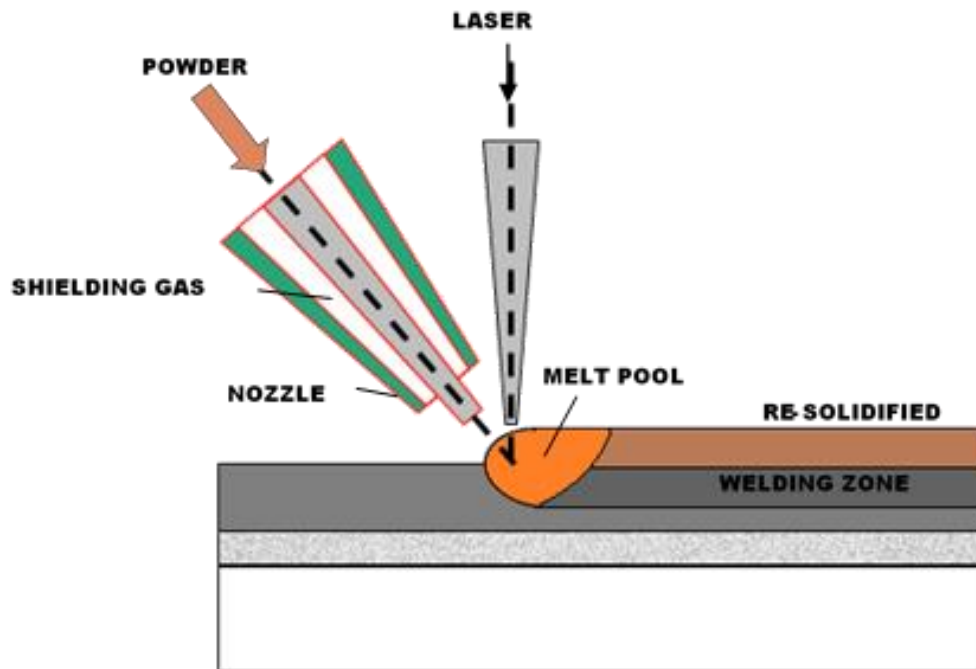
Hot isostatic pressing (HIP) is also commonly performed to collapse internal voids [13]–[17] and improve high cycle fatigue life compared to non HIPed PBF specimens (Figure 3.4). Microstructural changes such as grain growth occur in some materials during HIPing, although it has been demonstrated that internal voids, acting as stress raisers, are significantly more likely to cause premature failure than microstructure [17]. However, HIPing is not a satisfactory solution to internal porosity in all cases, since gas filled pores can re-open when the component is re-heated to the HIP temperature [18] so this may not be suitable for high temperature applications. Additionally, with the cost of AM already high, eliminating internal porosity without additional processing steps would be beneficial to the adoption of the process by the automotive industry.



**Figure 3.4. Fatigue behaviour of LPBF Ti-6Al-4V in a high cycle fatigue regime is improved after HIP treatment, from [15].**

### 3.2. Direct energy deposition

Direct energy deposition (DED), also known as blown powder AM or laser cladding, also uses a focused laser heat source to melt and consolidate powdered feedstock. However, in this technique the powder is delivered in a stream of inert shielding gas through a nozzle into the focal point of the laser, coincidentally with the surface of the substrate (Figure 3.5). Since the powder delivery nozzle is mounted on a 3 or 5 axis robot arm, the substrate does not have to be a flat plate, so DED can be used to add protrusions to existing components [19]. This means that DED can be used to repair a component by adding material to a damaged area which will later be machined to the final topology, an application utilised predominantly in the aerospace industry [20], [21].



**Figure 3.5. Schematic diagram of the DED process.**

Material deposition speeds for DED are faster than for powder bed techniques due to typical linear heat inputs up to 100 times greater than for PBF and layer thicknesses of up to 1 mm compared to tens of microns for PBF [22]. As a result, the powdered feedstock can be coarser than in PBF although, the resolution of the geometrical features is compromised. DED is not a suitable technique for the direct fabrication of a component such as a turbocharger turbine wheel, but it is currently employed in their repair within Cummins. During this process the damaged area is machined away, and scanned to create a CAD file of the required topology. After several washing stages the additional material is deposited and the surface is machined to the final geometry. In this application, the turbine wheel repair is made with a dissimilar material.

### 3.3. Binder jet printing

Binder jet printing (BJP) (Figure 3.6) is a powder bed AM technology for the direct production of components which is a hybrid technology combining powder bed AM and inkjet printing. The first step is similar to PBF, whereby a thin layer of metal powder is spread over a substrate. However, rather than selectively melting the layer a print head strategically deposits a liquid binding agent which bonds the powder particles. Further layers are deposited until the required component is built (Figure 3.7). Green BJP parts are not suitable for engineering applications because the as-printed condition is not fully dense. However, the bonded powder form can then be cured, sintered, infiltrated or HIPed to increase the density. At present, fully dense material can only be achieved with a limited selection of alloys [23].

The benefit of BJP over PBF is that it does not directly use heat during the process, so the material is not subjected to the same extreme local temperature fluctuation as in PBF and residual stresses do not accumulate during the build. Also, the complex thermal history resulting from the re-melting process in PBF is avoided, making prediction of phase formation, microstructure and grain structure less complicated. The BJP process enables consolidation of the powder on the scale of the whole component, leading to homogeneous microstructures.

Binder jetting has received renewed interest recently, particularly from the automotive sector, due to its potential for producing large parts from a range of different materials with fast production rates. BJP machine supplier GE Additive are working to satisfy the demand for this technology with the release of a new prototype BJP machine with larger and faster build capabilities than any other on the market.

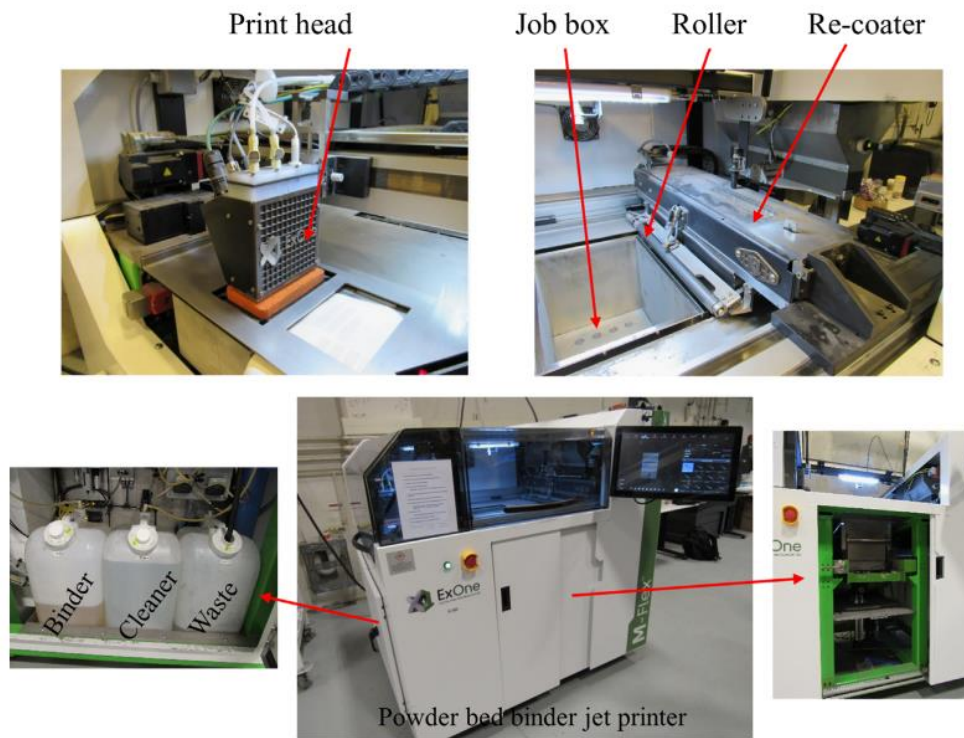


Figure 3.6. A powder bed binder jet printer, from [24].

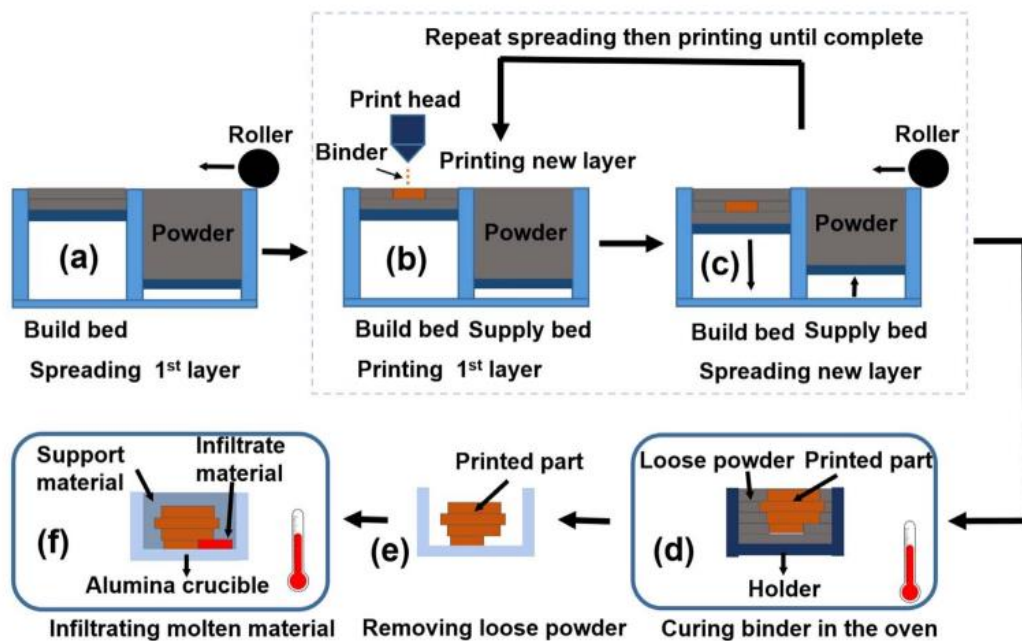


Figure 3.7. Schematic diagram of the BJP process, from [23].



### 3.4. LPBF Hardware

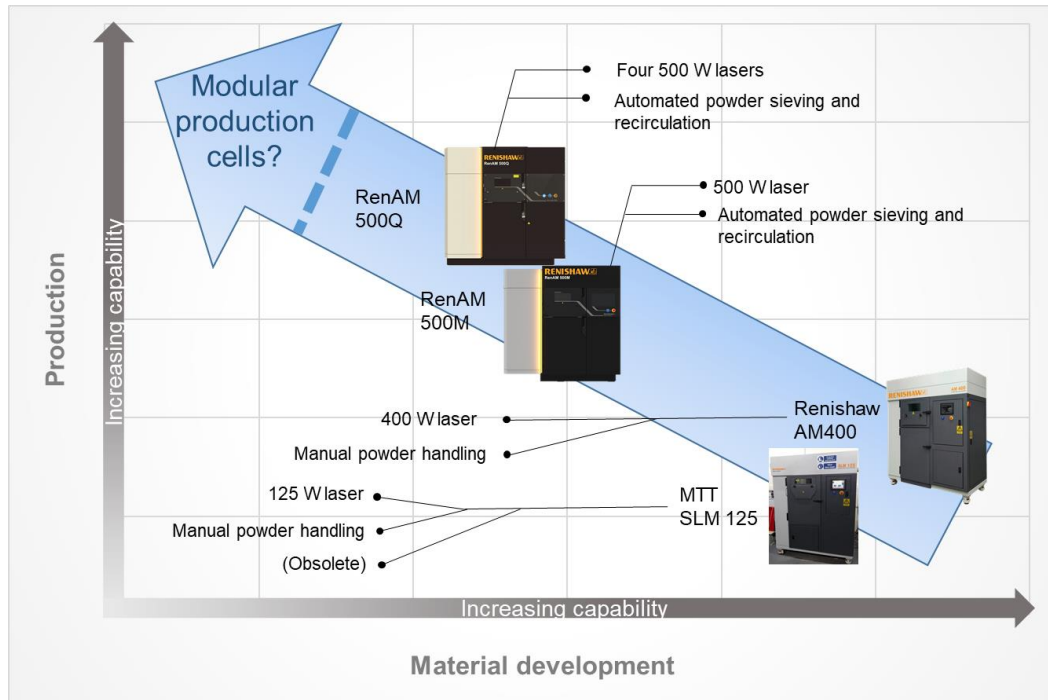
Historically, through the development of LPBF as a feasible method of direct production of metallic components, two dominant routes emerged in terms of machine suppliers. The first was EOS GmbH and the second contained all competing brands including Realizer, SLM Solutions, MTT and Concept Laser. EOS remains the largest vendor of metal AM machines, followed now by GE Additive after their acquisition of Arcam and Concept Laser. Renishaw plc, whose expertise historically lies in sensors and precision measurement instruments, acquired MTT Investments Ltd in 2011 kick-starting their journey into AM. A number of other machine suppliers are also active in the market including Additive Industries, Trumpf, and 3D systems.

At present, machine suppliers are racing to bring a truly production-ready, factory floor, LPBF platform to the market. Focus has been placed on increasing laser power, using multiple lasers, increasing build area, automating powder sieving and recirculating and incorporation of process monitoring. Renishaw's most recent offering is the RenAM 500Q which features four 500W lasers and integrated, automatic powder recirculation. EOS and Concept Laser also offer the multi-laser machines with integrated powder handling; EOS 400-4 (4 x 400W lasers) and Concept Laser M2 using Multilaser (2 x 200W or 2 x 400W lasers). The multi-laser approach is more beneficial than one high power laser for two reasons. Firstly, since each laser can operate independently, multiple parts can be scanned at once, or multiple areas of a large part can be simultaneously melted, reducing residual stresses whilst increasing build speed. Secondly, multiple lower powered lasers may be preferable over a single high power, high speed laser because this combination is known to contribute to irregularities in the flow of molten powder and inhomogeneity in the thermal history of the component leading to increased defect populations [25].

## The Application of AM to Ni-base Superalloys

At present, the main difference between machines marketed as “production ready” and those aimed towards research and development activities is in the ease of changeover between materials. Once a production machine has been used with a certain material the challenges involved with removal of all the powder effectively lock down the machine to that material indefinitely to avoid contamination. However, development machines, usually without automated powder handling systems, are significantly easier to clean due to easier access and removal of powder hoppers. Looking through the evolution of the Renishaw LPBF machine range (Figure 3.8) it is clear that the focus is towards increasing production capability rather than material development, although the Renishaw AM400 platform is still available as their flagship research and development machine.

Since LPBF components require various post-processing steps according to the requirements of the application, an alternative route towards production ready machines involves integration of additional capability. For example, “additive plus subtractive” manufacturing features both material deposition and machining technology or modular production cell concepts featuring heat treatment furnaces. These modular architectures would also minimise the need for human intervention, improving productivity, increasing repeatability and reducing operator exposure to hazardous powdered materials. At present, significant barriers prevent the immediate integration of these technologies, such as contamination of powdered feedstock from machining swarf, removal of the component from the substrate and system engineering challenges relating to high temperature processing. However, a handful of machine suppliers are adopting the modular approach to being production ready. Additive Industries’ MetalFab1 platform is a modular, customisable production cell capable of heat treatment and automated part handling. Other machine suppliers are expected to follow suit in the near future.



**Figure 3.8. Evolution of Renishaw LPBF platforms.**

## 4. Benefits, challenges and opportunities

Additive manufacturing provides a unique opportunity not available through conventional manufacturing techniques, provided the technology is used intelligently. It is important to develop a clear understanding of the reasons for choosing AM to produce a component in order to fully harness the benefits. For example, it is tempting to focus on the manufacturing aspect of AM by directing research attention exclusively towards the fabrication by LPBF of a product currently made using investment casting for the purpose of satisfying curiosity in the novelty, without considering AM as a whole, starting from component and alloy design. The true benefits of AM are gained when the full lifecycle and purpose of the component is considered, including application, material, geometry, performance requirements and life. All items listed here are related to the purpose behind producing the component. If a component is required as a prototype or performance indicator for an investment casting, the material, performance requirements and life will take lower precedence than the component geometry. Conversely, if a component is a premium product required as part of a low volume

## The Application of AM to Ni-base Superalloys

production run, all aspects must be designed with AM in mind from the outset in order to reap the benefits of AM.

Perhaps the most obvious and well publicised benefit of AM is the design freedom from the restrictions of conventional manufacturing techniques which enable complex geometries, thin wall sections and internal volumes, channels, lattices and removal of redundant material from unstressed regions of a component without adversely affecting strength or stiffness. Such structures are not achievable through investment casting or machining due to access requirements of tooling. Conventional manufacturing techniques have long been a source of disconnect between design engineers and manufacturing engineers, since the optimal design for performance has to be compromised for manufacturing. These barriers can be overcome using AM allowing design teams to work together on innovative products with novel component geometries. The design process involves finite element analysis of a current component to identify regions suitable for topology optimisation. This is followed by the use of structural optimisation software to perform a number of iterative optimisation loops assessing the suitability of the topology according to loading conditions [26], [27]. Weight savings of around 40% have been demonstrated [28], [29] through topology optimisation for AM, reducing material waste and reducing component inertia.

In addition to novel component designs, recent research has shown there is potential for producing functionally graded materials using AM [30]. Processing parameters can be varied throughout a LPBF build, altering the thermal experience of the material and in turn varying the microstructure and mechanical properties of the material. Grain structure, density and magnetic response can all be influenced by processing parameters. This ability is useful, since the material can be functionally graded to optimise for the best balance of processing speed vs performance. For example, it may be preferable to produce internal supporting lattice structures with lower density than the main component to speed up processing and reduce energy consumption.

AM offers unique flexibility in terms of when and where components are produced. LPBF machines in particular are usually relatively compact and can be located anywhere with a suitable power supply and powder containment facilities. Hence manufacturing can be done remotely, within a research and development facility or local to the end user, e.g. in a hospital producing surgical implants or within a service department for producing obsolete cast products.

The challenges facing implementation of AM can be divided into two categories; process barriers and cultural barriers. More specifically, the way in which the material responds to the process and its foibles and the way in which the engineering community responds to and perceives AM. Challenges remain for both component-process compatibility and material-process compatibility. Although AM removes the manufacturing restrictions of casting such as facilitating removal of the mould, avoiding thin sections and consideration of liquid metal's fluid lifetime and behaviour during pouring [31], it does have design restrictions of its own which must be taken into account. These include avoidance of closed hollow volumes which will trap powder, maintenance of sufficient clearance between features, minimum feature size (approx. 0.3-0.5mm depending on specific melting technology [29]), overhang and bridging. Careful consideration of component orientation in the build chamber is important because this not only affects the surface finish of the component but also its mechanical properties. Vertical walls are known to have better surface finish than structures with an overhang. Guidelines for maximum overhang possible without additional support vary according to the manufacturing machine and material. Removal of support structures adds another step to the manufacturing process so use of supports should be minimised for optimum production efficiency. AM components often exhibit anisotropic properties due to the thermal history of the material. This can be influenced through adjustment of the melting strategy; another important step to consider in the design process.

A comprehensive, multiscale treatment of AM planning and design is given in [32]. In depth reviews of the advantages and challenges of AM can be found elsewhere [33]–[36]. A summary is given in Table 4.

**Table 4. Advantages and challenges of AM**

Advantages	Challenges
<ul style="list-style-type: none"> <li>• Design freedom over traditional manufacturing methods to produce complex geometries including thin walls, enclosed structures and lattices</li> <li>• Improved innovation through better communication and collaboration between design and manufacturing engineers</li> <li>• Potential for functionally graded materials</li> <li>• Freedom of manufacturing location, remote or on-site</li> <li>• Direct production of components without costly moulds or tooling</li> <li>• Short lead times</li> <li>• Reduces inventory risk and improve revenue flow</li> <li>• Small production volumes are economically advantageous over traditional methods</li> <li>• Customisable products, increasing interaction between producer and customer</li> <li>• Obsolete products for which tooling no longer exists can be made via reverse engineering for service and repair</li> </ul>	<ul style="list-style-type: none"> <li>• Misconceptions about AM only being suitable for prototyping</li> <li>• Balancing cost and speed of production with purpose of component</li> <li>• Development of industry standards for powdered feedstock and AM components</li> <li>• Validation of mechanical properties of AM components against traditionally manufactured counterparts</li> <li>• Lack of design principles or best practice</li> <li>• Reducing feedstock contamination risk through standardised powder storage and reuse protocol</li> <li>• Automation of AM systems, monitoring and in operando feedback</li> <li>• Optimising support structures</li> <li>• Limited selection of materials available/suitable as metallurgical issues remain a barrier to production of more challenging alloy systems</li> <li>• Post processing usually required</li> <li>• Extensive health, safety and environmental requirements</li> </ul>

## 5. Efficiency of AM

A key benefit of AM, deserving of some additional discussion, is the saving in resources coming from reducing material waste, time and energy to produce a component compared to conventional manufacturing techniques like investment casting. The stages of producing a component via LPBF including the inputs and outputs in terms of energy and materials are illustrated in Figure 5. The orange ovals represent wasted material. Material usage can be reduced via two routes:

- Improving efficiency of material usage during the LPBF process
- Reducing material usage through weight saving component design

The aerospace industry utilises both routes in the production of reduced mass components such as seat buckles, hinges and brackets [37], [38]. The potential for significant efficiency improvements from use of carefully selected AM components in place of conventionally manufactured counterparts has been demonstrated through a case study on components deemed suitable for production via AM based on criteria including geometry, production volumes and application (usually non-load bearing). The analysis used data on raw material production and distribution, supply chain and emissions analysis in the cradle-to-gate life cycle inventory (LCI). Mass savings of between 35-65% were reported across the five components (Figure 5.1), with the most significant saving coming from the more massive components. Additionally, up to 6.4% reduction in aeroplane fuel consumption and a saving of up to 50% in energy used to manufacture the components was observed [38].

Despeisse et al [39] identify two additional areas in which AM can be used to improve resource efficiency, namely “make-to-order production” and “closing the loop”. Manufacturing on demand reduces inventory waste and risk, enabling the shift towards economies of scale through batch production of customised products. Closing the loop describes the benefits gained from repair and remanufacturing using AM, creating opportunities for service-based business models.

Preparation of a LCI is the first stage of a life cycle analysis (LCA) and includes alloy/feedstock production, printing, recycling, finishing, performance efficiency differences and end of life processing of the component. Numerous studies exist on

the LCI of AM vs conventional manufacturing [33], [38], [40]–[42]. While the benefits of AM in terms of material usage and manufacturing on demand for new or reconditioned parts are clear, the impact of AM on the sustainability of production are unclear. Challenges remain such as standardising the materials and processes, certifying and validating materials and their properties, scaling up the processes from laboratory based trials to production components and limited speed and reliability of AM technologies [33]. Additionally, there is large variation in energy and resource consumption between machines and usage models and little data available on environmental impact and process emissions of this emerging technology [43] making long term forecasting of sustainability difficult.

The cost barriers associated with AM contributing to preventing the widespread adoption of the technology into mainstream manufacturing can be mitigated by exploiting the opportunities for short, customisable production runs. In this application, it is important to utilise all available space in the build chamber to maximise efficiency [44]. Since the different available machines have different sized build chambers, the maximum benefit to be gained from simultaneous production of multiple components, in terms of energy consumption per kg, varies with machine manufacturer (Figure 5.2). A packing algorithm (Figure 5.3) has been developed which optimises the build platform packing and arrangement of components [45] to maximise production efficiency. This model highlights the advantage of processing numerous different components for different customers within the same build.



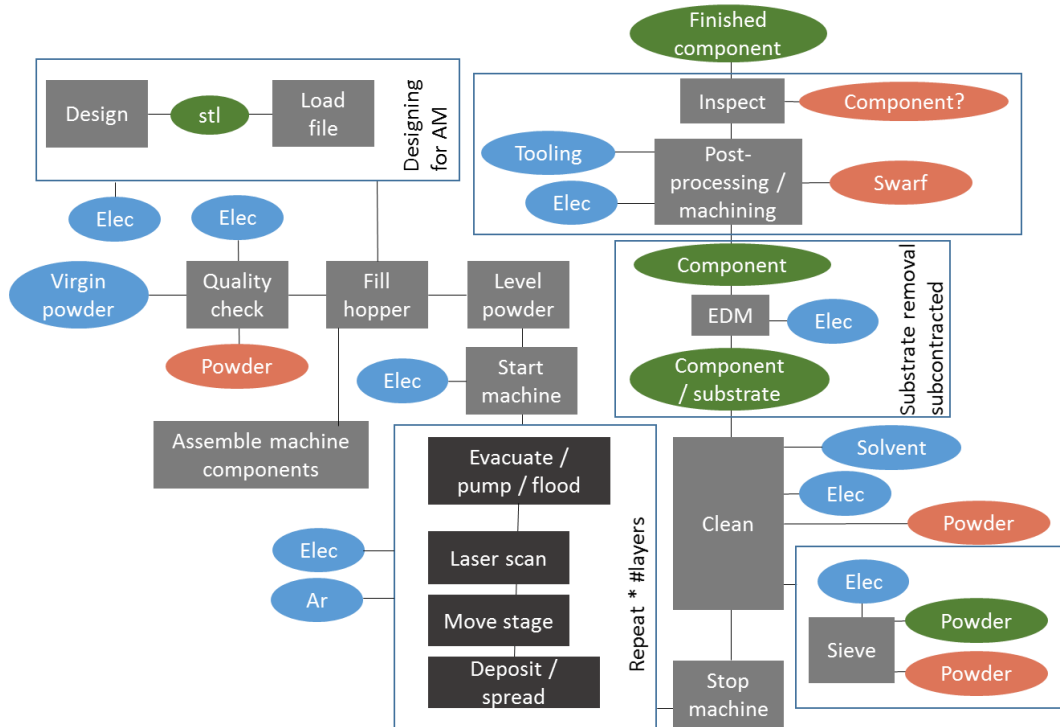


Figure 5. Energy flow for LPBF process.

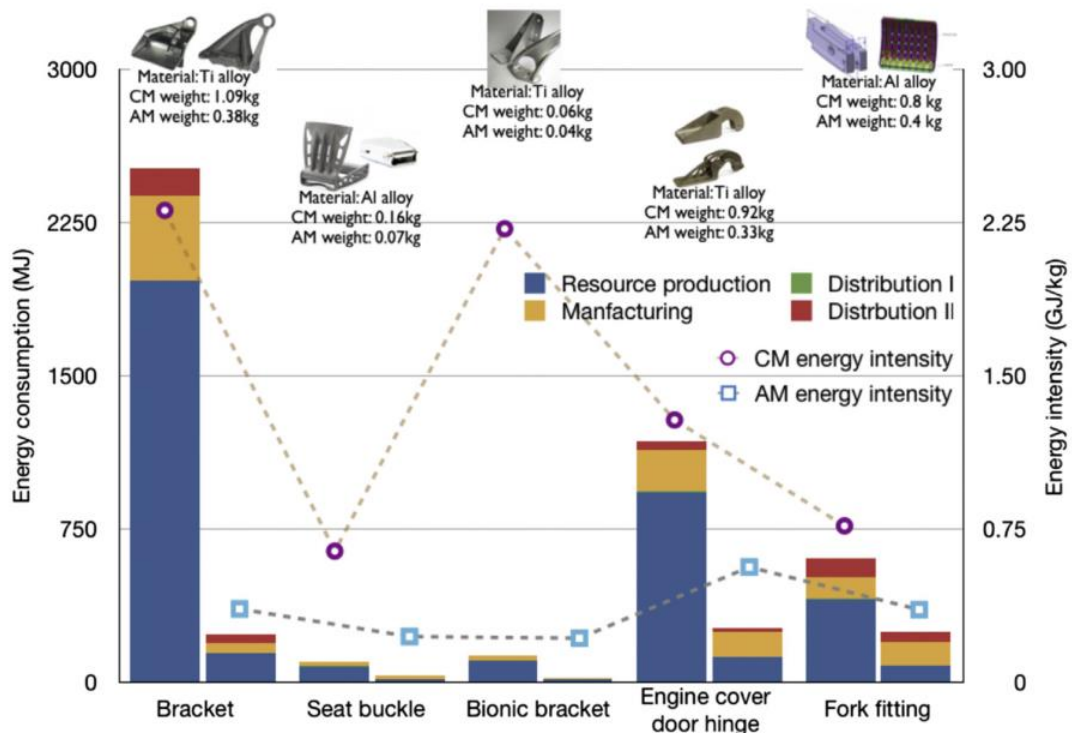


Figure 5.1. Comparison of energy consumption for AM vs CM for a number of aircraft components suitable for production via AM. From [38].

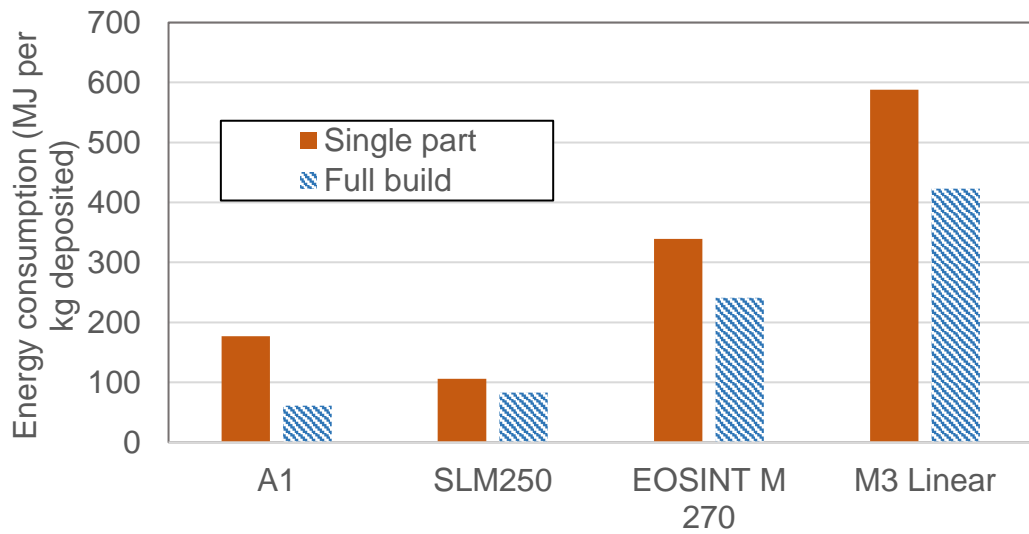


Figure 5.2. Energy consumption per kg deposited material vs machine supplier. Adapted from [44].

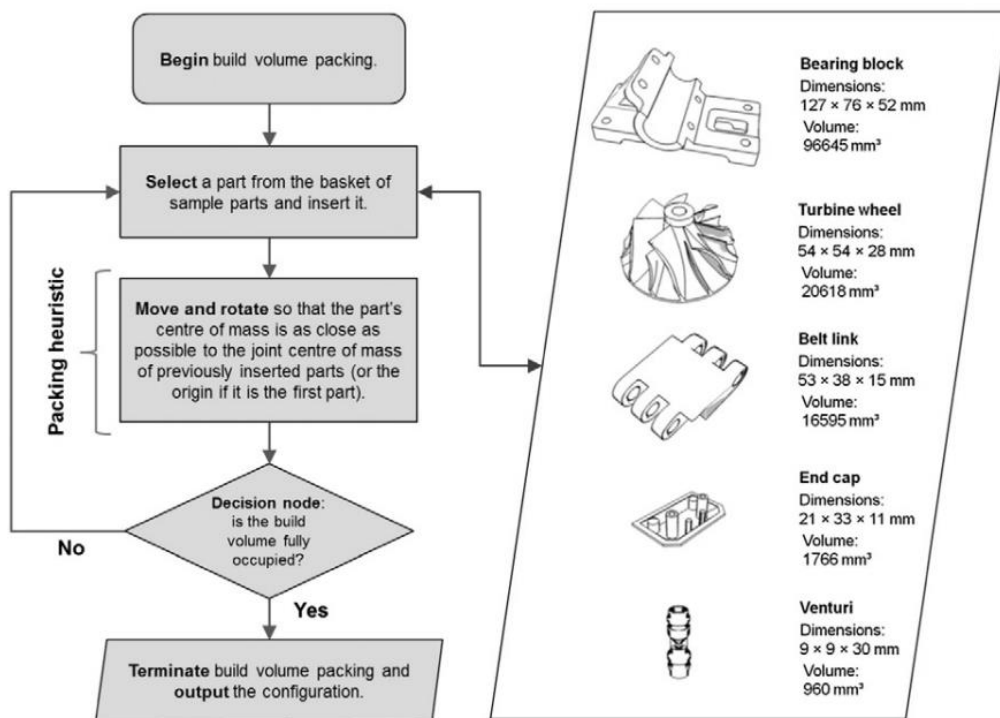


Figure 5.3. Flow chart of packing algorithm for optimal build platform usage. From [45].

## **6. Business case for AM within CMI**

This section presents the business case surrounding the use of AM within CMI for the production of components. Considering LPBF, two possibilities are presented; the production of low volume, high complexity production components with value added through design for AM and the use of LPBF to produce low volume service parts. Although these two manufacturing systems require differing inputs in terms of the pre-manufacturing procedure (e.g. design, customer ordering processes etc.) the reasons for LPBF being beneficial span the two applications. There are additional opportunities for the exploitation of AM techniques within CMI including use of BJP technology, and although the scope of this project restricts the experimental work to LPBF, the following discussion captures both possibilities.

### **6.1. Use of “Factory Physics”**

Factory physics refers to a systematic description of the behaviour of manufacturing systems, enabling improvements to be made to existing systems and facilitating the effective design of new ones [46]. In this section a “manufacturing system” is considered as the whole process from component conception to finishing and dispatch, including the placing of orders by the customer (rather than the specific AM hardware as referred to previously). Manufacturing systems can be divided into two types; push and pull. Put simply, a pull system limits the amount of work that can be in the system by beginning orders based on the status of the subsequent manufacturing step. Push systems produce inventory based on forecasted supply. Additive manufacturing processes are inherently suited to pull systems due to their applicability to low volume, customisable production runs with short lead times compared to CM techniques. In a pull system there is an inherent limit on the maximum inventory in the system and a strong emphasis on material flow. Disruptions in the production line do not cause unmanageable build-up of work because the in-built flexibility enables accommodation of scheduling, engineering or priority changes easily. Additionally, the limit on work-in-progress directly reduces the costs associated with inventory risk.

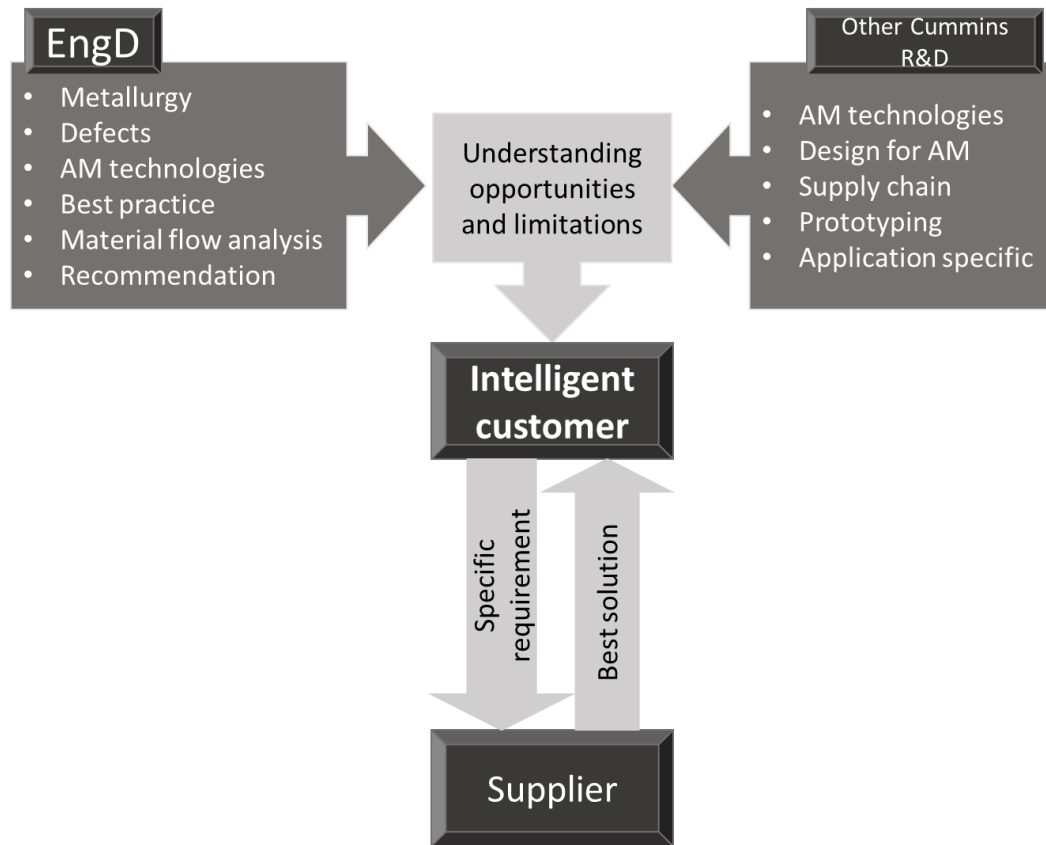
Although AM is inherently suited to a pull system, the nature of pull systems can be exploited to improve the output of AM. Pull systems need to contain processes with predictable flow, and low variability in cycle time in order to be able to quote and meet short lead times to customers. Careful and successful integration of AM into a pull system would require a detailed understanding of sources of variability in the AM technology, and methods of guaranteeing repeatability within manufacturing, furthering the development of the technology. To achieve the short cycle times and high throughput advertised as the main benefit of AM, the disruptive sources of variability must be reduced. This affects the choice of component, machine, material and post processing. Although not currently feasible, an ideal AM pull system would not involve any post processing at all in order to eliminate work-in-progress and potential for disruption between workstations.

As well as improving the technology, pull systems promote part quality because reject parts starve downstream processes. In order to eliminate this problem, the system requires statistical process control, created through quality-at-the-source procedures and process monitoring. To achieve low work-in-progress, high quality is essential, hence driving continual quality improvements. Statistical process control can be achieved by acceptance sampling, continual monitoring or by design of experiments (DOE). Acceptance sampling is not favourable because it slows down production and requires extra parts for testing, which are slow to produce using AM, so nullifies the main benefit of AM. Continual process monitoring is a feature which is beginning to be incorporated into LPBF hardware, however what is lacking is the knowledge to link the data collected to physical behaviours within the material. Design of experiments systematically vary inputs to determine the effect on quality measures using a variety of statistical tools. Data from multiple DOEs can be collected and used in machine learning algorithms to predict further material responses. After the cause and effect predictions have been experimentally validated, these models can be used to qualify the process rather than qualifying each individual component, or batch of components.

## 6.2. Applications

The logical consequence of utilising AM within a pull manufacturing system is that it should be used to produce components with short production runs, required in short lead times. Prototyping is a well-documented application of AM, however the costs associated with purchasing and running an AM machine prohibit occasional on-site prototyping. Prototypes suitable as performance demonstrators are easily obtainable at ever decreasing cost from external suppliers. For the purposes of material development, alternatives to R&D machine ownership also exist such as the Renishaw Solutions Centre which facilitates month by month rental of a machine alongside various other applicable technologies and access to their expertise. This type of facility is ideal for running short term DOE based projects to gain information about material behaviour or process optimisation for a certain application. At this stage a robust decision making process should be developed which can be used to decide whether AM is a suitable processing route for a certain component or application.

After sufficient information has been obtained through research projects in order to understand and predict the behaviour of a chosen material and component in an AM machine the company can act as an “intelligent customer”. This means that the complex inputs into an AM system and their benefits and limitations can be understood and used to discuss specific requirements with a supplier and obtain the most appropriate solution (Figure 6). The outcome of this may be that the business implications of using AM for a certain application are attractive and a production machine can be integrated into a pull system. Ultimately, the decision of whether a component is going to be produced via AM is based on cost, which is related to the application.



**Figure 6. Flow of information to and from an “intelligent customer”.**

Choosing the right technology for the right application and material is key to realising the full benefit of AM. Hence, a robust decision making process is needed to deduce whether AM will provide an advantage for a particular component and if so, which technology should be used. There is limited information available about the firm advantages to be gained by using various AM technologies, and the technologies are not yet sufficiently established that they could be employed immediately on a new application without considerable validation work. However, a Pugh matrix has been prepared to act as a guideline (Table 6).

**Table 6. Pugh matrix: Guidelines for choosing an appropriate AM process.**

	<b>Criteria</b>	<b>Datum</b>	<b>Comparators</b>	
		<b>LPBF</b>	<b>SEBM</b>	<b>BPJ</b>
<b>Component geometry</b>	Overhangs	S	-	+
	Minimum wall thickness	S	-	-
	Minimum feature size	S	-	-
	Large component volume	S	-	+
	Small component volume	S	S	S
	Internal features	S	S	-
<b>Output quality</b>	Internal defects	S	S	+
	Geometrical accuracy	S	-	-
	Fatigue critical components	S	-	-
	Surface roughness	S	-	-
<b>Feedstock</b>	Supply	S	S	+
	Cost	S	S	-
	Material usage efficiency	S	-	+
	Lower quality requirement	S	S	+
<b>Build</b>	Speed	S	S	+
	Production volume	S	-	+
	Process monitoring	S	S	S
	Automation	S	-	+
<b>Design</b>	Material reduction	S	S	S
	Assembly weight reduction	S	S	S
	Integration of Industry 4.0	S	S	S
	Integration of multiple components	S	S	+

### **6.3. Business case for LPBF within Cummins: The turbine wheel**

The turbine wheel is responsible for converting the heat energy from exhaust gas into mechanical work. The exhaust gas turns the turbine wheel at speeds of up to 200,000 rpm, which results in supersonic blade-tip speeds. The turbine wheel operates in a hostile environment of corrosive exhaust gases at temperatures of over 700 °C. Hence, high temperature creep resistance is essential for a robust system. The turbine wheel powers a compressor wheel which compresses fresh air and delivers it back to the engine, increasing the capacity to burn fuel, hence increasing the engine's power output.

There are two ways in which LPBF could be advantageous in the production of turbine wheels:

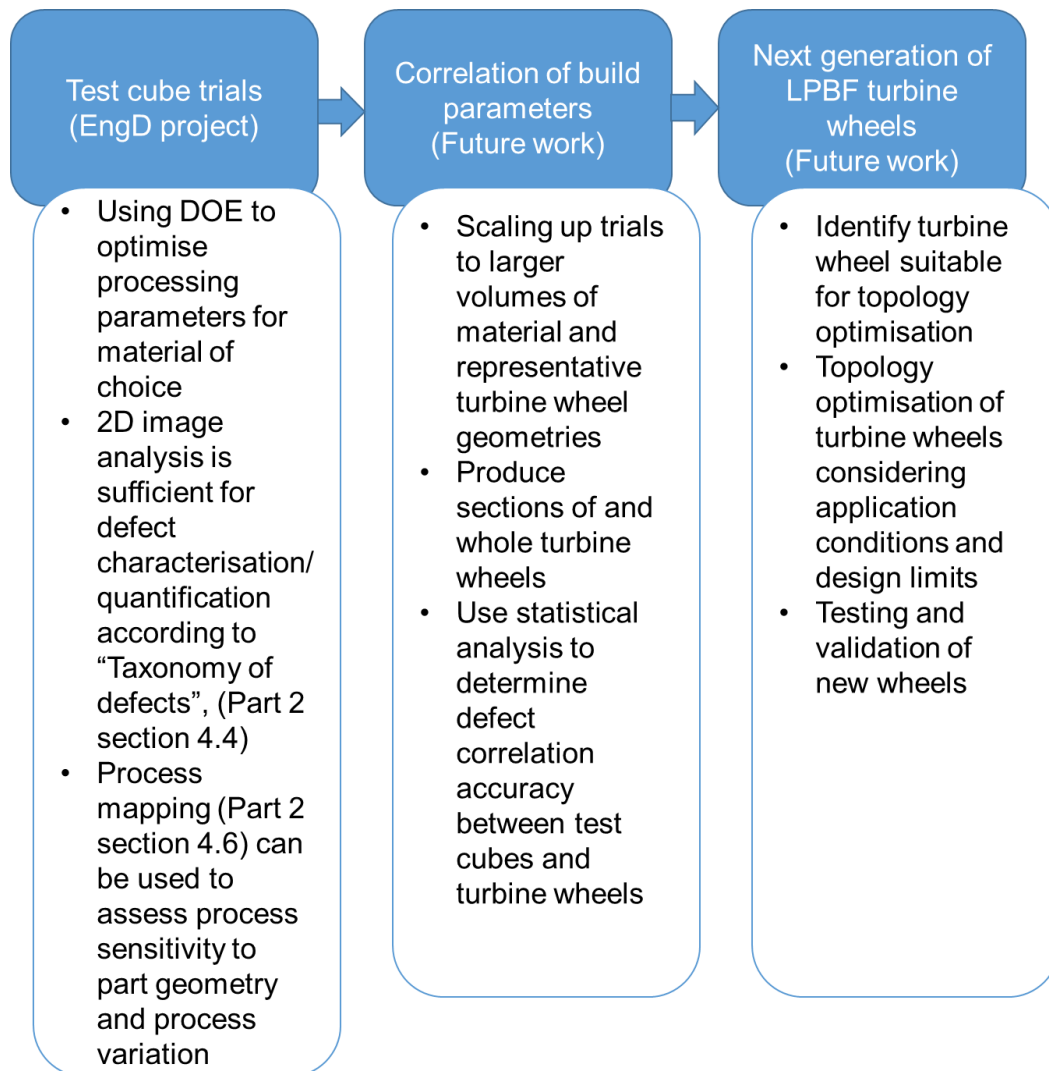
- 1) By overcoming some of the current limitations of conventional manufacturing, for example core shift during investment casting [47], design restrictions of investment casting [31] and production of costly investment casting moulds.
- 2) By adding value to a component through designing for AM and providing a business opportunity in a premium product with improved performance compared to a conventionally manufactured version of the component.

The first opportunity can be realised by offsetting the costs of AM against the costs of producing casting tooling by using it to manufacture components for which casting tooling no longer exists. For example, an obsolete service part or warranty case would represent an ideal application for pull manufacturing using LPBF even though this application does not benefit from the concepts of “designing for AM”.

For both of the above applications, a process must be followed in order to create a robust wheel. Assuming the metallurgical issues surrounding LPBF processing of high temperature nickel-base superalloys have been addressed and mitigated for (see part 2 for a full discussion) the LPBF process must be optimised for each new component. Through the experimental work conducted in Part 2 of this thesis, valuable information and experience has been gained and facilitated the production of a LPBF characterisation and optimisation flow chart (Figure 6.1) which describes



the steps which should be taken when using LPBF in a new application, taking the production of a new turbine wheel as an example.



**Figure 6.1. Route to LPBF of a new component.**

## 7. Impact of the project

A second “VOC” questionnaire was conducted at the end of this project in order to assess its effect on the way AM is perceived by the project stakeholders. A summary of the main outputs is given in Appendix 2. The project has been held in high regard within Cummins. Some key aspects of the impact of the project, taken from responses to the VOC are:

- 73% respondents envisaged AM adoption within the business to occur within the next 2-5 years
- 91% respondents said their perception of AM had changed as a consequence of the outputs of this project
- 82% respondents now have a better understanding of AM technologies, their applications and their limitations
- 91% respondents can see the benefits of using AM in a carefully selected application
- <1% respondents still believe AM is only suitable for prototyping
- 18% respondents think AM is less feasible as a production technology than they previously thought

Comments:

- “Able to rely on Charlotte’s work and experience as “in-house” expertise on the topic of Metal AM
- “This project has allowed key knowledge to be shared which is important to success of integrating AM into the business
- “This project has not changed how we do work in CTT but it has broadened the knowledge around asking for rapid prototypes and what the implications from these samples can be
- “I have got a much deeper understanding of how the Laser Powder bed system works and some of the difficulties

## 8. Summary of Part 1

- The scope of this EngD project was to assess the feasibility of LPBF of IN713C from a technical and commercial perspective.
- Powder bed fusion technologies are used for the fabrication of net shape components, from powdered metal feedstock, using either a laser or an electron beam as a focussed heat source.
- The benefits are most effectively realised for small components with complex geometries which cannot be produced via conventional manufacturing.
- LPBF hardware currently available on the market is better suited to research and development activities than production, however technologies which are designed to enable production such as automation and process monitoring are now emerging on the newest generation of LPBF machines.
- AM offers design freedom over traditional manufacturing methods and eliminates the need for costly casting tooling. This makes AM suitable for the production of obsolete service parts for which casting tooling no longer exists.
- Inventory risk is reduced through the use of AM since the short lead times and economic advantage of small production volumes enables customisable runs and production on demand.
- Integrating AM into the work flow improves innovation through better communication and collaboration between design and manufacturing engineers.
- Misconceptions about AM being suitable only for prototyping, as well as the expense of the hardware and lack of industry standards is inhibiting the wider adoption of the technology
- A limited selection of engineering alloys have been developed since metallurgical issues remain a barrier to production of more complex alloy systems.
- Three routes are visible for the business case for LPBF within Cummins:
  - Using LPBF to overcome current design limitations of conventional manufacturing.
  - Adding value to a component through “designing for AM”.
  - Using LPBF to manufacture obsolete service parts.

## PART 2

### Scientific studies

#### Contents

1. Introduction.....	44
2. Literature review.....	48
2.1. Nickel base superalloys .....	48
2.1.1. Definition and applications .....	48
2.1.2. Superalloy metallurgy .....	51
2.1.3. Weldability.....	54
2.2. Solidification .....	55
2.2.1. Solidification microstructures .....	57
2.2.2. Non-equilibrium processing of metals.....	60
2.2.3. Rapid solidification .....	61
2.3. Laser powder bed fusion defects .....	65
2.3.1. Porosity .....	65
2.3.2. Cracking.....	72
2.3.3. Solidification cracking models.....	76
2.3.4. Mitigation strategies against solid state cracking.....	81
2.3.5. Mitigation strategies against solidification crack nucleation.....	82
2.3.6. Mapping out the process .....	84
2.4. Summary of Chapter 2 .....	87
3. Experimental techniques.....	88
3.1. Renishaw SLM125 features and operation .....	88
3.2. Process terminology .....	89
3.3. Statistical experimental methods.....	90

3.3.1.	Design of experiments.....	90
3.3.2.	Linear regression.....	92
3.3.3.	Central composite design.....	92
3.3.4.	Analysis of variance (ANOVA).....	93
3.4.	Characterisation techniques.....	94
3.4.1.	Sample preparation.....	94
3.4.2.	Microscopy.....	97
3.4.3.	X-ray computed tomography (XCT).....	97
3.4.4.	Atom probe tomography.....	99
3.4.5.	Thermo-calc simulation.....	102
4.	Process mapping of LPBF IN713C.....	103
4.1.	Exploring the process space.....	103
4.1.1.	Experiment 1: Capturing the extremes of the process space.....	105
4.1.2.	A thought experiment: The concurrence of LOF and keyholing..	111
4.1.3.	Experiments 2, 3 and 4.....	112
4.2.	Melt pool modelling.....	115
4.3.	Concepts.....	120
4.3.1.	Attenuated parameters.....	121
4.3.2.	LOF conditions.....	122
4.4.	Taxonomy of defect types.....	128
4.5.	Minimising porosity in LPBF processed IN713C using response surface methodology with 2D and 3D characterisation techniques.....	134
4.5.1.	Fabrication of LPBF specimens.....	134
4.5.2.	Optical microscopy.....	135
4.5.3.	XCT powder characterisation.....	135
4.5.4.	Effect of process setting on overall defect area fraction.....	135

## The Application of AM to Ni-base Superalloys

4.5.5.	Individual defect analysis.....	140
4.5.6.	Implications.....	144
4.6.	Understanding the process space.....	146
4.7.	Summary of Chapter 4 .....	151
5.	Cracking.....	152
5.1.	LPBF test cube samples (Experiment 5) .....	152
5.2.	Image analysis and initial observations.....	153
5.3.	Modelling the solidification conditions.....	156
5.4.	Application of Clyne and Davies model .....	159
5.5.	Application of RDG model for HCS .....	161
5.5.1.	Rapid solidification or solute trapping? .....	161
5.5.2.	Dendrite spacing calculations .....	162
5.5.3.	Calculation of HCS .....	166
5.6.	Application of KGT model for segregation .....	172
5.6.1.	Methods.....	173
5.6.2.	Results and discussion .....	173
5.7.	APT of a cell boundary .....	175
5.7.1.	APT results and discussion .....	175
5.8.	TEM observations .....	181
5.9.	Summary of Chapter 5 .....	186
6.	Thesis summary: A hypothetical stroll around the process map .....	188
7.	Conclusions.....	191
7.1.	Part 1.....	191
7.2.	Part 2.....	191
8.	Further work .....	194
8.1.	Crack mitigation .....	194

8.2. Impact of defects of mechanical properties.....	194
8.3. Future work within Cummins.....	194
References.....	195
Appendix 1: Initial “Voice of customer” questionnaire .....	209
Appendix 2: Initial “Voice of customer” questionnaire .....	213
Appendix 3: SOP for Renishaw SLM125.....	215
Appendix 4: Method for Glyceregia etching of IN713C LPBF samples to reveal melt traces and dendritic structure.....	229
Appendix 5: Characterisation of powdered feedstock .....	230
Appendix 6: Analytical melt pool model.....	235
Appendix 7: Matlab code for numerical integration involved in calculations of HCS .....	241

## 1. Introduction

Turbocharging is central to improving the performance and reducing the fuel consumption of internal combustion engines for both on and off-highway applications. Enabling downsizing of an engine using a turbocharger to boost inlet pressure reduces fuel consumption by up to 14% and significantly reduces HC, CO and NO emissions [48]. In order to stay ahead of increasingly stringent emissions legislation, turbocharger OEMs are pursuing novel designs which can provide high efficiency over a wide range of engine speeds. The turbine wheel is a key component in this challenge since its material performance and aerodynamic behaviour at high temperature and high rotational load determine the efficiency, capacity and often, life of the turbocharger.

As discussed in part 1, the investment casting process, by which turbine wheels are conventionally manufactured, limits the scope for the design of novel turbine wheels. Additive manufacturing has the potential to offer increased design flexibility and innovation by bypassing the geometry restrictions of casting moulds, reducing component weight, and improving the design process by facilitating the fast acquisition of performance demonstrator parts. Realistically though, the cost and speed of AM restricts its use to low volume, high complexity, premium products. In addition to the benefits for new turbocharger designs for high end, specialist turbomachinery, AM also has a viable business case in the production of obsolete turbomachinery for which tooling no longer exists.

Immediate adoption of the technology is currently prohibited by two major factors. Firstly, the technology is relatively new, so confidence in the process both from a business perspective and in terms of process variability is low enough for AM to be considered a risky undertaking. The new nature of the process also means that costly AM machines are quickly made obsolete by a next generation, making it difficult to know when to enter the market. Secondly, the process is not well defined in terms of the behaviour of many common engineering materials, especially those suitable for high temperature applications such as the turbine wheel. This challenging aspect of AM will be treated throughout the remainder of this thesis.



High temperature engineering alloys such as nickel-base superalloys were designed to be used in the cast or wrought condition and as such are well suited to processing under these conventional manufacturing routes. However, processing them using laser based technology causes complex solidification behaviours and defect formation which are yet to be fully understood or controlled. A good place to start in describing the issues related to LPBF processing of these alloys is with a comparison of the processing physics of the two processes.

During investment casting, a wax pattern is coated with a ceramic material and then melted out of the new mould. Molten metal is then poured into the cavity and, once the metal has solidified, the ceramic mould is broken away. Thermally, this process comprises a large (relative to LPBF) volume of molten material, which upon contact with the mould will initially cool rapidly, this rate of cooling slowing as more metal is poured and the thermal mass of the casting increases. The majority of the casting volume will cool slowly. The difference in cooling rates between the outer edges and internal volume of the casting leads to a characteristic grain structure of finer columnar grains at the edge and coarser grains in the centre. This process is well understood, and grain structures can be tailored to suit the application with high confidence in the quality and variability of the output.

The conditions imposed on the material during LPBF are more complex, occurring over significantly shorter time frames and must be considered on a more local scale rather than on the scale of the component since the volume of molten material at any one time and the lifetime of the melt is significantly smaller than in investment casting. During LPBF, a laser heats a localised area of material, causing a tear drop or oval shaped pool of molten material. Heat from the melt conducts to the surrounding material creating a heat affected zone. The melt pool can be assumed to solidify at the same rate as the laser moves, which can be as fast as 4 m/s. The large thermal mass of the surrounding cold material causes the small melted region to cool rapidly. Some proportion of the affected material will be re-melted when the laser makes subsequent passes on neighbouring tracks or ensuing layers.

The high residual stresses caused by rapid cooling and the complex thermal history due to several re-melting or re-heating stages cause a plethora of complex,

interdependent, behaviours which are difficult to isolate, understand and control. Failure modes in LPBF manufactured materials generally fall within one of the following categories; voids (pores, cracks), geometrical inaccuracy (swell, deformation, droop) and chemical composition (evaporation of elements, contamination). This work focusses on the formation of various types of voids and how they are affected by the processing conditions. If processing conditions are selected such that insufficient energy is imparted to any part of the powder bed, the powdered metal feedstock will not be fully consolidated. This can occur if the scan speed is set too fast relative to the laser power and layer thickness, or if the melt tracks are spaced too far apart. If too much energy is delivered, through a combination of a high laser power and low scan speed, defects such as keyholing, melt splashing and solidification cracking are reported. These high energy defect types are largely independent of layer thickness, since the inevitable re-melting of previous layers causes splashing and keyholes in the same manner as would occur in a bed of powder, although it should be kept in mind that other effects such as difference in absorptivity and conduction differs between powdered and bulk metal and as such the energy available for the formation of these defects will differ.

Solidification cracking, occurring in the final stages of solidification, is an issue prevalent in, although not restricted to, precipitation strengthened nickel-base superalloys. It is exacerbated by a high ratio of laser power to laser speed, since this leads to larger melt pools, with longer lifetimes, allowing more time for elemental segregation. Processing in the solute trapping regime of rapid solidification should be beneficial for the reduction of solidification cracking, however this comes at the expense of stress relief cracking which occurs in the solid state due to high levels of residual stress. nickel-base superalloys which are generally regarded as unweldable due to high propensity for gamma prime formation, are also highly susceptible to solidification cracking during LPBF.

Defect formation in LPBF materials is a widely researched subject and mitigation and control of various defect types in alloys such as Ti-6Al-4V [4]–[7], stainless steel 316L [49], [50] and IN718 [12], [51] is now well understood. Processing maps such as those developed by Thomas et al [52] allow comparisons between different alloys and assist with visualisation and understanding of the process window for

different materials. Processing conditions for various alloy systems have been developed by machine suppliers which are suitable for producing material with density and defect populations transparent to those of castings and are commercially available for use with those machines. Having said this, post processing steps such as hot isostatic pressing, heat treatment and machining are usually necessary to achieve the desired properties. LPBF still requires optimisation to be the one-step processing technique as advertised in the media.

The most challenging barrier for the processing of high temperature nickel-base superalloys is that of cracking, particularly solidification cracking, and considerable disagreement still surrounds the exact mechanism for the formation of these defects. Sharp defects such as cracks are particularly detrimental to the fatigue life of materials, something which is of extreme importance to a component such as a turbine wheel which experiences high cyclic loads in service. Understanding how to process these alloys while avoiding solidification cracking could unlock the potential for lucrative possibilities for producing complex components not only for turbomachinery but for other high temperature applications in the automotive and aerospace sectors.

Part 2 of this thesis contributes to increasing the understanding of the behaviour of IN713C, a precipitation strengthened nickel-base superalloy used for investment casting of turbocharger turbine wheels, when processed using LPBF. IN713C has not been widely investigated under LPBF conditions because it is considered to be highly un-weldable due to its high titanium and aluminium content. Combined with its potential for use in specialist, or obsolete turbine wheel production, the particularly challenging nature of this alloy makes it an ideal candidate for an investigation into defect formation since it readily displays the features of interest.

Nickel base superalloys are introduced alongside a detailed discussion around LPBF solidification conditions. The processing and conditions are used within multiple literature models to assess the relative effects of changing solidification conditions on defect formation.

## 2. Literature review

### 2.1. Nickel base superalloys

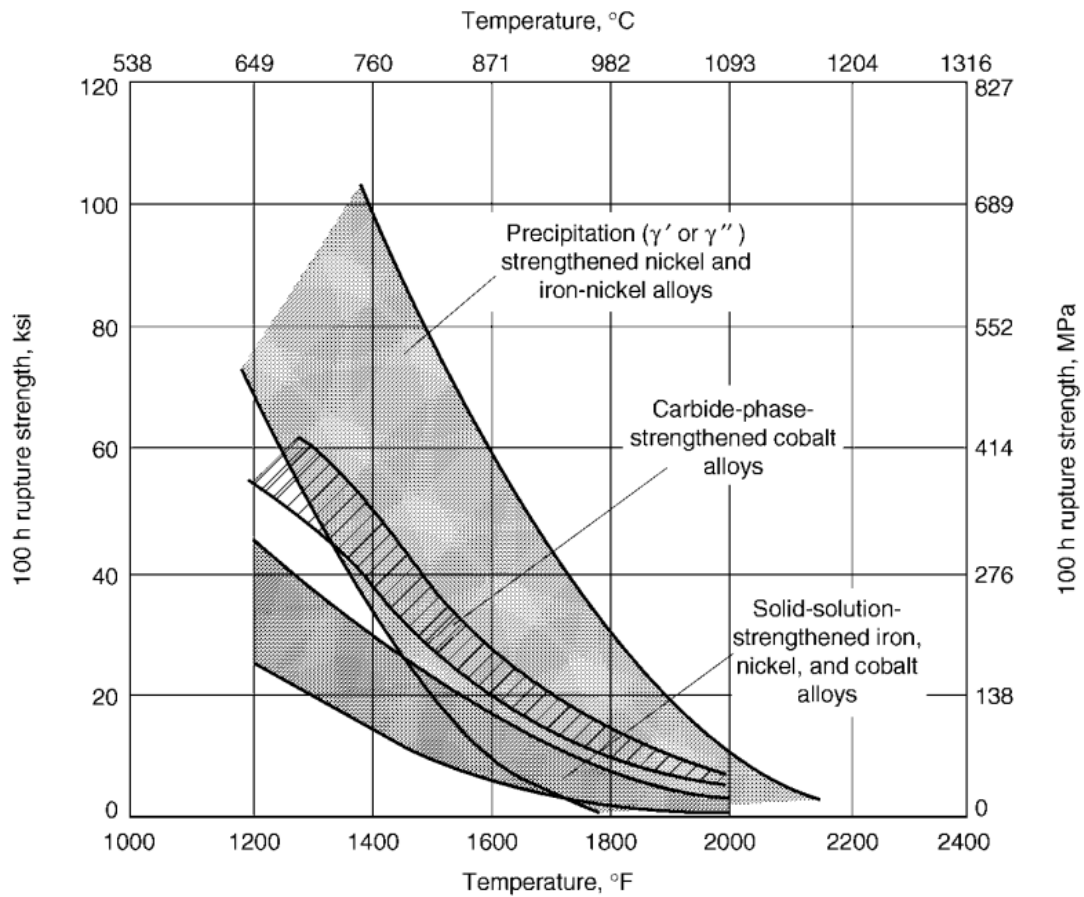
#### 2.1.1. Definition and applications

Superalloys are nickel, iron-nickel or cobalt-base alloys, invented for use in high temperature applications, generally above 1000 °C [53]. At temperatures up to 50% of the melting range (Kelvin), the strength of ordinary alloys becomes a function of the length of time it is measured, even if the load would not be sufficient to cause failure at room temperature. This elongation of the material over time at high temperature is called creep. Superalloys are usually cast or wrought, and contain large volume fractions of a hardening phase, significantly improving their creep rupture strength compared to ordinary alloys. Hence, superalloys are widely used in gas-turbines, chemical plants and petrochemical applications [54] and their upper limit for temperature is defined by incipient melting of constituent alloying elements, or by the dissolution of the strengthening phases. [53]

Strengthening of nickel-base superalloys is achieved by three mechanisms; solid-solution strengthening, work hardening and precipitation strengthening; the latter being superior in terms of creep rupture strength (Figure 2.1). The dominant strengthening mechanism depends on the alloy composition and processing route. Increasing demand for higher temperature applications lead to the emergence of precipitation strengthened superalloys. These were developed later and rely on the addition of aluminium and titanium to form strengthening  $\gamma'$  ( $\text{Ni}_3(\text{Al,Ti})$ ) precipitates, which are coherent with the fcc matrix phase ( $\gamma$ ) in nickel-base superalloys.

Nickel-base superalloys are the focus of this work, relating to the ultimate goal of applying laser powder bed fusion (LPBF) technology to turbomachinery, in particular Inconel 713C (IN713C) from which turbine wheels are cast in the conventional production route. IN713C is favourable because it is easily cast and has excellent high temperature properties [55] due to a high volume fraction of  $\gamma'$ . Excellent high temperature properties come at the expense of fabrication. Highly alloyed compositions with high fractions of  $\gamma'$  are generally regarded to be

un-weldable [56] due to a high susceptibility for cracking. This also causes difficulties in LPBF processing of these alloys [57], [58] due to the similarity in the thermal experience of the material between the techniques. Weldability is treated in more detail in section 2.1.3. For high temperature, highly stressed applications such as a turbocharger turbine wheel, a material which is more easily welded such as IN718 or Hastelloy X would not be suitable due to the dramatic reduction in stress rupture strength around the operating temperature of a turbine wheel (Figure 2.2).



**Figure 2.1. Stress rupture strengths of superalloys. From [53].**

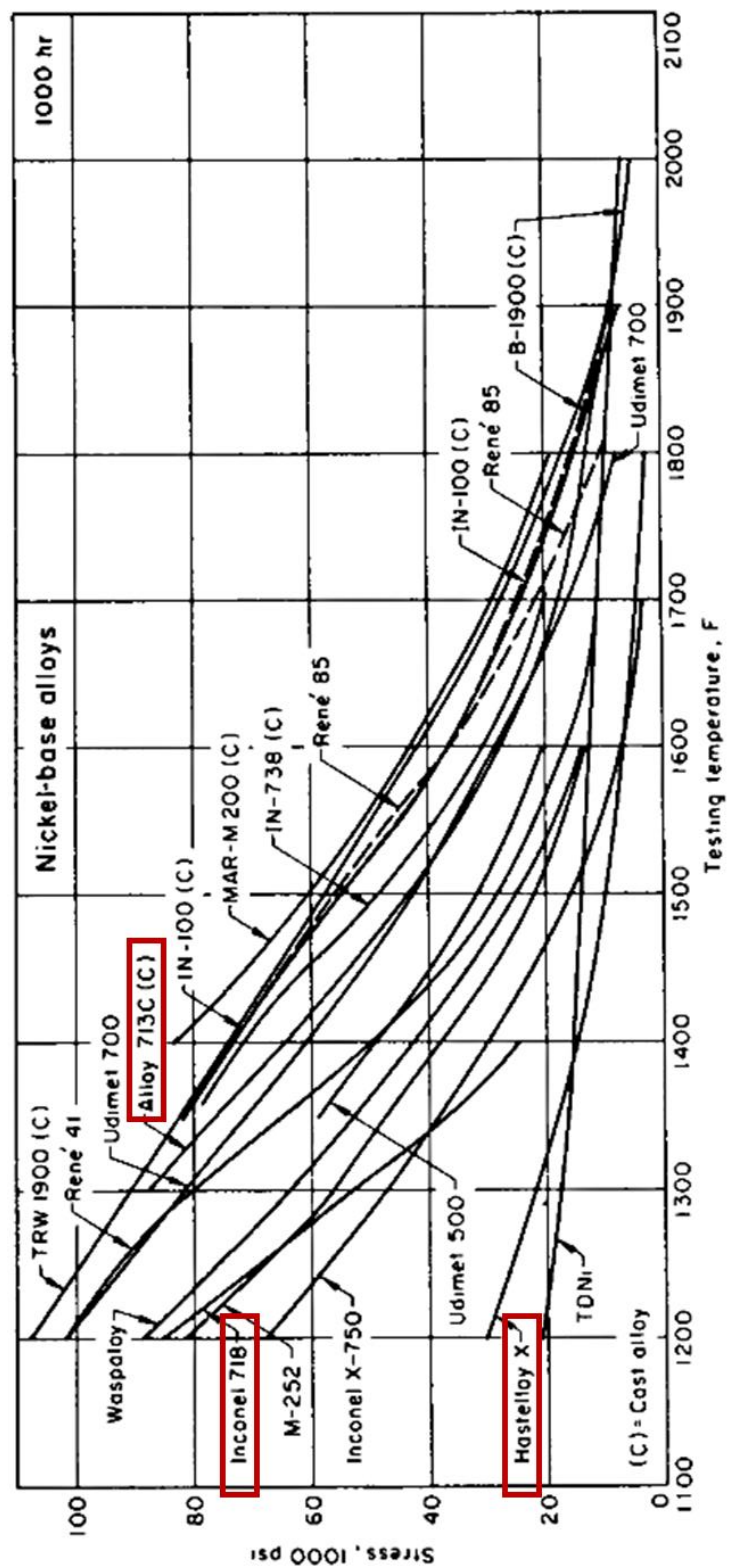


Figure 2.2. Comparison between 1000h stress rupture strength of Hastelloy X, IN718 and IN713C. From [53].

### 2.1.2. Superalloy metallurgy

The composition of IN713C, as well as the compositions of IN718 and Hastelloy X for the purposes of comparison are given in Table 2.1. Nickel–base superalloys have an austenitic, fcc matrix phase ( $\gamma$ ) which remains stable down to room temperature and hosts a number of secondary phases. Some of the secondary phases are engineered since they provide a benefit in terms of the properties of the superalloy and some detrimental phases are actively avoided (Table 2.2). The deleterious  $\sigma$ ,  $\mu$  and Laves phases are topologically close packed (tcp) and become detrimental to mechanical properties when present above trace amounts [53], leading to reduced ductility and premature failure. In IN713C the principal strengthening phase is  $\gamma'$ , however some nickel base superalloys precipitate both  $\gamma'$  and  $\gamma''$  such as IN718, in which  $\gamma''$  provides the dominant strengthening effect.

**Table 2.1. Nominal compositions of three superalloys.**

Element	IN713C	IN718	Hastelloy X
Cr	12.0-14.0	17.0-21.0	20.5-23.0
Fe	< 2.5	bal	17.0-20.0
Mo	8.0-10.0	2.8-3.3	8.0-10.0
Al	5.5-6.5	0.2-0.80	-
Ti	0.5-1.0	0.65-1.15	-
Zr	0.05-0.15	-	-
Nb	1.8-2.8	4.75-5.5	-
Cu	< 0.50	< 0.3	-
B	0.005-0.015	< 0.006	-
Co	-	< 1.0	1.5-2.5
Mn	< 0.25	< 0.35	0.2-1.0

Element	IN713C	IN718	Hastelloy X
Si	< 0.50	< 0.35	< 0.10
W	-	-	0.6-1
C	0.08-0.20	< 0.08	0.05-0.15
S	< 0.015	< 0.015	-
Ni	bal	50.0-55.0	bal

**Table 2.2. Secondary phases in nickel-base superalloys.**

Beneficial phases	Deleterious phases
Carbides (MC, M <sub>23</sub> C <sub>6</sub> , M <sub>6</sub> C, M <sub>7</sub> C <sub>3</sub> )	Sigma ( $\sigma$ ) tcp
Gamma prime ( $\gamma'$ ) fcc ordered Ni <sub>3</sub> (Al,Ti)	Mu ( $\mu$ ) tcp
Gamma double prime ( $\gamma''$ ) bct ordered Ni <sub>3</sub> Nb	Laves tcp
Eta ( $\eta$ ) hexagonal ordered Ni <sub>3</sub> Ti	
Delta ( $\delta$ ) orthorhombic intermetallic compounds Ni <sub>3</sub> Nb	

Adding alloying elements to a nickel matrix affects the phase stability of the alloy and consequently its mechanical properties. The effects of various alloying additions are summarised in Table 2.3. Elements with increasingly different sized atomic radii to nickel whilst retaining sufficient solubility are the best solid solution strengtheners, including cobalt, chromium, iron and molybdenum [54]. Titanium and aluminium contribute to precipitation strengthening by precipitating the  $\gamma'$  (Ni<sub>3</sub>(Al,Ti)) phase, while niobium is used for both solid solution strengthening and precipitation strengthening via precipitation of  $\gamma''$  (Ni<sub>3</sub>Nb). Molybdenum and tungsten have low diffusivity in nickel, hence improve creep strength.

IN713C contains up to 0.2 wt% carbon, hence it has the propensity to form carbides under certain processing conditions. MC-type carbides, with fcc structures, form



during the late stages of solidification from the grain boundary or interdendritic segregation of elements such as titanium, molybdenum or niobium. The MC-type carbides can be replaced by  $M_{23}C_6$  carbides when subjected to temperatures between 760°C-980°C, either during heat treatment or in service.  $M_{23}C_6$  carbides are stabilised by chromium and molybdenum. Between 815°C-980°C,  $M_6C$  carbides can form, when molybdenum content is above 6-8 atomic percent. IN713C contains approximately 4.5 atomic percent so is unlikely to form  $M_6C$  type carbides. Carbides can act as strengthening phases by restricting grain boundary sliding, but can also act as stress raisers in the microstructure, creating crack initiation points. Since the carbides reside along grain boundaries where liquid films are likely to form, this coincidence may increase the likelihood of cracking local to the boundaries.

**Table 2.3. Role of alloying elements in nickel -base superalloys, adapted from [53].**

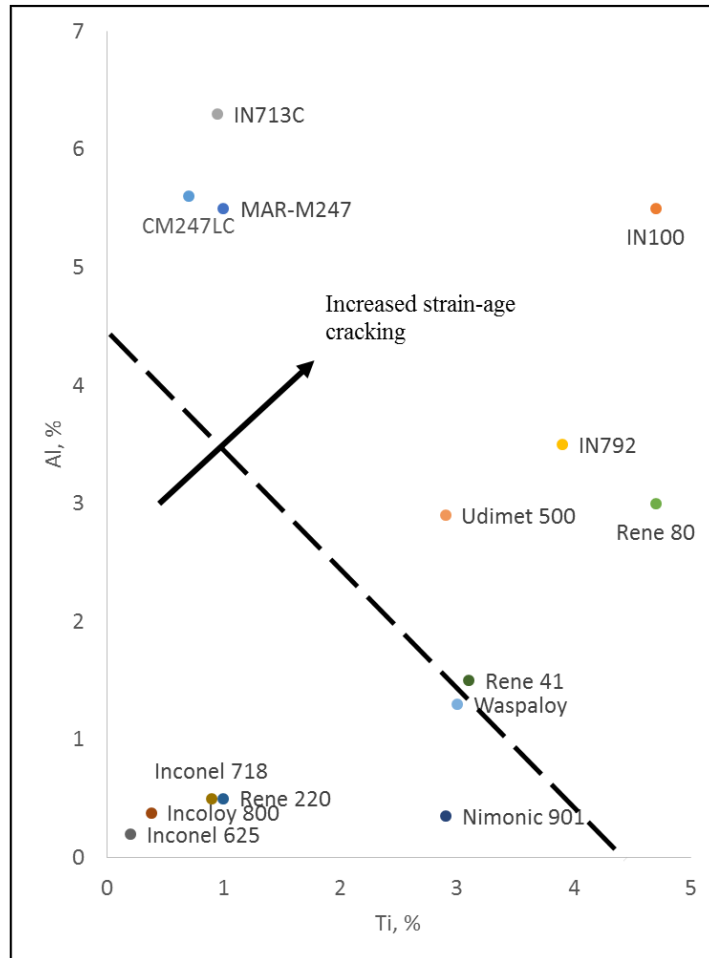
<b>Element</b>	<b>Effect</b>
Co, Cr, Fe, Mo, W, Ta, Re	Solid-solution strengtheners
W, Ta, Ti, Mo, Nb	MC carbide formation
Cr	$M_7C_3$ carbide formation
Cr, Mo, W	$M_{23}C_6$ carbide formation
Mo, W, Nb	$M_6C$ carbide formation
C, N	M(CN) carbonitride formation
Al, Ti	$\gamma'$ ( $Ni_{13}(Al,Ti)$ ) formation
Co	Raises solvus temperature of $\gamma'$
Al, Ti, Nb	Form hardening precipitates or intermetallics
Al, Cr	Oxidation resistance
B, Ta	Creep resistance

Element	Effect
B	Rupture strength
B, C, Zr	Grain boundary refiners

### 2.1.3. Weldability

Welding of nickel-base superalloys is affected by issues such as fusion zone solidification cracking, heat affected zone (HAZ) liquation cracking, ductility dip cracking (DDC) and strain age cracking (SAC), however SAC is specific to precipitation strengthened nickel-base superalloys and does not occur in any other class of superalloy. Alloying additions of titanium and aluminium in precipitation strengthened nickel-base superalloys, included to increase strength through rapid onset of  $\gamma'$  precipitation, result in their high susceptibility to SAC. SAC is a solid state cracking mechanism which usually occurs during post-weld heat treatment in the HAZ near the fusion boundary [54].

The rate at which  $\gamma'$  forms as a precipitate is a key factor in the susceptibility of an alloy to SAC and is affected by the aluminium and titanium content. The weldability diagram (Figure 2.3) describes the susceptibility to SAC of nickel-base superalloys according to their aluminium and titanium content. The HAZ is particularly vulnerable to SAC during the heating phase of the treatment, up to the solution annealing temperature. If this temperature cannot be reached quickly enough then the C-Curve temperature-time regime in which precipitation is possible is intersected meaning that hardening and stress relaxation occur simultaneously [54]. The result is high strain at grain boundaries causing grain boundary failure and cracking. It is unlikely that SAC is contributing to the crack susceptibility of IN713C during LPBF due to the rapid heating of the re-melted zone. However, the weldability diagram does reflect the processability of nickel-base superalloys using LPBF and provides a helpful illustration of those alloys in which achieving crack free structures is likely to be challenging. A detailed discussion of potential LPBF cracking mechanisms is given in section 2.3.2.



**Figure 2.3. Weldability diagram of nickel-base superalloys showing susceptibility to SAC. Adapted from [54].**

## 2.2. Solidification

Solidification plays a vital role not only in the economical production of metallic components through casting, but also to this project since the majority of the LPBF phenomena of interest (formation of defects) occur during the transition from the liquid to the solid phase. The solidification path, affected by the thermal history of the melt, influences the microstructure of the material and hence its mechanical properties. Thus, it is of great importance to understand and control solidification during any manufacturing process. In castings, solidification theory is well established and the final microstructures can be engineered with precision to achieve grain structures appropriate to the application; for example, radially oriented grains, single crystal nickel-base superalloys and directional casting [59].

## The Application of AM to Ni-base Superalloys

Fundamentally, solidification involves the extraction of heat from a melt by a heat flux, causing a decrease in enthalpy due to cooling and a decrease in enthalpy due to the liquid-solid phase transformation. Under slow cooling rate conditions (casting) the cooling rate, given by Equation 2.1 [60], depends on the heat flux away from the melt ( $q_e$ ) the ratio of the surface area of the casting ( $A$ ) to its volume ( $u$ ), the rate of formation of solid phase ( $df_s/dt$ ) and the ratio of the latent heat of fusion ( $\Delta H_f$ ) to the specific heat capacity ( $C_p$ ).

$$\dot{T} = \frac{dT}{dt} = -q_e \left( \frac{A}{uC_p} \right) + \left( \frac{df_s}{dt} \right) \left( \frac{\Delta h_f}{C_p} \right) \quad (\text{Eq. 2.1})$$

For a heat flux which is constant with time and uni-directional, the growth rate of the solid ( $V$ ) and the thermal gradient ( $G$ ) are de-coupled and can be independently controlled. The growth of the solid phase occurs in a direction which is parallel and opposite to the direction of heat flux. The cooling rate at a given location and time is given by Equation 2.2 [60].

$$\dot{T} = GV \quad (\text{Eq. 2.2})$$

This relationship is important because the ratio of  $G$  and  $V$  influences the stability of the solidification front and consequently, the microstructure.

### 2.2.1. Solidification microstructures

During solidification, the material goes through three stages; liquid, liquid plus solid (mushy zone) and solid. The mushy zone is where the characteristics of the microstructure are determined, including grain size, shape and orientation, concentration and distribution of alloying elements and various types of strain induced defects. It is in the mushy zone that the local solidification conditions dictate whether a microstructure will be columnar or equiaxed. There are two main forms of solidification microstructure; eutectic and dendritic. Which form proceeds depends on the solidification conditions and the composition. For alloys, the form is usually dendritic. [60]

Dendrite growth begins to occur when the solidification front velocity is fast enough to cause a planar solidification front to become unstable, producing first cells then dendrites (Figure 2.4) [60], [61]. Cells grow in a direction parallel and opposite to the direction of heat flux, whereas dendrites grow along a preferred crystallographic orientation ( $\langle 001 \rangle$  for cubic crystals) and each shares low angle grain boundaries with its neighbours. If the solidification front velocity becomes so fast that solute trapping occurs, the planar solidification front is re-established.

The stability of the interface is driven by the growth temperature of the microstructural features (Figure 2.5). When the dendrite formation temperature is greater than the planar front formation temperature, the planar front is morphologically unstable. A banded microstructure of cells or dendrites and the planar front can form when the solidification velocity is between the limit of absolute stability ( $V_a$ ) and the point where the planar front is re-established ( $V_{Tmax}$ ).

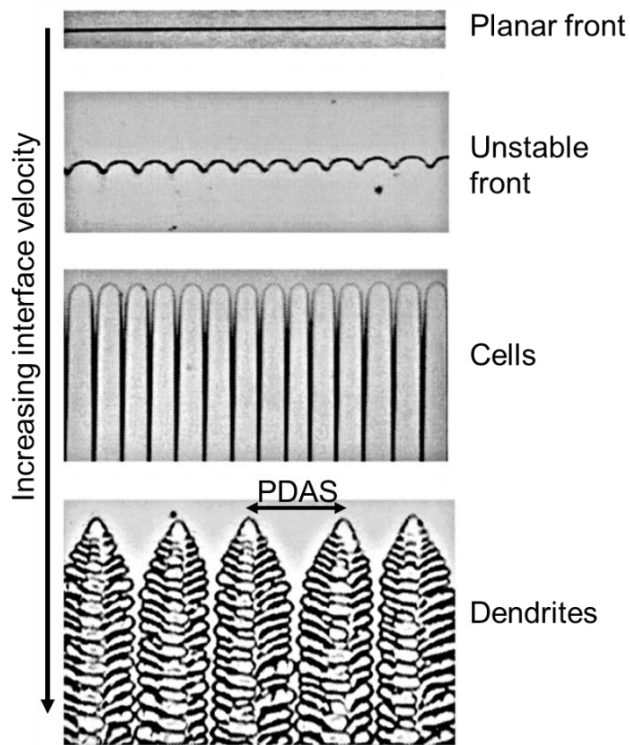


Figure 2.4. Evolution of the solidification front with increasing velocity. Primary dendrite arm spacing (PDAS) is labelled. Adapted from [61].

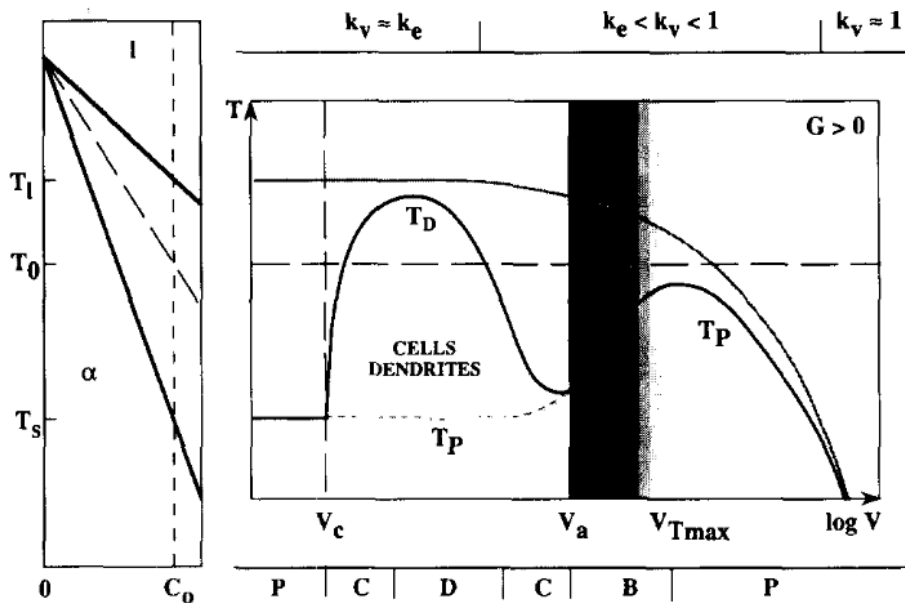


Figure 2.5. Interface response function typically observed in surface laser processing. Dendritic growth prevails when its formation temperature ( $T_D$ ) is greater than that of planar growth ( $T_P$ ). (P, plane front; C, cells; D, dendrites; B, bands). From [62].

The grain structure after solidification is also dependent on the solidification conditions and can be columnar, equiaxed or a mixture of both depending on the local conditions. Columnar grains form through competitive growth away from a heat sink whereas equiaxed grains grow radially from a central nucleus in a supercooled melt. In this case, the supercooled melt acts as the heat sink, so growth and heat flux are in the same direction in equiaxed growth. The columnar to equiaxed transition (CET) is dependent on the grain nucleation rate which can be increased by increasing the undercooling. Since undercooling is increased by increasing cooling rate, the CET is dependent on  $G$  and  $V$  (Equation 2.3) and two material specific constants  $n$  and  $K$ .

$$\frac{G^n}{V} > K \quad (\text{Eq. 2.3})$$

In directional solidification, the dendrites have a primary trunk and secondary dendrite arms. The separation distances between them are known as the primary and secondary dendrite arm spacing respectively (PDAS, SDAS). In equiaxed solidification, the dendrites do not have a primary trunk, so only one classification of dendrite arm spacing is necessary (DAS). Dendrite spacing is dependent on  $G$  and  $V$ . Numerous models exist for the calculation of dendrite spacing according to solidification conditions [60], [63], [64]. Alternatively, if measurements of dendrite spacing exist, the models can be used to calculate the conditions which led to their formation.

For the case of directional growth (columnar grains), Kurz and Fisher derive an expression for PDAS based on the length of the interdendritic liquid and the assumption that the trunk spacing is equal to the dendrite tip radius. Approximating the mean cross section of the dendrites to an ellipse and assuming the trunks are arranged in a close-packed hexagonal formation leads to the expression for PDAS ( $\lambda_l$ ) in Equation 2.4 [60] where  $\Delta T_0$  is the equilibrium solidification temperature range,  $D$  is the diffusion coefficient in the liquid and  $\Gamma$  is the Gibbs-Thompson coefficient. For non-equilibrium processing, this expression must be modified. This modification, along with other models for PDAS is discussed in section 2.2.3.

$$\lambda_1 = 4.3G^{-\frac{1}{2}} \left( \frac{\Delta T_0 D \Gamma}{Vk} \right)^{\frac{1}{4}} \quad (\text{Eq. 2.4})$$

SDAS is a function of time, since their ripening causes them to become coarser, more widely spaced and with fewer branches. Equation 2.5 [60] gives SDAS ( $\lambda_2$ ) where  $M$  is a composition dependent ripening parameter and local solidification time ( $t_f$ ) depends on solidification temperature range,  $G$  and  $V$ .

$$\lambda_2 = (Mt_f)^{\frac{1}{3}} \quad (\text{Eq. 2.5})$$

During solidification, solute redistribution causes local changes in composition. Under normal solidification conditions, assuming equilibrium at the interface, the partition coefficient ( $k_0$ ) describes the composition difference between the solid phase ( $C_S$ ) and the liquid phase ( $C_L$ ) according to Equation 2.6 [60].

$$k_0 = \left( \frac{C_S}{C_L} \right)_{T,P} \quad (\text{Eq. 2.6})$$

Equation 2.6 is only valid for very slow cooling rates or very high solute diffusivity in the solid. This situation results in no segregation since the liquid composition prior to freezing and the solid composition after freezing are both equal to the original composition. In all other situations (non-equilibrium) the partition coefficient becomes velocity dependent. This is treated in section 2.2.2.

### 2.2.2. Non-equilibrium processing of metals

Superior properties can be achieved from processing materials under non-equilibrium conditions. For example, metastability can be exploited to enhance strength by heat treatment of a non-equilibrium supersaturated solid solution [65].

In non-equilibrium conditions, the partition coefficient ( $k$ ) is dependent on solidification velocity (Figure 2.5). In this work, the expression given by Equation 2.7, formulated by Aziz using the continuous growth model [66], has been applied consistent with its use by Kurz, Giovanola and Trivedi (KGT) [67] where  $a_0$  is a length scale related to the interatomic distance. It can be seen that for low  $V$  or high  $D$ ,  $k = k_0$  and the situation returns to that described in Equation 2.6.



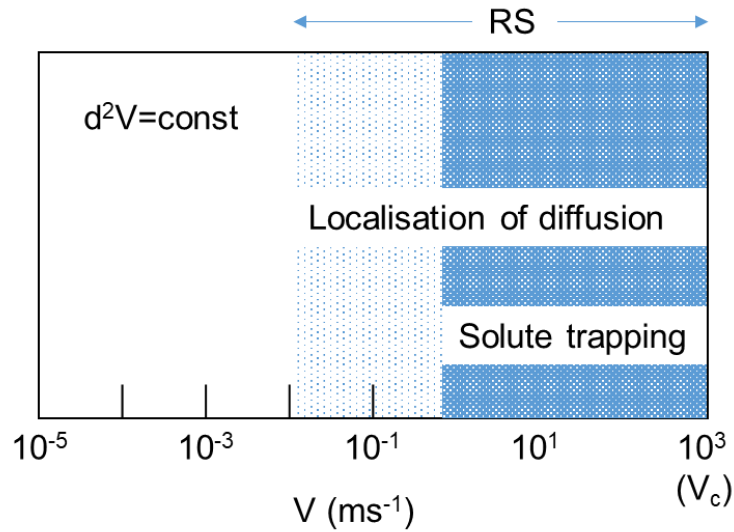
$$k = \frac{k_0 + (a_0V/D)}{1 + (a_0V/D)} \quad (\text{Eq. 2.7})$$

### 2.2.3. Rapid solidification

The term “rapid solidification” (RS) refers to the short time interval between initiation and completion of the phase transformation from liquid to solid with high velocity of the solidification front [65]. A high cooling rate is required and can be achieved using a heat sink. RS occurs in the range of solidification front velocities between  $10^{-2} \text{ ms}^{-1}$  to  $10^3 \text{ ms}^{-1}$ . Kurz and Trivedi established this range from the following conditions [62]:

- 1) The diffusion field becomes shorter than the microstructural scale when the Peclet number ( $P = Vd/2D$  where  $d$  is characteristic length scale, e.g. tip radius) becomes larger than unity. This occurs when the interface velocity is of the order of centimetres per second. (At interface velocities below RS conditions, the microstructure follows the relationship  $d^2V = \text{const.}$ )
- 2) The diffusion distance becomes comparable with the interface width and local non-equilibrium at the interface is established, leading to solute trapping. This occurs when the velocity of the interface, given by the ratio of diffusion coefficient to interface width, is of the order of metres per second.
- 3) The interface movement driven by atom attachment reaches the velocity of sound ( $V_c$ ) and cannot move any faster. This occurs when the interface velocity is in the order of kilometres per second.

The distinction between criteria 1 and 2 above gives rise to two RS regimes; localisation of diffusion and solute trapping (Figure 2.6).



**Figure 2.6. Rapid solidification regimes. Adapted from [62].**

In LPBF the melt pools are small (of order of  $100 \mu\text{m}$  wide [4], [5] and  $0.5\text{-}2 \text{ mm}$  long [68]) and are surrounded by solid, relatively cold, material. This acts as the heat sink, setting up high cooling rates ( $10^5\text{-}10^7 \text{ K/s}$  [68], [69]). With solidification front velocities equal to typical laser velocities between  $0.5 - 4 \text{ m/s}$ , LPBF processing lies within the RS region on the boundary between localisation of diffusion and solute trapping. The solidification front velocity varies with depth. On the surface of the melt pool it is coupled to the velocity of the heat source, so material solidifies at the same rate as it melts. The velocity decreases to zero at the bottom of the melt pool [62], [65]. Since  $G$  and  $V$  vary with position in the melt pool it is feasible that processing could occur on different sides of the solute trapping boundary in different parts of the melt pool and hence different parts of a component according to local solidification conditions. Solute trapping becomes an important consideration when dealing with solidification cracking susceptibility since stronger solute segregation can extend the vulnerable zone [70]. This is discussed in section 2.3.2.4.

Local conditions at the dendrite tip play an important role in predicting microstructure. Approximations of the dendrite tip radius form the basis for numerous models such as dendrite spacing and liquid concentration at the dendrite tip ahead of the solidification front. The latter can be calculated using Equation 2.8

from the KGT model [67] and will be used in 5.6 to investigate the relationship between local freezing range conditions at the dendrite tip and the cracking response of IN713 processed using LPBF.

$$C_l^* = \frac{C_0}{1 - (1 - k)Iv(P)} \quad (\text{Eq. 2.8})$$

Where  $C_0$  is nominal solute concentration and  $P = rR/2D$  is the Peclet number where  $r$  is dendrite tip radius. For  $P \gg 1$  the Ivantsov function approximates to  $Iv(P) \sim 1 - \frac{1}{P} + \frac{2}{P^2}$  [71]. The tip concentration varies with  $V$  and is high in the plane front – cellular regimes and lower at higher  $V$  [60].

Returning to the discussion of dendrite spacing, the two dominant models for PDAS by Kurz and Fisher [63] (Equation 2.9) and Trivedi [64] (Equation 2.10) involve the non-equilibrium partition coefficient and the non-equilibrium solidification temperature range  $\Delta T$  (difference between the dendrite tip temperature and the non-equilibrium solidus).

$$\lambda_1 = 4.3 \left( \frac{\Delta T}{G} \right)^{\frac{1}{2}} \left( \frac{D\Gamma}{Vk\Delta T_0} \right)^{\frac{1}{4}} \quad (\text{Eq. 2.9})$$

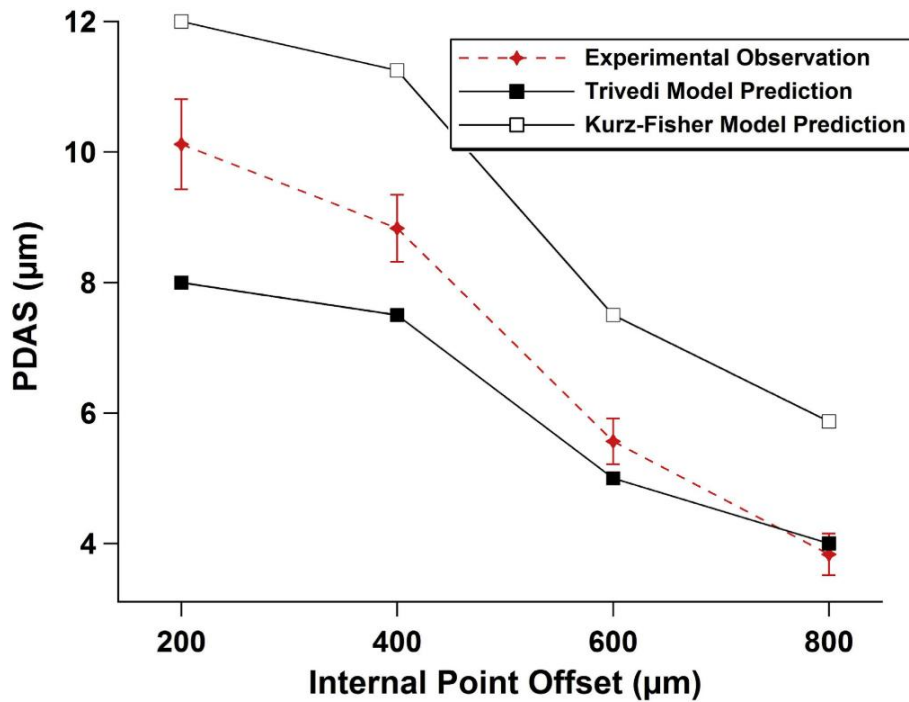
$$\lambda_1 = 2.83G^{-\frac{1}{2}} \left( \frac{\Delta T_0 LkD\Gamma}{V} \right)^{\frac{1}{4}} \quad (\text{Eq. 2.10})$$

Where  $\Gamma$  is the Gibbs-Thomson coefficient and  $L$  is a harmonic of perturbation constant. These equations apply in the high solidification front velocity range described by Equation 2.11.

$$V > \frac{GD}{\Delta T_0 k_0} \quad (\text{Eq. 2.11})$$

Equations 2.9 and 2.10 are both modifications to the Hunt model of PDAS in steady state growth [72], which was the first model to move away from the preceding ad-hoc approximations to  $\lambda_1$  [73], [74]. The Hunt model is based around the tip operating point of the dendrite and use the marginal stability criterion introduced by Langer and Muller-Krumbhaar (LMK) [75]. The LMK approach describes the stability of the dendrite to small perturbations away from its steady state shape and

combines this stability criterion with the steady state solutions discussed previously to locate the “tip operating point” of the dendrite in terms of tip radius and tip growth rate for a given undercooling. The Trivedi model differs from the Kurz and Fisher model by a more elaborate determination of tip radius and super saturation. The two models have been shown to be upper and lower bounds for the estimation of DAS in AM [51] (Figure 2.7) with experimental measurements for dendrite spacing lying in between.



**Figure 2.7. Comparison of experimentally measured and numerically predicted PDAS as a function of internal point offset (an electron beam PBF processing parameter). From [51].**

Empirical models for DAS have also been developed through comparison of microstructures formed under different thermal processing regimes. Davies et al [76] compared the microstructures formed by melt spinning IN718 ribbon with cast microstructures to obtain the relationship given in Equation 2.12.

$$\lambda_1 = (97 \pm 5) \dot{T}^{-(0.36 \pm 0.01)} \quad (\text{Eq. 2.12})$$

### **2.3. Laser powder bed fusion defects**

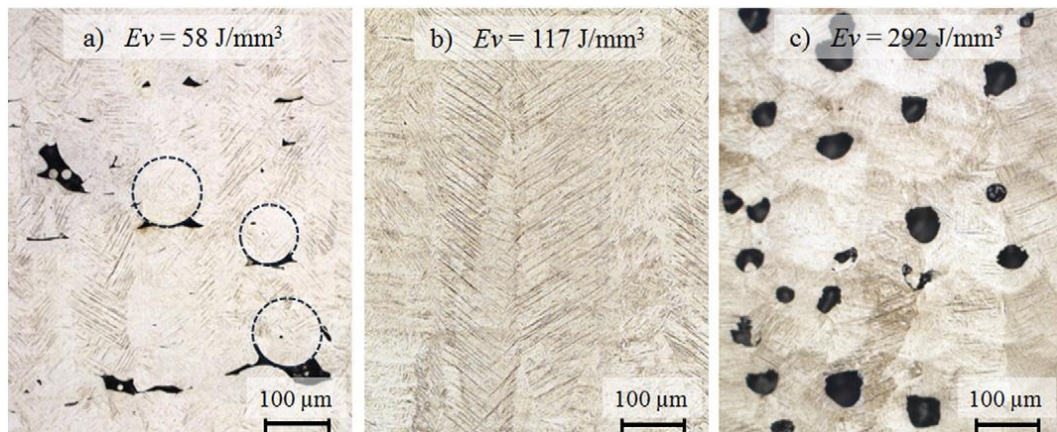
The LPBF process involves a large number of input factors which affect the quality of the material. These include process inputs which describe the system functionality (e.g. metal feedstock, laser power, laser speed), control factors related to the system design (e.g. machine hardware, machine set up) and external noise factors (e.g. part-to-part variation, feedstock variation, machine wear, contamination). Process inputs must be optimised using statistical experiments to understand and control the behaviour of a material in a LPBF system. Control factors must be chosen intelligently to ensure an appropriate combination of machine, material and application is made. Noise factors, although out of the control of the operator, should be understood in terms of their effect on process variability in order to minimise their detrimental effect on properties and process efficiency. Failure to understand and control the various input factors inevitably leads to the formation of defects (e.g. pores, cracks, segregation, and contamination).

By definition, all defects are detrimental to the mechanical properties of a material, however the extent to which properties are affected and the effect of this on the life of the component depends on the specific defect type. In AM samples, voids lead to early failure and lower ductility [17] especially those which are large and irregularly shaped [77]. The effect of defects on mechanical properties and fatigue life are also dependent on their position in the component, becoming more critical if they reside near a surface [78]. This section reviews the possible defect types observed in LPBF processed materials and the conditions under which they are observed.

#### **2.3.1. Porosity**

Three processing regimes are identified [14], [79] which are related to the energy density imparted to the powder bed by the heat source (Figure 2.8). The low power regime tends to produce lack of fusion (LOF) defects since insufficient energy is delivered to fully melt and consolidate the powder and to ensure re-melting of underlying layers to obtain layer adhesion. This regime can also lead to porosity through melt instabilities resulting in melt track discontinuity and regions of un-

melted powder [80]. LOF defects are large (usually on the scale of the melt pool) and are elongated in the plane of the layers [6]. The middle regime is one in which the energy imparted to the powder is optimised such that the powder is fully melted and melt pools overlap sufficiently to fully consolidate the powder. Should too much energy be imparted to the powder the third regime is entered where keyholing behaviours are reported [79]. Excess power causes penetration of vapour into the underlying solidified material.

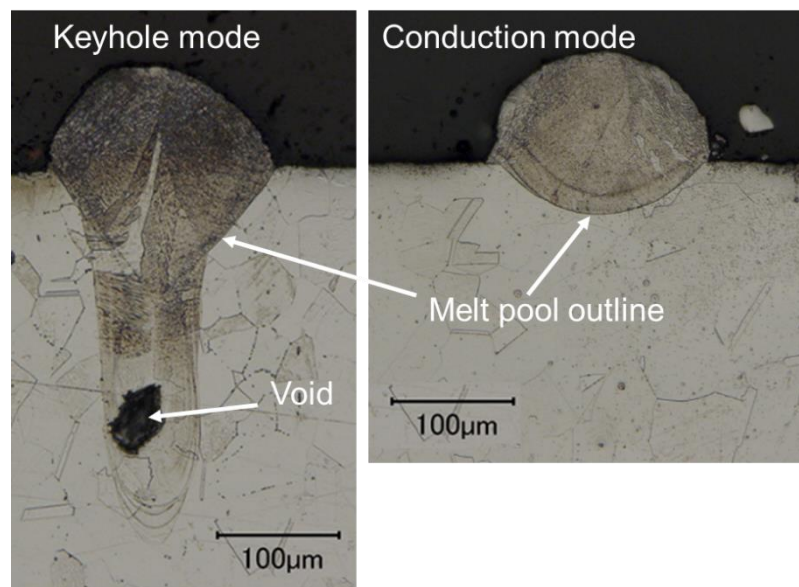


**Figure 2.8. Three processing regimes in Ti-6Al-4V corresponding to insufficient, correct and surplus input energy density resulting in lack of fusion, complete melting and keyholing respectively. From [14].**

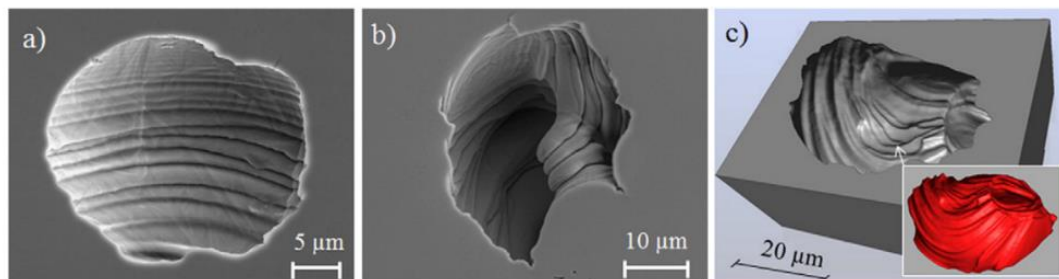
Keyholing behaviour refers to more than just the formation of voids. The keyhole mode is one in which the depth of the melt pool is controlled by evaporation of the metal rather than conduction of heat, which is normal in the optimum processing range (conduction mode) [50]. In keyhole mode the melt pool depths are significantly larger than in conduction mode and often contain a void near the deepest part of the pool, caused by the collapse of the vapour cavity after evaporation. In conduction mode, the melt pool cross section is approximately semicircular [81]. However, after the transition to keyhole mode melt pools can be characterised by a depth more than twice their width (Figure 2.9) [5], [50]. The transition point for keyhole mode melting has been expressed by King et al [50] in terms of a normalised enthalpy,  $\Delta H/h_s$ , where  $\Delta H$  is specific enthalpy and  $h_s$  is the

enthalpy at melting. For stainless steel 316L, with layer thickness of 50  $\mu\text{m}$ , the transition to keyhole mode was predicted to occur at  $\frac{\Delta H}{h_s} \approx (30 \pm 4)$ .

The voids formed during keyhole mode are easily identified, due to both their position at the base of the melt pool and their distinctive characteristics. Surface tension forces exert a shear force on the highly dynamic melt pool, which solidifies quickly, preserving the swirling features on the internal surface of the voids (Figure 2.10). These voids are usually spherical or oval and  $> 50\mu\text{m}$  in diameter [14].



**Figure 2.9. Examples of melt pools in LPBF 316L in keyhole mode and conduction mode. Adapted from [50].**



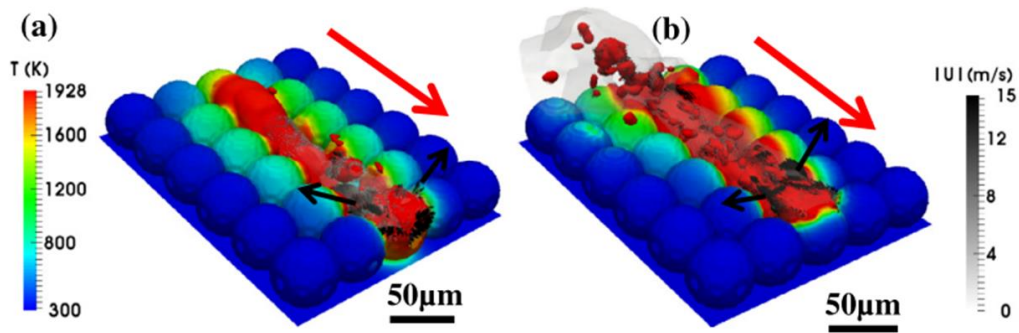
**Figure 2.10. Keyhole mode voids imaged using scanning electron microscopy (a,b) and x-ray computed tomography (c). From [14].**

Gas porosity is another void type defect observed during LPBF. Gas pores tend to be spherical and no larger than 50  $\mu\text{m}$  in diameter [6]; forming when gas is trapped within the solidifying structure. Gas residing in the pockets between powder particles may dissolve in the melt and remain there after solidification due to high solidification rates in LPBF processing, provided that thermodynamically and kinetically favourable conditions exist. This condition is exacerbated by the high temperature of the melt, increasing the solubility of the gas [6]. Alternatively, gas pores have been reported to result from retention of prior gas porosity in the powdered metal feedstock [82], [83]. Gas porosity may be able to be reduced by increasing the melt pool lifetime to allow gas bubbles more time to escape the surface tension of the melt [84].

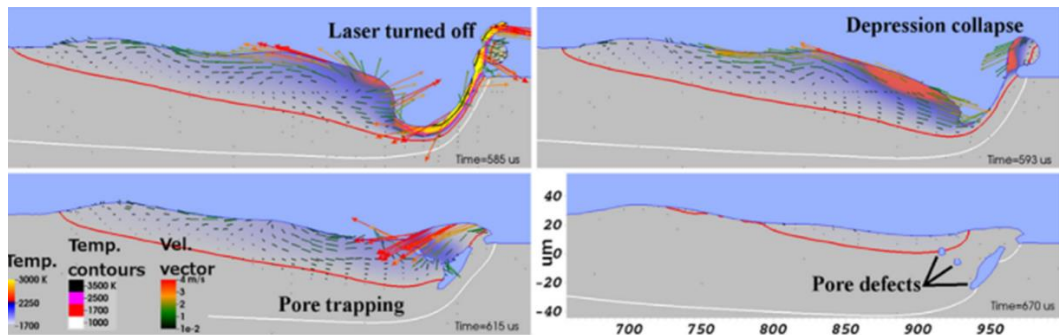
Vilaro et al [6] identify LOF defects and entrapped gas defects in the same sample in LPBF processed Ti-6Al-4V, the former being elongated and the latter spherical. They identify LOF defects as the most influential on tensile strength since LOF defects containing un-melted powder are visible on fracture surfaces. Gong et al [77] are in agreement in their study on LPBF and selective electron beam melting (SEBM) Ti-6Al-4V, reporting reduced hardness of samples containing LOF defects and no change in those containing gas porosity, concluding that the process is more tolerant to slight excesses of power than it is to insufficient power due to the effects of LOF defects on fatigue life.

Melt pool instabilities can cause splashing effects which also lead to porosity. Qiu et al [85] found that increasing the laser velocity decreased the stability of the melt pool and increase the scattering of molten material (Figure 2.11), increasing the occurrence of large, irregularly shaped voids with globular morphologies. The melt splashing was observed to occur alongside a blurred tail in high speed imaging of melt pools leading the authors to suspect that melt splashing and material evaporation occur simultaneously under the same processing conditions. Khairallah et al [86] describe melt splashing as a “bow wave” of liquid ahead of the laser spot which, upon its collapse, traps pores in the solidifying material (Figure 2.12).





**Figure 2.11. Thermal fluid flow prediction of the interaction between laser heat source and a bed of powder particles for low (a) and high (b) scan velocities. From [85].**



**Figure 2.12. Velocity vector field following a melt pool depression showing the mechanism for pore formation after melt splashing. From [86].**

Powder denudation around the melt pool causing a non-symmetric melt pool can also be a cause of irregularly shaped voids. This is caused by the entrainment of powder particles in the flow of gas resulting from the Bernoulli effect after vapourisation of the melt pool centre [86], [87]. Hence, this phenomenon also occurs in the high energy processing regime.

Design of experiments (DOE) and analysis of variance (ANOVA) have been used to study the relationships between processing parameters and porosity in CoCrMo by Monroy et al [88] and in AlSi10Mg alloy by Read et al [9]. Whilst both these studies acknowledge the presence of two types of pores originating from different sources, neither treats them independently in their analyses. Monroy uses ANOVA to investigate effects of layer thickness, laser power and laser velocity, finding layer thickness most strongly affecting the amount of porosity and velocity most

significant for pore size [88]. The interaction between layer thickness and laser velocity was significant on both responses. This study must be interpreted carefully since it was performed on a self-developed LPBF machine which features an inclined build platform. The ANOVA process is presented in a more sophisticated way in the study by Read et al who use DOE to find a two-factor interaction model with laser power, laser velocity and the interaction between these parameters [9]. They use the three processing regimes, linked to energy density to rationalise their findings.

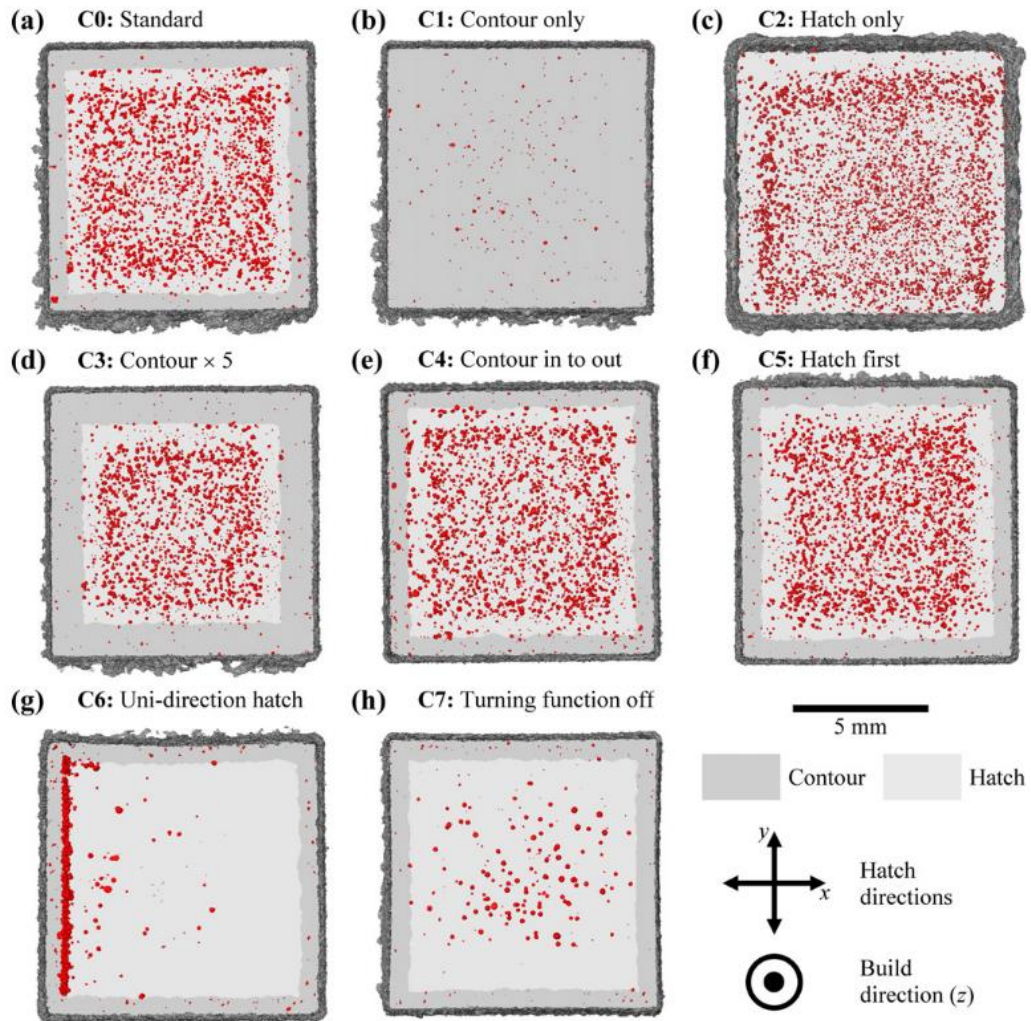
It must be noted that these kinds of studies are limited because the allocation of pore formation mechanisms to specific observations and quantification of porosity methods are often subjective. To quantify porosity in a sample many studies use the Archimedes method [4], [6], [77], [89] which gives a quick and easy indication of relative densities of a set of samples. However, this method has drawbacks. For example, with LOF defects the pores are likely to hold un-melted powder, which contributes to the weight of the sample, but not its robustness. Additionally, high surface roughness can lead to skewed results due to harbouring air bubbles on the surface. Gong and Thijs both acknowledge the limitations of this methodology [4], [77].

Sectioning a sample and taking micrographs gives a more accurate view of the density of that particular two-dimensional slice of the sample, but it is risky to attempt to extrapolate the information throughout the volume of the component since porosity and microstructures may be inhomogeneous and dependent on sample orientation in the build chamber and sampling direction. These issues may contribute to the apparent disagreement over pore formation mechanisms, but it is difficult to avoid without moving to costlier analysis techniques.

Some have tried to alleviate this problem using alternative observation systems and simulations of melt pool behaviour. Panwisawas et al correlate laser speed and layer thickness with melt flow behaviour in Ti-6Al-4V using high speed imaging and computational fluid dynamics (CFD) [90]. They find that when scanning the laser at over 2500 mm/s the melt tracks become irregularly shaped, resulting in melt track discontinuities and porosity. High speed imaging captured melt splashing at high

scanning velocity and some evidence of material evaporation. CFD modelling of the interaction between the laser and the powder predicted both these features as well as multi-directional unstable melt flows. Marangoni force and recoil pressure due to material evaporation and gas expansion are believed to affect stability the most, with Marangoni force arising from large thermal gradients caused by rapid cooling of the surface of the melt pool during evaporation. The elongated pores observed in the experimental part of this study do not feature any un-melted particles and reside in localised locations leading the authors to conclude that they are due to molten material flowing away from the surface during disrupted flow, solidifying and returning to the surface.

To obtain 3D information on porosity levels, types and distributions micro X-ray computer tomography (XCT) was used by Ziolkowski et al [49] and Tammas-Williams et al [84]. In the latter study, the influence of melt strategies on defect population in Ti-6Al-4V components manufactured by SEBM is investigated. Gas pores and LOF pores are distinguishable and their presence related to the scanning strategies employed. In particular, a decrease in gas porosity was found to correlate with an increase in energy density and LOF pores were predominantly located at the boundary between the hatching melt tracks and the contour melt tracks. The ability to “chase” porous defects towards the last melted region (Figure 2.13) demonstrates the potential for using re-melting to control the defect population and distribution.



**Figure 2.13. XCT scans showing porous defects in SEBM Ti-6Al-4V projected onto one plane showing the effect of modifying the scanning strategy on defect distribution. From [84].**

### 2.3.2. Cracking

Cracking in LPBF processed nickel-base superalloys is a complicated problem and one which divides opinion in the current debate surrounding the identification of the causes and mechanisms of cracking. Defect free LPBF processing of alloys with high temperature capabilities would unlock numerous opportunities through the production of complex geometries for high temperature aerospace and automotive applications where robust componentry is essential. This section outlines the mechanisms potentially responsible for the cracking behaviours common in

precipitation strengthened IN713C, discusses solidification cracking models and reviews mitigation strategies against cracking as suggested in the literature.

#### **2.3.2.1. Liquation cracking**

Liquation cracking is the result of liquid film formation, in the region neighbouring the fusion zone. During welding this material experiences temperatures between the liquidus and effective solidus of the alloy so a partially melted zone (PMZ) is formed in the heat affected zone (HAZ) due to melting of low melt point phases such as grain boundary carbides or  $\gamma/\gamma'$  eutectic [54]. Local strain cannot be accommodated by this liquid and the grain boundary pulls apart. Dupont et al [54] describe two mechanisms by which liquation can occur; segregation and penetration. Segregation causes liquation when solute or impurity elements diffuse to grain boundaries and reduce the local melting temperature. Penetration is more common in precipitation strengthened alloys and causes liquation via locally melted regions being intersected by a mobile grain boundary which is then wetted by liquid penetration.

#### **2.3.2.2. Hot cracking (stress relief cracking)**

Another potential mechanism for cracking in LPBF superalloys is hot cracking, a purely thermomechanical effect caused predominantly by residual stress in the component, occurring entirely in the solid state. Residual stresses are those remaining in the component after it has reached equilibrium with its environment [91]. This mechanism is particularly relevant to LPBF due to the high residual stresses resulting from large thermal gradients introduced by the laser. This concept is introduced by Mercelis and Kruth [91] who describe two mechanisms causing residual stress; the temperature gradient mechanism (TGM) and the cool down phase of molten top layers. TGM involves large thermal gradients around a laser spot due to rapid heating and slow conduction. The top layer expands but is restricted by the bottom layer introducing elastic compressive strains. When the yield strength of the material is reached the top layer is plastically compressed. Cooling of the top layer causes it to shrink but it is inhibited by the bottom layers causing tensile stress in the top layer and compressive stress below.

Mercelis and Kruth use a simplified theoretical model to predict a stress profile over components still attached to a base plate with maximum tensile stress at the top of the part decreasing with build height which reduces after removal from the base plate due to shrinkage and bending deformation. This prediction is validated experimentally using the Crack Compliance Method (CCM) which works by estimating the residual stress profiles as Legendre polynomials and calculating using finite element modelling (FEM) the strain that would correspond to this stress profile. Strain gauges were attached to the components before being sectioned by wire electrical discharge machining (EDM) while the strain is measured. The stress profiles are then calculated from the measured strain. The authors also note differences in stress levels after altering scan strategies. Although this study does not correlate its residual stress measurements with cracking levels in the LPBF components, it provides a comprehensive description of a mechanism which is likely to contribute to the cracking problem in LPBF superalloys.

Harrison et al [69] also take a thermomechanical viewpoint, reporting that the cracking mechanism in Hastelloy X LPBF components is solely due to hot cracking with no contribution from metallurgical effects. The authors aim to manipulate the chemical composition of the alloy to increase substitutional solid solution strengthening and hence increase yield strength, thus reducing susceptibility to the TGM and cracking. This work disputes the findings of Tomus et al [92] (who attribute grain boundary cracking to microsegregation) through calculations of rapid solidification conditions introducing solute trapping and hence inhibiting microsegregation. Harrison presents energy dispersive x-ray (EDX) spectroscopy line scans over cracks which support their statement, however, as pointed out by Cloots et al [89], the interaction volume of X-rays is of the order of microns; too large to detect microsegregation.

### **2.3.2.3. Ductility dip cracking**

Ductility dip cracking (DDP) is a sub-solidus cracking phenomenon occurring due to embrittlement of the microstructure at grain boundaries after coherent or partially coherent secondary phases form [93]. Usually, DDC is most commonly found in multi-pass welds and thick sections [54]. The exact mechanism for DDC is heavily

debated, however some suggested factors influencing DDC susceptibility include grain boundary carbides coarsening and acting as stress raisers, and grain boundary shearing, sliding and tortuosity [54], [93]. DDC can be reduced by minimising precipitation of secondary phases, minimising residual stress and altering the alloy chemistry [93], [94].

#### **2.3.2.4. Solidification cracking (hot tearing)**

Solidification cracking, sometimes referred to as “hot-tearing” occurs in the “mushy zone” during the final stages of solidification. Shrinkage strains become appreciable at this stage because solidified dendrites inhibit the flow of the melt. If the terminal liquid forms a continuous film along the grain boundary, the grain boundary can no longer accommodate the shrinkage strains and the grain boundaries separate forming a crack. Susceptibility to solidification cracking is related to metallurgical effects and the amount of local shrinkage strain present in the final stages of solidification. Alloys with wide solidification ranges due to compositions which promote low temperature reactions are most susceptible to solidification cracking because the mushy zone is wider. During solidification the elements P, S and B segregate to the liquid due to their low solubility in austenite and promote the formation of low melting point liquid films. [54]

Tomus et al [92] attribute crack initiation in Hastelloy X LPBF components to the thermomechanical and metallurgical effects of solidification or liquation cracking through investigations of two batches of powder with high and low Mn and Si content. They report cracks at grain boundaries and attribute them to microsegregation because thermodynamic calculations gave a lower effective solidification temperature when the Mn and Si content was high. However, no evidence of microsegregation is provided. Cloots et al [89] investigated IN738LC and used thermodynamic calculations to predict segregation of zirconium at grain boundaries resulting from “extreme” reduction in solidus temperature. Validation work with atom probe tomography shows 15-20% more concentrated zirconium and boron at grain boundaries than in the alloy. However, only one set of atom probe results is shown indicating a small data set may have resulted from the experiment.

### 2.3.3. Solidification cracking models

This section discusses solidification cracking in greater detail and compares literature models of solidification cracking sensitivity.

As mentioned previously, solidification cracking occurs in the mushy zone where, due to the range of solidification temperatures exhibited by alloys, the dendritic network grows within the remaining liquid. The ability of the remaining liquid to flow around the porous dendritic network is key to understanding solidification cracking. When the fraction liquid ( $f_L$ ) is within a range where the dendrites do not impinge on each other ( $0.1 < f_L < 0.6$ ) the liquid forms continuous films and as such can flow to accommodate the relatively easy deformation of the dendrites caused by thermal stresses. After the point where the dendrites coalesce and become interconnected ( $0.01 < f_L < 0.1$ ) the liquid is trapped between the solid dendrite arms and cannot flow to accommodate deformation [95].

Since the vulnerable region for solidification cracking is related to the fraction liquid, numerous models were developed based on the freezing range of the alloy. The larger the freezing range the higher the solidification cracking sensitivity. Additionally, compositional variations which promote the formation of low melting point films towards the end of solidification will widen the vulnerable mushy zone [54]. More sophisticated models use concepts related to the time spent in a vulnerable zone defined by the amount and coherency of the solid network. The main approaches to modelling this behaviour are discussed in the following sections.

#### 2.3.3.1. Clyne and Davies

The Clyne and Davies model for solidification cracking sensitivity [95] defines a cracking susceptibility coefficient (CSC) given by Equation 2.13.

$$CSC = \frac{t_v}{t_r} \quad (\text{Eq. 2.13})$$

Where  $t_v$  is the time spent in the vulnerable region ( $0.01 < f_L < 0.1$ ) and  $t_r$  is the time spent in a stress relaxation region ( $0.1 < f_L < 0.6$ ). This model was the first to use a time interval of solidification rather than a temperature range. Good agreement with



experimental measurements showed that the rate of change of local liquid fraction caused by the variation in solute level in the vulnerable region significantly affect the cracking susceptibility. The change in fraction liquid can be plotted with respect to time, depending on whether the heat flow is interface controlled (Mode 1: Constant cooling rate, Equation 2.14) or conductivity controlled (Mode 2: Constant rate of heat extraction, Equation 2.15) and used to determine  $t_r$  and  $t_v$  [95].

$$t = \frac{\frac{H}{C_P}(1 - f_L) + (T_M - T_L)(f_L^{k-1} - 1)}{\frac{H}{C_P}\left(1 - \left[\frac{T_M - T_E}{T_M - T_L}\right]^{-1/(1-k)}\right) + (T_L - T_E)} \quad (\text{Eq. 2.14})$$

$$t = \left( \frac{\frac{H}{C_P}(1 - f_L) + (T_M - T_L)(f_L^{k-1} - 1)}{\frac{H}{C_P}\left(1 - \left[\frac{T_M - T_E}{T_M - T_L}\right]^{-1/(1-k)}\right) + (T_L - T_E)} \right)^2 \quad (\text{Eq. 2.15})$$

Where  $T_M$  is the melting point of the base metal,  $T_L$  is the liquidus temperature of the alloy,  $H$  is the latent heat,  $C_P$  is the specific heat,  $T_E$  is the eutectic temperature and the fraction liquid is given by

$$f_L = \left( \frac{T_M - T}{T_M - T_L} \right)^{1/(k-1)} \quad (\text{Eq. 2.16})$$

### 2.3.3.2. Rappaz, Drezet and Grenaud model

The RDG model is based on mass balance over liquid and solid phases and in simple terms states that solidification cracking will occur if the local pressure in the terminal liquid falls below a given cavitation pressure,  $p_c$ . An expression for the solidification path (Equation 2.17) is used to calculate the mechanical deformation and shrinkage contributions to the pressure drop,  $\Delta p_c$  between the root and the tip of the dendrite during solidification, which may produce cavitation in the terminal liquid. The first and last terms on the right hand side of Equation 2.18 describe the mechanical deformation and shrinkage contributions respectively. For a uniform strain rate,  $\dot{\epsilon}_p$ , the cumulated deformation rate,  $E(T)$ , (Equation 2.19) depends only on the solidification path.

A Hot Cracking Sensitivity (HCS) index is defined based on the maximum deformation rate that can be sustained in the mushy zone before lack of liquid feeding leads to nucleation of a hot crack at the dendrite root and is calculated as the reciprocal of the maximum strain rate (Equation 2.20) that can be accommodated in the mushy zone before cavitation occurs (Figure 2.14). The RDG model enables a study of the relative risk of solidification cracking according to LPBF processing parameters using simple analytical modelling of the thermal history of the melt pool which has not previously been presented in such a way.

$$f_s(T) = \frac{1}{1 - 2\alpha_s^*k} \left[ 1 - \left( \frac{T_m - T}{T_m - T_L} \right)^{\frac{1-2\alpha_s^*k}{k-1}} \right] \quad (\text{Eq. 2.17})$$

$$\Delta p_c = \frac{180(1+\beta)\mu}{\lambda_2^2 G} \int_{T_S}^{T_L} \frac{E(T)f_s(T)^2}{(1-f_s(T))^3} dT + \frac{180v_T\beta\mu}{\lambda_2^2 G} \int_{T_S}^{T_L} \frac{f_s(T)^2}{(1-f_s(T))^2} dT \quad (\text{Eq. 2.18})$$

$$E(T) = \frac{\dot{\epsilon}_p}{G} \int f_s(T) dT \quad (\text{Eq. 2.19})$$

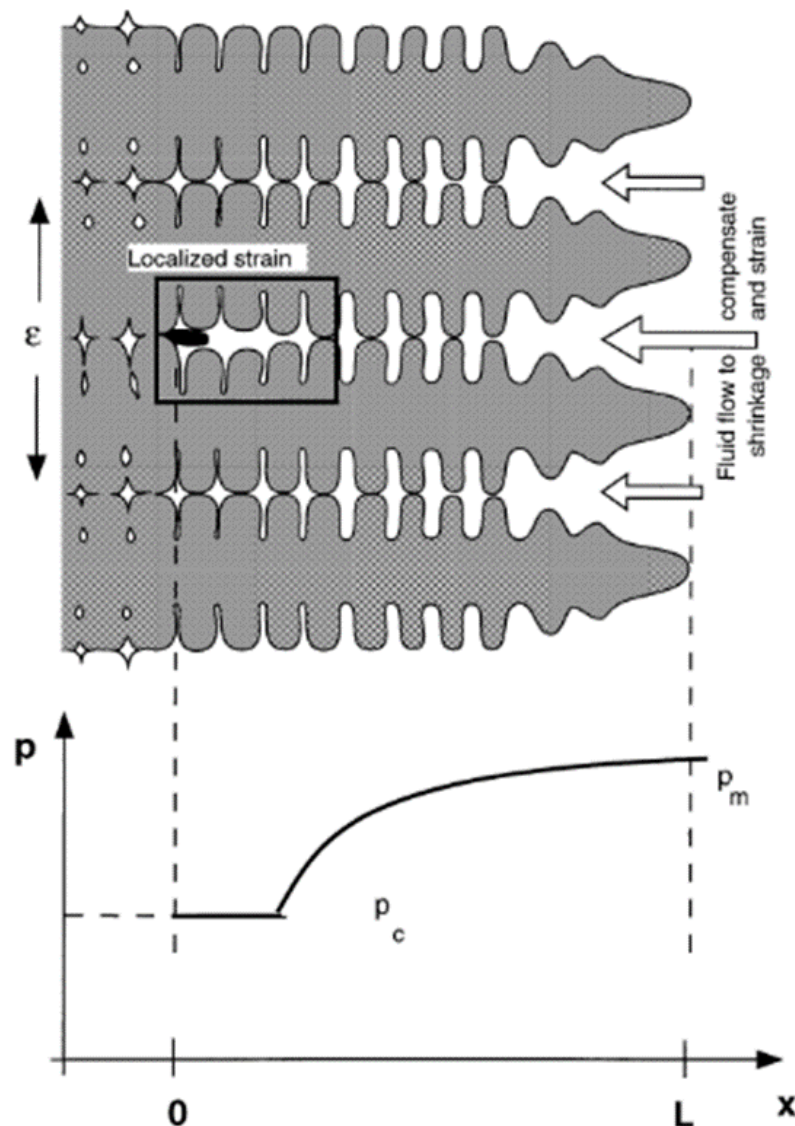
$$F(\dot{\epsilon}_p) = \frac{\lambda_2^2 G}{180(1+\beta)\mu} \Delta p_c - v_T \frac{\beta}{1+\beta} H \quad (\text{Eq. 2.20})$$

where 
$$H = \int_{T_S}^{T_L} \frac{f_s(T)^2}{(1-f_s(T))^2} dT \quad (\text{Eq. 2.21})$$

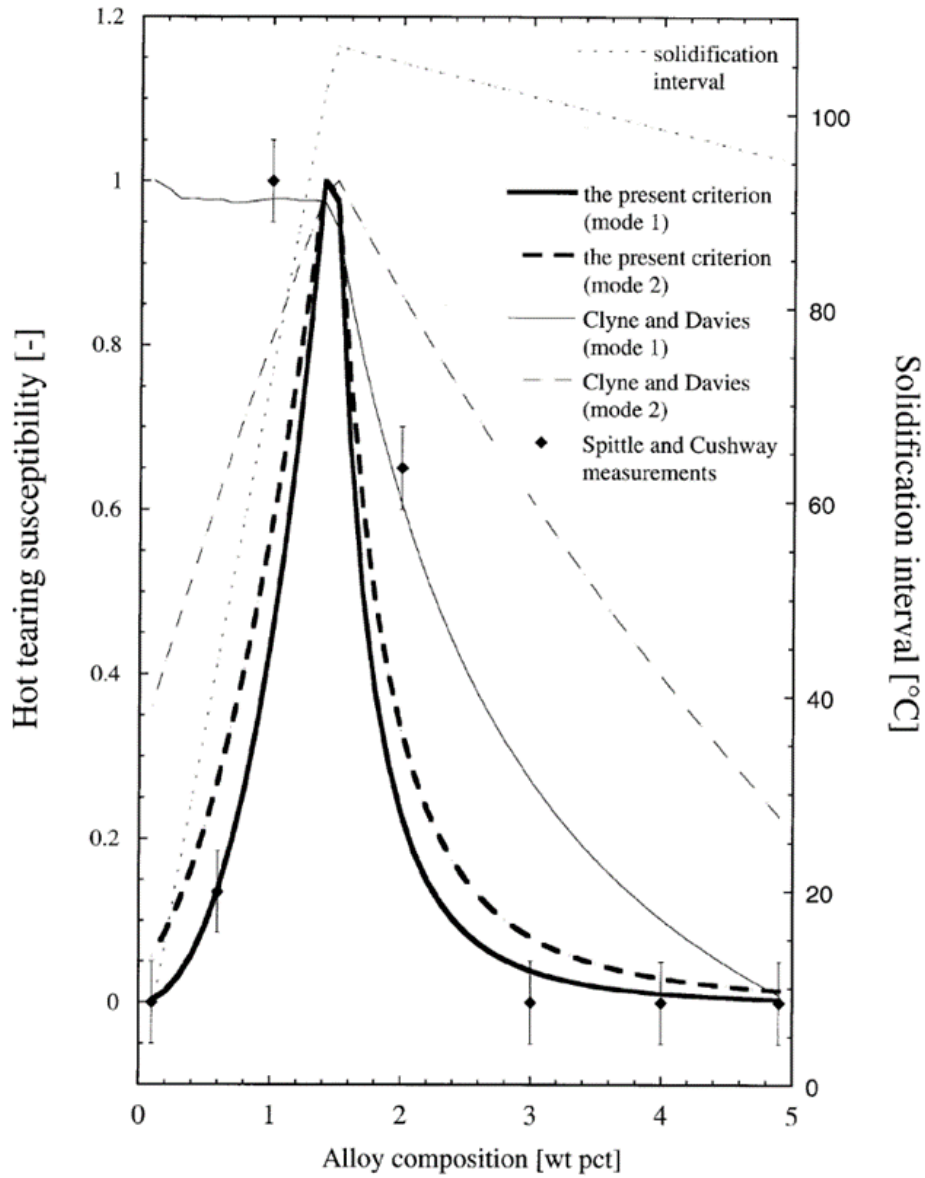
$\beta$  is a shrinkage factor,  $\mu$  is the liquid viscosity,  $v_T$  is the isotherm velocity and  $\alpha_s^*$  is the Fourier number for back diffusion in the solid.

The Al-Cu binary system is a good “model alloy” to compare theory to experiment and is very often used. The hot crack susceptibility curves for this alloy take a  $\Lambda$  curve form for both the Clyne and Davies and the RDG models (Figure 2.14) even though the approaches taken by each are very different. There is little difference between modes 1 and 2 when modelled using the RDG model, whereas the

difference is greater for the Clyne and Davies model. The comparison also indicates the discrepancy between the models is greater at the extremes of composition. This plot also shows that the solidification interval increases with increasing HCS. Experimental measurements of crack length correlate better with the RDG model, although it was noted by the authors that the HCS is an indication of crack initiation rather than propagation, so comparison of model and experiment is not straightforward.



**Figure 2.14. Schematic representation of the formation of a solidification crack between columnar dendrites as a result of localised strain causing a buildup of pressure in the interdendritic liquid, from [96].**

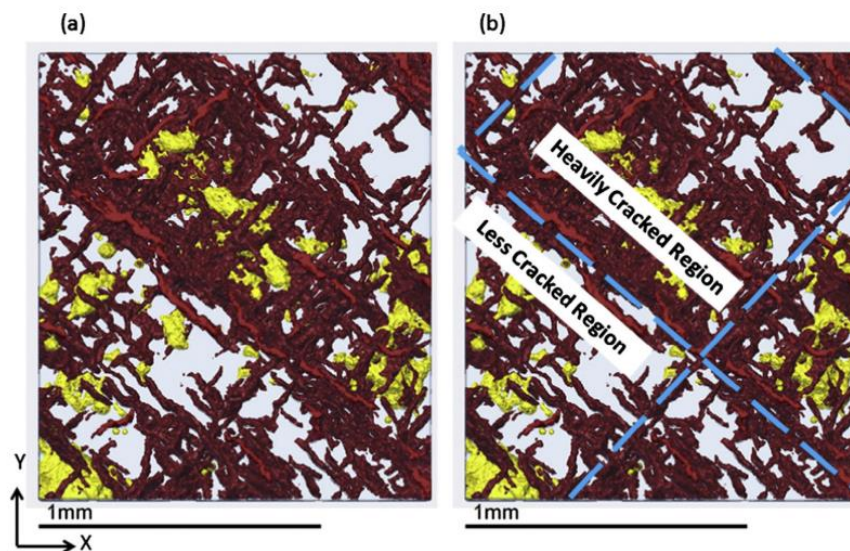


**Figure 2.15. Normalised HCS criterion for Al-Cu alloys with constant cooling rate (mode 1) or constant heat extraction (mode 2) compared with Clyne and Davies model for CSC, from [96].**

### 2.3.4. Mitigation strategies against solid state cracking

Avoiding cracking in LPBF processed nickel-base superalloys is challenging because the requisite conditions for multiple cracking mechanisms can be occurring in the same sample as a result of the complex nature of the melting-solidification-re-melting-precipitation path. To assist with reducing solid state cracking, the main goal is to reduce the residual stress in the material. (This is also a necessary factor in the reduction of solidification crack propagation.) Pre-heating the baseplate is one method of reducing the thermal gradient, hence reducing the residual stress. This has been shown to reduce cracking in M2 tool steel [97] and enhance yield strength and ductility through reduction of residual stress in Ti-6Al-4V [98].

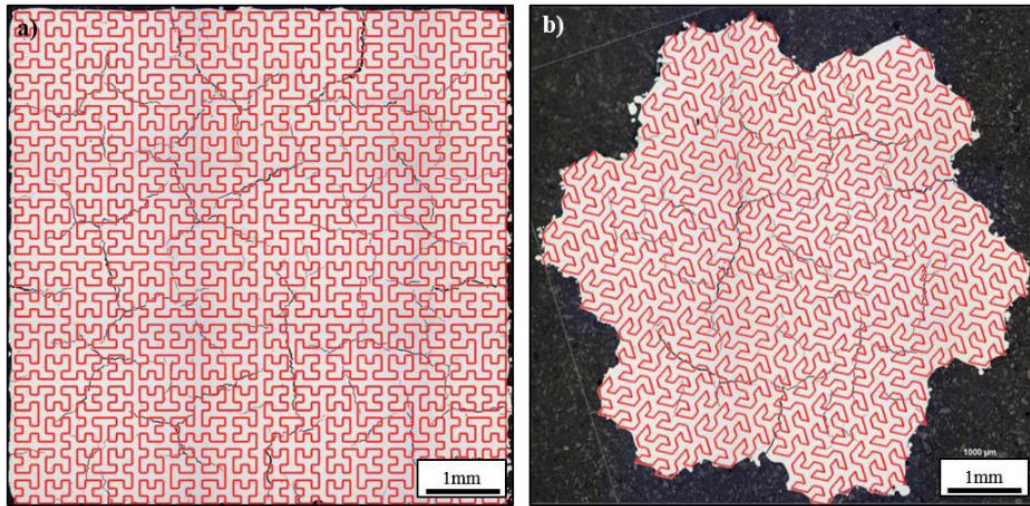
Reducing the cooling rate by shortening the length of the scan tracks has been suggested as a method for reducing residual stress. However, the use of an island scan strategy, in work by Carter et al [99], re-distributed the cracks in “unweldable” nickel-base superalloy CM247LC to the island boundaries rather than eliminating them (Figure 2.16).



**Figure 2.16. Micro XCT data showing cracks (red) and voids (yellow), with cracking distributed along island boundaries (dashed lines) in CM247LC.**

**From [99].**

Another study by Catchpole-Smith et al [100] used fractal scan strategies to reduce the length of the scan vector even further, adopting values as small as 100  $\mu\text{m}$ . Although the bulk density was improved using the fractal scan strategy, cracking was not eliminated. Rather, the cracks which formed were wider but shorter than those forming during the island scanning strategy tested in the same study.



**Figure 2.17. Fractal scan strategies overlaid on to the resulting cracked deposits in CM247LC. From [100].**

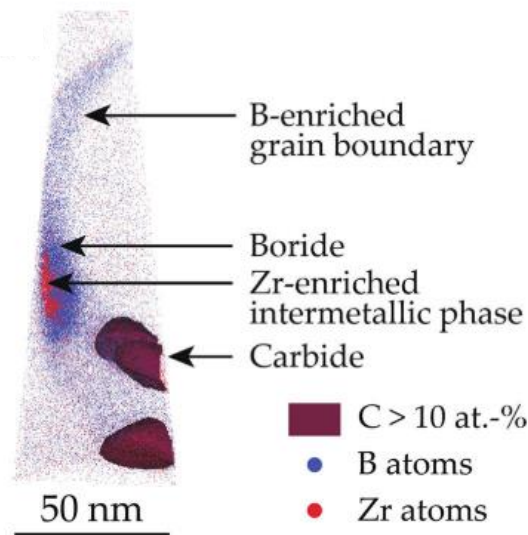
### **2.3.5. Mitigation strategies against solidification crack nucleation**

Although decreasing the cooling rate may be beneficial for solid state cracking, it is likely to be detrimental for solidification cracking. Increasing the amount of time the alloy spends in the mushy zone increases the time for segregation, increasing the chance of producing low melting point films at grain boundaries and hence increasing the propensity for solidification cracking. However, it may be possible to maintain a reduced cooling rate situation (to reduce solid state cracking) whilst avoiding solidification cracking by learning from the Clyne and Davies model. It may be possible to alter the chemistry of the alloy slightly to change the solidification path, affecting the relative time spent in the vulnerable zone compared to the relaxation zone.

Changing the chemistry and changing the processing parameters should both affect the susceptibility to solidification cracking according to the RDG model, since this



model takes into account the cooling rate (process controlled) and the solidification path (alloy controlled) of the material. Elements such as zirconium, carbon and boron are known to segregate to interfaces during solidification in castings and have been shown to do so also in LPBF nickel-base superalloy IN728LC [101]. Hence, adjusting the relative quantities of these elements may be beneficial. The effects of boron, zirconium and carbon on solidification cracking of a  $\gamma'$  strengthened nickel-base superalloy under casting conditions showed that there is an optimum balance to be found between these elements, with too low carbon and too high boron and zirconium leading to increased solidification cracking tendencies [102]. This was explained not by the solidification cracking models outlined above, but by the concurrence of high amounts of  $\gamma/\gamma'$  eutectic and high zirconium contents, since zirconium promotes the formation of liquid films.



**Figure 2.18. Atom probe tomography dataset showing boron enrichment on the cell boundary, with carbide, boride and intermetallic phase precipitation.**

**From [101].**

It should be noted at this point that superalloy compositions were designed to achieve the desired mechanical properties when in the cast or wrought condition. So, changing the alloy chemistry to make it friendlier for LPBF whilst maintaining the required mechanical properties presents a complicated challenge since the affected alloy will need to be re-qualified. Additional complications arise because the mechanical properties of the alloy are directly related to the microstructure of

the material, which has already been changed by changing from conventional manufacturing to LPBF.

The need to re-qualify an alloy is avoided if the adjustment to the composition is made within the specification. Harrison et al [69] did this in their investigation into the effects of changing the alloy chemistry of solution strengthened alloy Hastelloy X on its crack susceptibility. The authors aimed to reduce thermally induced micro-cracking by increasing the tensile strength of the alloy through modification of its composition. A 65% reduction in cracking was reported from increasing the composition of the strongest solid solution strengthening elements.

### 2.3.6. Mapping out the process

During LPBF sufficient energy must be imparted to the metal powder in order to melt and fully consolidate it. The user has the flexibility to choose the most appropriate means of delivering that energy through the manipulation of a range of processing parameters as listed in Table 3.1.

The same energy per unit volume can be achieved using multiple combinations of processing parameters. Hence, previous work in laser processing of metals [103]–[105] has shown it is instructive to group parameters together to reduce the number of variables. Early work by Breinan and Kear [105] focusses on the fundamentals of laser processing and considers the energy density output of a laser and heat transfer equations as the basis for a sound approximation to the process. With the continued development of laser AM machinery, studies by Ion et al [103] and Picasso and Rappaz [104] consider laser parameters specific to scanning laser beams for AM. More recently, Thomas et al [52] aim to improve the understanding of the effect of processing parameters in AM technologies through the application of parameterisation to existing data sets. The parameters combine to give an expression for energy density (Equation 2.22) or energy per unit volume.

$$E_0 = \frac{q}{vth} \quad (\text{Eq. 2.22})$$

Normalisation with respect to the laser beam radius and thermo-physical properties of a given material allows comparisons to be made between different materials with



different processing technologies (Figure 2.19) Normalised parameters are dimensionless and denoted by starred symbols. Ion et al [103] show that the parameters are normalised according to Equations 2.23 to 2.26 with respect to  $r_B$ .

$$q^* = \frac{Aq}{r_B \lambda (T_m - T_0)} \quad (\text{Eq. 2.23})$$

$$v^* = \frac{v r_B}{\alpha} \quad (\text{Eq. 2.24})$$

$$h^* = \frac{h}{r_B} \quad (\text{Eq. 2.25})$$

$$l^* = \frac{l}{r_B} \quad (\text{Eq. 2.26})$$

Hence, the normalised energy density is given by;

$$E_0^* = \frac{q^*}{(v l h)^*} \quad (\text{Eq. 2.26})$$

The normalised process map, when set out as in Figure 2.19 using the normalised parameters above, should be used as a planning tool or a scaffold around which experiments can be designed or analysed. It is not a predictive model, but can be used to assess the conditions under which defects are likely to occur and helps to explain the reasons for their formation.

Wang et al [106] have shown how the process map may be used in their work on AM of stainless steels. They use the concept of normalised energy density to understand how to identify a suitable processing window for the material which will minimise defects while optimising build efficiency.

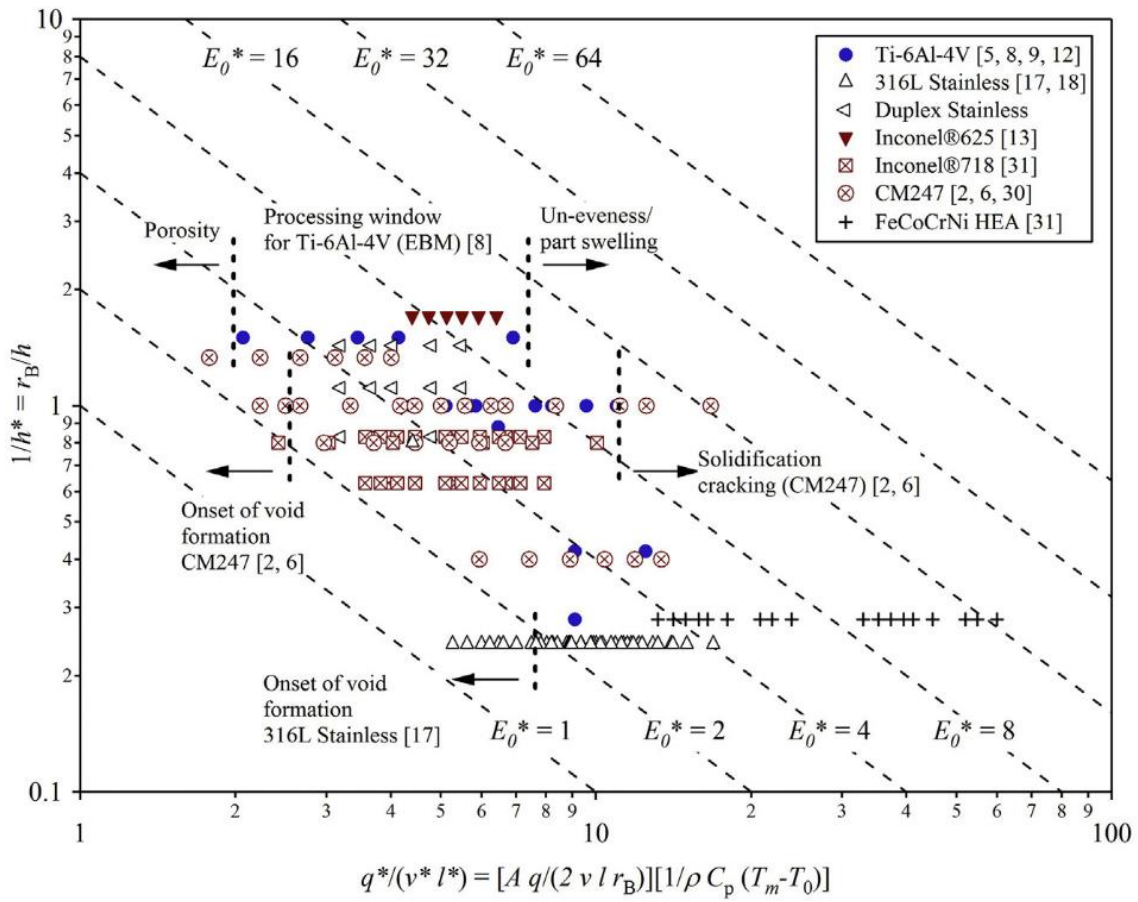


Figure 2.19. Normalised process map for AM of a range of alloy systems with data extracted from literature, from [52].

## 2.4. Summary of Chapter 2

Nickel-base superalloys, for use in high temperature applications, exhibit significant improvements in UTS and creep rupture strength compared to ordinary alloys at temperature generally above 1000°C. In nickel-base superalloy IN713C precipitation hardening is the dominant strengthening mechanism and relies on aluminium and titanium to form  $\gamma'$  ( $\text{Ni}_3(\text{Al,Ti})$ ) precipitates which are coherent with the fcc  $\gamma$  matrix. However, the same feature which makes precipitation strengthened nickel-base superalloys superior in the conventionally cast form makes them difficult to process via LPBF. They are generally regarded to be “unweldable” due to a high susceptibility for solidification cracking.

The similarities between welding operations and laser melting mean that solidification cracking is a major problem in LPBF processing of such superalloys. When an alloy with a chemistry susceptible to the formation of liquid films on the grain boundaries is subjected to the high thermal gradients and residual stresses present in LPBF, micro-cracks form extensively during processing. The production of crack-free, precipitation strengthened nickel-base superalloys has not yet been demonstrated. The literature on LPBF of IN713C is particularly sparse.

Processing maps are useful for developing an understanding of a suitable process window for a material which can be easily compared to other alloys and processes. However, a strong focus on the effect of the total energy density imparted to the powder bed throughout the available literature is potentially masking the subtleties of the process. Particularly, the effect of changing individual processing parameters on the local conditions in the melt and the resulting response of the material in terms of defect formation.

The present work aims to investigate the behaviour of IN713C when processed with LPBF using statistically designed experiments and sophisticated characterisation and analysis techniques. A processing map of the optimised processing window is presented alongside detailed analysis of the effects of straying beyond its boundaries. The cracking behaviour of the alloy is probed using a series of literature models, enabling suggestions to be made for strategies which may reduce the crack susceptibility.

### **3. Experimental techniques**

#### **3.1. Renishaw SLM125 features and operation**

All LPBF fabrication was conducted at the University of Sheffield on a Renishaw SLM 125 machine featuring a modulated 200W Ytterbium fibre laser. The instrument has a 125 mm x 125 mm x 80 mm build volume. The platform is dosed with powder through a spring loaded slot, gravity fed mechanism which is driven by the motion of the wiper arm. Powder is spread over the substrate by a wiper with a rubber insert. The chamber is evacuated of oxygen then flushed with argon flowing from right to left during the build. Renishaw SLM systems have a unique Safe Change Filter, capturing the nanoparticulate combustion products resulting from the melting process which are potentially harmful and preventing them from coming into contact with the operator. The open architecture of Renishaw SLM systems is ideal for research and development purposes as the operator has the freedom to change an extensive list of processing parameters to suit a particular material or component. CAD files can be uploaded to a networked PC from a modelling package and hatching and slicing takes place on software such as Magics or Autofab. The file is then converted into a .stl file before being transferred to the LPBF machine. The operator controls the set up and running of the machine using the built in computer touch screen.

The laser is modulated externally to give short bursts of power. Since the laser is modulated rather than pulsed, these bursts do not produce more power than the average output of the laser. The modulation means that the laser is only switched on whilst it is stationary. This is advantageous as a means of influencing the residual stress on a component and hence reducing the propensity for residual stress cracking, however laser modulation influences the actual power and speed of the laser, both of which must be adjusted if a comparison against a continuous wave laser system is to be made (discussed in section 4.3.1).

The standard operating procedure for the Renishaw SLM 125 machine is provided in Appendix 3.

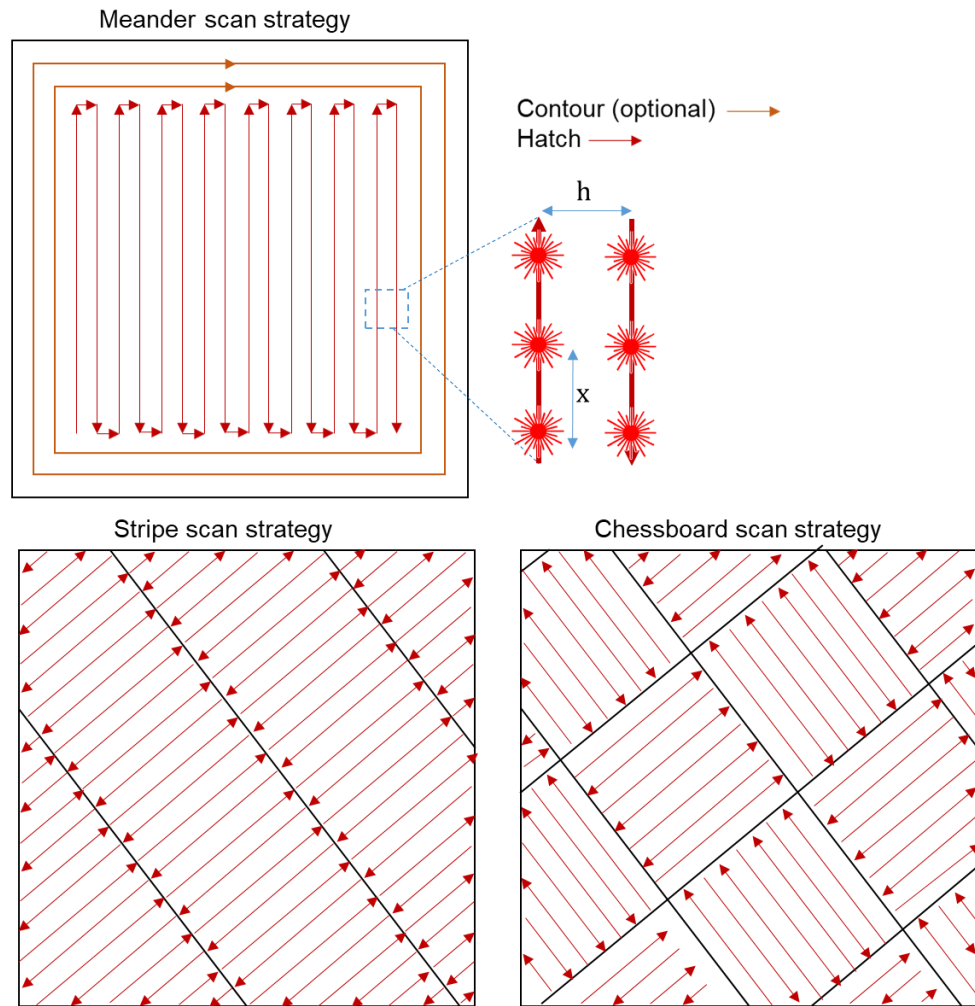
### 3.2. Process terminology

The main process parameters influencing the energy imparted to the powder are given in Table 3.1. The modulated nature of the laser means it is necessary to specify the exposure time,  $\tau$ , and distance between exposure points,  $x$ , rather than the speed of the laser beam, as is usual for most other LPBF machines. The laser travels a distance,  $x$  whilst switched off, then switches on whilst stationary. The laser can be programmed to scan the powder layers in a variety of patterns (Figure 3.1), the most common of which being the meander scan strategy, whereby the laser scans the outer contours of the slice before hatching the internal volume. In a standard meander strategy, the hatching rotates  $67^\circ$  between slices with the distance between neighbouring scan tracks labelled as the hatch spacing,  $h$ . An apparent scan speed can be calculated using the idle speed of the laser (the travel speed of the laser while switched off). This value was previously measured for the Renishaw SLM125 as 4.1 m/s using a high speed camera. Other scan strategies have also been trialled during this work, including stripe and chessboard. Whilst the meander strategy offers the highest build rate, the stripe and chessboard pattern can be used to create a more homogeneous distribution of residual stresses.

**Table 3.1. LPBF processing parameters and associated symbols.**

Processing Parameter	Symbol	Description
Laser power	q	Nominal laser power
Laser velocity*	v	Speed of laser traversing the powder
Hatch spacing	h	Distance between melt tracks
Layer thickness	l	Thickness of individual powder layers
Beam radius	r <sub>B</sub>	Radius of laser beam

\*  $v = x / ((\tau + t))$  where  $t = 4.1$  m/s.



**Figure 3.1. Renishaw SLM 125 scan strategies.**

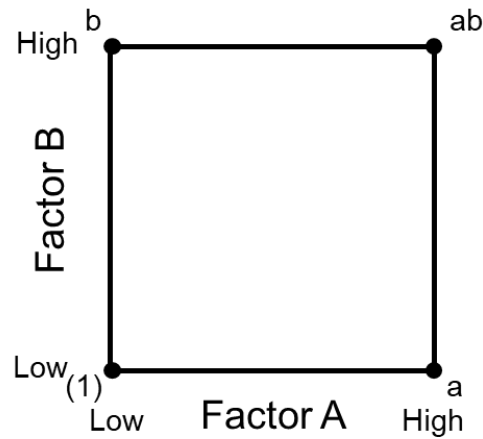
### **3.3. Statistical experimental methods**

#### **3.3.1. Design of experiments**

Design of Experiments (DOE) was employed to efficiently collect and analyse data. Designed experiments save time and resources by laying out the number of necessary runs within a design space needed to accurately model the response whilst randomising the runs and eliminating experimenter bias. Numerous types of DOE exist, so a choice must be made as to the most appropriate design for each experiment. The simplest designs are  $2^k$  factorial designs, suitable for fitting a first order model with interaction and providing information about the main effects. Before attempting a more complicated DOE for a new process it is usually

necessary to perform a screening experiment to determine which controllable variables are most important in affecting the response; the  $2^k$  factorial design is suitable for this purpose since a response surface can be modelled over a large region of operability with relatively few runs.

A  $2^k$  factorial design with two factors is called a  $2^2$  factorial design (Figure 3.2). The factors  $A$  and  $B$  are investigated at a “high” and “low” level, with the high level of each factor denoted by its lower case letter. The low level of each factor is indicated by the absence of the corresponding lower case letter and the point representing the low level of both factors is labelled  $(1)$ . The  $2^k$  factorial experiments are replicated  $n$  times.



**Figure 3.2. The  $2^2$  factorial design.**

The effects of the factors are denoted by the same capital letters as the factors. Additionally,  $AB$  denotes the effect of the interaction of factor  $A$  and factor  $B$ .

The main effect of a factor (also called the average effect) is given by the change in a response produced by a change in level of a factor averaged over all the levels of the other factor (Equations 3.1-3.3). For example, the main effect of factor  $A$  is the difference between the average of  $ab$  and  $a$  and the average of  $b$  and  $(1)$  where the lower case letters now represent the total response over all  $n$  replicates.

$$A = \frac{1}{2n} [ab + a - b - (1)] \quad (\text{Eq. 3.1})$$

$$B = \frac{1}{2n} [ab + b - a - (1)] \quad (\text{Eq. 3.2})$$

$$AB = \frac{1}{2n} [ab + (1) - a - b] \quad (\text{Eq. 3.3})$$

These equations are used to assess the relative effects of each factor, hence deduce which factors are likely to be important. If the result is large and positive, it suggests that the measured response will increase as the factor is increased from the low to high value. The opposite is true if the result is negative. For a result much smaller than the other two results it can be assumed that this factor, or the interaction between factors, is insignificant. Analysis of variance (treated later) can be used to confirm these suggestions.

### 3.3.2. Linear regression

After estimating the relative importance of the factors involved in a process, their effects can be converted into a regression model which describes the predicted response at any point in the design space. This is useful for predicting a factor combination which improves the response. The first order regression model describes the response  $y$  in terms of coded variables  $x_k$  and regression coefficients  $\beta_k$ . The error caused by unknown variables or process noise is given by  $\varepsilon$ .

$$y = \beta_0 + \beta_1 x_1 + \beta_2 x_2 + \varepsilon \quad (\text{Eq. 3.4})$$

$$x_1 = \frac{A - (A_{low} + A_{high})/2}{(A_{high} - A_{low})/2} \quad (\text{Eq. 3.5})$$

$$x_2 = \frac{B - (B_{low} + B_{high})/2}{(B_{high} - B_{low})/2} \quad (\text{Eq. 3.6})$$

So, if factor  $A$  is at the high level,  $x_1 = +1$  and if factor  $A$  is at the low level  $x_2 = -1$ . The same applies for factor  $B$  and  $x_2$ .

### 3.3.3. Central composite design

After identifying the important controllable variables and region of interest, it may be desirable to accurately model the response in a smaller processing window



around an optimum point. Central Composite Design (CCD) and Box Behnken Design (BBD) both allow second order approximations thus describing curvature in the response surface; a common feature when considering a small region of interest near the optimum.

Fitting a second order response surface requires at least three levels of each input variable and at least  $1 + 2k + k(k-1)/2$  distinct points in the design. If  $2k$  axial points are added to the  $2k$  level factorial the resultant design is a CCD which is a spherical (or near spherical) design and this satisfies the above requirements. The researcher must select appropriate values of axial distance,  $\alpha$  and number of centre points,  $n_c$ , or these can be calculated using appropriate statistical rules.

### 3.3.4. Analysis of variance (ANOVA)

ANOVA tests the statistical significance of a fitted response model by testing the null-hypothesis (i.e. there is insufficient evidence to suggest the observation was due to the experimental factors). Therefore, the null-hypothesis must be disproved for the model to be statistically significant. To test the null hypothesis, firstly the residuals (errors) are calculated as the difference between the predicted response and the observation. Then the  $F_0$  statistic is calculated according to Equation 3.7 and the null hypothesis is rejected if the P-value for  $F_0$  is less than  $\alpha = 0.5$  (for 95% confidence).

$$F_0 = \frac{SS_R/k}{SS_E/(n - k - 1)} \quad (\text{Eq. 3.7})$$

Where  $SS_R$  and  $SS_E$  are the regression sum of squares and the error sum of squares,  $k$  is the number of terms in the regression model and  $n$  is the number of observations. It should be appreciated that, although P-values are commonly used to test a null hypothesis, this method faces criticism due to the possibility of misuse of the method and misinterpretation of the importance of a result [107], [108]. In this work, statistical software package Minitab was used to plan and randomise the DOEs and compute the ANOVA.

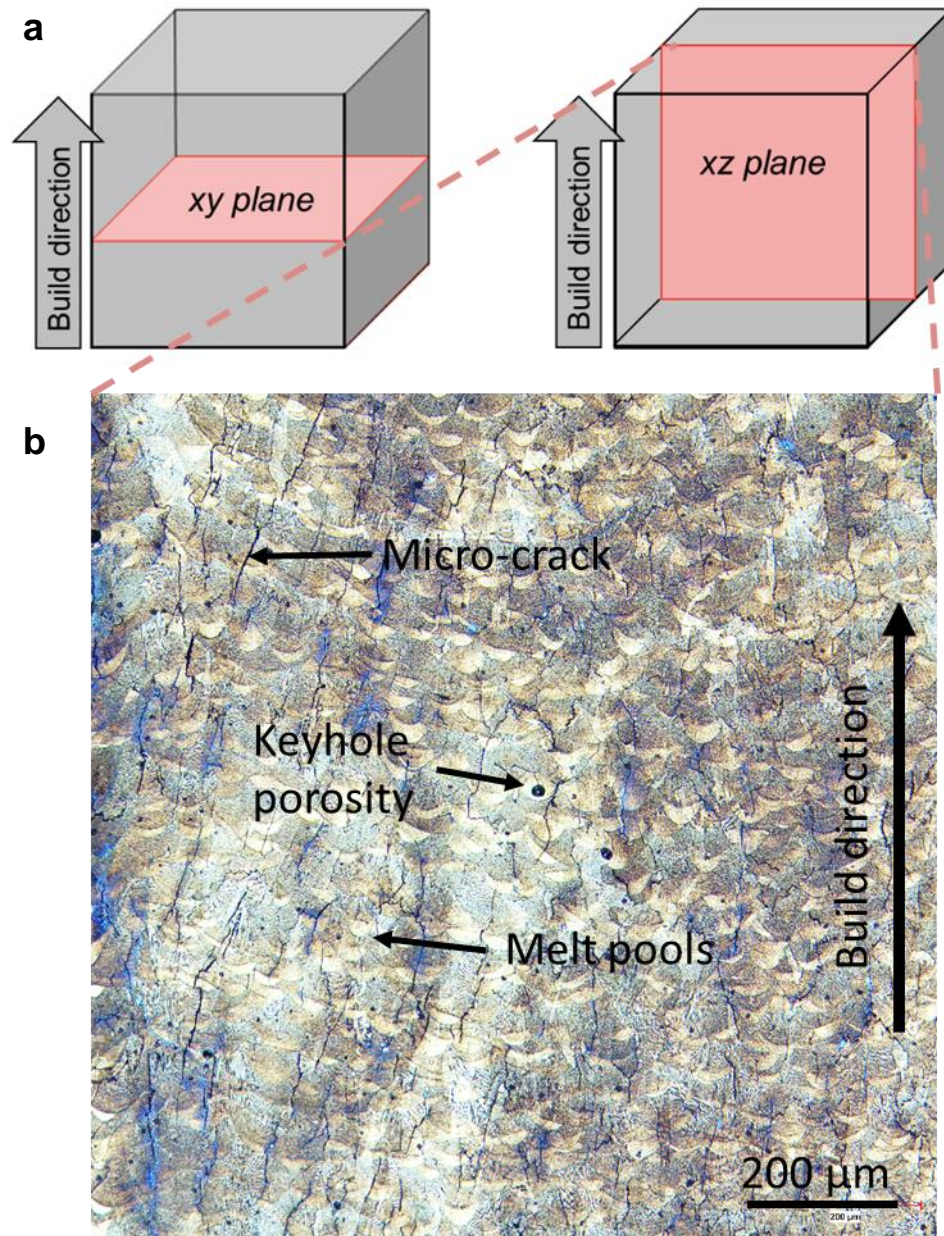
### **3.4. Characterisation techniques**

#### **3.4.1. Sample preparation**

IN713C powder sourced from Sandvik Osprey Ltd was used for all builds. The powder was inspected and characterised, the results of which are detailed in Appendix 5. LPBF specimens were all built directly onto the substrates without the use of pin supports. Although pin supports mean that the parts can be easily removed from the substrate using a chisel, initial trials indicated problems with the pins swelling during the build and affecting the rest of the part. Building directly onto the substrate meant that the wiper blade did not suffer any damage from swollen pins but the parts required electrical discharge machining (EDM) to remove them from the substrate.

The test cubes were then mounted in clear or conductive resin in either the XY or XZ orientation (Figure 3.3). The XY orientation gives a top down view of the melt pools. Sections in this orientation feature circular melt pool traces and cracking appears to propagate in many directions. Most samples were mounted in the XZ orientation. Sections in this plane show “fishscale pattern” melt pool traces and cracking propagates in the Z direction (build direction). This orientation was chosen for most sample sets because the difference between melt splashing defects and LOF defects can be distinguished since non-adhesion between the layers can be seen as elongated pores.

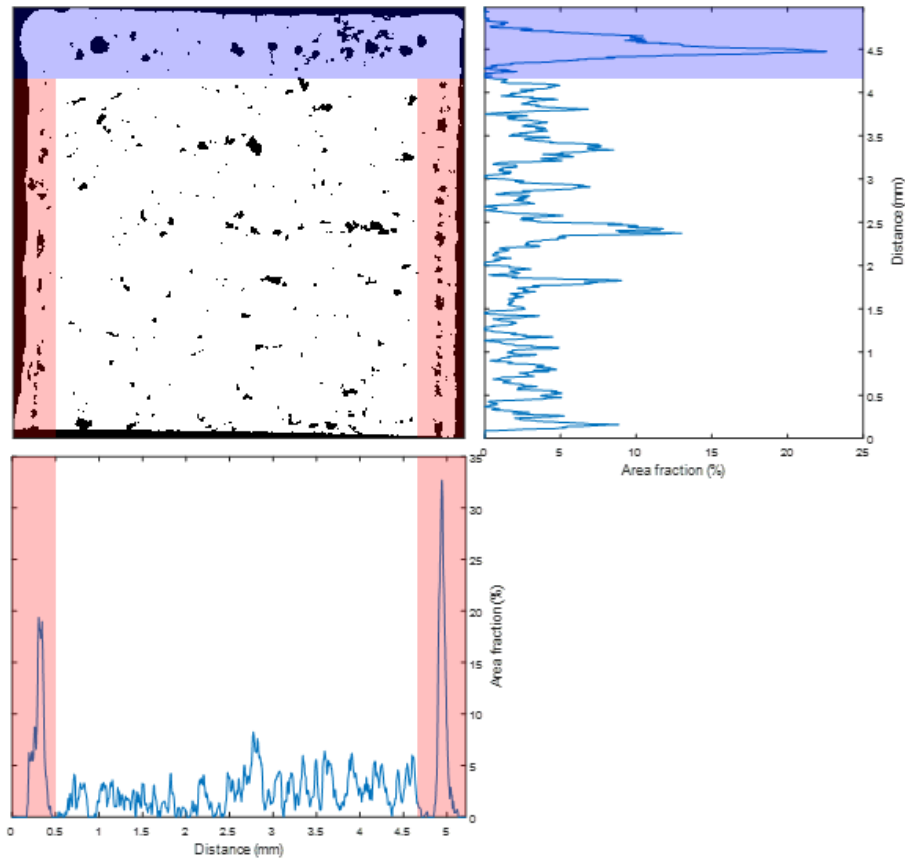
An identical preparation routine using an automatic polisher was used on all samples. This ensured consistent height locations were investigated. Mounted samples were ground using coarse grit paper to remove at least 2 mm of material to reveal a plane beneath the outer contours. It was shown that the outer regions display different defect behaviours to the central volume (Figure 3.4). For all defect quantification, only the bulk volume was considered. This is a valid method because in production parts the outer surface is often machined away so it is less important. However, some analysis has been performed of the outer skins in this project.



**Figure 3.3. a) XY and XZ planes within test cubes, b) characteristic “fish scale” pattern of melt pools as observed in XZ plane.**

## The Application of AM to Ni-base Superalloys

The samples were all polished to 1  $\mu\text{m}$ . For analysing porosities larger than 50  $\mu\text{m}$ , this level of sample preparation is sufficient. However, for analysing smaller porosities and cracking, the samples must be etched to remove polishing debris. Etching is also necessary for revealing the microstructure and melt pool traces prior to scanning electron microscopy in order to observe the dendritic microstructure. A methodology for etching IN713C LPBF specimens using Glyceregia is given in Appendix 4.



**Figure 3.4. Area fraction of pores across the area of the micrograph showing that porosity is approximately constant over the measured area (white) and other phenomena are influencing porosity in the boundary between meander hatching and the contour scan.**

### **3.4.2. Microscopy**

Optical micrographs used for 2D image analysis of defects were obtained of each prepared surface of LPBF test cubes using a Leica DM LM/P optical microscope and analysed using ImageJ software with self-developed thresholding macros. A good polish is essential for achieving accurate measurements since computer based thresholding techniques cannot distinguish between a metallurgical defect and a polishing scratch. Three images of each specimen were taken and the average porosity across the sample was calculated. Scanning electron microscopy (SEM) was performed on a Phillips XL30 SEM at CTT in secondary electron and back scattered electron modes (except for those instances where SEM micrographs were obtained during focused ion beam sample preparation). Operating conditions for the SEM were accelerating voltage of 10kV and working distance of approximately 7 mm.

Transmission electron microscopy (TEM) was used in this work to investigate the influence of process settings on the dislocation and precipitate behaviours in LPBF processed IN713C. All TEM work was performed by Dr Jo Sharp at the University of Sheffield using a JEOL 2010F instrument with an accelerating voltage of 200kV. Samples were prepared by Dr Le Ma also at the University of Sheffield using the focused ion beam lift out method on a FEI Helios NanoLab UC dual-beam FIB instrument.

### **3.4.3. X-ray computed tomography (XCT)**

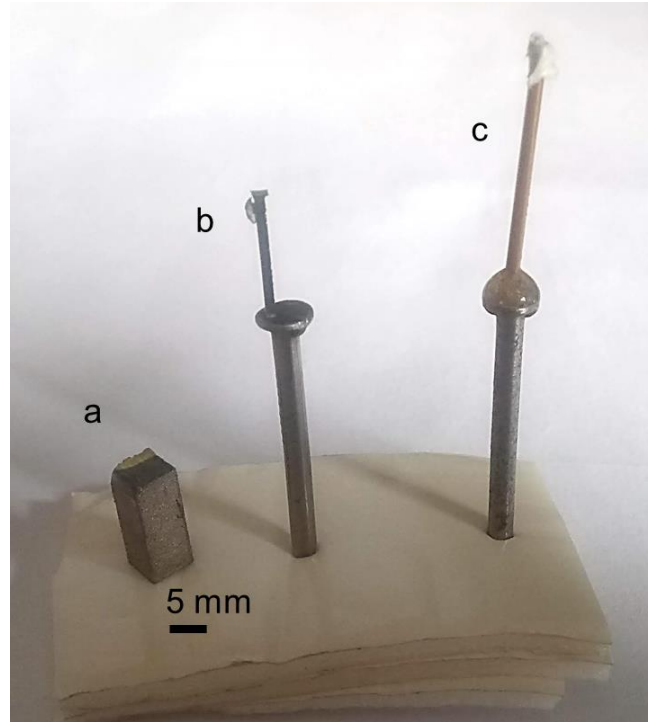
XCT is useful for investigating defects in AM materials because it allows quantification and characterisation of individual defect types, their characteristics and their distribution within a sample. As a non-destructive tool, XCT can be used to capture this information without compromising the integrity of the sample. In XCT, numerous radiographs with varying projections are reconstructed using a computer based mathematical algorithm to create a 3D representation of the sample [109].

This technique has previously been used with various AM systems including SEBM Ti-6Al-4V [84] and LBPF Ti-6Al-4V [14]. In this study, XCT was performed using

two different instruments with different resolution. Resolution is limited by the size of the sample, so lower resolution scanning was useful for characterising whole test cubes (Figure 3.5a) while higher resolution scanning was used to characterise smaller defects such as cracks on smaller specimens sectioned from a central location of test cubes (Figure 3.5b). A sample of IN713C powder was also examined using higher resolution XCT by containing it inside a small polyimide tube (Figure 3.5c). The XCT analysis of LPBF IN713C specimens is given in chapter 4.

XCT was conducted at the Henry Mosley X-ray Imaging Facility at the University of Manchester. Macroscale analysis of whole, as-deposited samples was conducted using the Nikon Metrology 225/320 kV Custom Bay system, whereas higher resolution analysis of small machined specimens was performed using the Versa 500 system. Scanning of whole samples was performed using 3142 projections of 1 s exposure, with a 180 kV accelerating voltage, a 130  $\mu$ A current and a tungsten reflection target. In contrast, for the small, machined specimens, 2000 projections with 4 s exposure time were acquired with an accelerating voltage of 120 kV, power of 10 W and tungsten transmission target.

Proprietary software from Nikon and Xradia was used to reconstruct 3D data from the projections for the whole and machined samples respectively. The imaging conditions were chosen such that a voxel size of 5.8  $\mu$ m was achieved for the whole samples, which allowed the entire sample to be imaged, whereas a voxel size of 1.5  $\mu$ m was used for machined samples, which allowed high resolution imaging, with the caveat that only a small volume could be analysed. To positively identify features from XCT data, they must have a size approximately twice that of the voxel size and the noise within the data would also impact the ability to measure a feature. Further discussions of the factors influencing defect detection by XCT are available elsewhere [110]. The XCT data was analysed using Avizo 8.0 software. A global threshold was applied to segment the data into a binary volume (solid/void), and pores were identified, quantified and further divided based on their characteristics into their likely origins.



**Figure 3.5. XCT samples a) full test cuboid, b) Sectioned volume from central region of test cuboid, c) Powder sample contained within a polyimide tube.**

#### **3.4.4. Atom probe tomography**

APT is an advanced, state-of-the-art technique for the characterisation of materials at the atomic level. The technology has seen numerous developments since the conception of the 1D atom probe; a field ion microscope coupled with a time of flight mass spectrometer for chemical identification [111]. The latest iteration of 3D atom probe is the local electrode atom probe (LEAP<sup>®</sup>), featuring a local electrode in close proximity to the specimen (Figure 3.6). In this study, a Cameca LEAP 5000 instrument was used to study segregation behaviours in LPBF IN713C at the University of Oxford.

An atomically sharp tipped sample is required for APT. Such samples are milled using a focused ion beam; a process which is often challenging and time consuming. The sample is cryogenically cooled within the APT instrument and held at a positive voltage, almost sufficient to cause surface atoms to evaporate from the tip. A pulsed laser is then incident upon the sample, causing the evaporation of one or two atoms per pulse. It is important to choose the correct pulsing voltage to minimise the



probability of a multiple evaporation event since the data collection rate is compromised by multiple atoms arriving at the detector simultaneously [112]. The collected atoms are identified according to their time of flight and the data can be used to create a virtual 3D reconstruction of the tip.

APT has several limitations. Most obvious is that the very small volume of material comprising the sharp tip may not be representative of the bulk, or may not capture the feature of interest. Additionally, the combination of a destructive technique with the highly critical nature of the operating settings means premature failure of samples is common. It is usual to consider APT as a complimentary technique to more conventional characterisation methods. [113]

APT has been used previously to investigate elemental segregation in electron beam PBF nickel-base superalloys in relation to cracking behaviours [83]. Using this method, the authors were able to identify local compositional enrichment of minor elements such as boron to cell boundaries, indicating the presence of liquid films which contribute to crack susceptibility.

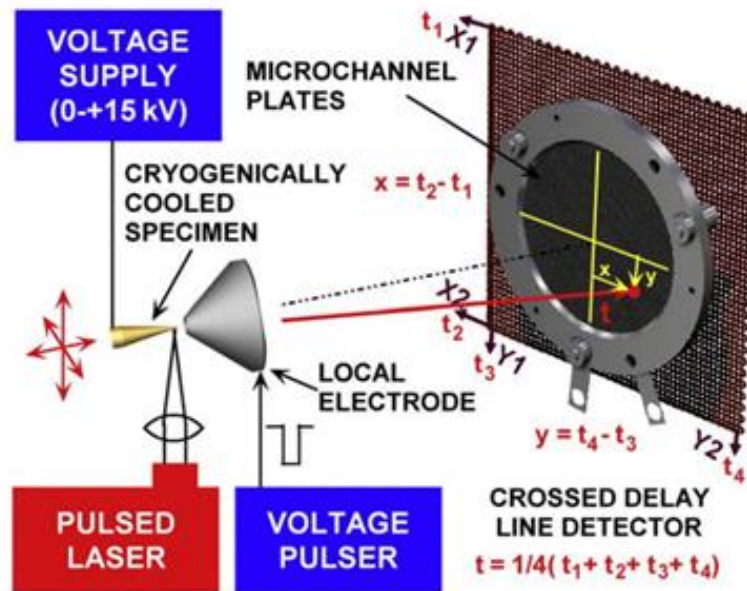


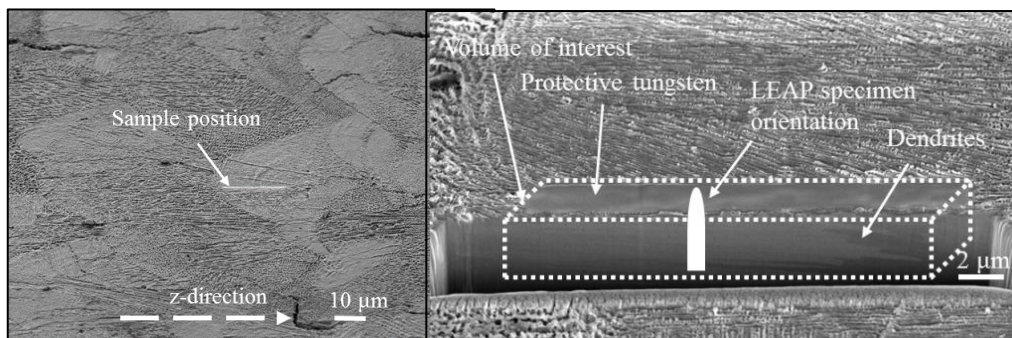
Figure 3.6. Schematic diagram of a local electrode atom probe. From [63].

In the present work, observations of microsegregation were made possible using atom probe tomography (APT) through collaborative work with University of

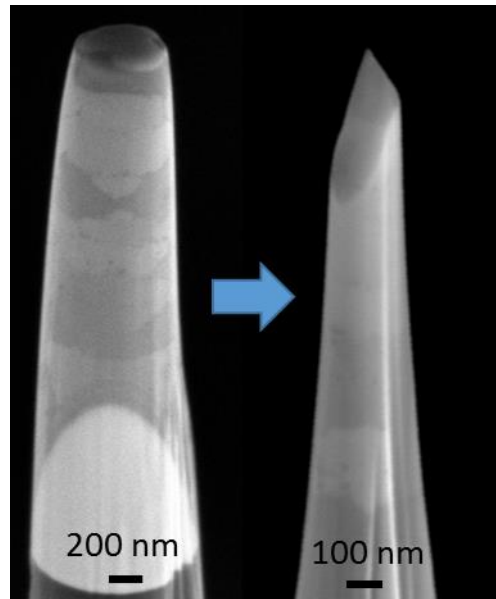


Oxford. Atom probe sample preparation, operation of the atom probe, tomographic reconstruction and analyses were performed by Dr Andrew London under the supervision of Prof. Michael Moody. Four samples were focussed ion beam (FIB) milled from a specimen of LPBF IN713C produced using laser power of 180 W, layer thickness of 20  $\mu\text{s}$ , exposure time of 71  $\mu\text{s}$  and spot separation and hatch spacing of 52  $\mu\text{m}$ .

A Zeiss NVision 40 Gemini FEG SEM was used for FIB milling and imaging. The volume of interest (Figure 3.7) was lifted from the bulk by FIB milling with a gallium ion beam before being cut into smaller sections of approximately 1  $\mu\text{m}$  wide, each of which was attached to a post on a pre-fabricated silicon coupon. Specimens were then milled into a cylindrical shape using annular mill patterns of 700 pA at 30 kV followed by finer milling using 40 pA at 30 kV and finally polished to a sharp tip (Figure 3.8) using 300 pA at 2 kV. Specimens were loaded into a Cameca LEAP<sup>®</sup> 5000 and held under vacuum of  $5 \times 10^{-11}$  Torr at a temperature of 40K for the atom probe tomography. The tip was subjected to 40 pJ laser pulses at a rate of 200 kHz to induce atom evaporation. Time-of-flight detectors collect the evaporated atoms one or two at a time as they escape from the sample. Four samples were analysed. Peak overlaps in the mass spectra were resolved using the novel methodology described in [114].



**Figure 3.7. Position and sampling volume of material used to prepare APT tips in the indicated orientation. Note the left image is skewed in the vertical direction due to the inclination of the electron detector altering the projection of the image.**



**Figure 3.8. Atom probe sample preparation stages resulting in a sharp tip.**  
**Note the difference in scale between the images.**

#### **3.4.5. Thermo-calc simulation**

Thermo-calc is a software package for the calculation of phase equilibria, phase diagrams, phase transformations and thermodynamic properties of multi-component systems [115]. It works by connecting with material specific databases, to find the equilibrium state of a system using algorithms based on the work of Mats Hillert [116]. Databases are developed using the CALPHAD approach [117]. The limitation of using Thermo-calc simulations is that they rely upon an appropriate choice of database for the given alloy system, and cannot predict the presence of any phases which do not appear in the database. However, for nickel-base alloys, the TCNi8 database has been extensively developed to include all the important nickel-base superalloy phases within a 27 element framework [118].

In this work, Thermo-calc was used to simulate the solidification path of IN713C using the Schiel method in order to calculate the length of time the material spends in the vulnerable zone for solidification cracking. Additionally, property diagrams were prepared to deduce the relationship between alloy composition and freezing range. The TCNi8 database was used throughout.

## 4. Process mapping of LPBF IN713C

This chapter aims to discuss the development of a process map for LPBF IN713C. The implications of the map for building a component are presented and discussed in Chapter 6. Developing a detailed understanding of the response of a material to processing under different regimes is important for two reasons:

- 1) A process map acts as a transferrable bank of information, enabling comparisons to be made between different materials and processes. This can be used to instruct the identification of suitable processing conditions for a new material/machine combination.
- 2) A process map can be used alongside DOE to optimise processing parameters and mitigate for defects.

### 4.1. Exploring the process space

Several experiments were conducted to obtain information on the defect formation response of IN713C under various processing conditions (Figure 4.1). For simplicity, small cubes were chosen as experimental test specimens. All samples were built with 20  $\mu\text{m}$  layer thicknesses based on previous experience with similar materials. A summary of the experiments is given in Table 4.1.

**Table 4.1. Summary of LPBF experimental builds.**

Experiment	Description
1	4-factor DOE spanning the breadth of the process space defined by the physical limitations of the Renishaw SLM125.
2	3-factor DOE limited to the process window in which porosity was minimum in Experiment 1. $q' = 180 \text{ W}$ .
3 (a-d)	Set of four 3-factor DOEs, $q' = 200 \text{ W}$ .
4	3-factor DOE, energy densities comparable to 3a, $q' = 125 \text{ W}$ .
5	A constant energy density experiment, $q' = 200 \text{ W}$ .

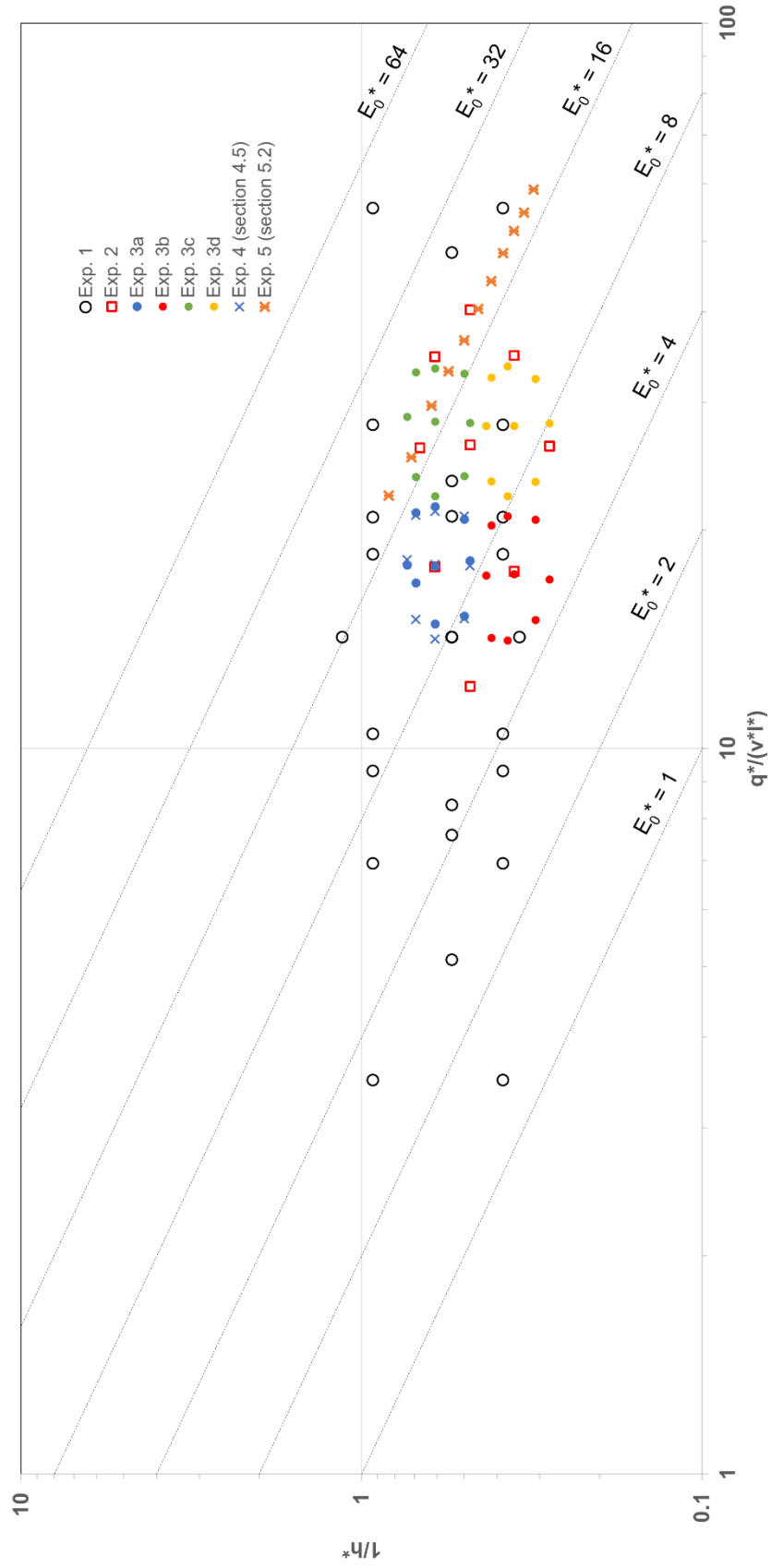
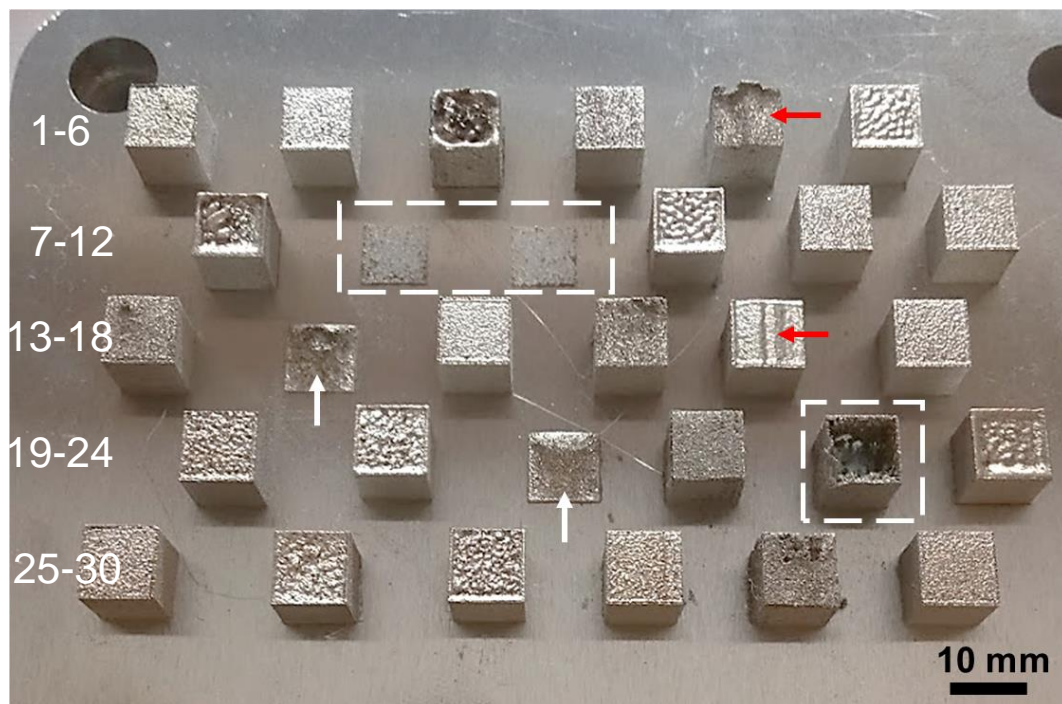


Figure 4.1. Position of experiments on the process map.

#### 4.1.1. Experiment 1: Capturing the extremes of the process space

Experiment 1 was performed over the widest processing space possible whilst maintaining a constant layer thickness, defined by the limitations of the Renishaw SLM125 machine. This was a four-factor DOE generated using Minitab with the factors  $q$ ,  $\tau$ ,  $x$  and  $h$ . Normalised input energy density ranged from 1.34 to 51.46. Cubic samples of IN713C with side length 10 mm were deposited on a stainless steel substrate. The samples were arranged on the substrate in a random order, then allocated an ID according to their position (Figure 4.2). The aim of this experiment was to capture all possible defect outcomes. The processing parameters are given in Table 4.2.



**Figure 4.2. Experiment 1 test cubes. Dotted boxes; failure to build due to insufficient energy density, vertical arrows; parts aborted due to excessive swelling, horizontal arrows; swelling on top cube led to geometrical inaccuracy on lower cube due to wiper damage. Wiper direction top to bottom.**

**Table 4.2. Processing parameters used in Experiment 1.**

<b>ID</b>	<b>q'</b> <b>(W)</b>	<b>τ</b> <b>(μs)</b>	<b>x</b> <b>(μm)</b>	<b>h</b> <b>(μm)</b>	<b>q*/(v*I*)</b>	<b>1/h*</b>	<b>E<sub>0</sub>*</b>	<b>Comment</b>
1	135	55	80	46	14.25	0.54	7.74	Visually acceptable
2	135	55	80	46	14.25	0.54	7.74	Visually acceptable
3	180	80	40	27	55.58	0.93	51.46	Very poor surface finish
4	135	55	136	46	8.36	0.54	4.54	Visually acceptable
5	90	80	120	65	9.31	0.38	3.58	Swell
6	135	90	80	46	23.38	0.54	12.71	Poor surface finish
7	135	55	24	46	48.31	0.54	26.25	Very poor surface finish
8	135	20	80	46	5.12	0.54	2.78	Failed
9	90	30	120	65	3.49	0.38	1.34	Failed
10	180	80	120	27	18.53	0.93	17.15	Poor surface finish
11	180	30	40	65	20.84	0.38	8.02	Visually acceptable
12	135	55	80	46	14.25	0.54	7.74	Visually acceptable
13	180	30	120	27	6.95	0.93	6.43	Swell
14	90	30	40	27	10.48	0.93	9.70	Aborted
15	180	80	120	65	18.53	0.38	7.13	Visually acceptable
16	72	55	80	46	7.60	0.54	4.13	Swell
17	200	55	80	46	20.90	0.54	11.36	Wiper damage
18	135	55	80	46	14.25	0.54	7.74	Visually acceptable
19	90	80	40	65	27.94	0.38	10.75	Visually acceptable
20	135	55	80	22	14.25	1.14	16.25	Visually acceptable

ID	$q'$ (W)	$\tau$ ( $\mu$ s)	$x$ ( $\mu$ m)	$h$ ( $\mu$ m)	$q^*/(v^*l^*)$	$1/h^*$	$E_0^*$	Comment
21	90	80	120	27	9.31	0.93	8.62	Aborted
22	180	30	120	65	6.95	0.38	2.67	Visibly porous
23	90	30	120	27	3.49	0.93	3.23	Failed
24	180	80	40	65	55.58	0.38	21.38	Poor surface finish
25	135	55	80	46	14.25	0.54	7.74	Visually acceptable
26	90	80	40	27	27.94	0.93	25.87	Visually acceptable
27	180	30	40	27	20.84	0.93	19.30	Visually acceptable
28	135	55	80	46	14.25	0.54	7.74	Visually acceptable
29	90	30	40	65	10.48	0.38	4.03	Visibly porous
30	135	55	80	73	14.25	0.34	4.89	Visually acceptable

The main observations from Experiment 1 are shown in Figure 4.3. Five samples failed to build. Three of these were given insufficient energy to fuse any powder (white points) while two were aborted after some layers (grey points) before excessive swelling of the part caused problematic damage to the wiper. Where enough energy was delivered to fuse some of the powder within a layer, but not sufficient for full consolidation between layers, lack-of-fusion type porosity occurs (blue points). These pores are arranged with some linear periodicity in the direction parallel to the layers. Keyholing behaviour (orange points) and melt splashing (pink points) were both observed when surplus energy was imparted to the powder. The central point of the DOE (yellow point) consisted of five replicates. Each displayed different defect types, with each void type occurring at least once within this subset.

Figure 4.4 shows the relative defect populations for the three void types, with LOF increasing most steeply over the smallest range of energy densities, illustrating the heightened sensitivity of build density to LOF voids compared with keyholing or splashing voids. The average density of samples containing LOF voids was 91.24%

compared to 98.69% for samples in the keyholing regime. Hence, the processing window for subsequent investigations was narrowed to the right hand side of the design space probed in Experiment 1.

Some samples contained both keyhole and LOF type porosities. This seems counter intuitive since the two types of pores are elsewhere observed to occur in separate processing regimes [14]. However, the observations can be explained by considering the effect of the individual process parameters on the local melt pool conditions (section 4.1.2).

Cracking was more prevalent in the samples processed at higher energy density and was minimised in those samples with high fractions of LOF voids (Figure 4.5). This cracking behaviour is discussed in detail in chapter 5.



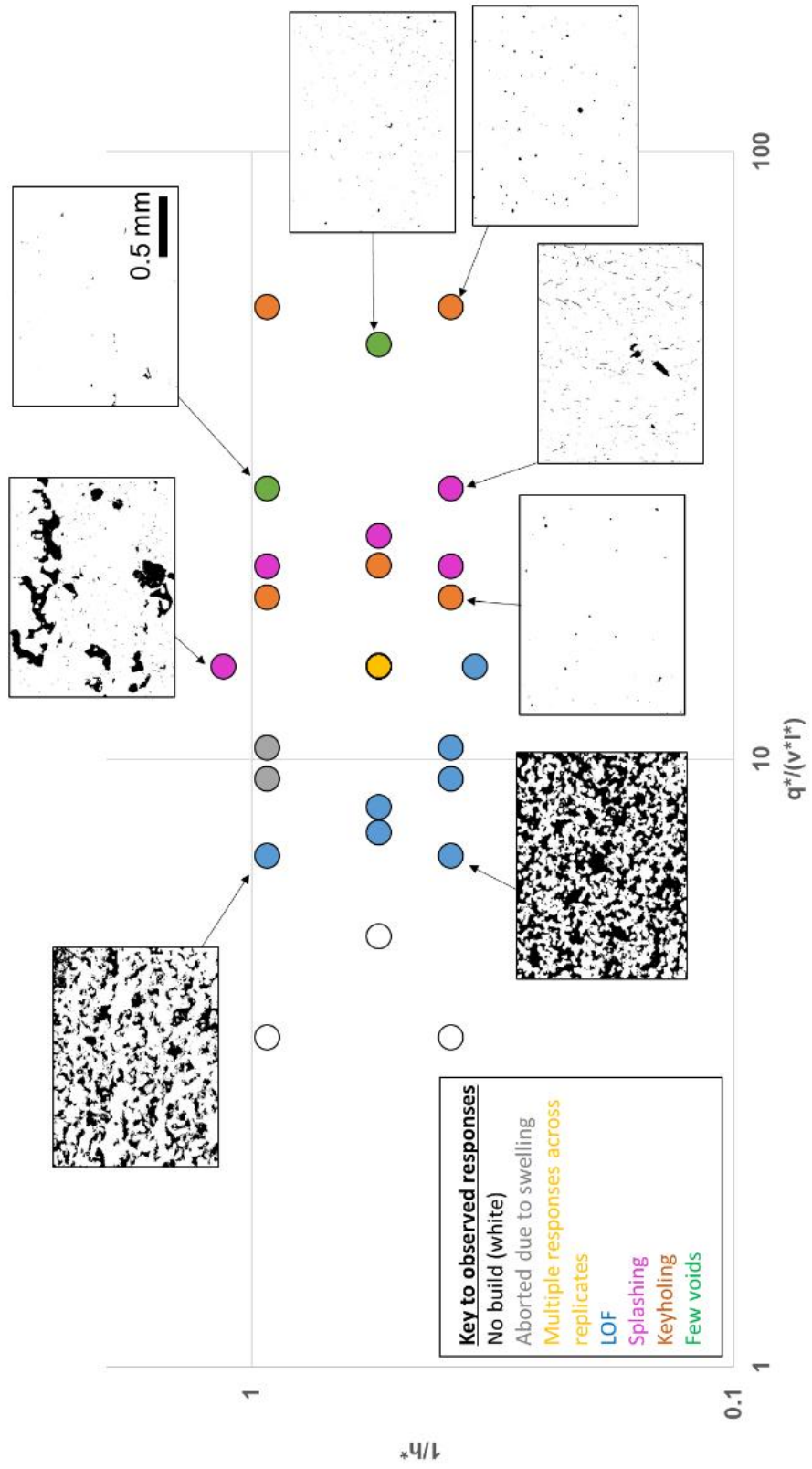
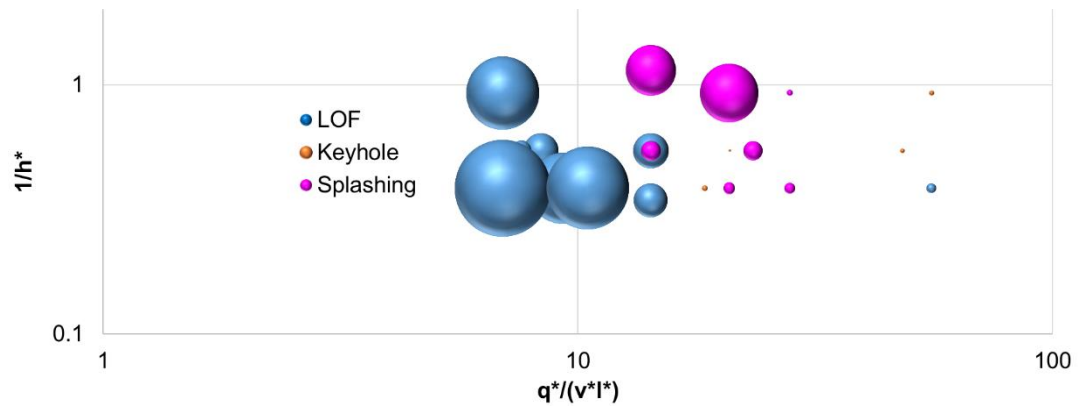
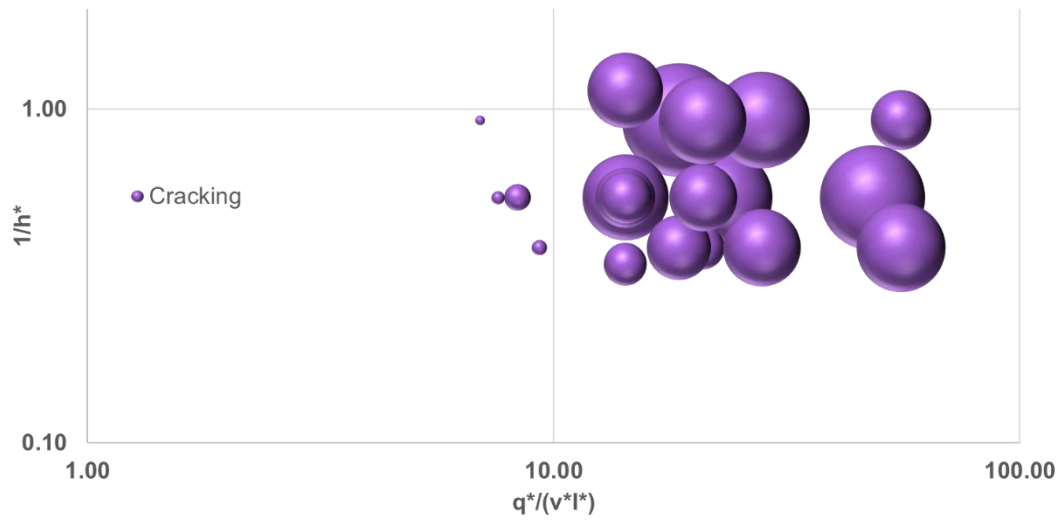


Figure 4.3. Defect outcomes from Experiment 1. Inset images: masks of defects. All inset images to same scale.



**Figure 4.4. Defect outcomes from Experiment 1. Bubble size represents relative area fraction of defect on micrograph.**



**Figure 4.5. Experiment 1. Bubble size represents relative area fraction of total cracking.**

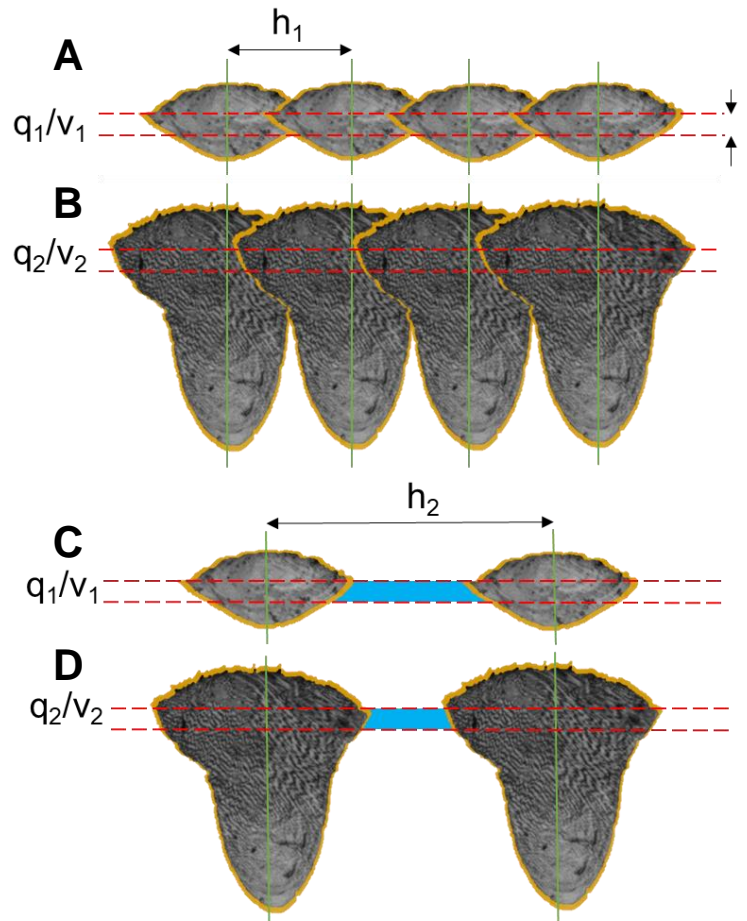
#### 4.1.2. A thought experiment: The concurrence of LOF and keyholing.

The importance of considering the effects of the individual processing parameters as well as the input energy density can be explained by the following thought experiment. Consider the four combinations of processing parameters;

<b>A</b>	$(q_1, v_1, h_1: E_0^*{}_A)$
<b>B</b>	$(q_2, v_2, h_1: E_0^*{}_B)$
<b>C</b>	$(q_1, v_1, h_2: E_0^*{}_C)$
<b>D</b>	$(q_2, v_2, h_2: E_0^*{}_D)$

where  $(q_1, h_1) < (q_2, h_2)$  and  $(v_2 < v_1)$  such that  $E_0^*{}_C < E_0^*{}_A = E_0^*{}_D < E_0^*{}_B$ . Layer thickness is kept constant. Although these combinations of parameters make up a 3 factorial experiment, only the four extreme combinations are considered here. For parameter set A, the melt pools are sufficiently overlapping that no un-melted (LOF) regions remain (Figure 4.6A). Increasing the energy density moves the processing into the keyholing regime for parameter set B (Figure 4.6B). This does not provide any benefit in terms of melt pool overlap, but increases the probability of forming keyhole voids and reduces the build rate. Parameter set C has lower energy density than parameter set A, since the hatch spacing is set wider. In this case, it is set to a value wider than the minimum necessary melt pool overlap so LOF voids are present in between the melt tracks (Figure 4.6C). Increasing the power and decreasing the scanning velocity leads to an increase in energy density in parameter set D, to a value equal to that in parameter set A. However, the combination of  $q_2$ ,  $v_2$  and  $h_2$  does not produce full overlap since the resulting transition to keyhole mode melting increases the melt depth but does not sufficiently increase the melt width to compensate for using the wider hatch spacing. So, in this scenario, LOF voids still form between the melt tracks even though a high energy density is used and melting is in the keyhole regime (Figure 4.6D). Hence, it is possible for LOF voids and keyhole voids to be present in the same sample since keyhole voids are a function of energy input local to the melt

pool whereas the presence of LOF voids depends on volumetric energy density. The same effect is possible in the scanning direction if the spot separation is greater than the melt pool width. Concepts for predicting melt pool overlap are presented in section 4.3.



**Figure 4.6. Thought experiment on the effect of changing individual processing parameters.**

#### 4.1.3. Experiments 2, 3 and 4.

Experiments 2, 3 and 4 were two-factor DOEs, maintaining constant input power within each DOE, to further refine the processing window. Experiment 2 used an input laser power of 180 W. The results indicated that extensive porosity occurred when energy density was above  $E_0^* = 16$ . Porosity was lowest towards the left side of the design space, so Experiments 3a and 3b were positioned in this area to assess the effect of using a higher input laser power.

A common misconception is that the energy density can be imparted to the powder using any combination of processing parameters to the same effect on structure, leading some to use high laser powers and fast scanning velocities to reduce build time. However, the outcome in terms of defects is sensitive to the way in which the energy is delivered, and increasing power and velocity is detrimental as shown through a comparison between Experiments 2, 3 and 4. Experiments 2 and 4 used an input laser power of 125 W whereas Experiment 3a-d used 200 W. Experiments 3a-d (Figure 4.7) lie within the energy density range  $4 < E_0^* < 16$  and display LOF just as readily as those in the lower energy density levels in Experiment 1. However, no melt splashing behaviours were observed in Experiments 3a-d. The samples processed at energy densities around  $E_0^* = 8$  contained a significant amount of LOF porosity, which presented itself in distinctive lines in the direction of the layers. These are likely to be due to the wide spot separations used to achieve the stated energy densities with the high laser power. In Experiment 4, when similar energy densities to those in Experiment 3a were comprised of a lower laser power, the range of defect responses in terms of the extent of LOF was less extreme (Figure 4.8). The possibility of producing LOF defects even with high laser power or high energy density is discussed next.

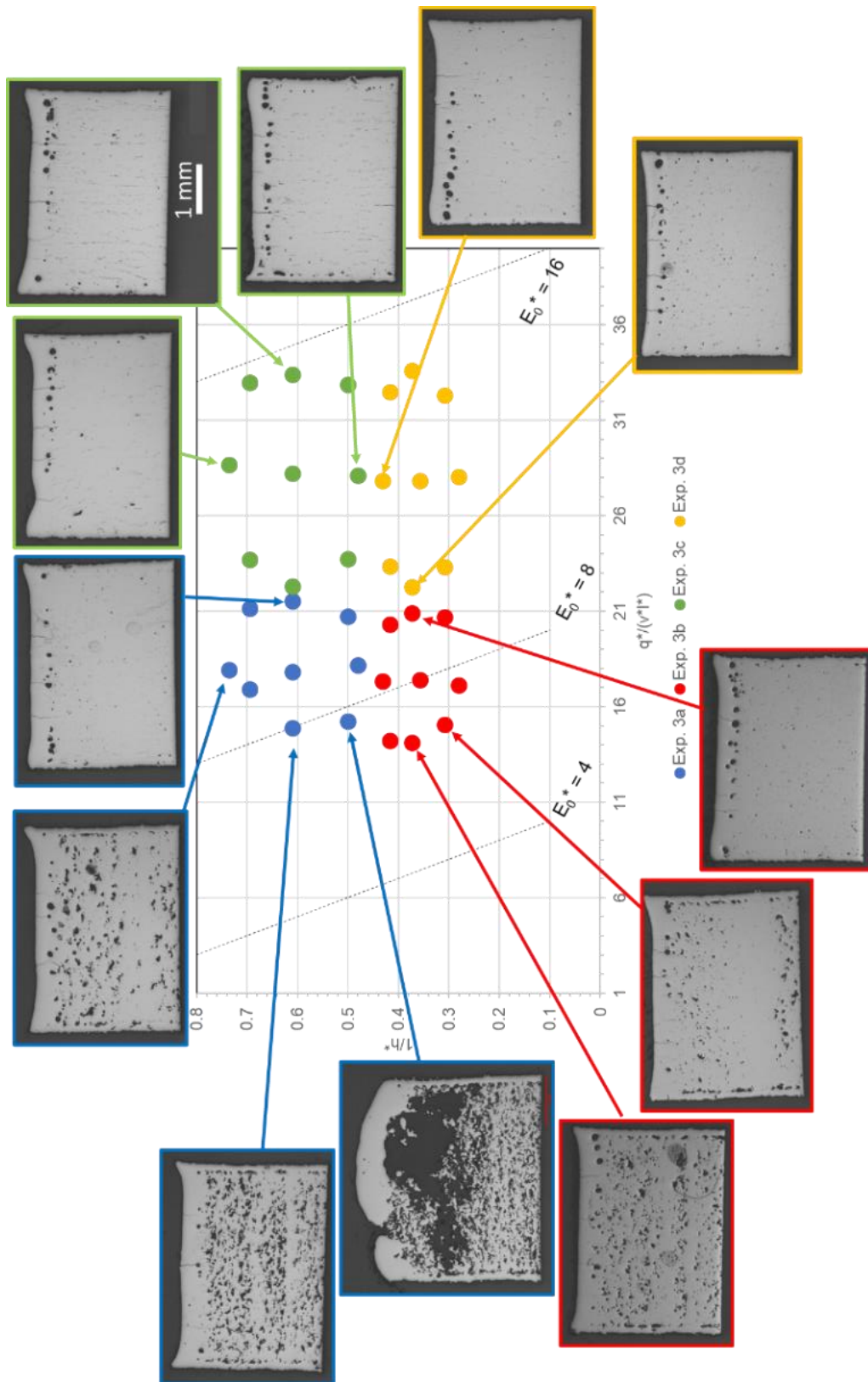
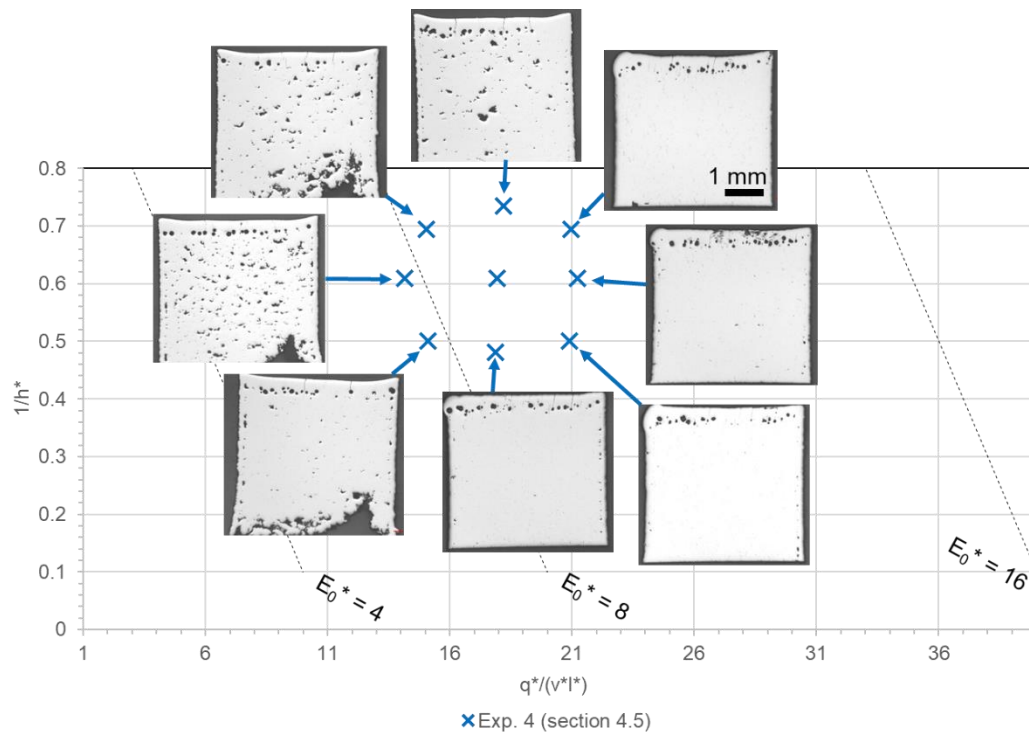


Figure 4.7. Experiments 3a-d. All inset images to same scale.



**Figure 4.8. Experiment 4. All inset images to same scale.**

Conducting physical experiments to assess defect populations is necessary but time consuming. Hence, correlating the measured responses to a model of the process provides a useful tool for predicting the outcome of a new set of processing parameters. Further analysis of a selection of these experiments is presented in the following sections.

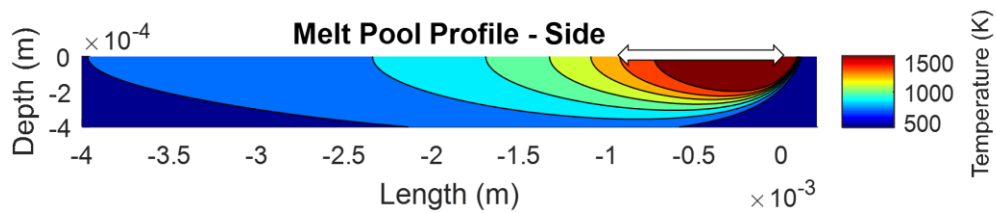
## 4.2. Melt pool modelling

To delve further into the observed defect behaviours and map out the LPBF process, it is useful to have a validated model which can be used to predict the thermal behaviour of the melt and hence the melt pool characteristics. The outputs of such a model can be used to predict whether LOF, keyholing or solidification cracking is likely to occur under a given set of processing conditions. In this work, an analytical model developed at the University of Sheffield by Felicity Freeman was used to calculate the melt pool characteristics for given input parameters (see Appendix 4 for model details).



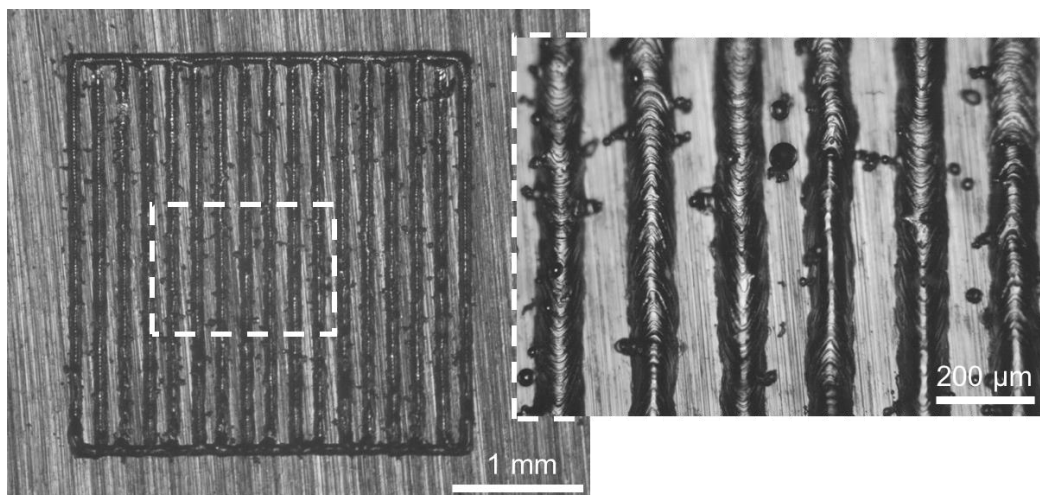
## The Application of AM to Ni-base Superalloys

The analytical model, [119] based on a modified Eagar [81] approach for a pulsed, Gaussian laser beam with corrections for the latent heat of melting, requires inputs of thermophysical properties of the alloy, sample size and LPBF processing parameters. Outputs of the model were melt pool dimensions, volume of the melt pool which is predicted to boil and the cooling rate of the melt pool. The cooling rate is taken at the top surface on the centre line of the melt pool between the liquidus and solidus isotherms (Figure 4.9). The volume of material which boils gives information on the transition point from conduction to keyhole mode.



**Figure 4.9. Example of a side profile view of the simulated melt pool. White arrow indicates position of calculation of thermal gradient.**

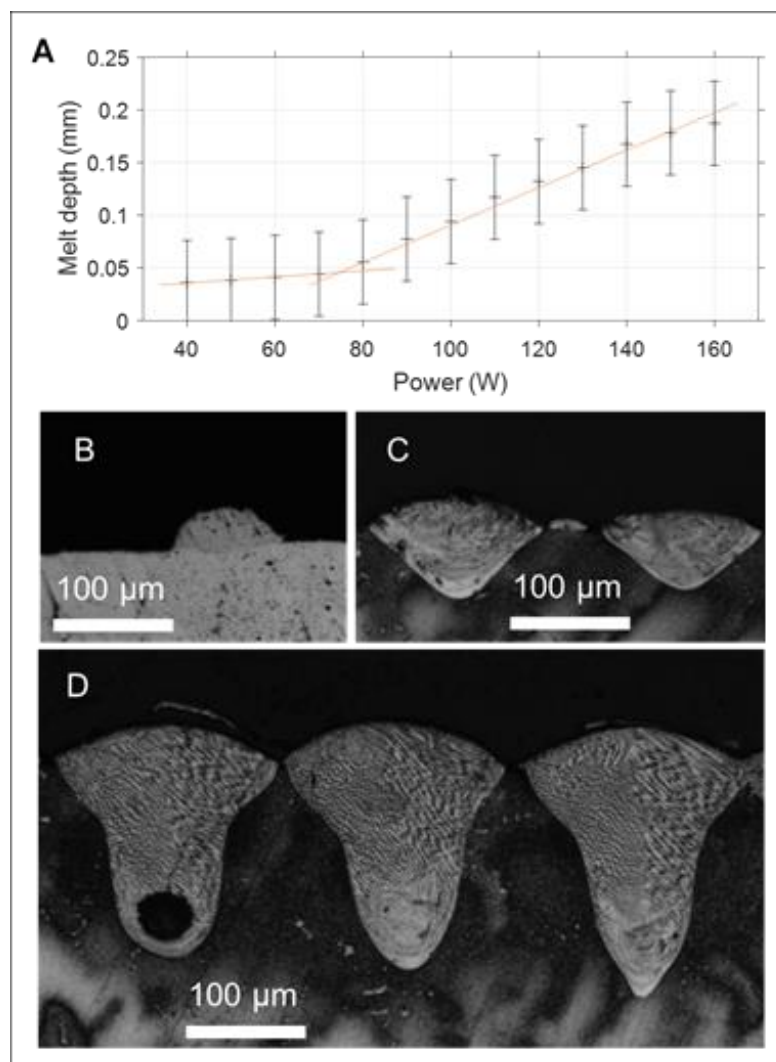
To validate the output of the model, single melt tracks (Figure 4.10) on cast IN713C covered with a single powder layer were performed. The melt tracks were sectioned, polished and etched before measurements of their depth and width were made using image processing software ImageJ [120].



**Figure 4.10. Melt tracks in cast IN713C covered with a single powder layer using power = 70 W, h = 200  $\mu$ m, x = 200  $\mu$ m and  $\tau$  = 100  $\mu$ s.**

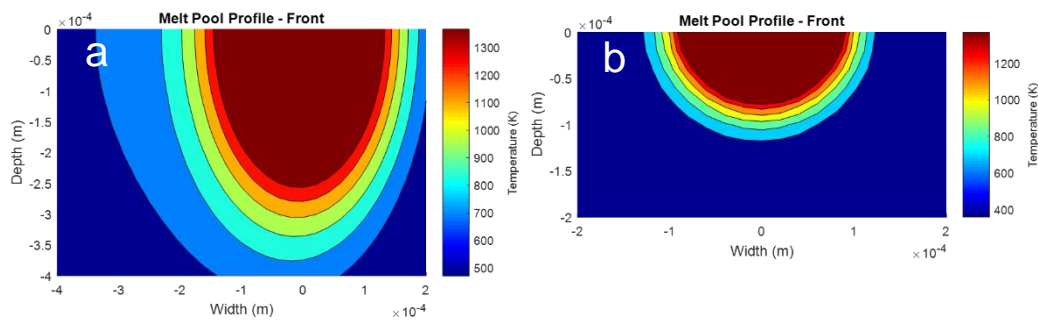


When the point spacing and exposure time were kept constant ( $x = 30 \mu\text{m}$ ,  $\tau = 100 \mu\text{s}$ ) and the laser power varied, the melt width increased linearly, whereas the melt depth displays two clear regimes (Figure 4.11). The intersection between these regimes is where the melt pool shape begins to display the characteristic “nipped in” waist of keyhole mode. However, this is occurring significantly before the depth reaches twice the width as stated in the literature [5], [50]. In fact, the melt depth was smaller than the melt width for every tested parameter combination. Hatch spacing was set to  $200 \mu\text{m}$  which was sufficiently wide to avoid melt track overlap.



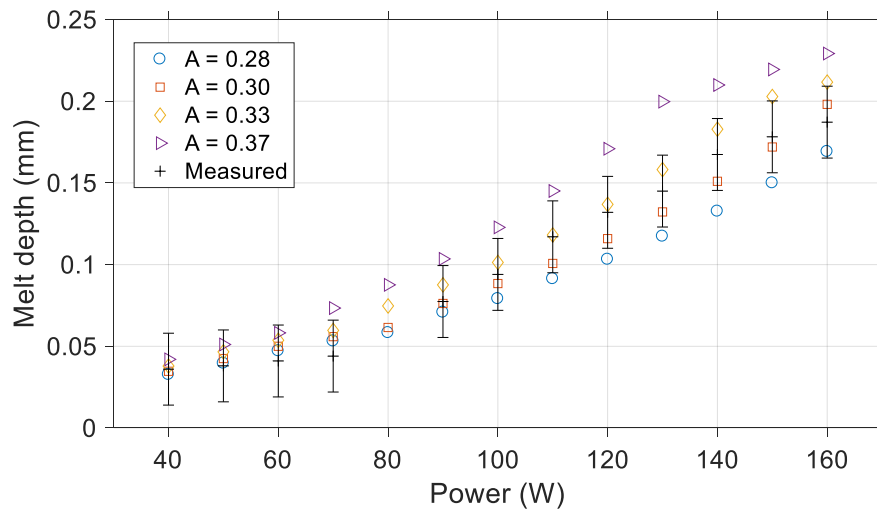
**Figure 4.11. Measured melt pool depths (A). Sectioned and etched melt pools using laser powers of 40 W (B), 90 W (C) and 160W (D) showing the transition to keyhole mode.**

The model required some optimisation to achieve good agreement with the measured melt pool dimensions. This was done by using the absorptivity,  $A$ , as a calibration factor. It was important to avoid an overestimation of the melt dimensions because this could cause their thermal fields to overlap, contributing extra thermal energy to neighbouring melt tracks. This can be seen in the thermal field images of the melt pools (Figure 4.12) as the thermal field becomes non-symmetric when it interacts with a neighbouring field. This is not representative of the experimental setup since the melt tracks were not observed to overlap.



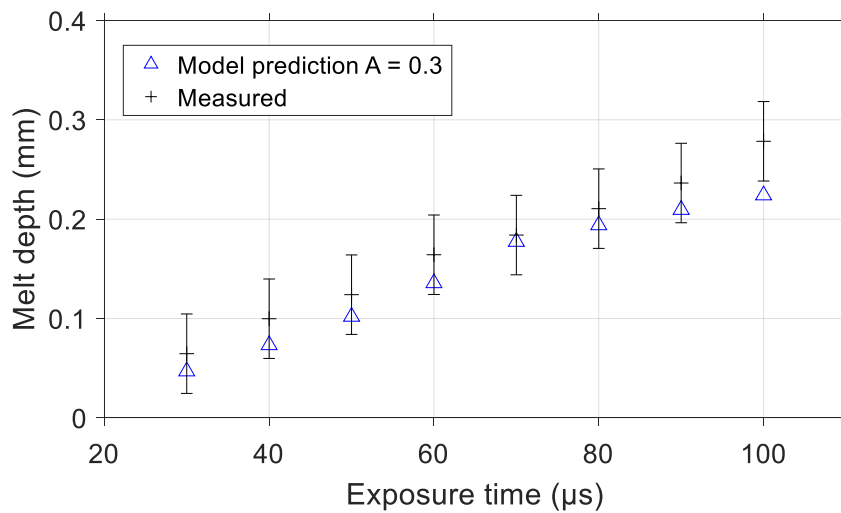
**Figure 4.12. Colour maps of the thermal field predicted by the analytical model using absorption factors of a)  $A = 0.4$  and b)  $A = 0.3$ .**

The model gives good agreement with the experimental measurements of melt pool depth at all the tested values of  $A$ , however as laser power was increased, increasing the size of the melt pool, the effect of changing  $A$  became more significant (Figure 4.13). The best agreement with the measured values was obtained for  $A = 0.3$  (Figure 4.15).

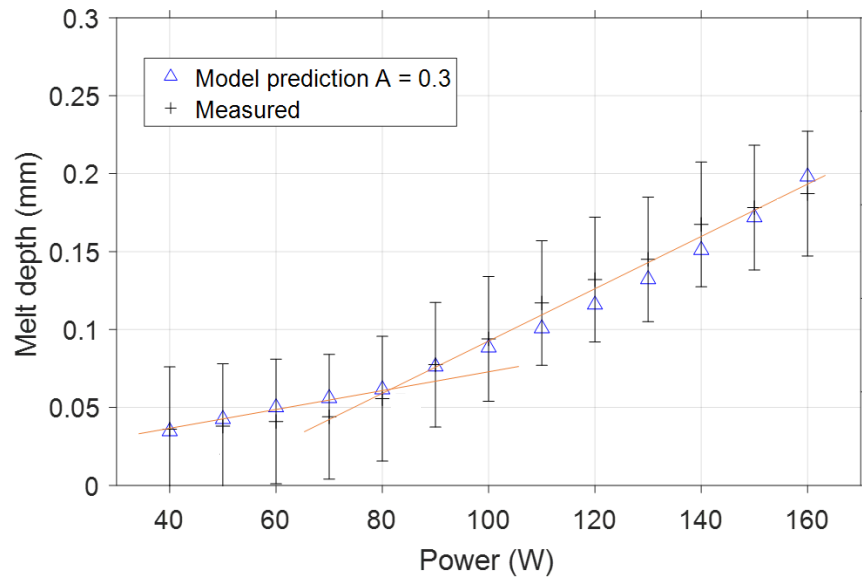


**Figure 4.13. Measured and predicted melt pool depths with changing laser power for various absorption factors.  $A = 0.3$  gives closest agreement with experimental measurements.**

When laser power was held constant and exposure time was varied, the model continued to return predictions of melt pool depth with good agreement to the experimentally measured values for  $A = 0.3$  (Figure 4.14).



**Figure 4.14. Measured and predicted melt pool depths for constant laser power of 200 W and varied exposure times.**



**Figure 4.15. Measured and predicted melt pool depths using model absorptivity factor  $A = 0.3$ .**

The transition between conduction mode and keyhole mode is evident in the model predictions and the measured values as the gradient of the power vs melt depth plot becomes steeper as keyhole mode dominates (Figure 4.15). When correlated with the experimental results, the model predicts that the keyholing regime begins when the volume of the melt pool which boils is above  $4.5 \times 10^{-14} \text{ m}^3$ . This corresponds to a cooling rate of  $3.8 \times 10^5 \text{ K/s}$ .

### 4.3. Concepts

After identifying the various defect types produced by LPBF processing in different regions of the process map, and armed with an analytical model of melt characteristics, three thought experiments were undertaken to aid the understanding of the process map. Firstly, when making a comparison between different LPBF processes, care must be taken to compare the process windows fairly, ensuring that the parameters are treated in such a way that the actual absorbed energy by the material is described. Hence, the concept of “attenuated parameters” was introduced. The other thought experiments presented in this section are related to the lack-of-fusion regime since the initial observations indicated the relatively sudden onset of this behaviour and increased sensitivity to a change in process settings compared to the high energy regime.

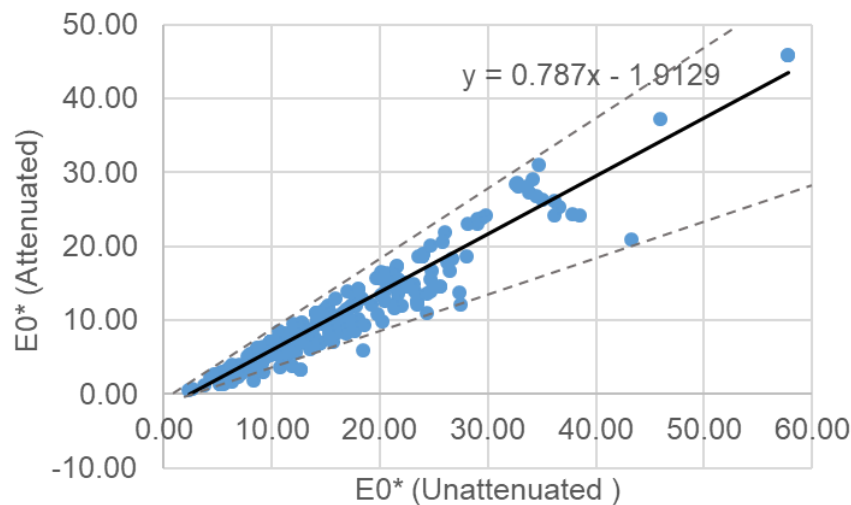
### 4.3.1. Attenuated parameters

In section 3.1.1 the concept of modulated lasers was presented. Since the Renishaw 125 system used in this work uses a modulated laser, it is necessary to adjust the laser power and laser velocity accordingly to account for the attenuation factor caused by the cumulative effect of the laser spending some of the time switched off during its travel time across the bed (before comparing with a continuous laser process). The input laser power specified by the operator,  $q'$ , and velocity of the laser are attenuated by factors related to the travel time ( $t$ ) of the laser while it is switched off. The laser velocity for the Renishaw machine is a calculated value, contrary to other machines where it is a direct input to the process. Attenuated power and velocity are given in Equations 4.1 and 4.2.

$$q = q' \frac{\tau}{(\tau + t)} \quad (\text{Eq. 4.1})$$

$$v = \frac{x}{(\tau + t)} \quad (\text{Eq. 4.2})$$

After making this adjustment, processing windows for specific materials can be easily compared to those used on other machine platforms. The attenuation produces energy densities lower than those predicted using  $q'$  (Figure 4.16). Attenuated parameters are used throughout this work for process mapping and representation of all experiments, however when processing parameters are quoted in experimental methodologies, these refer to the input values of power,  $q'$ .



**Figure 4.16. Un-attenuated vs attenuated energy density.**

### 4.3.2. Lack-of-fusion (LOF) conditions

In this section, the relationship between process settings and LOF defect formation is considered through two thought experiments. Firstly, dimensional analysis is used to relate LOF to normalised energy density. Next, the problem of LOF is considered according to the minimum necessary overlap of the melt pools to achieve full consolidation of the powder.

#### 4.3.2.1 The Buckingham Pi Theorem

The Buckingham Pi Theorem was used to relate the processing parameters to the LOF response. The Buckingham Pi Theorem forms the basis of dimensional analysis and can be successfully applied to numerous problems [121]. The usefulness of the theorem is fully exploited when used to describe an unknown response in a physical problem through a mathematical relationship. The physical law described by such a relationship is independent of the units designated to each process variable.

Independent physical variables thought to affect the response were listed. The method described in teaching material from MIT Open Course Ware [122] was used to obtain functions which describe the defect populations in terms of process variables. The chosen factors to which the theorem was applied are given in Table 4.3 and the dimensional analysis derivation is given in Equations 4.3 - 4.10.

**Table 4.3. Factors influential to LOF used in the Buckingham Pi Theorem.**

Factor	Dimension
%LOF	[ ]
$Aqt/x$	[MLT <sup>-2</sup> ]
$\rho$	[ML <sup>-3</sup> ]
$C_p$	[L <sup>2</sup> T <sup>-2</sup> ]
$l$	[L]

$$[MLT^{-2}]^a [ML^{-3}]^b [L^2T^{-2}]^c [L] = [M^0L^0T^0] \quad (\text{Eq. 4.3})$$

$$a + b = 0 \quad (\text{Eq. 4.4})$$

$$a - 3b + 2c = -1 \quad (\text{Eq. 4.5})$$

$$-2a - 2c = 0 \quad (\text{Eq. 4.6})$$

$$a = -b = -c \quad (\text{Eq. 4.7})$$

$$a = -\frac{1}{2} = -b = -c \quad (\text{Eq. 4.8})$$

$$\Pi_2 = \left(\frac{Aq\tau}{x}\right)^{-\frac{1}{2}} \rho^{\frac{1}{2}} (C_p \Delta T)^{\frac{1}{2}} l = \left(\frac{\rho C_p \Delta T x}{Aq\tau}\right)^{\frac{1}{2}} l \quad (\text{Eq. 4.9})$$

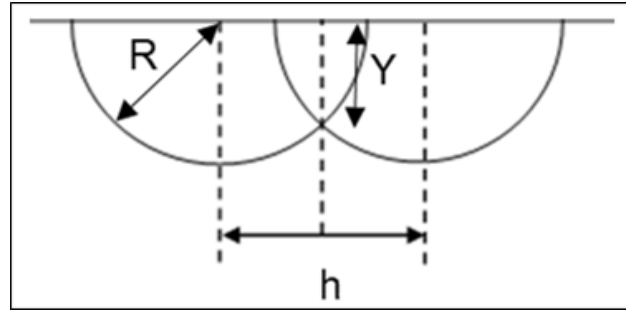
Letting the second term be squared:

$$LOF(\%) = C \left(\frac{\rho C_p \Delta T}{Aq} \frac{x}{\tau} l^2\right) \propto E_0^{*-1} \quad (\text{Eq. 4.10})$$

Where  $C$  is a constant of proportionality and layer thickness can be substituted for hatch spacing. Application of the Buckingham Pi Theorem indicates that LOF is inversely proportional to energy density (Equation 4.10), as expected.

#### 4.3.2.2. Theory of overlapping hemispheres

In a general sense, achieving sufficient overlap between neighbouring melt pools to avoid LOF requires the formation of a melt pool deep enough so that the depth of the overlapping portion ( $Y$ , Figure 4.17) takes a value greater than the thickness of one layer. Assuming that the melt pools can be approximated to hemispheres (i.e. processing in conduction mode) a simple geometrical relationship has been derived between layer thickness, hatch spacing ( $h$ ) and predicted melt pool radius ( $R$ ) as the criterion for avoiding LOF.



**Figure 4.17. Overlapping circles showing the relationship between hatch spacing ( $h$ ), predicted melt pool radius ( $R$ ) and depth of the overlap ( $Y$ ).**

Assuming the melt pools are spherical with radius  $R$ , the geometry of overlapping circles (Figure 4.17) gives the maximum overlap depth of two melt pools to be;

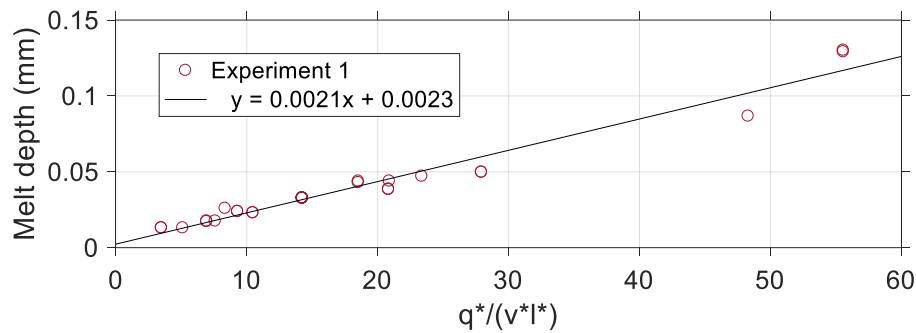
$$Y = \left( R^2 - \left( \frac{h}{2} \right)^2 \right)^{\frac{1}{2}} \quad (\text{Eq. 4.11})$$

If the melt pools are not predicted to overlap at all,  $R^2 < (h/2)^2$  and there will be no mathematical solution. For full consolidation of powder, expression 4.12 must be satisfied.

$$l < \left( R^2 - \left( \frac{h}{2} \right)^2 \right)^{\frac{1}{2}} \quad (\text{Eq. 4.12})$$

An estimate of the melt pool radius is required for this calculation. In order to develop a readily utilisable model for LOF which can make fast predictions of the likelihood of LOF, a relationship between input areal energy density and predicted melt pool depth (from the analytical melt pool model detailed in Appendix 4) was obtained. Figure 4.18 shows the linear relationship between the normalised areal energy density ( $q^*/(v^*l^*)$ ) and the model's prediction of melt depth for the parameter sets from Experiment 1. The linear relationship gives a simple way of predicting melt pool depth (radius) from the processing parameters.

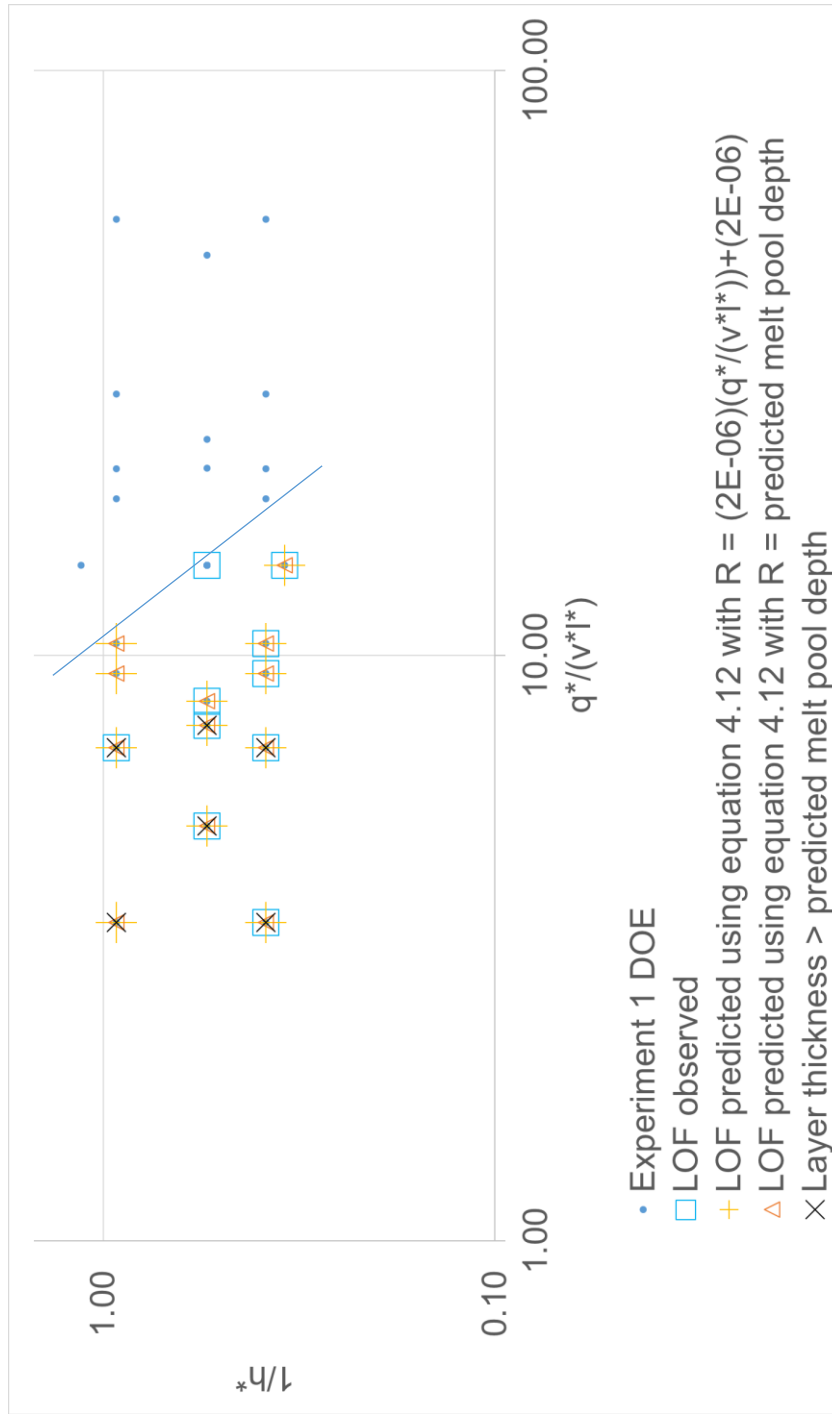




**Figure 4.18. Linear relationship between areal energy density and predicted melt pool depth with the process settings of Experiment 1.**

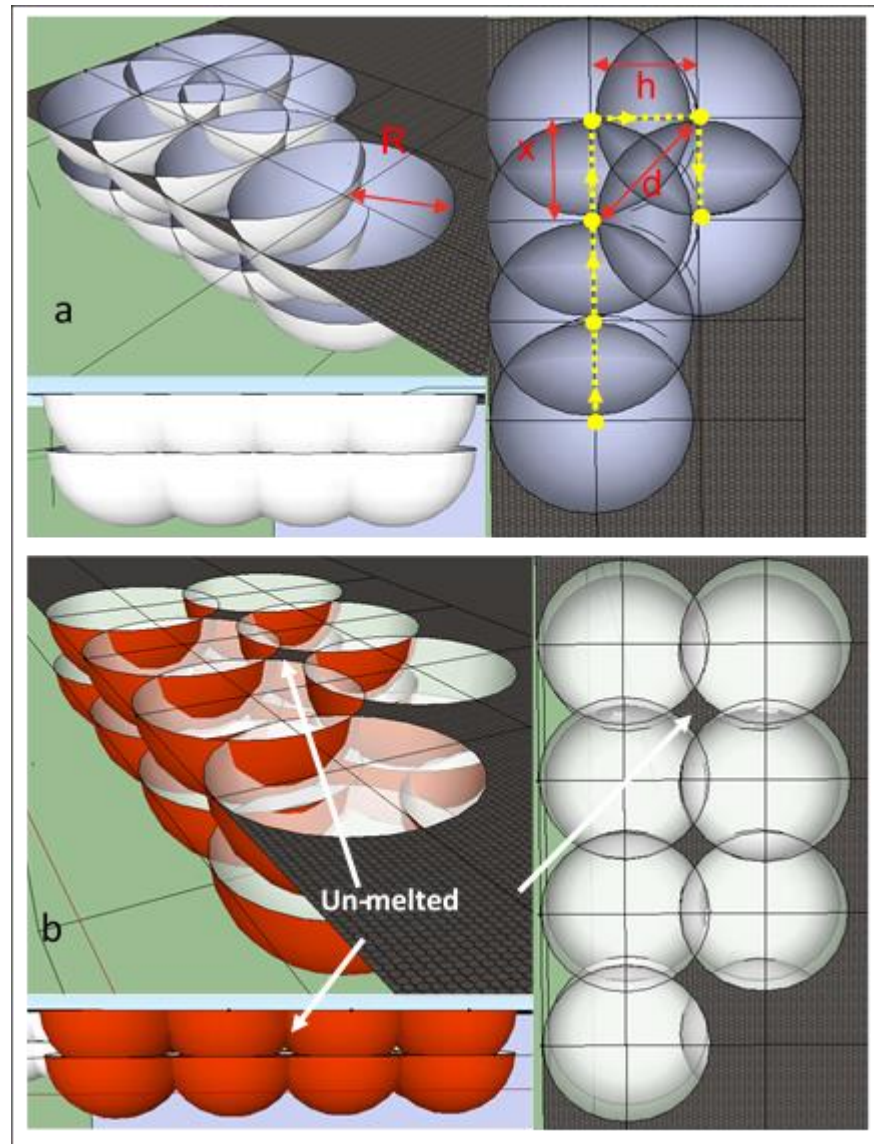
This method of estimating  $R$  saves the computational time associated with analytical modelling. Its ability to predict LOF defect formation through the LOF condition in Equation 4.12 was assessed for the process settings used in Experiment 1. The direct output of melt pool depth (as an estimate of  $R$ ) was also used in Equation 4.12 as a comparison.

In Figure 4.19 the predicted occurrences of LOF using the various estimations of melt pool radius are plotted alongside the observed LOF for Experiment 1. This plot also shows that the derived LOF condition is more accurate in predicting LOF behaviour than a straight forward comparison of melt pool depth and layer thickness, confirming the need to consider the three dimensional nature of the overlap problem. Comparing the predicted melt pool depth to the layer thickness doesn't change the predicted likelihood of LOF occurring with changing energy density. However, the Buckingham Pi Theorem suggests LOF increases with decreasing energy density, in agreement with the experimental observations.

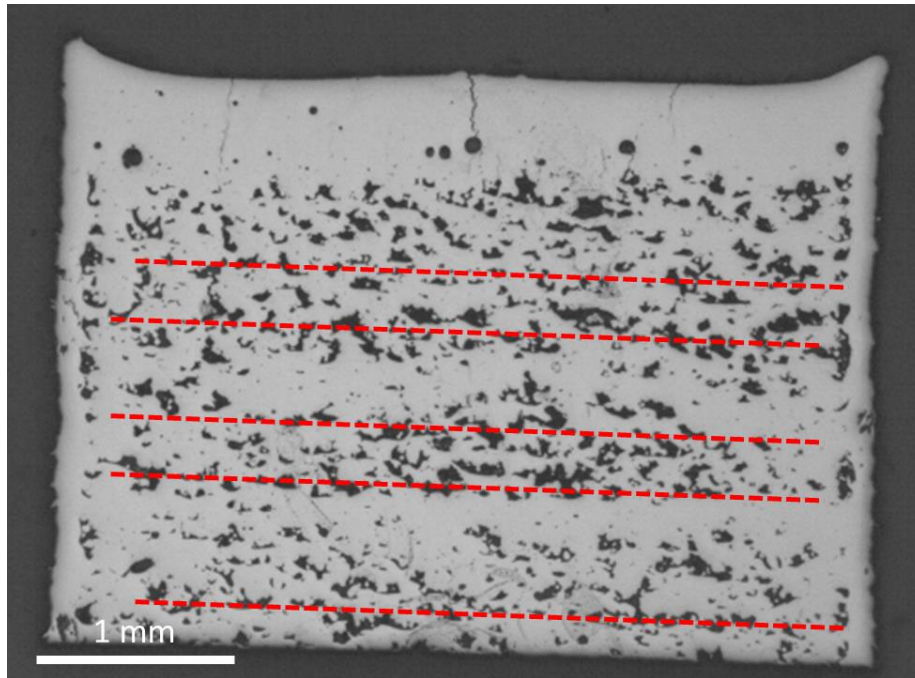


**Figure 4.19. Predicted and observed occurrences of LOF voids for process settings in Experiment 1. The straight line indicates the cut-off point for LOF void formation.**

According to Figure 4.20 cavities resulting from this lack of overlap are expected to lie in regular arrays. Due to the rotation of the scan, in practice these are not always observed, although several instances where the plane of the arrays coincided with the sectioned plane occurred in the experiments (Figure 4.21).



**Figure 4.20. Overlapping hemispherical melt pools illustrating the cases of a) optimum overlap and b) insufficient overlap (LOF).**



**Figure 4.21. An example of the linear distribution of LOF voids in a sample from Experiment 3a. The LOF voids are aligned in the plane of the layers indicating insufficient energy has been imparted to the material to consolidate the powder layers.**

#### **4.4. Taxonomy of defect types**

Although defect formation in LPBF materials is complex and depends on multiple contributing factors including processing parameters, thermo-physical properties, local solidification conditions and bulk cooling conditions, the main defect types can be categorised in a general sense according to the energy density regime under which they form. Six main types of defects have been identified in the LPBF IN713C and their characteristics were classified and categorised in 2D and 3D using SEM and XCT imaging techniques

Generally, keyhole pores occur when too much energy is imparted to the powder and LOF defects occur when the energy density is insufficient for full melt pool overlap (Figure 4.22). However, as described in 4.1.2. it is possible for the two

regimes to occur simultaneously. Melt splashing voids (Figure 4.23) also occur at the high energy end of the scale. Gas pores (Figure 4.23), possibly arising from retention of prior gas porosity in the powdered feedstock, can occur over the whole input energy range, even being found within the optimum processing window, although they are less prevalent at higher energies when the melt pool lifetime is longer and they have more time to escape the surface tension of the melt. The occurrence of cracking is more difficult to correlate with energy density, as will be explained in section 5, however solidification cracking is more likely to occur at high energy density and solid state stress relief cracking is more likely to occur at lower energy densities (Figure 4.24). The characteristics of these six defect types are summarised in Table 4.4.

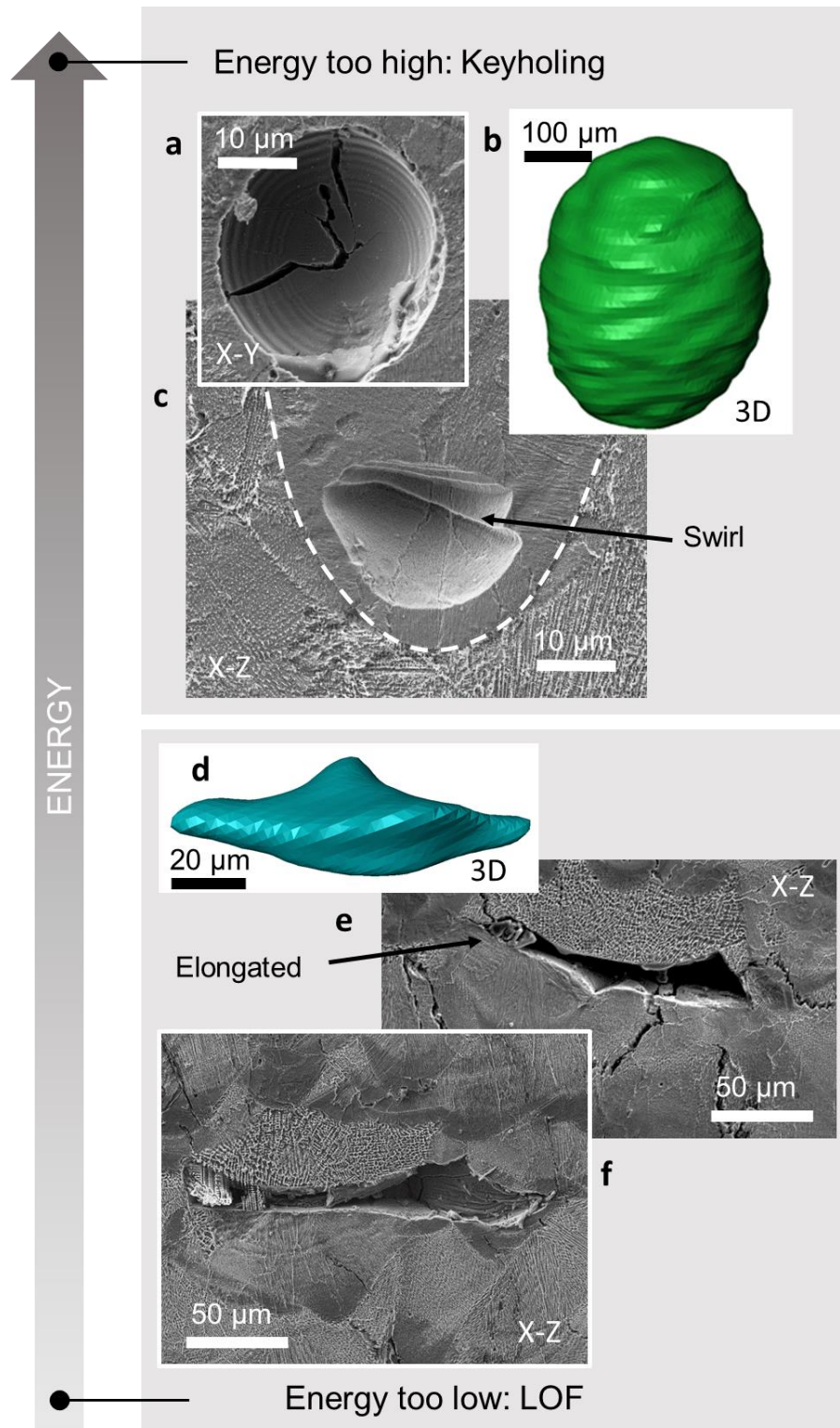
**Table 4.4. Characteristics of six types of LPBF defects observed in IN713C**

<b>Defect</b>	<b>Energy regime</b>	<b>Morphology</b>	<b>Size</b>	<b>Position</b>
Keyhole	High	Spherical, oval or hemispherical, smooth interior, swirl pattern resulting from turbulent flow	20 – 200 $\mu\text{m}$ diameter	Bottom of a melt pool, often seen at the turn around position of the laser
LOF	Low	Elongated in plane of layers, sharp features, often containing powder	100 – 200 $\mu\text{m}$ length	Often occurring in lines parallel to layers
Splashing	High	Convolutated but smooth features, can contain trapped powder	$\sim 500 \mu\text{m}$	Randomly distributed

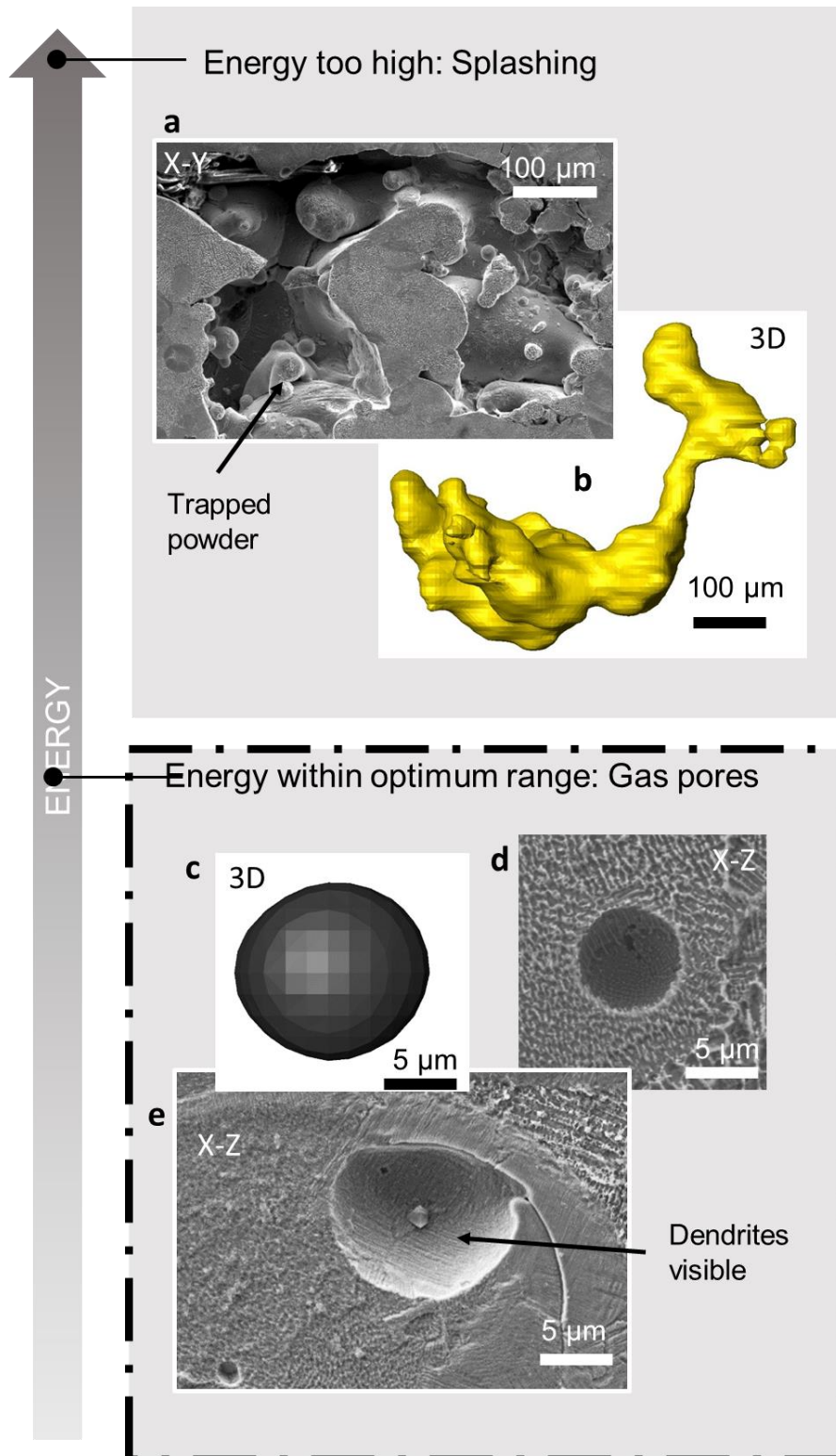
## The Application of AM to Ni-base Superalloys

<b>Defect</b>	<b>Energy regime</b>	<b>Morphology</b>	<b>Size</b>	<b>Position</b>
Gas pores	All	Small and spherical, dendritic structure can be seen on internal surface	< 50 $\mu\text{m}$	Randomly distributed
Solidification cracking	High	Zig-zag, reminiscent of a “tear”, crack surfaces are smooth with evidence of liquid film, blunt crack tips	Length on scale of melt pool	Intergranular, often interconnected/connected to stress relief cracks to form wider network
Stress relief cracking	Low	Straighter and sharper than solidification cracks with no evidence of liquid film	Can extend across several layers	Throughout the material, often connected with/propagating from a solidification crack or irregularly shaped pore



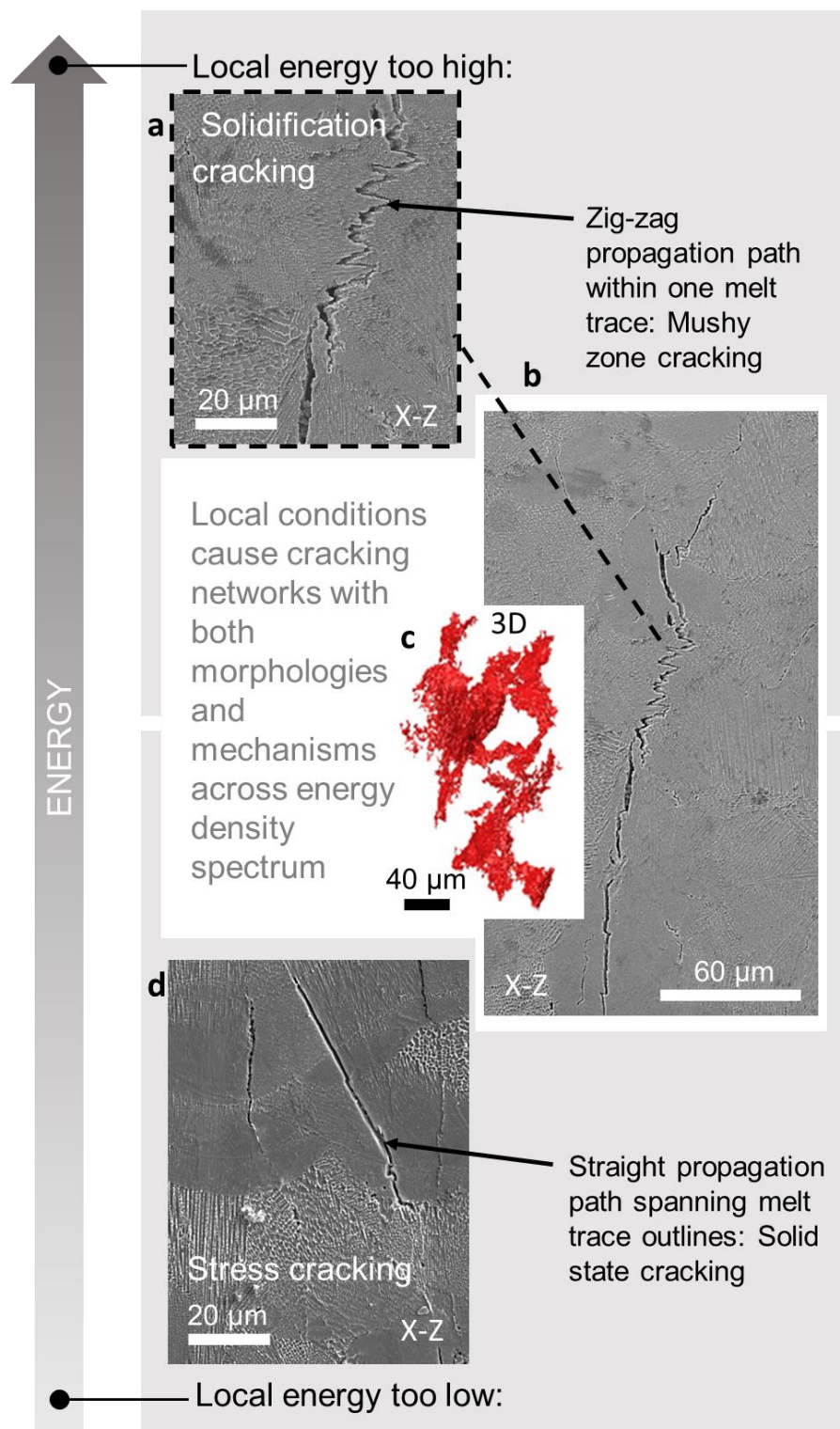


**Figure 4.22. Taxonomy of defects 1: Keyhole voids [a) SEM micrograph with characteristic swirl pattern on inner surface viewed in XY plane, b) XCT reconstruction, c) SEM micrograph XZ plane] and LOF voids [d) XCT reconstruction, e,f) SEM micrographs in XZ plane showing elongated morphology].**



**Figure 4.23. Taxonomy of defects 2: Splashing pores [a) SEM micrograph showing trapped powder in XY plane, b) XCT reconstruction] and gas porosity [c) XCT reconstruction, d,e) SEM micrographs in XZ plane showing dendritic structure].**





**Figure 4.24. Taxonomy of defects 3: Cracking defects [a) SEM micrograph of characteristic zig zag propagation of solidification crack in XY plane, b) interconnected stress cracks and solidification cracks, c) XCT reconstruction of interconnected cracks, d) SEM micrograph in XZ plane of straight propagation path of stress crack spanning a melt trace outline.**

#### **4.5. Minimising porosity in LPBF processed IN713C using response surface methodology with 2D and 3D characterisation techniques**

Since little understanding exists on defect formation in LPBF processed nickel-base superalloy IN713C, this study aimed to elucidate the relationships between processing parameters and defect characteristics through systematic 2D and 3D analysis of defect populations in LPBF test specimens. The objectives of the study were:

- To characterise and quantify defect types in IN713C processed using a range of input energy densities using conventional image analysis and XCT.
- To investigate the sensitivity of defect formation to individual processing parameters.
- To correlate gas porosity with prior gas contamination of powdered feedstock.
- To identify processing parameters resulting in maximum density using DOE and RSM.

##### **4.5.1. Fabrication of LPBF specimens**

13 cubic test specimens, of size 4.1 mm x 4.1 mm x 4.1 mm, were built directly onto a stainless steel substrate using a set of processing parameter combinations occupying a design space on the normalised energy map described by a CCD (Experiment 4, Figure 4.1) with energy densities normalised against material properties.

A selection of parameter combinations, indicated in Table 4.5 with superscript X were used to fabricate a second set of larger samples (4 mm x 4 mm x 9 mm) for XCT analysis. A small section was taken from the sample labelled subscript Y for high resolution XCT scanning. A laser power of 125 W and layer thickness of 20  $\mu\text{m}$  was used for all samples. Following the LPBF build completion, samples were removed from the substrate by wire electrical discharge machining and examined in the as-deposited state.

**Table 4.5. Normalised energy densities corresponding to LPBF processing parameters. Superscripts X and Y indicate parameters used to produce low and high resolution XCT samples respectively.**

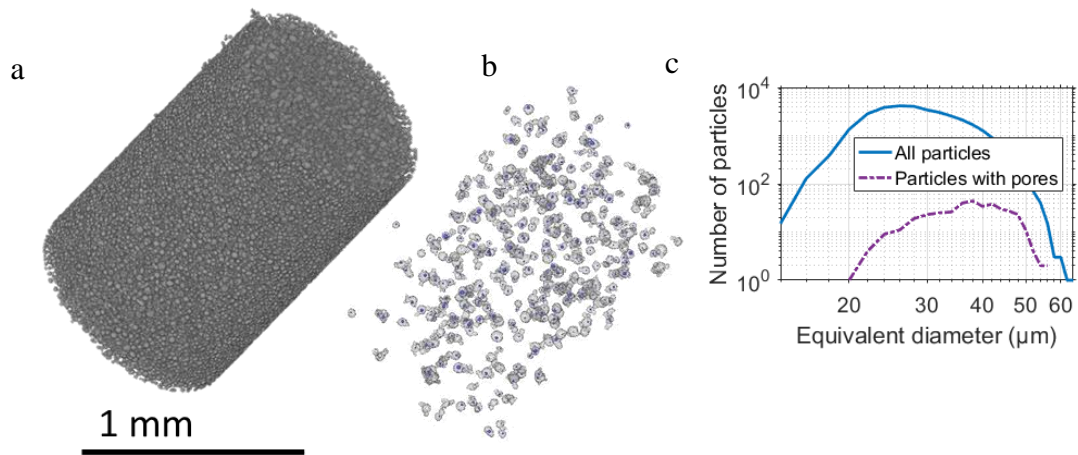
Sample ID	$q^*/(I^*v^*)$	$1/h^*$	$E_0^*$
1	17.93	0.61	10.93
2	18.21	0.74	13.39
3 <sup>X</sup>	17.86	0.48	8.59
4	14.16	0.61	8.63
5	21.23	0.61	12.95
6 <sup>X</sup>	15.05	0.69	10.45
7 <sup>X</sup>	20.96	0.69	14.55
8 <sup>X</sup>	15.09	0.50	7.54
9 <sup>X</sup> <sub>Y</sub>	20.89	0.50	10.45

#### 4.5.2. Optical microscopy

Samples were sectioned in the x-z direction, where x and z are the wiper and build directions respectively, and polished to 1  $\mu\text{m}$ . Optical micrographs were analysed using ImageJ software [120] with automatic thresholding settings to avoid operator bias. Processing parameters were optimised using Response Surface Regression and ANOVA, as described in section 3.3, and were subsequently used to manufacture a sample during a second LPBF build.

#### 4.5.3. XCT powder characterisation

High resolution XCT analysis indicated that 374 of 33427 powder particles examined (1.12 %) contained a pore. These pores were predominantly spherical, indicative of argon trapped during atomisation. The overall volume fraction of pores in the powder feedstock sample was 0.03%. Sphericity (as defined as how closely the shape of a particle matches that of a sphere, with sphericity = 1) of the powder particles was low, with more than half the particles having a sphericity of less than 0.9. Figure 4.25 shows that pores occur preferentially in larger particles. The mean particle equivalent diameter was 30  $\mu\text{m}$ .



**Figure 4.25. a) 3D representation of a sample of powder feedstock scanned using high resolution XCT, b) visualisation of those powder particles containing voids (blue) and c) distribution of particle sizes in feedstock sample. Note, figure indicates number density not volume density.**

This study focused only on the internal structure of the test cubes for measurements of total porosity, since different defect features are created close to the outer edges due to the interaction of the outer contour laser scans with the internal meander hatching. In this study all quantification of defect populations was conducted on the inner volume of samples, i.e. the portion melted by the hatching strategy. It has been shown that it is acceptable to ignore the outer portions of the micrographs for the purposes of this study (Figure 3.4) because the internal porosity is approximately constant over the area of measurement (6.63 mm<sup>2</sup>). The external skins experienced different processing conditions to the internal volume (which is dominated by hatching strategy) therefore results obtained from the internal volume are used in the present analysis.

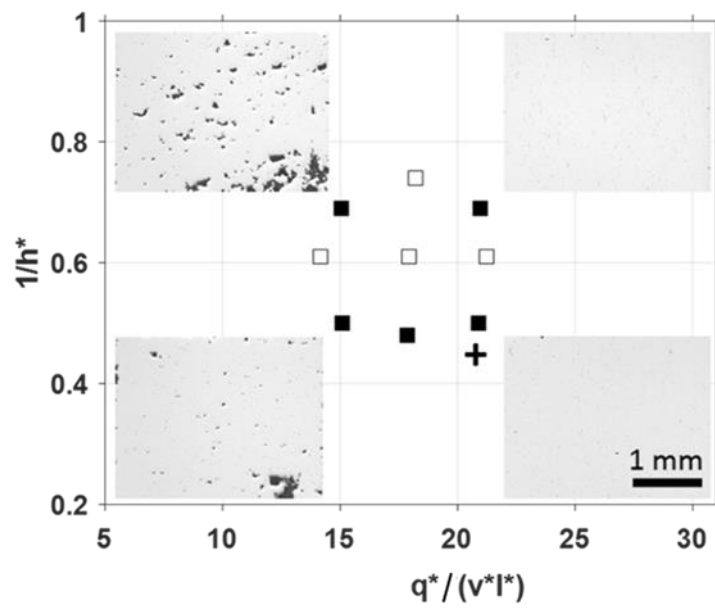
#### **4.5.4. Effect of process setting on overall defect area fraction**

Total porosity was observed to vary across the investigated process window, increasing with scan velocity. Mapping out the defect response on the processing parameter map (Figure 4.26) illustrated that the effective laser scan speed, influenced by the exposure time, had the greatest effect on overall porosity, with increased velocity leading to a more unstable melt track and more porosity [90].

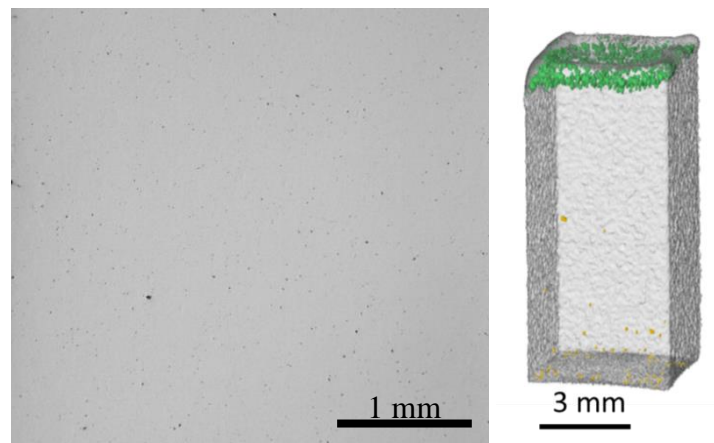
Changing the hatch spacing also affected the average pore size. At small hatch spacing the optical micrographs show that there are fewer irregular voids, but those which did form were larger than those occurring in samples with wide hatch spacing. RSM was performed using the software Minitab, to optimise the parameters for minimised porosity. RSM gave the point at which the porosity response was minimised for the central composite design with an R-squared value of 94%. A trial LPBF build was performed (Figure 4.27) using the optimised parameters which resulted in less than 0.05% porosity when measured using image analysis. The sample was scanned using 5.8  $\mu\text{m}$  voxel size XCT and found to contain 0.075% porosity in the bulk of the volume.

In order to assess the effect of process settings on the resulting total porosity, the melt pool conditions were modelled using the analytical model described in Appendix 4. The model was used to calculate melt pool dimensions and cooling rate ( $\dot{T}$ ). Cooling rate is more strongly influenced by scan velocity than hatch spacing (Figure 4.28) suggesting that for the given set of processing parameters, the cooling rate of the material is sufficiently fast that the residual heat in the melted region has dissipated before the laser returns on the neighbouring raster, thus is not making a significant contribution to the melt pool size for these samples.

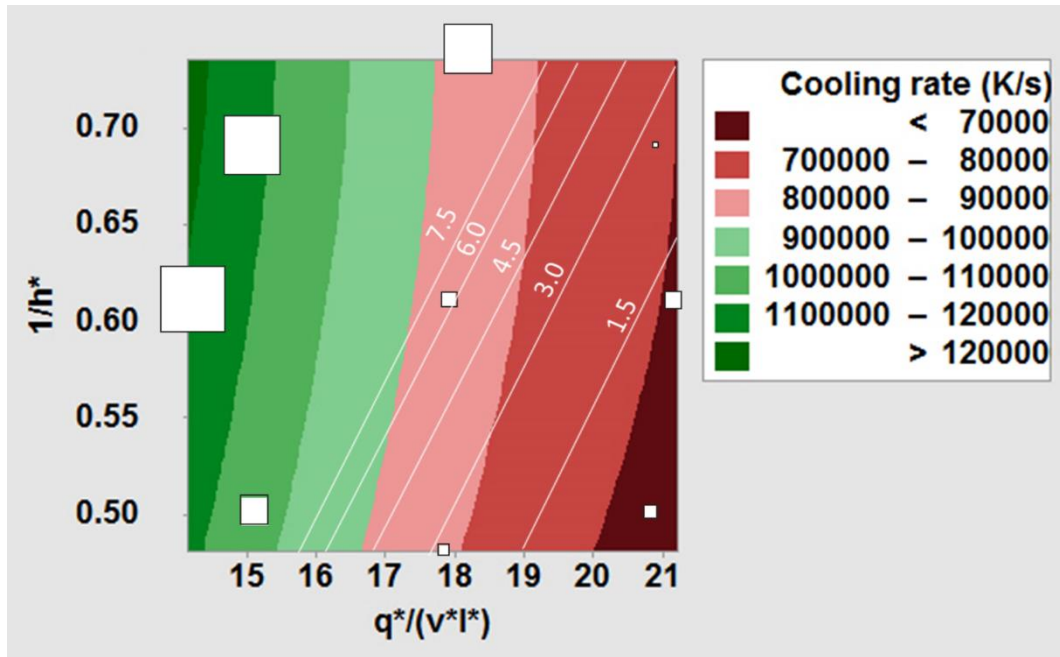
According to the model, using the same energy density but over a 40% wider hatch spacing by decreasing laser velocity (e.g. sample 9 compared with sample 6) the cooling rate is slower and the melt volume is 27 % larger. When melt volume is larger, the total porosity decreases. This can be attributed to increased overlap depth between layers since the decrease in laser velocity between samples 6 and 9 resulted in a predicted increase in re-melting from 4.7 layers to 9.1 layers, even though the centres of the laser paths are spaced further apart. As full density is approached, increasing the melt volume further has a reducing effectiveness (Figure 4.29).



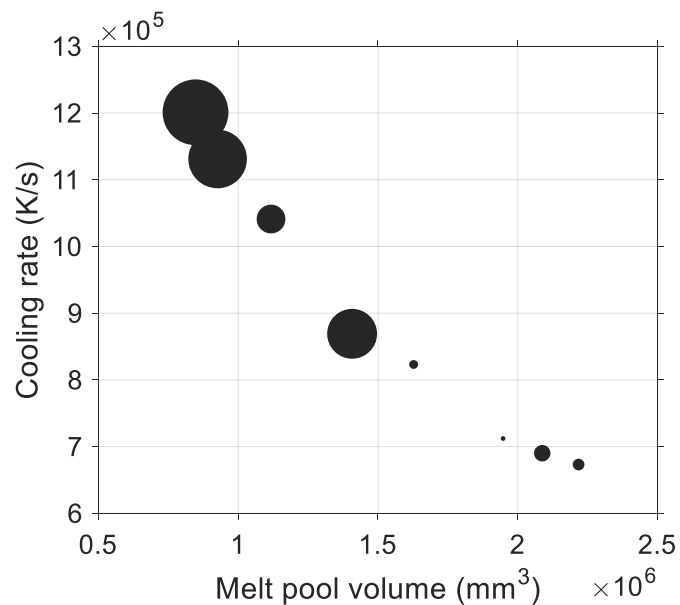
**Figure 4.26. Central composite design describing the processing parameters used to fabricate the LPBF specimens showing reduced porosity as effective scan velocity decreases. Filled markers indicate parameters used to produce XCT samples. Location of optimised parameters according to RSM is indicated by a cross (+). All inset images to same scale.**



**Figure 4.27. Trial build using RSM optimised parameters gave 0.058% porosity when measured using 2D image analysis and 0.075% total porosity in the bulk volume when measured using 5.8  $\mu\text{m}$  voxel size XCT. Once again, the pores at the top of the sample (green) have been excluded from the quantification.**



**Figure 4.28. Response surface of calculated cooling rates. Overlaid squares indicate relative total porosity at the DOE points. Overlaid white lines show the result of RSM regression analysis indicating how porosity changes with processing parameters.**



**Figure 4.29. Influence of melt pool volume and cooling rate on total porosity. Relative total porosity indicated by size of points.**

#### 4.5.5. Individual defect analysis

In order to understand the origins of the defects observed it is necessary to examine their size, morphology and frequency in more detail. The costs associated with XCT precludes the examination of all samples, however, high and low resolution XCT has been used to examine selected samples and categorise the defects. Pores were sorted into two main types; spherical (aspect ratio  $< 1.41$ ) and irregular. With  $5.8 \mu\text{m}$  voxel size XCT, spherical pores were separated into two categories; small (equivalent diameter  $50 < 80 \mu\text{m}$ ) and large (equivalent diameter  $> 80 \mu\text{m}$  and within  $100 \mu\text{m}$  of top surface). Using  $1.5 \mu\text{m}$  voxel size XCT the defects were sorted into spherical pores (equivalent diameter  $< 10 \mu\text{m}$ , aspect ratio  $< 1.41$ ), irregular pores (manually selected) and cracks (else).

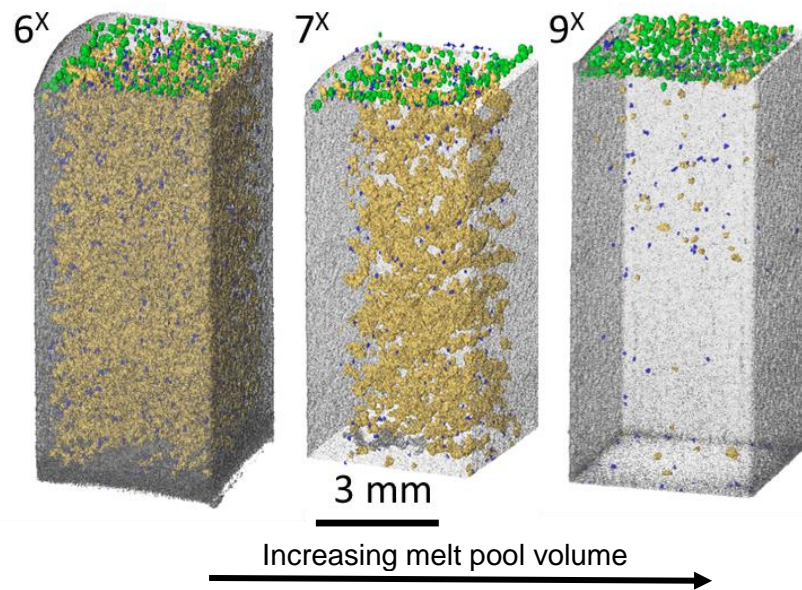
A 3D representation of each sample was reconstructed from the  $5.8 \mu\text{m}$  voxel size XCT (Figure 4.30). Large irregularly shaped voids (yellow) vary in volume fraction significantly between samples, while small gas pores (blue) show less variation between samples. Large spherical pores residing just below the top skin (green) are ubiquitous amongst the samples. In the limited sample set, increasing energy density reduced the volume fraction of small gas pores. Providing more energy to the powder creates a larger melt pool, which remains liquid for longer, allowing the gas bubbles more time to escape [84]. Leung et al [123] show that re-melting and complex, fast flowing melt pools also facilitate pore coalescence and escape from the surface.

The lower resolution XCT results confirm that the samples with the highest total porosity are from those containing large irregular voids. All XCT samples contained some large irregular pores and shape factor analysis showed that there was no significant difference in pore morphology between samples processed at high and low energy densities. All samples contained irregular pores with shape factors between 4 and 5. These large irregular pores showed a similar trend (Figure 4.31) as in the 2D analysis with high porosity in samples processed with high laser velocities, creating a smaller melt pool which cools more quickly than those with slower scan velocities.

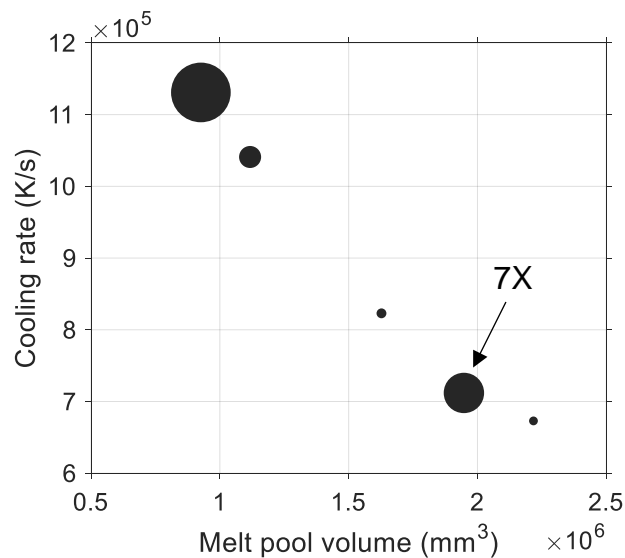


Since the melt pool depths resulting from even the fastest scan speed in the sample set are more than four times deeper than the layer thickness and at least four times wider than the hatch spacing, the large irregular pores are unlikely to be due to lack of fusion between the layers. Additionally, the voids are distributed randomly throughout the sample volume rather than in inter-layer locations as would be expected from incomplete melting. Instead, the rapid scan velocity observed to exacerbate the effect is likely to be forming unstable melt pool behaviours leading to melt pool splashing and discontinuities in the melt track. Irregular melt tracks leading to porosity were simulated using computational fluid dynamics (CFD) and experimentally confirmed by Panwisawas et al. [90]. The authors attributed the non-spherical porosity to unstable melt flows and melt splashing. A fast scan speed produced a high thermal gradient and set up a flow perpendicular to the powder bed, which acted to lift the melt away from the substrate and form voids. The morphology of the large pores observed in this paper is consistent with them resulting from melt track instability since they are irregular and convoluted, but elongated in the plane of the layers as predicted by the model [90].

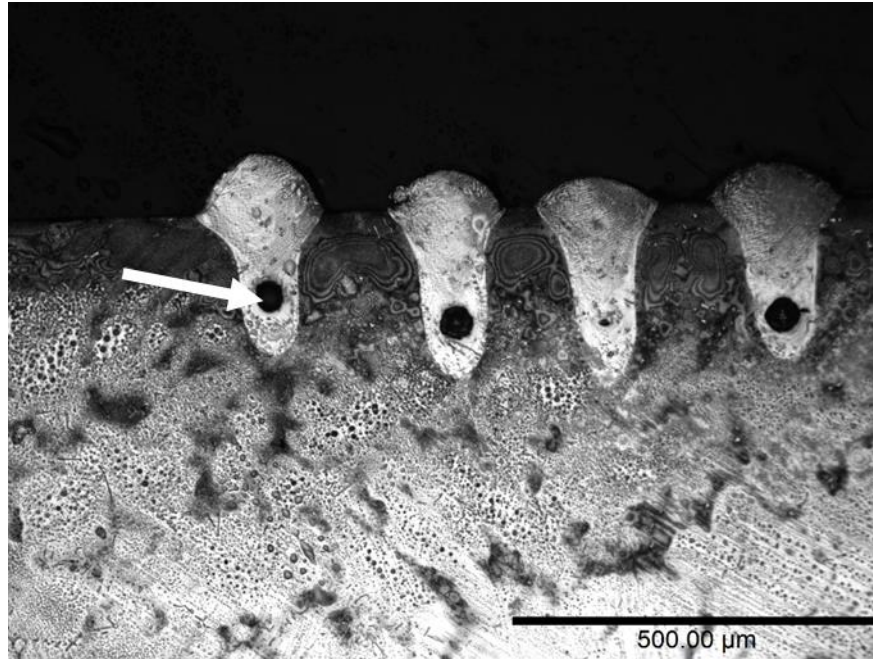
The apparently anomalous sample 7X, shown in Figure 4.31 appears to feature an unexpectedly high volume fraction of large irregular pores based on its melt volume and cooling rate. However, this can be explained by looking at the result in the context of the process map, as discussed in section 4.6, figure 4.34.



**Figure 4.30. 3D reconstruction of samples 6X, 7X and 9X scanned using 5.8  $\mu\text{m}$  voxel size XCT. Small spherical pores are shown in blue, large irregular voids are shown in yellow and large spherical pores residing under the top skin are coloured green.**



**Figure 4.31. Variation in large irregular porosity measured using XCT with melt pool volume and cooling rate. Relative porosity indicated by size of points.**

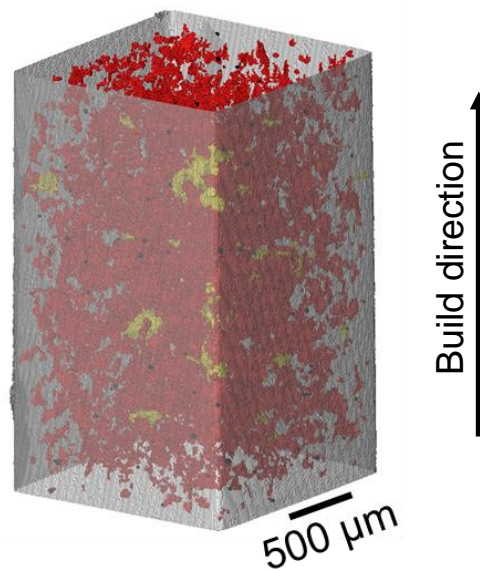


**Figure 4.32. Keyhole pores (example arrowed) observed in single melt tracks using  $q'=200$  W,  $h = 200$   $\mu\text{m}$ ,  $x = 30$   $\mu\text{m}$  and  $\tau = 100$   $\mu\text{s}$ .**

The large spherical pores shown in green in Figure 4.30 under the top layer arise due to re-scanning of the top layer without adding any extra powder. This is designed to improve the surface finish of the top skin. However, when similar settings were used to melt single tracks in solid IN713C, keyholing was observed (Figure 4.32). Clearly the re-melting of the top skin requires some optimisation to avoid keyholing in the top layers.

Precipitation strengthened nickel-base superalloys are well known to crack under laser processing [10], [58], [83], [100], [124], [125], however no cracks could be observed in the lower resolution XCT data highlighting the importance of appropriate resolution examination when optimising processing parameters. In contrast, the 1.5  $\mu\text{m}$  voxel size XCT was able to detect these cracks, which were measured to be 2-5  $\mu\text{m}$  wide and present in volume fractions between 1-1.6%. The cracks form a uniformly distributed, coherent network (Figure 4.33) throughout the samples and propagate in the build direction, consistent with observations in other studies [124], [125].

Comparison of the volume fraction gas pores measured by high resolution XCT of the powder and solid material reveals some differences, being 0.01-0.02 % in the solid versus 0.03 % in the powder. This indicates that gas within the powder is able to escape the melt pool during processing. King et al [32] also suggest that trapped gas should be able to escape given a sufficiently deep melt pool using models of the melt pool dynamics. Larger irregular voids were also observed in the high resolution XCT (0.2-0.5%) and are randomly distributed throughout the sample volume displaying similar morphologies to those observed in the lower resolution XCT.



**Figure 4.33. 3D reconstruction of sample 9<sub>Y</sub> scanned with 1.5 μm voxel size XCT showing coherent network of cracks (red), irregular shaped voids (yellow) and gas pores (black).**

#### **4.5.6. Implications**

In this chapter it has been demonstrated that 2D image analysis techniques were sufficient for the optimisation of LPBF processing parameters for minimising porosity and the development of LPBF processing strategies to obtain high density material. The results from 2D image analysis were used in conjunction with RSM to optimise process settings, achieving porosity of 0.05%. In addition, it enables the identification of suitable samples or parameter sets for further more complex and costly characterisation using XCT.

It has been shown elsewhere that elongated defects are the most damaging to fatigue life [126]. From this viewpoint the LPBF process may be more tolerant to a slight surplus of energy than it is to insufficient energy due to the effects of lack of fusion on fatigue life [77]. However, excess energy either throughout the layer or locally produces non round pores which also must be avoided. This work has shown that it is not just the amount of energy which affects the pore formation in the material but also the way in which the energy is delivered. Here, the combination of exposure time and hatch spacing have been shown to influence the amount and type of pore formation more strongly than the overall energy density. This has important implications for the development of processing parameters for certain geometries, a concept which will be discussed in chapter 6.

XCT has shown that the 0.03% volume fraction of argon gas contamination of the powdered feedstock can account for the small, spherical gas porosity present in the LPBF samples at volume fractions between 0.01 – 0.02%. In addition to this, powder particles with non-spherical morphologies degrade the spreading performance of the powder and may lead to increased inhomogeneity in the powder bed and the formation of large irregularly shaped voids. Hence it may seem logical to seek higher quality powder for LPBF processing. For example, plasma atomisation produces powders with higher sphericity, fewer satellite particles, and lower levels of gas contamination than gas atomised powders [127], [128].

However, this higher quality is offset by a commensurate increase in cost. Powder bed AM is best suited to production of small, complex, premium components. The main advantage being gained from designs which cannot be produced through conventional manufacturing routes. However, the premium price of such components must be balanced with the cost of production and this work shows that it is possible to reduce porous defects within LPBF components through manipulation of processing parameters without the need for premium feedstock.

#### 4.6. Understanding the process space

The results from all the experiments presented in Chapter 4 were collated and used to produce a map of the process space for LPBF IN713C (Figure 4.34). The absolute values shown in this process map are specific to IN713C test cubes built using a Renishaw SLM125 system with 20  $\mu\text{m}$  layers and a laser spot size of 25  $\mu\text{m}$ . However, the trends are expected to be transferrable to other LPBF systems.

Two thresholds for LOF are shown in Figure 4.34. LOF1 was derived using the expressions for melt pool depth and the concept of minimum necessary melt pool overlap (section 4.3.2.2) reproduced as Equations 4.13 and 4.14 below. Substituting the predicted melt pool depth as the hemispherical melt pool radius,  $R$ , and rearranging for  $h$  gives an expression for the maximum possible hatch spacing which can be used (for a layer thickness of 20  $\mu\text{m}$  and beam radius of 25  $\mu\text{m}$ ) for each value of areal energy density, whilst still achieving full melt pool overlap.

Translating into normalised parameters gives the equation of the threshold marked LOF1 (Equation 4.15). This equation has a quadratic term arising from the trigonometry involved in the overlapping hemispheres mathematics, so the expression does not describe a relationship which is strictly inversely proportional to normalised energy density. However, Figure 4.34 shows that the approximation holds for areal energy densities around, and greater than, the process window.

$$R = 0.0021 \left( \frac{q^*}{(v^*l^*)} \right) + 0.0023 \quad (\text{Eq. 4.13})$$

$$l < \left( R^2 - \left( \frac{h}{2} \right)^2 \right)^{\frac{1}{2}} \quad (\text{Eq. 4.14})$$

$$\frac{1}{h^*} = \frac{0.0025}{2 \sqrt{(0.0021 \left( \frac{q^*}{v^*l^*} \right) + 0.0025)^2 - 0.002^2}} \quad (\text{Eq. 4.15})$$

The region labelled LOF2 arises from a combination of empirical results of Experiments 1-4 combined with the LOF parameter developed using the Buckingham Pi Theorem (reproduced as Equation 4.16). Since LOF was shown to vary as the inverse of input energy density, an expression was derived empirically from experimental observations, for the onset point of LOF (Equation 4.17). This is a linear relationship between normalised areal energy density ( $q^*/(v^*l^*)$ ) and the inverse of normalised hatch spacing ( $1/h^*$ ). A straightforward rearrangement of Equation 4.17 shows that LOF voids were observed for  $E_0^* < 7.39$ .

$$LOF(\%) = C \left( \frac{\rho C_p \Delta T}{Aq} \frac{x}{\tau} l^2 \right) \propto E_0^{*-1} \quad (\text{Eq. 4.16})$$

$$\left( \frac{1}{h^*} \right) = 7.39 \left( \frac{q^*}{(v^*l^*)} \right)^{-1} \quad (\text{Eq. 4.17})$$

Figure 4.34 shows that this empirically derived LOF threshold, based on experimental observations of the onset of LOF, defines a smaller process window than the one described by LOF1. This means that LOF voids were observed in samples using hatch spacings smaller than the minimum hatch spacing required for LOF void formation according to Equation 4.15. A possible reason for this difference is the deviation of the actual melt pool shape away from true hemispheres. At the outer edges of the melt pools, the depth tends to be less than that of a true hemisphere (Figure 4.11B). This would have the effect of creating LOF voids, with the types of morphologies shown in Figure 4.22 (d-f).

The threshold for the keyhole regime was obtained using the correlation between the experimental observation of keyholing in melt tracks and the result of the analytical melt pool model. The onset of keyholing was observed to correlate with a volume of boiling material of  $4.5 \times 10^{-14} \text{ m}^3$  which is the case for all points lying to the right of the line labelled “Keyhole regime” in Figure 4.34.

For the purpose of clarity, it is important to discuss the reasons behind this threshold for keyhole behaviour being a vertical line, independent of hatch spacing. Although the transition to keyhole mode melting occurs when too much energy is imparted to the material, it is the way in which the energy is delivered which is important, rather than the overall energy density. The analytical melt pool model showed that

## The Application of AM to Ni-base Superalloys

for a sufficiently large sample, the melt pool was not significantly affected by the hatch spacing (see section 5.3) and as such, the transition to keyhole mode can occur at high or low energy density, given a suitable combination of  $q$  and  $v$  to exceed the threshold.

The threshold for melt splashing was obtained by observations of the onset of this behaviour. At regions of high energy density (top right corner of process map) keyholing and melt splashing can occur within the same sample. However, due to the physical limitations of the Renishaw SLM125 machine, there are few instances where the necessary conditions would occur. The minimum hatch spacing achievable on this platform is 20  $\mu\text{m}$ , which places an upper limit of  $1/h^* = 1.25$  on the process space.

Returning to the analysis of the XCT samples from section 4.5.6, the observed occurrences of porosity in samples 6X, 7X and 9X (Figure 4.30, Figure 4.31) can be better understood in the context of the process map (Figure 4.34). Samples 6X and 7X both lie on the threshold line for melt splashing defects, which explains their high levels of irregular porosity. However, sample 9X, which had low porosity, lies within the recommended processing window.

According to the process map, melt splashing and LOF behaviours can also occur in the same sample and this was observed in Experiment 1. This correlation can be explained in physical terms since, although melt splashing is most significantly affected by a reduction in hatch spacing, the behaviour is known to be exacerbated by fast scan velocities, which also reduce the areal energy density leading to the formation of LOF voids.

On this process map, the keyholing and LOF regions are not shown to overlap in an area which is physically accessible on the Renishaw SLM125 system. However, in previous discussions (section 4.1.2), it was shown that theoretically the two phenomena could occur simultaneously. The remaining portion of the process map (shaded yellow) represents the recommended processing window for IN713C within which the defect response is at a minimum.



Since both thresholds were found using a methodology involving melt pool modelling, the positions of these boundaries have some flexibility, and can be considered to have some “thickness” defined by any error in the melt pool model, or experimental error in the defect quantification. The effect of straying outside of this window and its effect on the design of a processing strategy for a component are discussed in chapter 6.

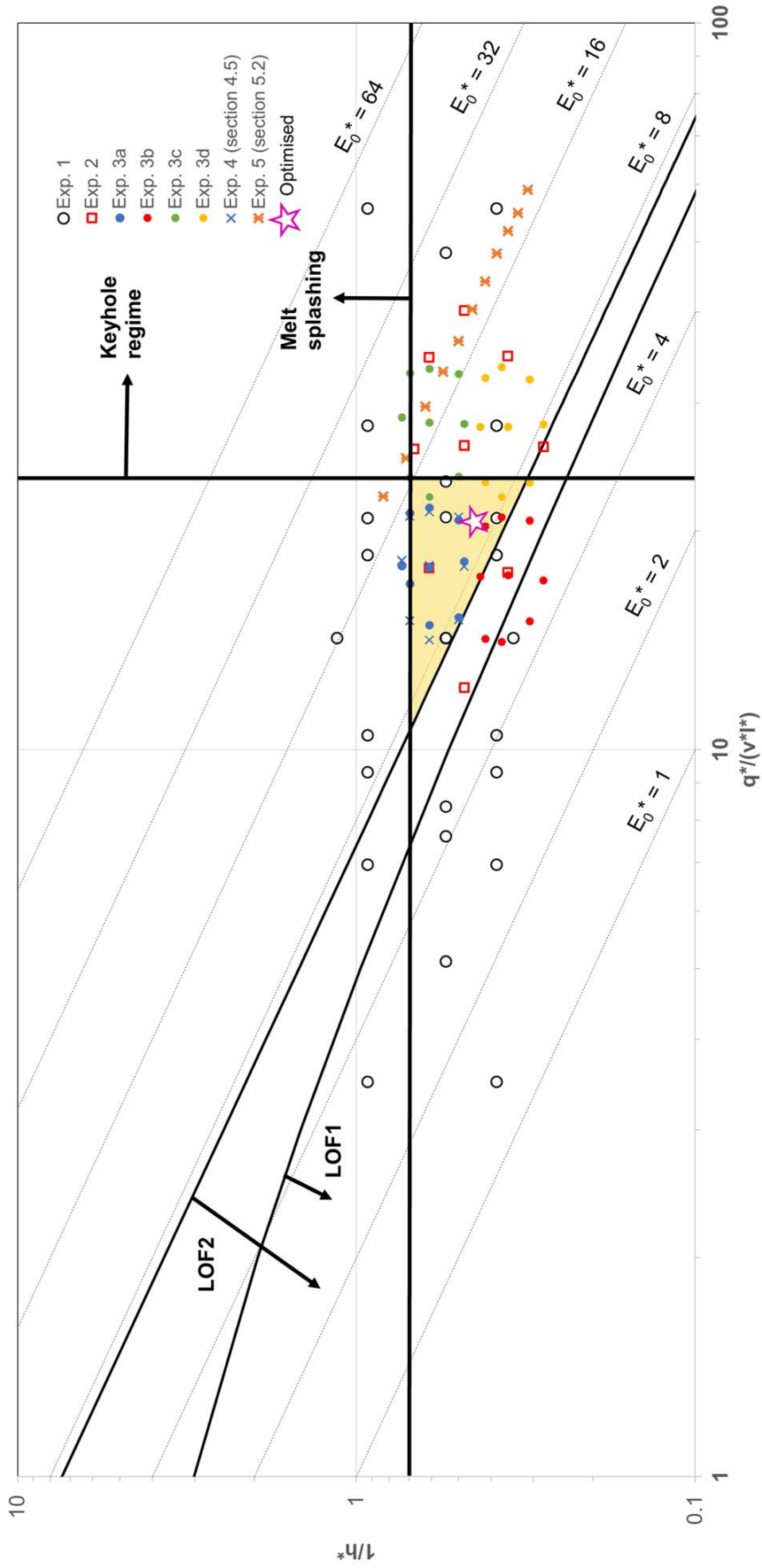


Figure 4.34. Process map for LPBF IN713C using Renishaw SLM125 system. Yellow shaded area indicates processing window.

#### 4.7. Summary of Chapter 4

- The experiments presented in chapter 4 captured the necessary information on the defect response of IN713C according to changes in process settings to facilitate the development of a process map for the material under LPBF conditions using a Renishaw SLM125.
- Statistical DOE has been effectively employed to investigate the whole process space accessible within the physical limitations of the Renishaw SLM125 system and identify parameters for which porosity was minimised.
- An analytical melt pool model, validated using melt track experiments, was used to calculate melt pool characteristics for given input processing parameters
- LOF behaviour has been described using the theory of overlapping hemispheres with predicted melt pool radii from the melt pool model.
- The Buckingham Pi Theorem of dimensional analysis was used to derive an inverse relationship between LOF behaviour and input energy density. This relationship was confirmed through experimental observations.
- A detailed “Taxonomy of defects” was developed, documenting all the observed defect types in terms of size, morphology and distribution, with 2D and 3D images.
- Statistical analysis of 2D images allowed the production of an LPBF sample of IN713C containing 0.05% volume fraction porosity when measured by 2D image analysis and 0.08% when measured using XCT.
- XCT allowed characterisation of individual defect types.
- Spherical gas porosity was the only defect type thought not to be forming as a direct result of a “loss of control” in the LPBF process. Rather, it is thought to originate from gas bubbles trapped within the powdered feedstock. It was reduced by increasing the input energy density allowing gas bubbles more time to escape the melt pool.
- A process map of IN713C has been developed, indicating the thresholds for formation of LOF, keyholing, melt splashing and the optimum processing window for minimisation of these defects.

## 5. Cracking

Although the solidification conditions of LPBF are substantially different to those experienced during casting, literature models which describe the susceptibility of an alloy to cracking during casting are still useful when applied to laser processed materials. In this section, casting models by Clyne and Davies [95] and Rappaz, Drezet and Gremaud [96] are applied to LPBF IN713C as well as a rapid solidification model by Kurz, Giovanola and Trivedi [67]. The model predictions are compared to experimental measurements of crack populations in test cube specimens. The application of these models aids the understanding of how LPBF processing parameters affect defect formation in “un-weldable” nickel-base superalloys.

### 5.1. LPBF test cube samples (Experiment 5)

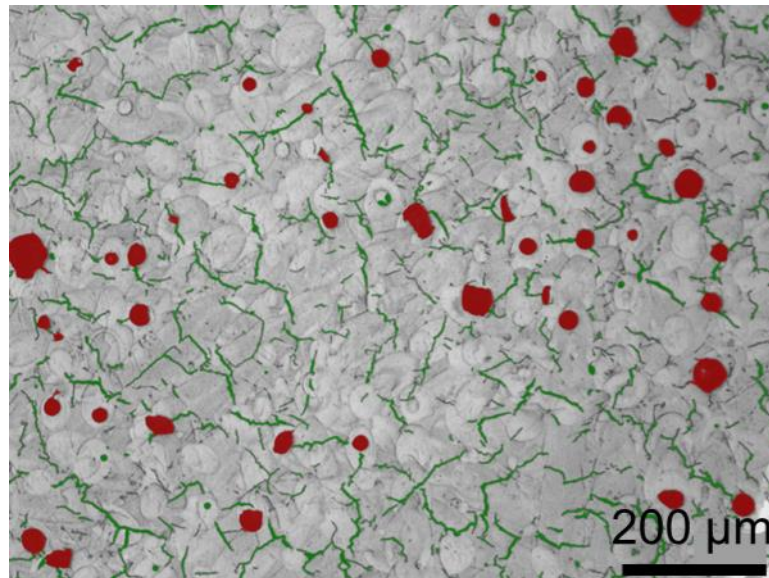
Eleven 10 mm x 10 mm x 10 mm cube samples were built from IN713C using input laser power of 200 W, layer thickness of 20  $\mu\text{m}$  and remaining parameters given in Table 5.1. Their position on the process map is shown in Figure 4.1. The samples in this set all lie on a line of constant energy density ( $E_0^*$ ). They were sectioned in the XY plane, polished as described in section 3.4.1 and etched according to the work instruction in Appendix 2.

**Table 5.1. Experiment 5 processing parameters.**

ID	x ( $\mu\text{m}$ )	h ( $\mu\text{m}$ )	$\tau$ ( $\mu\text{m}$ )	$q^*/(v^*l^*)$
1	80	80	155	58.90
2	75	75	135	54.72
3	70	70	119	51.68
4	65	65	103	48.17
5	60	60	87	44.08
6	55	55	73	40.35
7	50	50	60	36.48
8	45	45	49	33.10
9	40	40	39	29.64
10	35	35	29	25.19
11	30	30	22	22.29

## 5.2. Image analysis and initial observations

Image segmentation and quantification of defect types was performed using image analysis software, MIPAR. The pores and cracks were separated using a built in algorithm based on the morphology of the features (Figure 5.1). This software also allowed the separation of interconnected pores and cracks. Defects were quantified according to the total fraction of the image area they occupied.

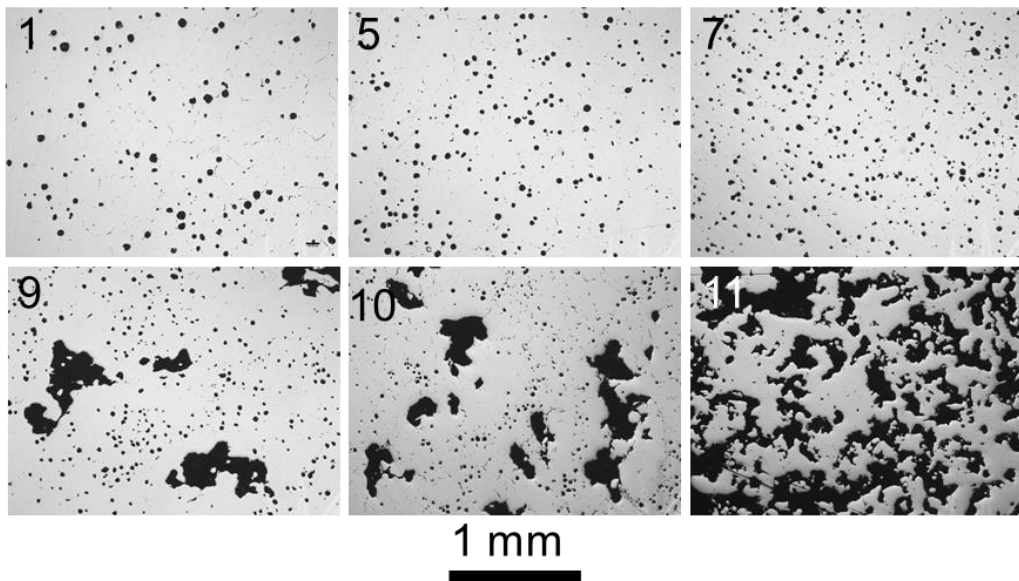


**Figure 5.1. Discriminated pores (red) and cracks (green) using MIPAR.**

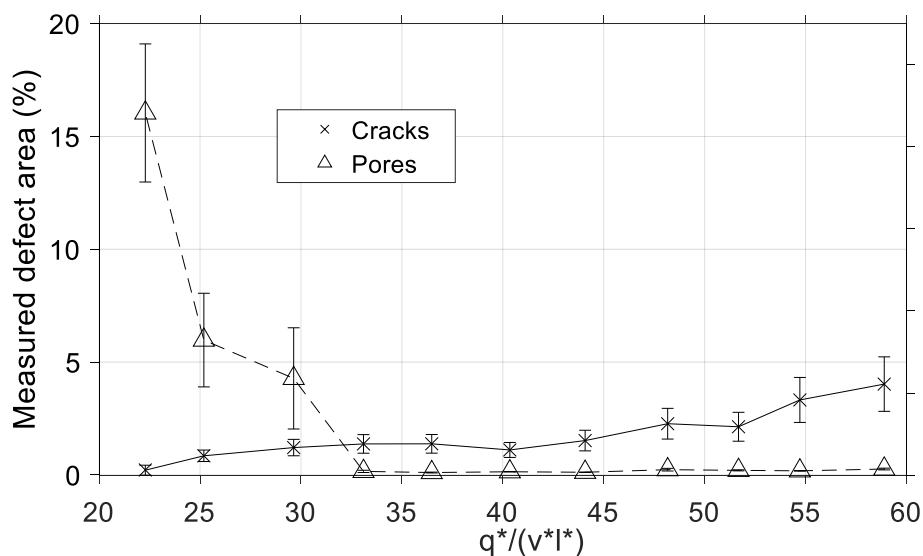
The 11 samples in Experiment 5 were all built with approximately the same energy density ( $E_0^* \approx 18$ ) consisting of a constant input laser power of 200 W, constant layer thickness of 20  $\mu\text{m}$  with varying values of  $x$ ,  $h$  and  $\tau$ . The defect response to processing under these conditions is obviously different (Figure 5.2), showing that the processing parameters are significantly influential on the type, frequency and volume fraction of voids and cracks.

Although this chapter is primarily focussed on cracking behaviours, it is instructive to hold that discussion in the context of the porosity also resulting from each processing condition (Figure 5.3). Sample 1, processed with the highest areal energy density, displayed extensive cracking and large keyhole voids. As the areal energy density was reduced, the keyhole voids became smaller and more frequent. Melt splashing voids began forming as the areal energy density was reduced (and

as the hatch spacing decreased correspondingly) and increased in area fraction with decreasing areal energy density, accompanied by a reduction in cracking. The keyhole behaviours observed in this experiment can be explained by the coalescence of the voids, as observed in [123], as they are remelted, since samples processed with higher areal energy density formed a larger melt pool, so more material was re-melted and more voids given the opportunity to coalesce. The cracking behaviour is analysed in detail in the following sections.



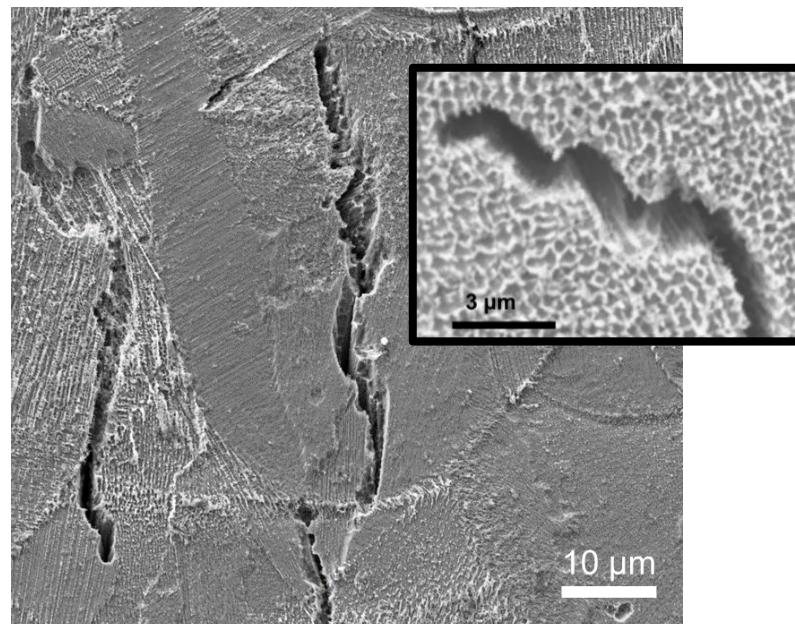
**Figure 5.2. Porosity ranging from keyholing in high energy samples (1-8) to splashing voids at low energy (11).**



**Figure 5.3. Experimentally measured defect populations from Experiment 5.**

Two distinct types of crack morphologies were observed. Cracks with zig zag propagation paths and smooth, rounded features on the crack surface (Figure 5.4) are indicative of cracking in the presence of a liquid film [54], [83], [102], while the material is in the mushy zone. Solidification cracking and liquation cracking both occur due to the presence of a liquid film. In welding operations, it is relatively straightforward to discriminate between these two crack types due to the clear boundaries between the fusion zone (solidification cracking) and the heat affected zone (liquation cracking).

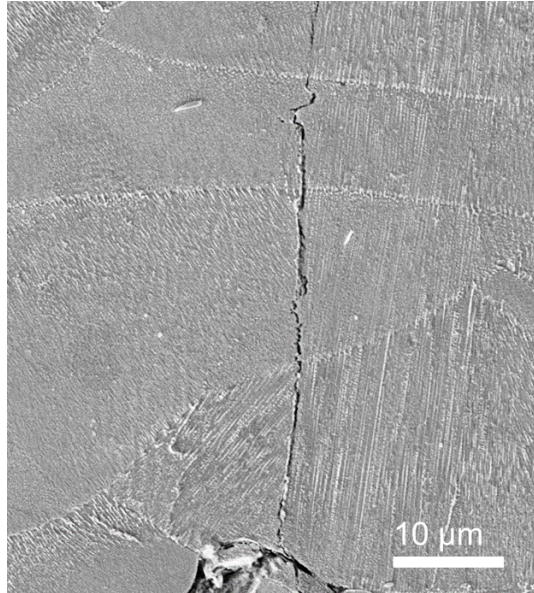
However, in LPBF the thermal history of the material is complicated by the series of melting and re-melting cycles. Visible dendritic structure on the crack surface is strong evidence for solidification cracking since this indicates the presence of elemental segregation and a liquid film [56]. Additionally, the rounded crack tip and zig zag morphology are indicative of ductile tearing [83]. These cracks are usually contained within a melt pool unless their path has been extended by the propagation of a connected solid state crack which, when combined with the dendritic structure, suggests that they occur in the mushy zone during the final stages of solidification. Hence, cracks displaying such features were attributed to solidification cracking in this work.



**Figure 5.4. Solidification cracks exhibiting zig zag morphologies, rounded features and dendritic structures on fracture surface (inset).**



Solid state, stress relief cracking can be identified by brittle fracture and straight propagation paths [102]. The stress relief cracks observed in this work span several melt pools confirming they occur entirely in the solid state (Figure 5.5). Cracking was relatively low for those samples with an incoherent network of solidified material.



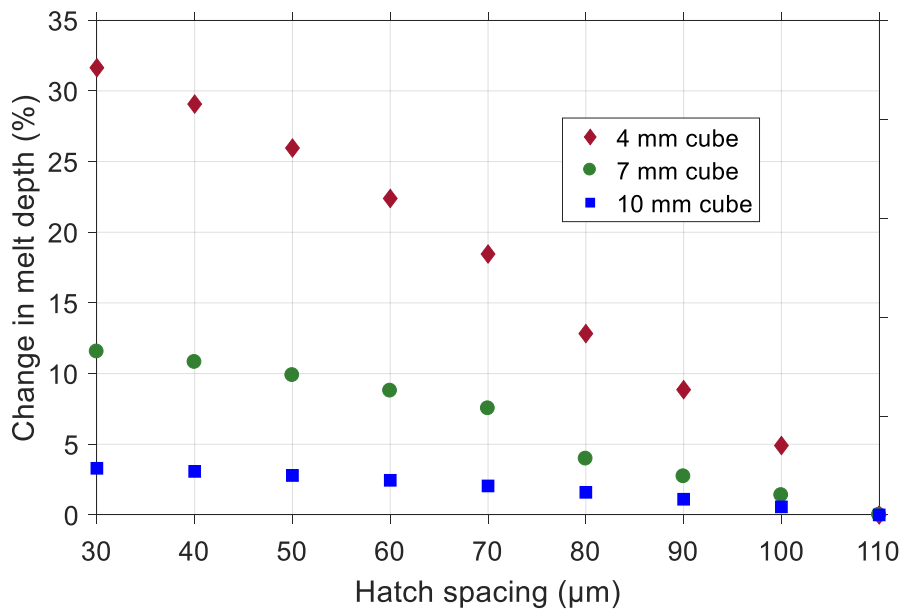
**Figure 5.5. Solid state, stress relief crack propagating from a defect and spanning several layers.**

### **5.3. Modelling the solidification conditions**

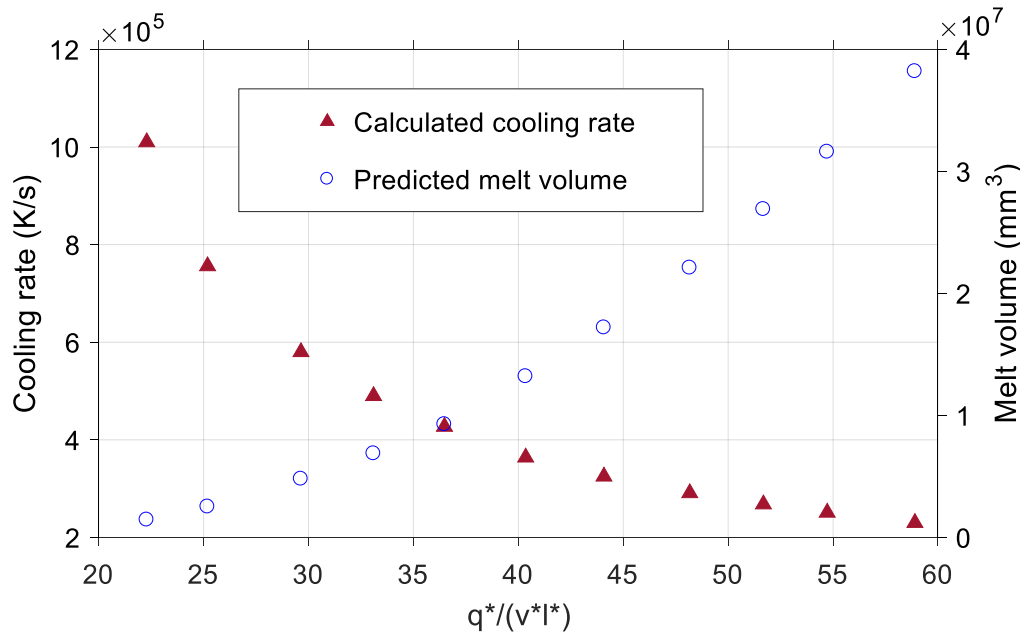
The analytical melt pool model described in Appendix 4 was used to calculate the cooling rate of the melt pools produced using each of the processing parameter combinations given in Table 5.1. To reduce the complexity of the problem, the results were discussed in terms of an areal energy density ( $J/m^2$ ) rather than a volumetric energy density, by neglecting the effect of hatch spacing. This was confirmed to be a valid methodology for a sufficiently large sample size by running the model for a variety of sample sizes (Figure 5.6). This is because the melt pool model considers the conditions for a melt pool in the centre of the top surface of the sample, sufficiently far away from the edge that it has already solidified before the laser returns and edge effects are not taken into account. (The material is still warm, so in-situ heat treatment effects can be interrogated using this model, but the actual



melt is unaffected). The effect of hatch spacing is greater as sample size decreases and hatch spacing decreases. For a 10 mm cube (the sample size used in experiment 5) the difference in melt volume between  $h = 110 \mu\text{m}$  and  $h = 30 \mu\text{m}$  keeping all other parameters constant is 3.3 %. According to the melt pool model, as areal energy density ( $\text{J}/\text{m}^2$ ) increases the melt pool volume also increases and the cooling rate decreases as might be expected (Figure 5.7). The predicted cooling rates and thermal gradients for Experiment 5 are given in Table 5.2.



**Figure 5.6. Influence of hatch spacing on predicted melt pool for three sizes of test cube.**



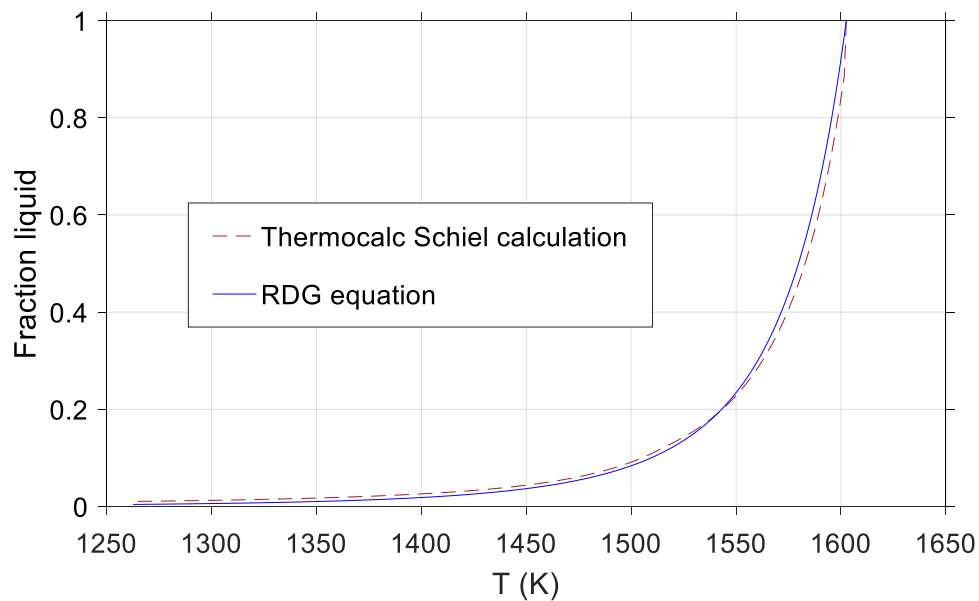
**Figure 5.7. Calculated cooling rate and corresponding predicted melt volume as a function of areal energy density.**

**Table 5.2. Predicted cooling rates and thermal gradients for Experiment 5.**

ID	$q^*/(v \cdot I^*)$	$\dot{T}$ (x 10 <sup>5</sup> K/s)	G (x 10 <sup>5</sup> K/m)
1	58.90	2.30	5.02
2	54.72	2.51	5.12
3	51.68	2.68	5.21
4	48.17	2.91	5.33
5	44.08	3.25	5.51
6	40.35	3.64	5.71
7	36.48	4.27	6.17
8	33.10	4.90	6.53
9	29.64	5.80	7.07
10	25.19	7.56	8.11
11	22.29	10.10	9.83

#### 5.4. Application of Clyne and Davies model

The Clyne and Davies model for cracking susceptibility, detailed in section 2.3.3.1 requires information on the solidification path of the alloy, including the eutectic temperature. For a simple binary alloy this information is easily obtainable, however for a highly alloyed superalloy the calculations are not so straightforward. Thermo-calc was used to model the solidification path of IN713C. This was



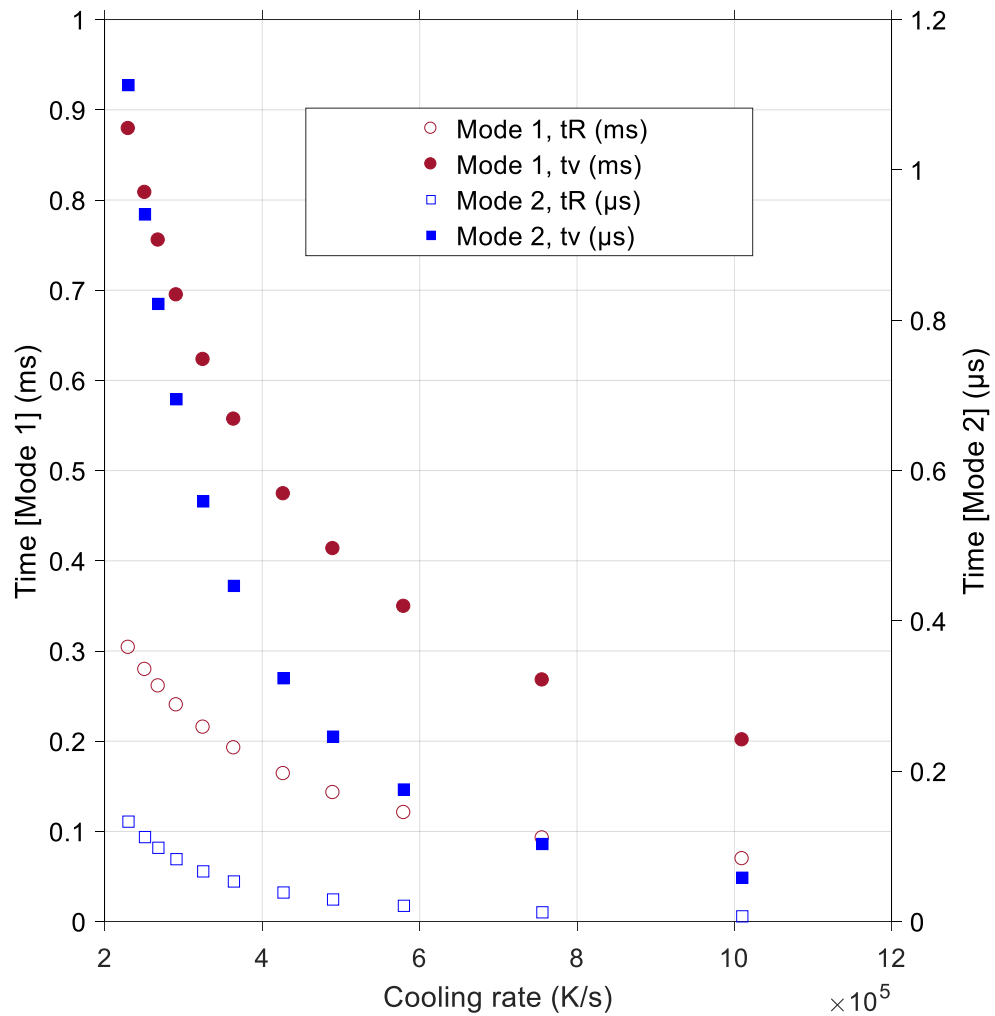
compared against the solidification path calculated according to the equation in the RDG model (Equation 2.16) and the two calculations showed good agreement (Figure 5.8).

**Figure 5.8. Solidification path of IN713C by Thermocalc Scheil calculation and RDG method.**

The Thermo-calc simulation values of  $f_L$  were used to obtain the temperature ranges for which the alloy is within the liquid feeding regime ( $0.1 < f_L < 0.6$ ) and the interdendritic separation regime ( $0.01 < f_L < 0.1$ ). Next, using the cooling rate calculated using the analytical model described in Appendix 4, the time spent in each of these regions,  $t_v$  and  $t_R$ , was calculated for both mode 1 and mode 2. The temperature range for the liquid feeding regime was 84 K and the temperature range for the interdendritic separation regime was 243 K. For cooling rates between  $2.3 \times 10^5$  K/s and  $1.01 \times 10^6$  K/s this gave  $t_v$  and  $t_R$  values of the order of milliseconds for

mode 1 and tens of microseconds for mode 2. Although the time spent in each regime varies for different cooling conditions (Figure 5.9) the ratio of the two times, which gives the “crack susceptibility coefficient” (Equation 2.13) was constant for each parameter set, showing that the Clyne and Davies model, whilst containing a solidification rate dependent term, is not set up to give a value for cavitation according to processing conditions.

Yet, it is evident from the experimental work performed here that the cracking behaviour is dependent on the process condition. Clearly, the Clyne and Davies model for CSC is not especially helpful in understanding the phenomenon at work in the present case. A more sophisticated method of assessing crack susceptibility was required.



**Figure 5.9. Time spent in vulnerable zone and relaxation zone according to cooling rate for Clyne and Davies Mode 1 and Mode 2.**

## 5.5. Application of RDG model for HCS

The Rappaz, Drezet and Gremaud model for hot crack susceptibility considers both the alloy chemistry (through the solidification path,  $f_s(T)$ ) and the processing conditions since it includes terms relating to the thermal gradient and the resulting microstructural scale. Hence, it is possible to use the RDG model to assess the relative probability for solidification crack nucleation for samples processed under a range of LPBF conditions. The model's sensitivity to initial conditions was explored by using three different approaches to the approximation of dendrite spacing; an empirical expression [76], the Kurz and Fisher model [63] and the Trivedi model [64]. However, firstly a discussion around the rapid solidification behaviour occurring in the test cube samples is helpful in understanding the cracking regimes.

### 5.5.1. Rapid solidification or solute trapping?

If the material is solidifying in the portion of the rapid solidification (RS) scale in which solute trapping occurs, then solidification cracking should not occur at all since it requires some elemental segregation to initiate the presence of a liquid film. Using the conditions set out in 2.2.3, it is clear that LPBF processing in Experiment 5 is occurring in the RS regime since the interface velocities are between 0.45 and 1 m/s. To deduce whether solute trapping was occurring, the ratio of the diffusion coefficient of the solute in solid nickel to the interface width was compared to the interface velocity.

At the surface of the melt pool, the interface velocity takes a maximum value, equal to the laser velocity [129]. The interface width,  $\delta$ , was taken to be on the order of atomic spacing,  $10^{-9}$  m as in [69]. Since boron is a rapid diffusing element known to segregate to interfaces in nickel-base superalloys [102], [130], [131] it was chosen for the calculation. The interface diffusion coefficient in the liquid,  $D_i$ , was assumed to be of the same order as the solid diffusion coefficient at the melting point such that the Arrhenius equation for diffusivity [132] (Equation 5.1) applies.

$$D_i = D_0 \exp(-Q/RT) \quad (\text{Eq. 5.1})$$

The calculation of the diffusion coefficient,  $D_i$ , requires knowledge of the diffusion pre-factor,  $D_0$ , and the activation energy for diffusion,  $Q$ . Two literature values of  $D_0$  have been compared (Table 5.3) to highlight the sensitivity of the calculation to the input parameters. The calculations were performed at the melting point of pure Ni (1728 K).

**Table 5.3. Calculations of ratio of interface diffusion coefficient to interface width.**

Ref	$D_0$ (m <sup>2</sup> /s)	Q (kJ/mol)	$D_i$ (m <sup>2</sup> /s)	$D_i/\delta$
[131]	$6.6 \times 10^{-7}$	96.3	$8.10 \times 10^{-10}$	0.81
[133]	$1.1 \times 10^{-6}$	$96.3 \pm 1.3$	$1.35 \times 10^{-9}$	1.23

For solute trapping to occur the ratio  $D_i/\delta$  must be exceeded by the interface velocity which ranged from 0.45 to 1 m/s with decreasing areal energy density. Table 5.3 shows that the choice of a diffusion pre-factor moves the limit for solute trapping, however it is evident that the fastest cooling samples lie in the region of, though not necessarily beyond, the solute trapping boundary.

### 5.5.2. Dendrite spacing calculations

The RDG model is highly dependent on the dendrite spacing since both the mechanical and shrinkage contributions to cavitation pressure are functions of  $\lambda^{-2}$ . Hence, multiple methods of estimating the DAS were used in order to test this sensitivity. The model results were also compared to measured dendrite spacings for four of the LPBF samples. Measurements were made using image analysis software ImageJ on SEM micrographs of etched samples. Equation 5.2 taken from Davies' empirical model for DAS contains values which were developed for IN718 [76]. These values were used in this study since no literature data was available for IN713C. The parameters taken from reference [51] are also for IN718 for the same reason. The parameters used in the calculations are given in Table 5.4. Parameters used in the calculations of DAS with Equations 5.2 to 5.4.

$$\lambda_{1(D)} = (97 \pm 5)\dot{T}^{-(0.36 \pm 0.01)} \quad (\text{Eq. 5.2})$$

$$\lambda_{1(KF)} = 4.3 \left(\frac{\Delta T}{G}\right)^{\frac{1}{2}} \left(\frac{D\Gamma}{Vk\Delta T_0}\right)^{\frac{1}{4}} \quad (\text{Eq. 5.3})$$

$$\lambda_{1(T)} = 2.83G^{-\frac{1}{2}} \left(\frac{\Delta T_0 LkD\Gamma}{V}\right)^{\frac{1}{4}} \quad (\text{Eq. 5.3})$$

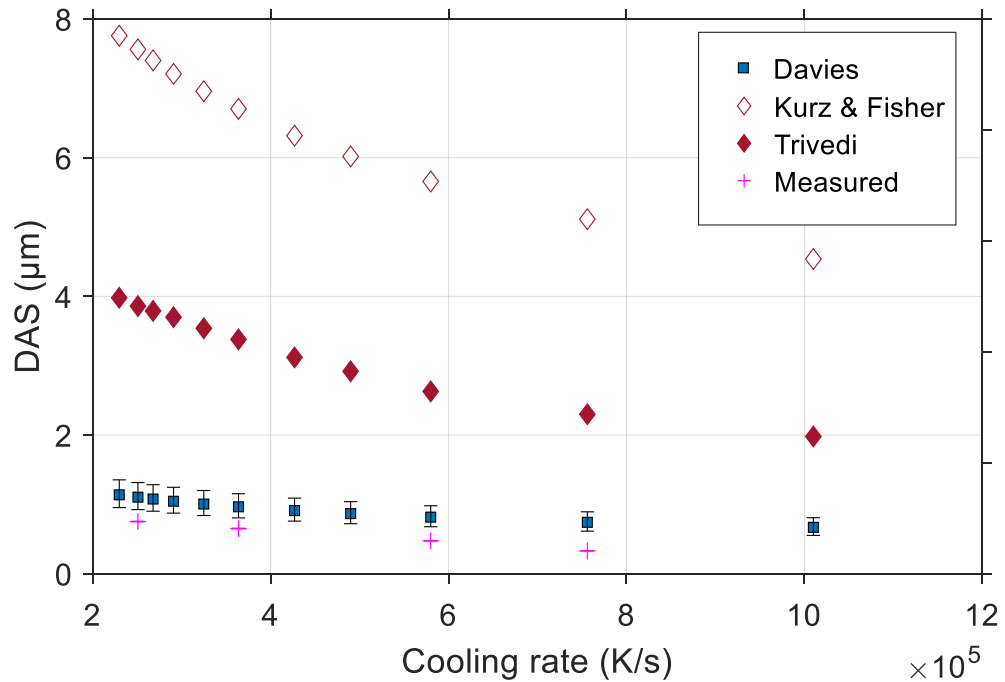
**Table 5.4. Parameters used in the calculations of DAS with Equations 5.2 to 5.4.**

Parameter	Value	Source
$G$	Various	Calculated using melt pool model
$\dot{T}$	Various	Calculated using melt pool model
$V$	Various	Equal to laser velocity
$\Delta T$	235 K	Calculated using Thermo-calc
$\Delta T_0$	30 K	[134]
$D$	$3 \times 10^{-9} \text{ m}^2/\text{s}$	[51]
$\Gamma$	$1 \times 10^{-7}$	[51]
$k$	0.45	[51]
$L$	28	[51]

Using values of thermal gradient calculated using the melt pool model detailed in Appendix 4 with an absorption factor of 0.3,  $\lambda_{I(KF)}$  and  $\lambda_{I(T)}$  both overestimate the DAS compared to the experimental measurements,  $\lambda_{I(KF)}$  by a factor of 10 and  $\lambda_{I(T)}$  by a factor of 5.  $\lambda_{I(D)}$  also over estimates the DAS, but the difference is smaller (Figure 5.10). The discrepancy between the calculated and measured values can be attributed to a number of phenomena including an inaccuracy in the melt pool

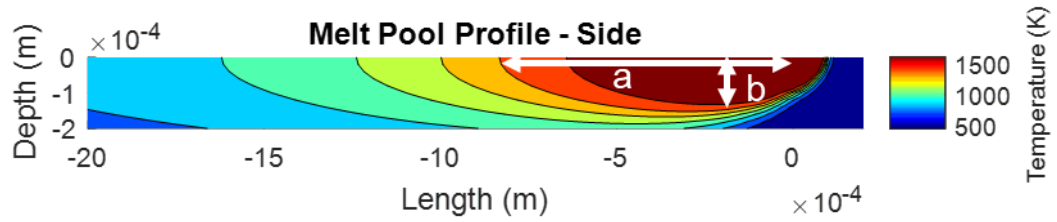
model used to calculate  $G$  and  $\dot{T}$ . Reasons for this could include a difference in absorption efficiency between that suitable for melt track experiments and that suitable for a test cube build or the location at which the thermal gradient is calculated in the model.

To probe for the reason behind this disagreement between the predicted and measured DAS by developing the concept of melt pool calculation position, a thought experiment was performed. The melt pool model calculates the thermal gradient on the surface of the melt pool between the solidus and liquidus (Figure 5.11 labelled *a*). However, the same difference in temperature occurs over a much shorter distance in the depth direction of the melt pool (Figure 5.11 labelled *b*).



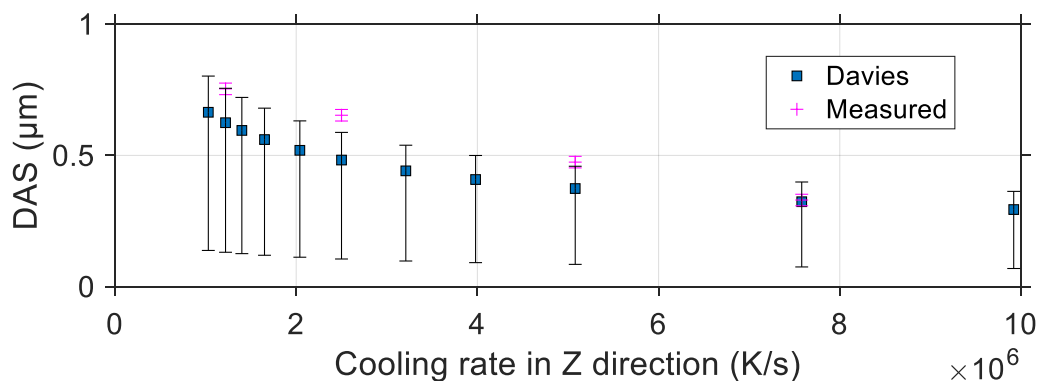
**Figure 5.10. Measured and calculated DAS using cooling rate and thermal gradient predicted from melt pool model with  $A = 0.3$ . Note error bars on measured quantities are  $0.02 \mu\text{m}$ .**





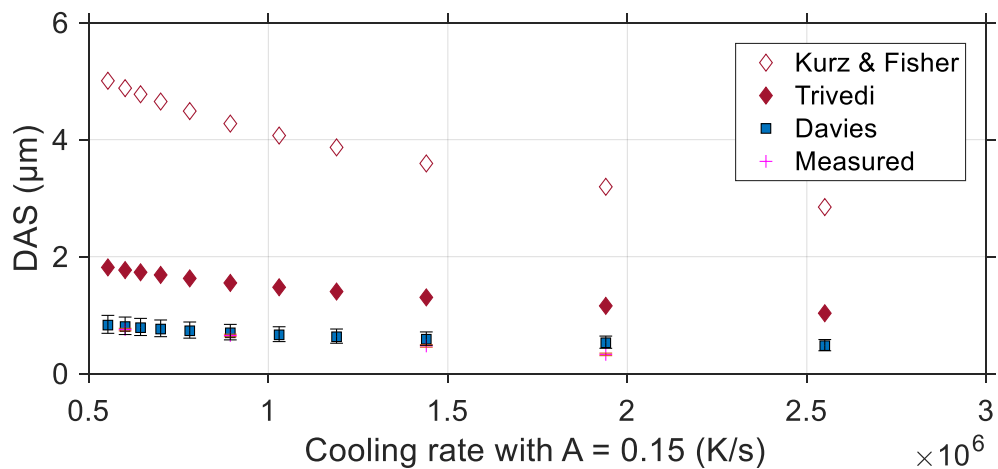
**Figure 5.11. An example melt pool profile showing a) the position of the thermal gradient as calculated by the model between the liquidus and solidus temperature and b) a higher thermal gradient between the same two temperatures in the depth direction.**

Using the calculated melt pool depth, this alternative thermal gradient was calculated and used in the empirical model of DAS since this model showed the closest agreement to the measured values compared to the Kurz and Fisher model and the Trivedi model. A significant improvement in the agreement between the predicted and measured values indicates that the thermal gradient was at least partially responsible for the discrepancy.



**Figure 5.12. DAS calculated with the Davies model using a thermal gradient calculation in the Z direction.**

The discrepancy in thermal gradient from the melt pool model can be rectified by reducing the absorptivity value model from 0.3 to 0.15. This also reduces the Kurz and Fisher, and Trivedi model predictions, moving them closer to the measured values (Figure 5.13). As the cooling rate increases the Davies model becomes less accurate. As explained by Davies, this is because the model becomes increasingly sensitive to experimental error as the cooling rate increases [76]. The empirical model provided the closest approximation to the measured values, but the HCS calculation was done with all three models (for  $A = 0.15$ ) and also using a constant DAS to assess the sensitivity of the RDG model to DAS.



**Figure 5.13. Predicted DAS using the thermal gradient (hence cooling rate) from the melt pool model with  $A = 0.15$ .**

### 5.5.3. Calculation of HCS

HCS was calculated using the Equations 2.16 - 2.20 (section 2.3.3.2) with the terms described in Table 5.5. Four different approximations of DAS were investigated: Case 1 assumes a constant DAS, while Case 2 compares the Davies model, Kurz and Fisher model and Trivedi model for DAS. Matlab code was developed to deal with the numerical integration (Appendix 5). The results were assessed in relation to input energy density and measured cracking response.

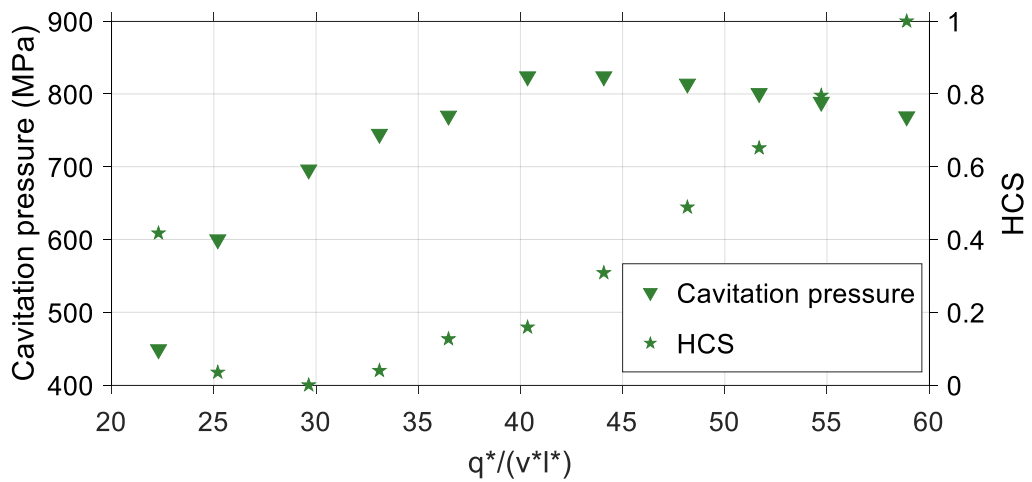
**Table 5.5. Parameters used in the calculation of HCS.**

Parameter		Value	Units	Ref
Strain rate	$\dot{\epsilon}_p$	$v_s/\lambda_1$	$s^{-1}$	
Shrinkage velocity	$v_s$	$\beta v_T$	$m s^{-1}$	
Shrinkage factor	$\beta$	$(\rho_s - \rho_l) - 1 = 9.1 \times 10^{-2}$	–	
Viscosity of melt	$\mu$	$4.5 \times 10^{-3}$	$kg m^{-1} s^{-1}$	[135]

**Case 1: Assuming a constant dendrite spacing**

In the first instance, the strain rate,  $\dot{\epsilon}_p$  was assumed to be constant for each parameter set and was calculated as the ratio of solidification velocity to estimated dendrite arm spacing (initially assumed to be constant across all parameter sets). Using a constant DAS of 1  $\mu m$  the cavitation pressure increases with increasing energy density to a maximum point then it starts to decrease again (Figure 5.14). The HCS shows the opposite behaviour.

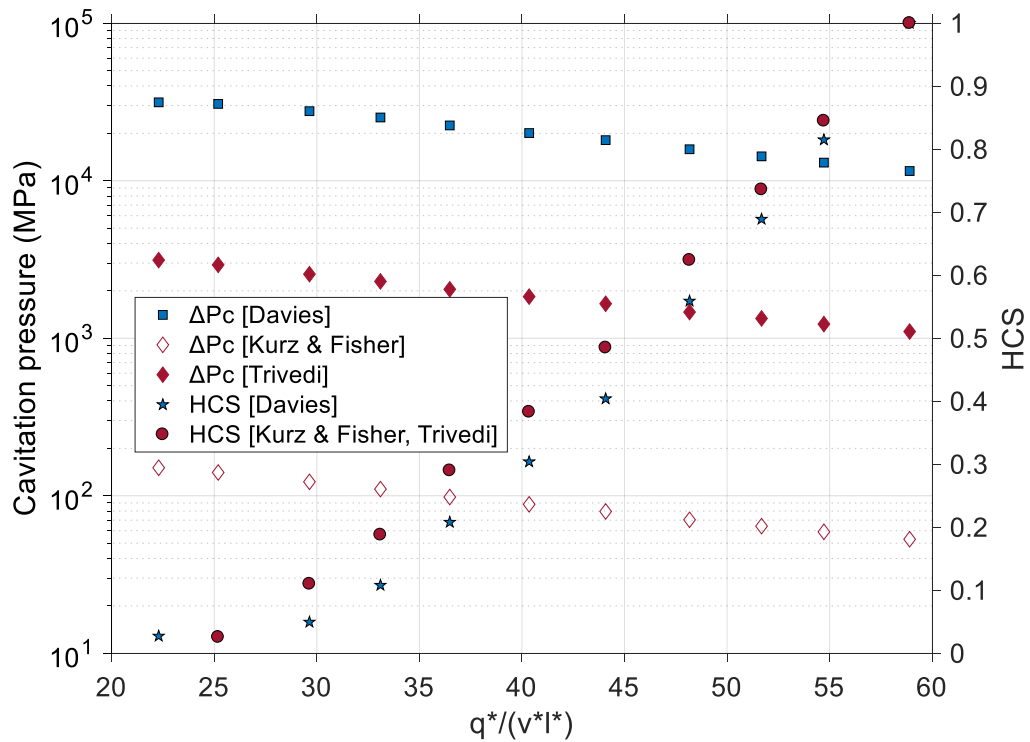
Physically, as the energy density increases, the melt volume increases, decreasing the cooling rate and increasing the DAS, which reduces the cavitation pressure. However, if DAS is treated as a constant, the strain increases at a faster rate than it would if DAS was scaling with cooling rate (because it now only depends on shrinkage velocity, not DAS). The mechanical contribution to pressure drop goes as  $\dot{\epsilon}/G$  so the scaling of this term is also non-physical if DAS is treated as a constant. Crucially, the mechanical contribution to pressure drop goes as  $1/\lambda^2$  so this has the most significant effect on the cavitation pressure and hence the HCS. It is clear that a more sophisticated estimation of DAS is required to reflect the physical response of the microstructure to the different initial conditions.



**Figure 5.14. Predicted cavitation pressure and HCS as a function of areal energy density for a constant DAS of 1  $\mu\text{m}$ .**

**Case 2: Using literature models of dendrite spacing**

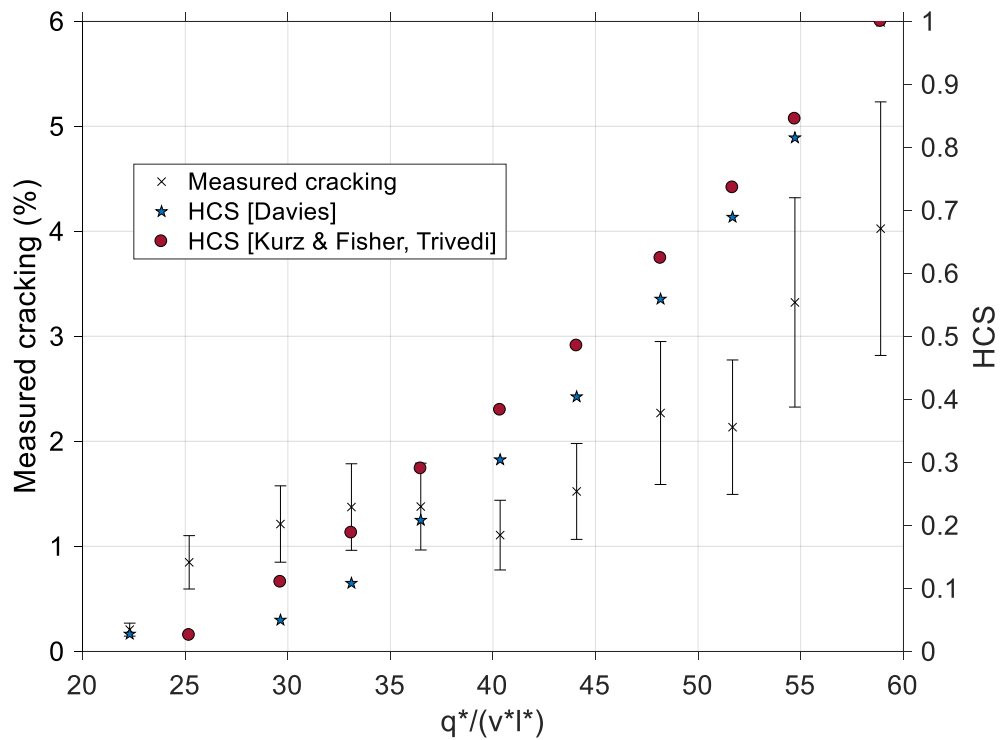
In case 2, the three approximations for DAS shown in Figure 5.13, using cooling rates calculated using the melt pool model with  $A = 0.15$  were used in the RDG model for HCS. Now that DAS is allowed to scale with the cooling rate, the cavitation pressure decreases almost linearly with increasing areal energy density (Figure 5.15). The shrinkage contribution to cavitation pressure is negligible compared to the mechanical contribution for both models. The Kurz and Fisher model predicts a wider DAS which results in a smaller difference in pressure between the dendrite root and tip compared to the Trivedi model.



**Figure 5.15. Mechanical and shrinkage contributions to cavitation pressure using the Kurz and Fisher, and the Trivedi models for DAS. Note log scale for pressure. Normalised HCS increases with increasing areal energy density, following the same trend for the Kurz and Fisher, and Trivedi models of DAS.**

The Kurz and Fisher model predicts a higher susceptibility to cracking than the Trivedi model, however, this is inconsequential since the trends are the same and the RDG model, when used in this way, is only suitable for making relative comparisons between samples. Hence, these two models for DAS are equally suitable for this purpose. The HCS increases with increasing energy density (Figure 5.15) as expected, since increasing the energy density increases the melt pool volume, decreases the cooling rate and leaves more time for segregation.

The measured crack area fraction decreased linearly with increasing pressure drop, with a corresponding decrease in the predicted HCS (Figure 5.16). This suggests that the HCS is a useful indication of the relative likelihood of cracking.



**Figure 5.16. HCS and measured cracking.**

The HCS calculation has been shown to be useful in assessing the relative likelihood of solidification cracking in LPBF IN713C since the decrease in cavitation pressure with increasing areal energy density lowers the threshold for void formation. However, the comparison between HCS and measured crack area is not straight forward for three main reasons. Firstly, this model is an indication of tendency for solidification cracks to nucleate and does not give any information on the likelihood of propagating a crack from the cavity. Hence, any voids which have nucleated due to solidification cracking mechanisms but not yet propagated due to unfavourable conditions will be missed from the measurement. The low melting point films which lead to crack nucleation are themselves insufficient to cause a crack to propagate. A thermal stress or solidification shrinkage stress is required.

During processing, these stresses can be considered on two length scales. Macro-scale thermal stresses due to the Thermal Gradient Mechanism and cooling of top layers as described by Mercelis and Kruth [91] lead to tensile stresses in the top layers, since their shrinkage upon cooling is restricted by already solidified material underneath. These thermal stresses are likely to be particularly detrimental for

solidification cracking since they will act on the mushy zone to pull dendrites apart before they fully coalesce. These stresses are extremely complex due to the complex thermal path involving melting, re-melting and heat affected zone. However, the shrinkage stresses are larger when a larger volume of material is shrinking, hence works with the increased time for elemental segregation to increase the likelihood of nucleation and propagation of a solidification crack with increasing energy density and melt pool volume.

Thermal stresses are also present on the scale of the melt pool. A smaller melt pool created using a low energy density will experience faster cooling and faster solidification rates than a larger melt pool. Hence, on the scale of the melt pool the thermal gradient is significantly faster. (The thermal gradient for sample 11, processed with lowest energy density, is almost three times greater than that for sample 1). A large thermal gradient due to this rapid solidification leads to high residual stress. The complex nature of the thermal experience of the material, which varies not only according to the position in the bulk volume but also on the scale of the melt pools goes some way to explaining the complicated nature of cracking in LPBF processed material.

The second factor which complicates the correlation between measured cracking and HCS is the observation of multiple crack types within each sample. The measurement of total cracked area takes account of all observed cracks in the material. Although it is possible to split up the cracks into distinct classes according to their morphology and surface features, doing so using automated image analysis techniques is extremely challenging. Straight, solid state cracks were frequently observed to propagate from cracks which had previously taken a zig-zag interdendritic path, adding a further level of difficulty. To extend this work in the future, a method of separating the crack types to enable individual quantification of the different classes should be developed. This could involve the use of machine learning techniques.

The final factor influencing the measured crack area which should be addressed is the presence of pores. Since the sample set was processed with a wide range of energy densities, some of the samples at the lower end of the energy spectrum were

not fully dense. Voids can act as stress raisers in a material, the extent to which this is problematic depends somewhat on their morphology. Sharp pores are known to initiate failure more prevalently than round ones. However, in this experiment, total crack area continued to decrease with decreasing energy density even after the initiation of large irregularly shaped voids after sample 8. Sample 11 exhibited a very high level of porosity and almost no cracking. This may be because the porous structure of sample 11 will deform more easily to accommodate and therefore resolve the residual stress before initiating cracking.

It is clear due to the observations of different crack types and different microstructures within the same sample that the susceptibility to solidification cracking is specific to local solidification conditions. Different phases solidify at different rates, even for the same cooling rate, so for a constant cooling rate, the rate of change of fraction liquid will vary according to the phase field. If different phases were forming during the LPBF process, then this would further complicate the model of solidification crack susceptibility. However, although precipitate formation was observed (see section 5.8) no evidence of a major second phase (i.e. gamma prime) was found.

Based on the results of this experiment, it is recommended that the energy density is minimised as much as possible without compromising the density of the material in order to decrease the melt pool size, increase the cooling rate and decrease the time available for segregation in order to reduce HCS. This also has the effect of reducing the shrinkage stress necessary to propagate a solidification crack.

### **5.6. Application of KGT model for segregation**

Even if thermal and shrinkage stresses during the build can be reduced, a component processed under conditions which lead to crack nucleation but not propagation may fail in service when placed under an applied load. Hence, it is important to reduce the tendency of the material to nucleate a crack rather than focus on removing the stress necessary to propagate one. Hence, the Kurz, Giovalola and Trivedi model was applied to the 11 parameter sets to assess the relative tendency for elemental segregation.



### 5.6.1. Methods

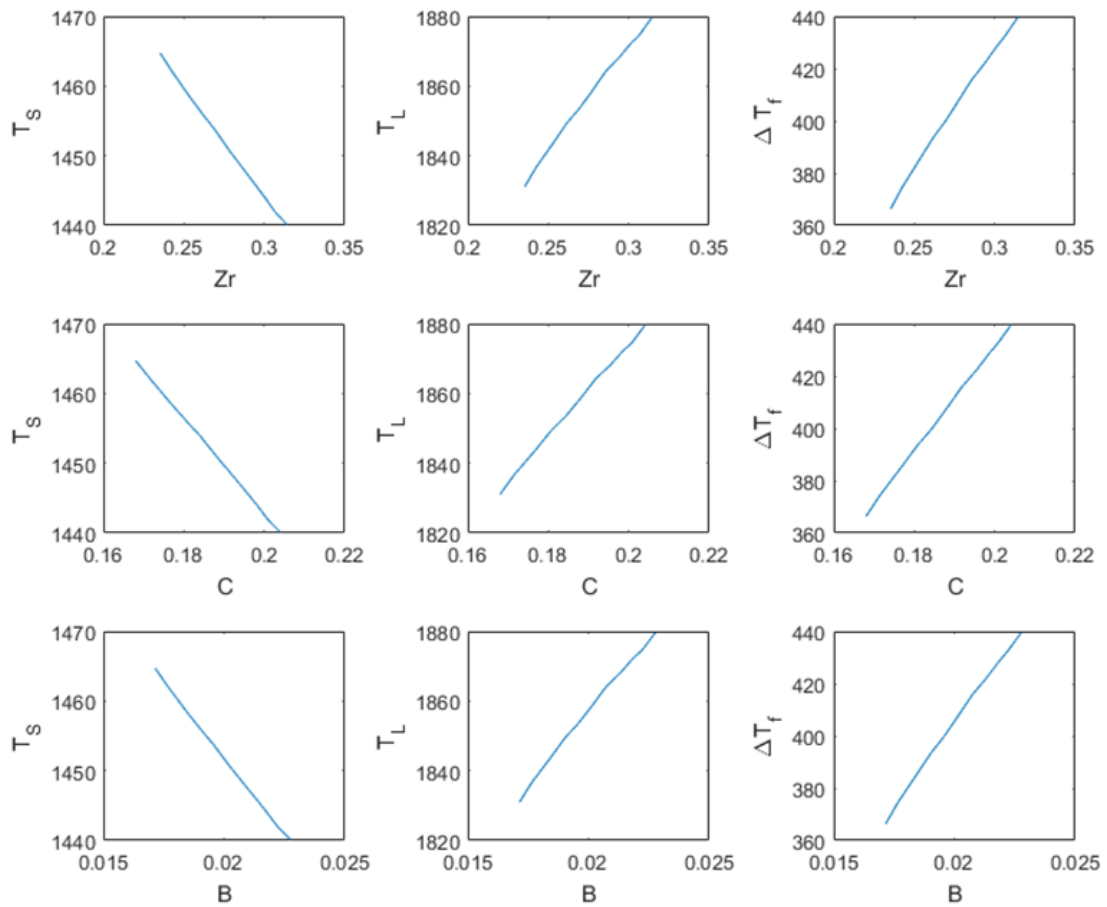
The KGT model was applied for the same eleven processing conditions considered in section 5.1. The concentration of zirconium, carbon and boron in the terminal liquid was calculated using Equation 5.4 from the Kurz, Giovanola and Trivedi model [67]. The dendrite tip radius was approximated to 100 nm. The equilibrium partition coefficient,  $k_0$ , was found through thermodynamic simulations and used in Equation 5.5 for the calculation of the velocity dependent partition coefficient,  $k$ . The length scale related to the interatomic distance,  $a_0$ , was taken as 4 nm. The liquid diffusion coefficients used for zirconium and boron in nickel were  $2 \times 10^{-9} \text{ m}^2/\text{s}$  [136] and  $2.42 \times 10^{-9} \text{ m}^2/\text{s}$  [137] respectively. Liquid diffusivity of carbon was assumed equal to that of boron due to lack of literature data. Thermodynamic calculations using Thermo-calc software with the database TCNi8 under equilibrium assumptions, were made of the local liquid compositions for each processing condition to obtain the solidus temperature, liquidus temperature and freezing range.

$$C_i^* = \frac{C_0}{1 - (1 - k)Iv(P)} \quad (\text{Eq. 5.4})$$

$$k = \frac{k_0 + (a_0V/D)}{1 + (a_0V/D)} \quad (\text{Eq. 5.5})$$

### 5.6.2. Results and discussion

As the energy density was decreased the calculated cooling rate increased due to smaller melt pool dimensions. This leaves less time for segregation, meaning that the compositions of zirconium, carbon and boron in the terminal liquid decreased with decreasing input energy density. Lower concentrations of these trace elements results in a smaller freezing range. This is illustrated by the results of thermodynamic calculations showing that as the concentration of zirconium, boron and carbon increased, the solidus temperature decreased, the liquidus temperature increased and the resulting freezing range increased (Figure 5.17).



**Figure 5.17. Solidus temperature, liquidus temperature and freezing range (K) of the terminal liquid with zirconium, carbon and boron concentrations (wt %) varying according to the calculated liquid concentration at the dendrite tip.**

For this set of 11 processing conditions, the cooling rate ranged from  $5.53 \times 10^5$  K/s at the maximum input areal energy density to  $2.55 \times 10^6$  K/s at the minimum, according to the output of the melt pool model with  $A = 0.15$  (in line with section 5.5.3). The effect of this increase in cooling rate was to reduce the freezing range of the terminal liquid from 440 K to 366 K. This difference in freezing range of 74 K occurred as a result of the predicted decrease in concentration of zirconium, boron and carbon with increasing cooling rate (Table 5.6) and corresponds to the observed increase in cracking in Experiment 5 (Figure 5.16).

**Table 5.6. Range of concentrations of zirconium, boron and carbon in terminal liquid, calculated using Equation 5.4.**

(wt %)	At minimum $\dot{T}$	At maximum $\dot{T}$
<b>Zr</b>	0.314	0.235
<b>B</b>	0.023	0.017
<b>C</b>	0.204	0.168

Applying this information to the process window identified in section 4.6 (Figure 4.34) gives an insight into the range of segregation behaviour, and corresponding variation in the tendency to crack, likely to be observed in the optimised processing window. At the outer edges of the envelope, using  $1/h^*$  equal to that of the optimised point, the areal energy density ranges from 17.3 to 22.9. This change is 15% of the change in areal energy density between the extreme points of Experiment 5, suggesting that over the span of the processing window there could be a change in freezing range of the terminal liquid of 11 K. These approximations have been made based on building a 10 mm cube, as per Experiment 5.

### 5.7. APT of a cell boundary

Atom probe tomography was used to probe the segregation behaviour of elements local to cell boundaries and compare the observations to the calculations made in section 5.6. APT was performed on four atomically sharp tipped samples of IN713C prepared using FIB milling from the same LPBF test cube specimen. A Cameca LEAP 5000 instrument was used with a vacuum of  $5 \times 10^{-11}$  Torr and a temperature of 40K. The tip was subjected to 40 pJ laser pulses at a rate of 200 kHz.

#### 5.7.1. APT results and discussion

In each of the four APT specimens, nano-scale clusters of atoms were observed (Figure 5.18) which appear to lie in regular bands of approximately 200nm separation. In total, 49 clusters were observed, although some which are joined together appear as one in the analysis so the actual number is reduced and average

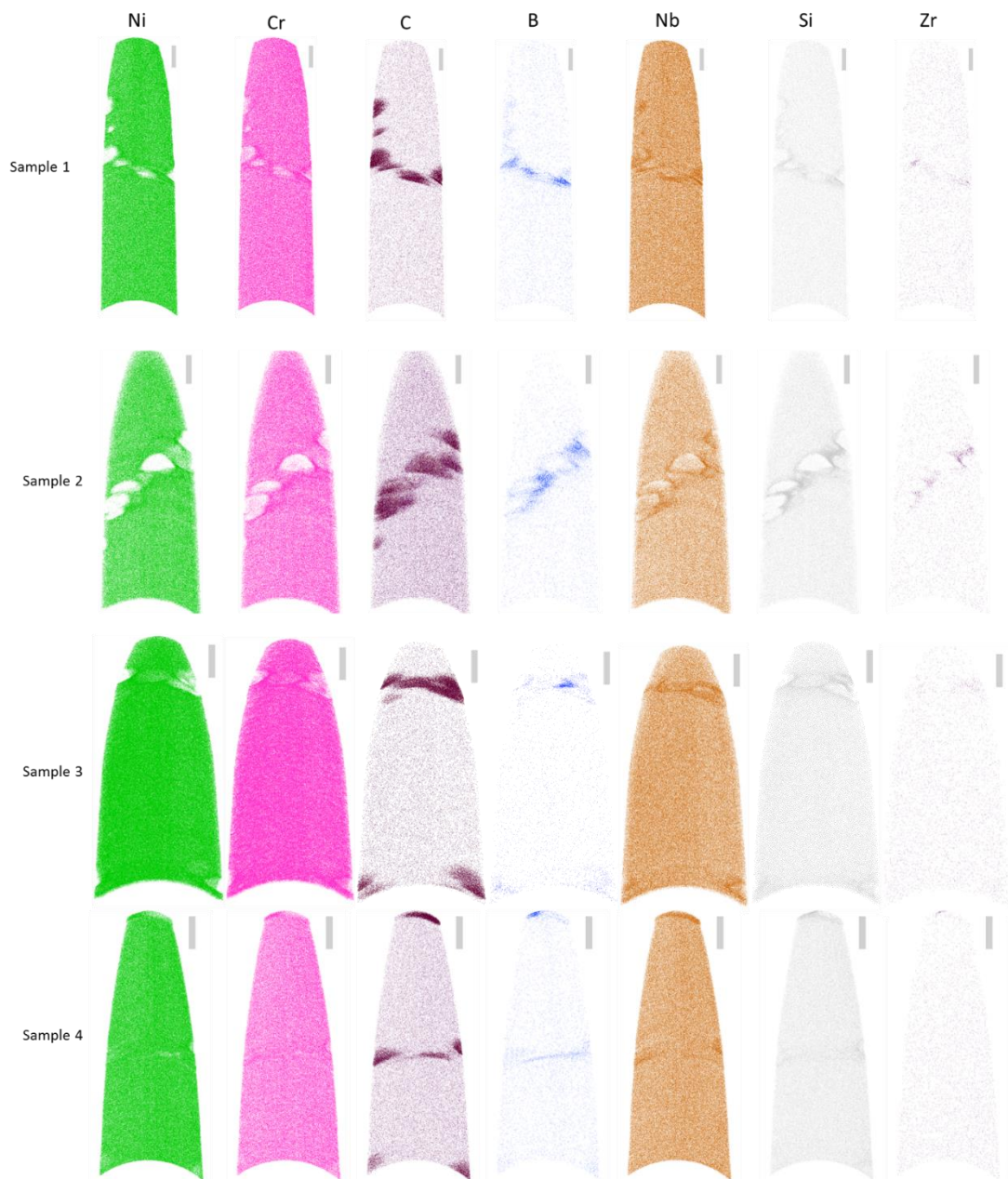
size increased. Depth profile line scans of the atom probe reconstruction (Figure 5.19), taken through entire data sets for each sample parallel to the analysis direction indicate depleted levels of Ni and Fe in these regions. Al levels across the band fluctuate in a “W” shape. All other elements indicated in the figure are enriched over the band region. The mean composition of the clusters (Figure 5.20) shows they are predominantly composed of carbon. Errors in the analysis of mean cluster composition are given as the standard deviation of the mean composition over all four samples. Composition of the clusters is largely independent of their size for clusters larger than 7 nm radius (Figure 5.21). For small clusters nickel, niobium and carbon concentration varies with radius.

The atomic clustering is occurring in a region approximately 20 nm wide, spanning the secondary dendrite arm boundary. Boron is driven to this location by thermodynamics because occupying a site within the extra free volume created by the boundary reduces the energy of the system. Chromium, molybdenum, titanium, niobium and silicon are tending to associate with boron over the bands of clusters. Boron has low bulk solubility in nickel; elements with low bulk solubility have a higher enrichment factor in the grain boundary (GB) [37].

It has been shown that in nickel-base superalloys chromium, molybdenum, boron and carbon are enriched across GBs, while nickel and aluminium are depleted [39, 40] which is consistent with the observations in the present study. In nickel-base superalloy 617B treated at 700°C [39] GBs are decorated with primary and secondary  $M_{23}C_6$  carbides, enriched in chromium, depleted in nickel and with a heterogeneous composition. At the GB,  $\gamma'$  precipitates are found close to the carbides. The interfaces between the carbides and  $\gamma'$  and between the carbides and  $\gamma$  matrix are both enriched in boron, while interfaces of  $\gamma/\gamma'$  are not. The  $\gamma'$  phase is enriched with Al and Ti but depleted in chromium, cobalt and molybdenum. No aluminium or titanium was found in the carbide, which is 66 at% chromium. An aluminium rich zone is reported around the carbide particles accompanied by enrichment of titanium and Ni and depletion of Cr and Mo relative to the matrix. B has low solubility in nickel and hence a high GB enrichment factor so boron segregation on GBs, enhanced GB cohesion and promoted precipitate formation are likely [37].

The “W” shaped aluminium profile observed in the depth profile across a cluster band (Figure 5.19) displays enrichment of aluminium in the region surrounding the carbide rich clusters, in agreement with observations in [39] however it is not accompanied by any nickel enrichment. Depletion of chromium and molybdenum in this zone may be occurring. In the atom map reconstructions, carbon and boron are not co-located rather, boron tends to accumulate on the edges of the carbon rich clusters. This may fall in line with observations in [39] which explain that the flux of boron towards  $M_{23}C_6$  particles is higher than that of carbon due to high boron mobility in the  $\gamma$  matrix.

A correlation is found between the approximate cell spacing (200 nm) and the periodicity of the cluster bands indicating the diffusion may be occurring on this scale rather than to GBs due to the fast solidification times associated with LPBF. Line scans of the atom probe data across individual clusters are needed in order to see the compositions of the various components of the cluster bands since the total cluster composition does not indicate whether carbides and precipitates are present, thus explaining the presence of aluminium and titanium alongside enrichment of chromium, molybdenum, boron and carbon. Individual line scans would also assist in deducing the stoichiometry of the clusters to discover the structure of the carbide particles. If  $M_{23}C_6$  carbides are found to be nucleating in the LPBF samples, this could be contributing to the crack susceptibility of the alloy through the high dislocation density caused by their incoherence with the matrix.

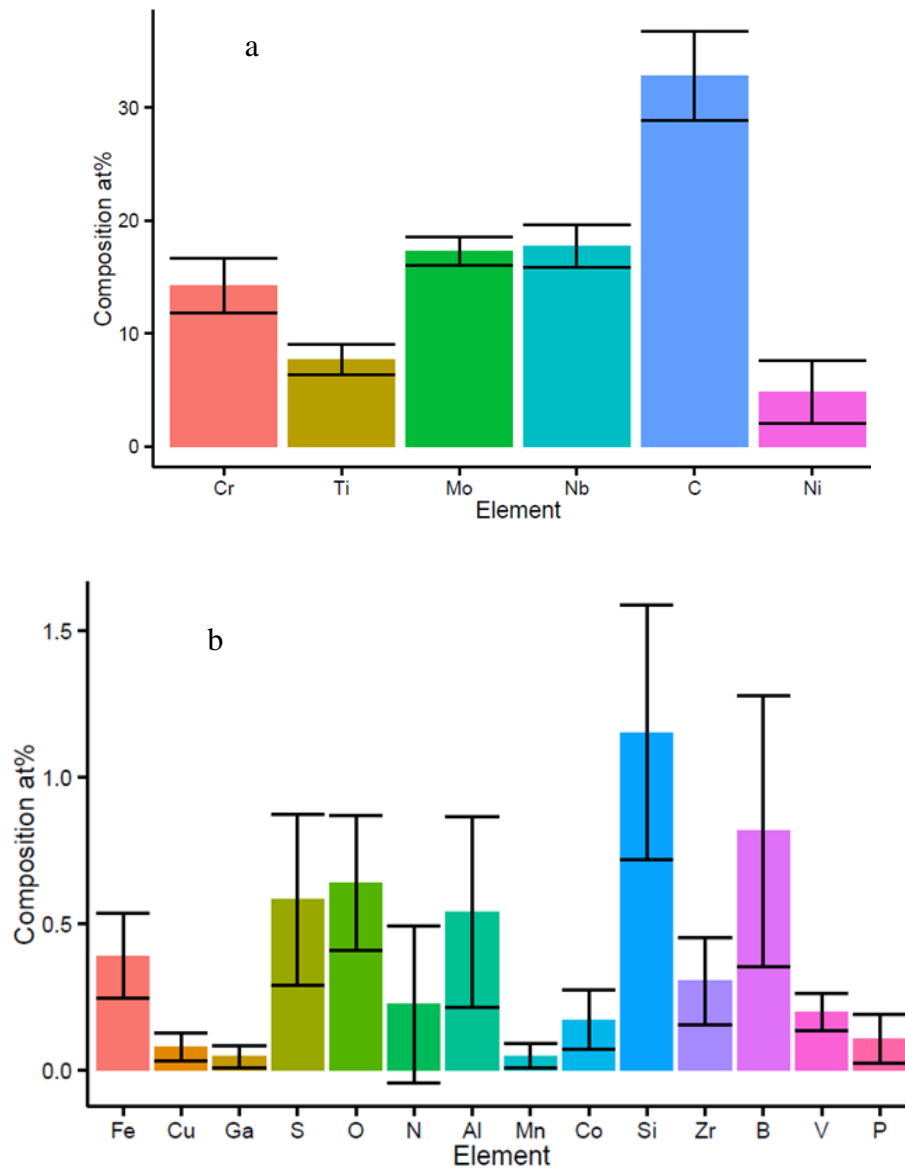


**Figure 5.18. Atom maps from all four samples showing the spatial distribution of concentration of elements. Scale bar = 25 nm. Slice thickness = 10 nm.**



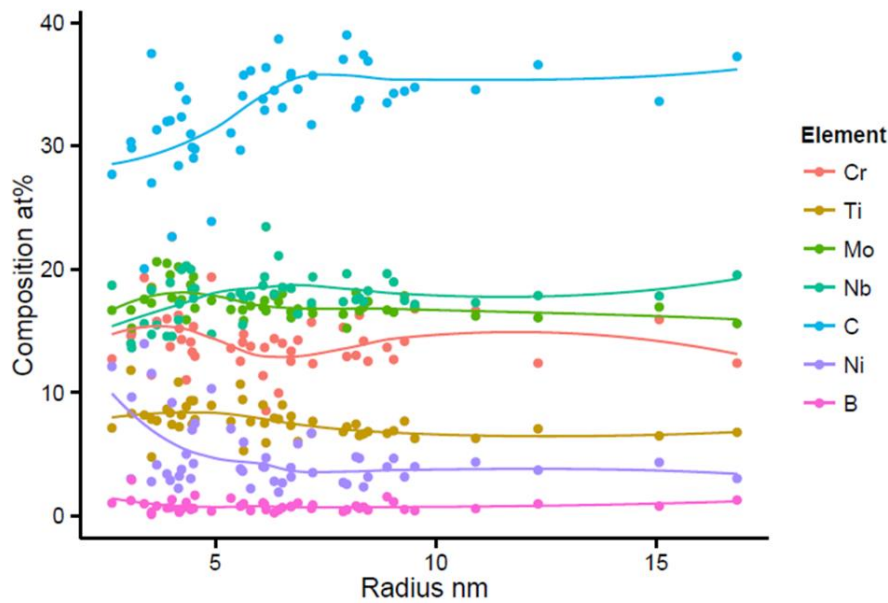
**Figure 5.19. Depth profile line scan across a cluster band.**

# The Application of AM to Ni-base Superalloys



**Figure 5.20. a) and b) Mean composition of clusters, at%.**

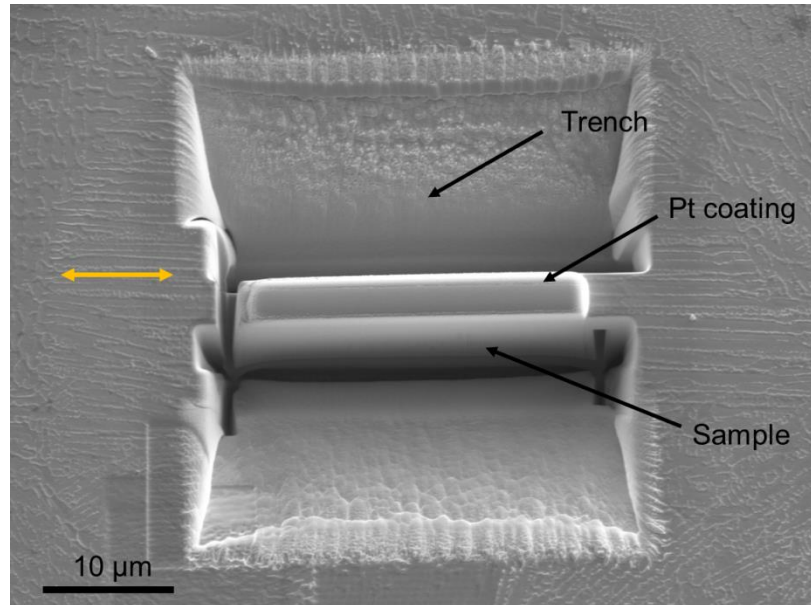




**Figure 5.21. Composition against radius of all 49 detected clusters.**

### 5.8. TEM observations

Two samples (numbers 2 and 10) were taken from the set of LPBF test cubes used in Experiment 5 for an investigation into whether the observed cracking behaviours could be correlated to dislocation or precipitation behaviours in the material. TEM sample preparation was performed by Dr Le Ma and the TEM was operated by Dr Jo Sharp, both at the University of Sheffield. TEM samples were produced using FIB milling from one test cube produced with high areal energy density (sample 2) and one produced with lower areal energy density (sample 10). The samples were both taken from planes parallel to the direction of the cells in the microstructure (Figure 5.22).



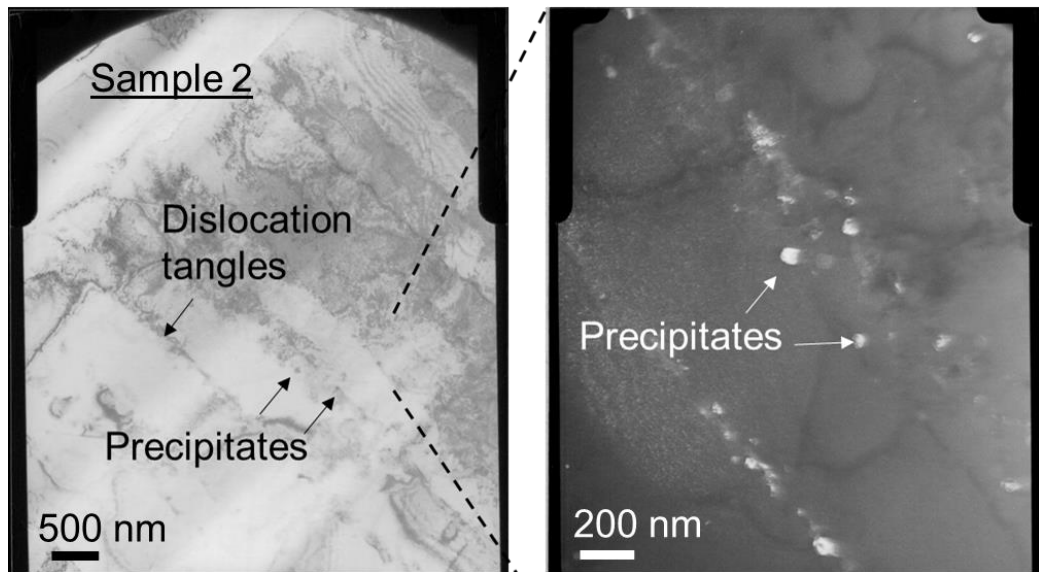
**Figure 5.22. FIB sample preparation of sample 2. Cell direction indicated by yellow arrow.**

The cellular microstructure was evident in both samples. The average cell spacing from 20 measurements in each sample was  $661 \pm 84$  nm and  $417 \pm 41$  nm for sample 2 and 10 respectively. This shows that the structure is refined on the cellular scale by an increase in cooling rate resulting from reducing the areal energy density input to reduce the melt pool size in the same way that the dendrite spacing is affected by this change.

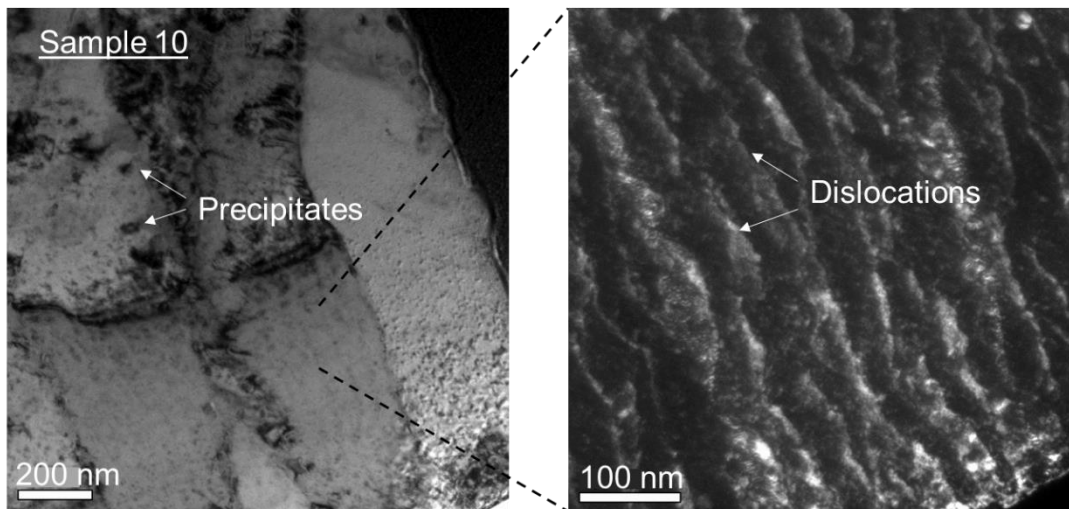
In sample 2 the dislocations and precipitates were observed to lie on and near to the cell boundaries. Only one dislocation slip system could be identified, with the Burgers vector,  $\underline{b} = \frac{a}{2}[101]$ . Conversely, in sample 10, dislocations and precipitates could be seen in the cell interiors as well as on the boundaries. The dislocations were regularly spaced in the cell interiors. In this sample, multiple slip systems were identified. It is postulated that this difference in distribution of dislocations and precipitates is due to the difference in time available for recovery. Melt pool modelling, considering the in-situ heat treatment effect of the returning laser paths, suggested that the “cold” sample spends  $0.1 \mu\text{s}$  in the temperature range

between the gamma prime precipitation temperature and the solidus temperature; 100 times shorter than the time spent by the “hot” sample in this range. The limited results presented in this section suggest this time may be sufficient to account for the observed recovery in sample 2. The TEM samples taken from sample 2 spanned each side of a crack. Skilled FIB thinning allowed retention of the material on both sides of the crack up to the crack tip. The TEM showed precipitates lining up along the crack (Figure 5.27). This has also been observed elsewhere [83], [138].

The TEM observations indicate that there is significant strain energy stored in the LPBF material due to the high density of dislocations, which could contribute to the cracking tendency. This would not be alleviated by post process annealing since the material ruptures under the residual stress soon after solidification. However, if the material could be encouraged to recover further during the process by in-situ heat treatment, without compromising the solidification cracking susceptibility, this may help to alleviate stress cracking. Future work is required to develop an image analysis technique to discriminate between the two crack types, quantifying the levels of each. This would enable a more conclusive argument to be drawn about the dependence of solid state cracking on dislocation and precipitation behaviours according to the energy density input.



**Figure 5.24. Bright field TEM micrograph from the high energy sample showing dense dislocation tangles on cell boundaries. Inset: dark field TEM micrograph showing precipitates aligned on cell boundaries.**



**Figure 5.25. Dislocations are regularly spaced in the cell interiors of the low energy sample.**

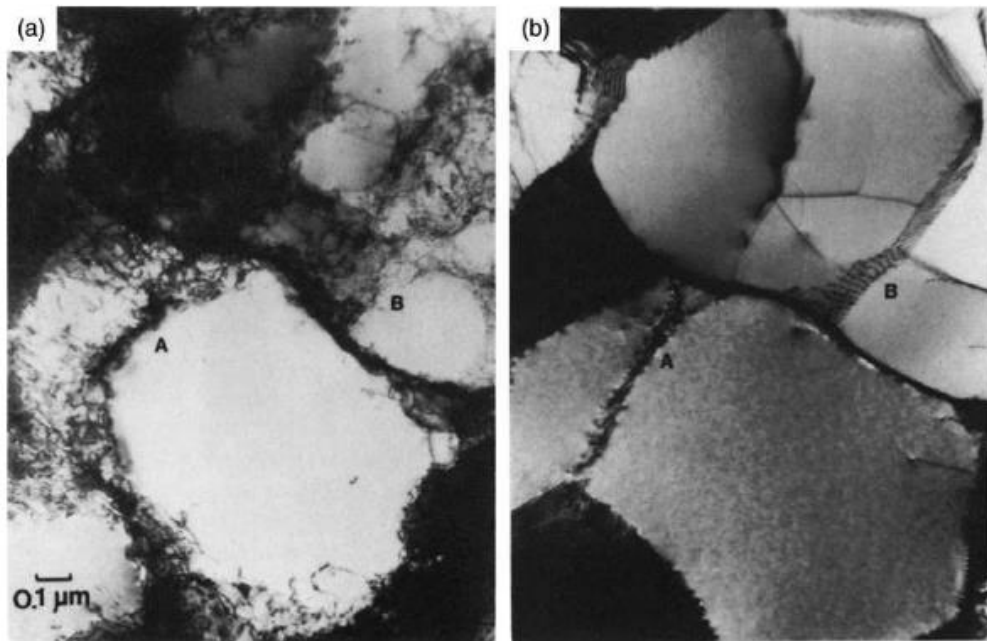


Figure 5.26. TEM micrographs of aluminium a) deformed 10% and b) same area after 2 minute anneal at 250 °C. From [139].

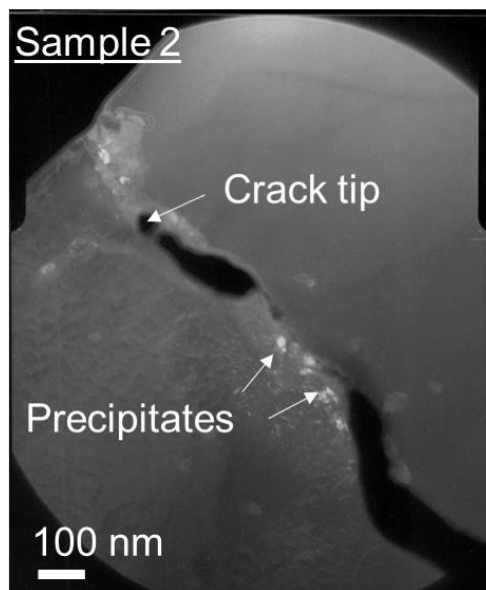


Figure 5.27. Dark field TEM micrograph from the high energy sample showing precipitates aligned along the crack edge.

### 5.9. Summary of Chapter 5

- Precipitation strengthened nickel-base superalloys such as IN713C suffer from extensive cracking when processed via LPBF due to a combination of their chemistry (high fraction of  $\gamma'$  forming elements, titanium and aluminium) with the high residual stress inherent to the process.
- To investigate the relationship between crack susceptibility and process settings, eleven test cube samples were built (Experiment 5) and their defect populations were quantified using image analysis.
- Cracking was found to increase as areal energy density was increased.
- Porosity decreased with increasing areal energy density. Keyhole voids were observed in samples processed with high areal energy density. These voids reduced in size but increased in frequency with decreasing areal energy density. The samples processed with lower areal energy density and narrower hatch spacing displayed increasing volume fractions of melt splashing porosity. Melt splashing pores and keyhole voids were observed to occur in the same samples.
- Solid state stress cracks with straight propagation paths and solidification cracks with zig zag propagation paths were observed to occur in the same samples and were frequently interconnected.
- An analytical melt pool model was used to calculate the solidification conditions for each parameter set.
- The Clyne and Davies model was applied to each parameter set but was found to be unhelpful in the current situation since it is only dependent on the alloy composition rather than the cooling conditions.
- The Rappaz, Drezet and Gremaud model for hot crack susceptibility considers both the alloy chemistry and the solidification path, so could be used to correlate the crack susceptibility with process conditions.
- The HCS index increased with increasing areal energy density, a trend which is in agreement with the measured crack populations.

- The RDG model was sensitive to the dendrite spacing, so several approximations for DAS were investigated. Davies' empirical model for DAS gave the best agreement with measured DAS.
- The KGT model was also applied for the eleven sets of processing conditions, showing that the concentrations of zirconium, carbon and boron in the terminal liquid increased with increasing input areal energy density due to an increase in time available for segregation. This composition change causes an increase in the local freezing range of the terminal liquid, corresponding to an increase in crack susceptibility.
- Calculations of interface diffusion showed that LPBF processing occurs within the rapid solidification regime, close to the boundary of solute trapping. However, APT showed enrichment of elements including chromium, niobium, zirconium, boron, and carbon at cell boundaries indicating sufficient time is available for some local solute redistribution during LPBF.
- TEM gave an insight into the dislocation and precipitation behaviour in LPBF IN713C. Precipitates were observed to align with cell boundaries and along a crack edge. Some evidence of dislocation recovery was observed. Further work is required in order to identify the types of precipitates forming in these samples.

## **6. Thesis summary: A hypothetical stroll around the process map**

A common theme throughout this work is the link between solidification conditions and defect formation. A process map has been developed which describes the optimum processing window for LPBF of IN713C test cube specimens and the thresholds for the onset of each defect type. Various processing regimes have been identified according to the formation of defect types. The processing regimes are not mutually exclusive. Defects are observed to form as a result of the process conditions, possibly with the exception of gas porosity, and the dominant defect is a result of prevalent processing conditions. Hence, it is possible to observe multiple defect types in the same sample. The defects are an observable symptom of a particular “loss of control” in the process. In this short chapter, the reader is accompanied on a hypothetical stroll around the process map. A commentary is provided to discuss the effect of straying (deliberately or otherwise) outside of the optimised process window and the implications this has on designing the processing strategy for a component.

The thresholds shown on the map were derived using a combination of empirical deductions and an analytical melt pool model, both of which have some associated error. Hence, the threshold lines on the map can be considered to have some “thickness” which in effect, makes the useful process window smaller. This has implications for the design and production of a component. Ways in which it would be possible to stray outside the processing window, without purposefully changing the physical input parameters, and the potential result in terms of defect formation must be considered when designing a processing strategy for a particular component.

Beginning at the point marked “Optimised” in Figure 4.34, consider the ways in which the material could end up “too hot” or “too cold” compared to the response illustrated by the map. The process map is based on modelling and observations of test cube specimens. However, the material in a component with a more complex geometry would experience varying thermal history according to the local cross



section. For thin walled sections, the material will be warmer than expected due to the reduction in the turnaround time of the laser through short scan vectors and from the reduced conduction of heat away from the region due to lower heat conduction in the surrounding powder. In this case, the risk of forming melt splashing voids is increased since this effect is comparable to reducing the hatch spacing in small test cube samples. Since the material in this scenario is beginning at a higher temperature than expected, this has the effect of reducing the temperature difference on the x-axis on the normalised energy plot, thus moving the processing further towards the right. Hence, it may be easier to transition into keyhole melting model

LOF voids were observed to increase in volume fraction rapidly, soon after passing the threshold. Additionally, large, elongated voids are known to be the most damaging in terms of fatigue life. Hence, it would be important to understand the “thickness” of the LOF threshold in order to avoid moving into this regime in any part of a component. However, it is expected to be more difficult to “accidentally” move left on the process map than it is to move right, since it has been shown in this work that above a certain cross section size (around 5-7 mm) the effects of turnaround time and hatch spacing are less significant. Keyhole voids are round, so they are less problematic in terms of fatigue life. They are also smaller and are present in smaller volume fractions than LOF voids, even at the extreme of each regime. So, it is easier, and safer to inadvertently stray to the right side of the map than the left.

Through this project, it has not been possible to eliminate cracking in LPBF IN713C. However, it has been shown that it is affected by the processing conditions, and worsens with increasing areal energy density. Additionally, it has been demonstrated that solidification cracking is sensitive to the local solidification conditions via the RDG and KGT models, with a correlation between higher areal energy density, increased segregation, a wider local freezing range and increased cracking. Hence, if the material was caused to remain hotter than expected due to thin cross sections (moving to the right on the map), it would be more susceptible to solidification cracking since the length of time spent in the vulnerable zone would increase.

## The Application of AM to Ni-base Superalloys

Overhangs and component edges can be considered in the same way as a thin section. In both these cases the material experiences slower conduction of heat due to being in contact with powder. Hence, remains hotter than material in contact with larger, solid, thermal masses.

The above discussion can be used as a basis for further work in defining the specific effects related to changing component geometry on defect populations. Thus influencing the design of a process specific to a component. It may be necessary to adjust the input processing parameters in order to compensate for a predicted shift in position on the map, away from “optimal” conditions. However, the risk still remains of over or under compensating, due to error in the design or variation in the process.

To summarise, within the allegedly optimised region on the process map, the outcome in terms of material response and defect formation has the potential to be different to that indicated on the map. This is because local solidification conditions are very sensitive to locally imposed thermal conditions, which are influenced by component geometry. These changes in solidification conditions can move processing from low to high defect formation potential over a small spatial range on the map. Further work is required to elucidate the exact nature of the relationship between component geometry and material response, in order to instruct the design process for a component and its LPBF processing strategy.

## 7. Conclusions

### 7.1. Part 1

- An introduction to powder bed fusion, direct energy deposition and binder jet printing was given and their capabilities, applications and limitations were compared. Laser powder bed fusion (LPBF), the main focus of this work, was discussed in terms of development of the hardware necessary for building components in a production environment, alongside a review of the benefits, challenges and limitations of AM.
- The most suitable applications for the use of LPBF within Cummins were identified to be:
  - Using LPBF to overcome current design limitations of conventional manufacturing.
  - Adding value to a component through “designing for AM”.
  - Using LPBF to manufacture obsolete service parts.

### 7.2. Part 2

- A process map was developed for LPBF IN713C using statistical design of experiments, advanced characterisation techniques and thought experiments which probed the fundamental behaviour of the system.
- Test cube specimens were built using a Renishaw SLM125 machine with multiple processing parameter combinations spanning the breadth of the process space bounded by the physical limitations of the machine. This meant that the full range of defect types was observed including lack-of-fusion (LOF) voids, keyhole voids, gas pores, solid state cracking and solidification cracking.
- A “Taxonomy of defects” was prepared, detailing the morphology, size and distribution of the various defects types and the conditions under which they usually form.
- Keyhole voids were observed to form at high energy density. These voids featured a swirl pattern on their internal surface and were located at the bottom of the characteristic shaped melt pools.

## The Application of AM to Ni-base Superalloys

- LOF voids were elongated in the plane of the layers and contained particles of un-melted powder. These formed when the melt pools did not overlap sufficiently.
- Melt splashing voids were observed at high energy densities. These voids were irregularly shaped and contained trapped particles of un-melted powder.
- Gas porosity, thought to originate from retention of prior gas porosity in the powdered feedstock, was randomly distributed throughout a sample volume and were reduced by increasing the input energy density, allowing more of them to escape the melt pool.
- Solidification cracks, with characteristic zig-zag morphology, rounded, blunt crack tips and dendritic structure on the crack faces were observed in all samples. These cracks were often interconnected with solid state stress cracks, which propagate with a straighter path.
- LOF behaviour was described using the theory of overlapping hemispheres with predicted melt pool radii estimated using an analytical melt pool model.

$$l < \left( R^2 - \left( \frac{h}{2} \right)^2 \right)^{\frac{1}{2}}$$

- The Buckingham Pi Theorem of dimensional analysis was used to derive an inverse relationship between LOF behaviour and input energy density. This relationship was confirmed through experimental observations.

$$LOF(\%) = C \left( \frac{\rho C_p \Delta T}{Aq} \frac{x}{\tau} l^2 \right) \propto E_0^{*-1}$$

- Porosity was minimised using response surface methodology allowing the production of LPBF IN713C containing 0.05 % porosity. These “optimised” parameters lie at the centre of the defined process window.
- Cracking was observed to increase as areal energy density was increased. This relationship was consistent with the RDG model for hot crack susceptibility, which predicts a greater probability of solidification cracking for samples processed with higher energy.

- The KGT model indicated that the concentrations of zirconium, carbon and boron in the terminal liquid increased with increasing input areal energy density causing an increase in the local freezing range of the terminal liquid, corresponding to an increase in the measured cracking.
- Calculations of interface diffusion showed that LPBF processing occurs within the rapid solidification regime, close to the boundary of solute trapping. However, APT showed enrichment of elements including chromium, niobium, zirconium, boron, and carbon at cell boundaries indicating sufficient time is available for some local solute redistribution during LPBF.
- TEM gave an insight into the dislocation and precipitation behaviour in LPBF IN713C. Precipitates were observed to align with cell boundaries and along a crack edge. Some evidence of dislocation recovery was observed.
- The main conclusion from this work is that the material and defect response of IN713C when processed via LPBF is highly sensitive to local solidification conditions, which in turn are very sensitive to locally imposed thermal conditions. So, within the allegedly optimised region, deviations from the situation defined in the process map due to part geometry, process variability or another “loss of control” can see the boundaries of the process window shift and blur. This is important when designing a processing strategy for a component, since a thorough understanding of the consequences of straying outside the process window, deliberately or otherwise, will inform the necessary compensation needed to ensure defects are avoided.

## **8. Further work**

### **8.1. Crack mitigation**

- In this work, all LPBF material was analysed in the as-deposited state. Post processing techniques such as HIP, shot peening and laser peening may be beneficial to reducing residual stress and closing some of the voids. It is known that these techniques are not an “easy fix” for defects, but an investigation on how to exploit their benefits may reveal some potential for reducing defects.
- The use of a heated bed to reduce the residual stress in LPBF material should be investigated as it may be beneficial in reducing the propensity for propagation of cracks.
- In this work, a method for assessing the relative likelihood of nucleating solidification cracks according to process settings has been derived. This should be extended to include other “un-weldable” superalloys. In doing so, it may be possible to identify alloy chemistries which are less susceptible to cracking.
- Altering the scanning strategy to involve either pre- or post-melting scanning for pre-heating or in-situ annealing is an interesting avenue which may offer some benefit in terms of avoidance of cracking.

### **8.2. Impact of defects on mechanical properties**

- This work has made significant progress in characterising origin, frequency and size of defects however it was not within the scope to establish the effect of these defects on the mechanical properties of the material. This should be investigated in order to elucidate the impact of deviating outside the optimised process window.

### **8.3. Future work within Cummins**

- The correlation of the material response to the optimum processing parameters for test cubes with that for larger components with different geometries.
- Preparation of a document detailing best practice for parameter optimisation.
- A project on the optimisation of the topology of a component.
- Assessment of the application of the technology to other components.

## References

- [1] L. C. Ardila et al., “Effect of IN718 recycled powder reuse on properties of parts manufactured by means of Selective Laser Melting,” *Phys. Procedia*, vol. 56, no. C, pp. 99–107, 2014.
- [2] H. Asgari et al., “On microstructure and mechanical properties of additively manufactured AlSi10Mg\_200C using recycled powder,” *Mater. Sci. Eng. A*, vol. 707, no. July, pp. 148–158, 2017.
- [3] “Arcam EBM.” [Online]. Available: <http://www.arcam.com/wp-content/uploads/arcamebm-corp-brochure-fnlv3.pdf>.
- [4] L. Thijs et al., “A study of the microstructural evolution during selective laser melting of Ti-6Al-4V,” *Acta Mater.*, vol. 58, no. 9, pp. 3303–3312, 2010.
- [5] H. Gong et al., “Melt Pool Characterization for Selective Laser Melting of Ti-6Al-4V Pre-alloyed Powder,” *Solid Free. Fabr. Symp.*, pp. 256–267, 2014.
- [6] T. Vilaro, C. Colin, and J. D. Bartout, “As-fabricated and heat-treated microstructures of the Ti-6Al-4V alloy processed by selective laser melting,” *Metall. Mater. Trans. A Phys. Metall. Mater. Sci.*, vol. 42, no. 10, pp. 3190–3199, 2011.
- [7] S. S. Al-Bermani et al., “The origin of microstructural diversity, texture, and mechanical properties in electron beam melted Ti-6Al-4V,” *Metall. Mater. Trans. A Phys. Metall. Mater. Sci.*, vol. 41, no. 13, pp. 3422–3434, 2010.
- [8] L. Thijs et al., “Fine-structured aluminium products with controllable texture by selective laser melting of pre-alloyed AlSi10Mg powder,” *Acta Mater.*, vol. 61, no. 5, pp. 1809–1819, 2013.
- [9] N. Read et al., “Selective laser melting of AlSi10Mg alloy: Process optimisation and mechanical properties development,” *Mater. Des.*, vol. 65, pp. 417–424, 2015.
- [10] D. E. Cooper et al., “Additive layer manufacture of Inconel 625 metal matrix

- composites, reinforcement material evaluation,” *J. Mater. Process. Technol.*, vol. 213, no. 12, pp. 2191–2200, 2013.
- [11] Z. Wang et al., “Residual stress mapping in Inconel 625 fabricated through additive manufacturing: Method for neutron diffraction measurements to validate thermomechanical model predictions,” *Mater. Des.*, vol. 113, pp. 169–177, 2017.
- [12] T. Trosch et al., “Microstructure and mechanical properties of selective laser melted Inconel 718 compared to forging and casting,” *Mater. Lett.*, vol. 164, pp. 428–431, 2016.
- [13] F. Wang, “Mechanical property study on rapid additive layer manufacture Hastelloy® X alloy by selective laser melting technology,” *Int. J. Adv. Manuf. Technol.*, vol. 58, no. 5, pp. 545–551, 2012.
- [14] G. Kasperovich et al., “Correlation between porosity and processing parameters in TiAl6V4 produced by selective laser melting,” *Mater. Des.*, vol. 105, pp. 160–170, 2016.
- [15] G. Kasperovich and J. Hausmann, “Improvement of fatigue resistance and ductility of TiAl6V4 processed by selective laser melting,” *J. Mater. Process. Technol.*, vol. 220, pp. 202–214, 2015.
- [16] S. Leuders et al., “Structural components manufactured by Selective Laser Melting and Investment Casting—impact of the process route on the damage mechanism under cyclic loading,” *J. Mater. Process. Technol.*, vol. 248, pp. 130–142, 2017.
- [17] S. Leuders *et al.*, “On the mechanical behaviour of titanium alloy TiAl6V4 manufactured by selective laser melting: Fatigue resistance and crack growth performance,” *Int. J. Fatigue*, vol. 48, pp. 300–307, 2013.
- [18] C. Qiu, N. J. E. Adkins, and M. M. Attallah, “Microstructure and tensile properties of selectively laser-melted and of HIPed laser-melted Ti-6Al-4V,” *Mater. Sci. Eng. A*, vol. 578, pp. 230–239, 2013.
- [19] C. Selcuk, “Laser metal deposition for powder metallurgy parts,” *Powder*



- Metall.*, vol. 54, no. 2, pp. 94–99, 2011.
- [20] L. Sexton et al., “Laser cladding of aerospace materials,” *J. Mater. Process. Technol.*, vol. 122, no. 1, pp. 63–68, 2002.
- [21] S. Nowotny et al., “Laser Beam Build-Up Welding: Precision in Repair, Surface Cladding, and Direct 3D Metal Deposition,” *J. Therm. Spray Technol.*, vol. 16, no. 3, pp. 344–348, 2007.
- [22] B. E. Carroll, T. A. Palmer, and A. M. Beese, “Anisotropic tensile behavior of Ti-6Al-4V components fabricated with directed energy deposition additive manufacturing,” *Acta Mater.*, vol. 87, pp. 309–320, 2015.
- [23] T. Do, P. Kwon, and C. S. Shin, “Process development toward full-density stainless steel parts with binder jetting printing,” *Int. J. Mach. Tools Manuf.*, vol. 121, pp. 50–60, 2017.
- [24] A. Mostafaei et al., “Brief data overview of differently heat treated binder jet printed samples made from argon atomized alloy 625 powder,” *Data Br.*, vol. 9, pp. 556–562, 2016.
- [25] C. Li, Y. B. Guo, and J. B. Zhao, “Interfacial phenomena and characteristics between the deposited material and substrate in selective laser melting Inconel 625,” *J. Mater. Process. Technol.*, vol. 243, pp. 269–281, 2017.
- [26] C. Emmelmann et al., “Laser additive manufacturing and bionics: Redefining lightweight design,” *Phys. Procedia*, vol. 12, no. PART 1, pp. 364–368, 2011.
- [27] B. Vayre, F. Vignat, and F. Villeneuve, “Designing for additive manufacturing,” *Procedia CIRP*, vol. 3, no. 1, pp. 632–637, 2012.
- [28] M. Tomlin and J. Meyer, “Topology Optimization of an Additive Layer Manufactured (ALM) Aerospace Part,” *7th Altair CAE Technol. Conf. 2011*, pp. 1–9, 2011.
- [29] K. Salonitis and S. Al Zarban, “Redesign optimization for manufacturing using additive layer techniques,” *Procedia CIRP*, vol. 36, pp. 193–198, 2015.

- [30] D. Mahmoud and M. Elbestawi, "Lattice Structures and Functionally Graded Materials Applications in Additive Manufacturing of Orthopedic Implants: A Review," *J. Manuf. Mater. Process.*, vol. 1, no. 2, p. 13, 2017.
- [31] H. W. Stoll, "Casting Design and Processes," in *Casting Design and Performance*, Ohio: ASM International, 2009, pp. 9–37.
- [32] W. E. King et al., "Laser powder bed fusion additive manufacturing of metals; physics, computational, and materials challenges," *Appl. Phys. Rev.*, vol. 2, no. 4, p. 041304, 2015.
- [33] S. Ford and M. Despeisse, "Additive manufacturing and sustainability: an exploratory study of the advantages and challenges," *J. Clean. Prod.*, vol. 137, pp. 1573–1587, 2016.
- [34] W. Gao et al., "The status, challenges, and future of additive manufacturing in engineering," *Comput. Des.*, vol. 69, pp. 65–89, 2015.
- [35] B. Berman, "3-D printing: The new industrial revolution," *Bus. Horiz.*, vol. 55, no. 2, pp. 155–162, 2012.
- [36] C. Boig, M. Burkinshaw, and I. Todd, "The application of additive manufacturing to turbomachinery," *Proc. 13th Int. Conf. Turbochargers Turbocharging*, pp. 261–269, 2018.
- [37] R. Dehoff et al., "Case study: Additive manufacturing of aerospace brackets," *Adv. Mater. Process.*, vol. 171, no. 3, pp. 19–22, 2013.
- [38] R. Huang et al., "Energy and emissions saving potential of additive manufacturing: The case of lightweight aircraft components," *J. Clean. Prod.*, 2014.
- [39] M. Despeisse and S. Ford, "The role of additive manufacturing in improving resource efficiency and sustainability," *IFIP Adv. Inf. Commun. Technol.*, vol. 460, no. 3, pp. 129–136, 2015.
- [40] K. Kellens, R. Mertens, D. Paraskevas, W. Dewulf, and J. R. Duflou, "Environmental Impact of Additive Manufacturing Processes: Does AM

- Contribute to a More Sustainable Way of Part Manufacturing?,” *Procedia CIRP*, vol. 61, Section 3, pp. 582–587, 2017.
- [41] D. Thomas and S. Gilbert, “Costs and Cost Effectiveness of Additive Manufacturing - A Literature Review and Discussion,” *NIST Spec. Publ.*, vol. 1176, pp. 1–77, 2014.
- [42] M. Baumers et al., “The cost of additive manufacturing: Machine productivity, economies of scale and technology-push,” *Technol. Forecast. Soc. Change*, vol. 102, pp. 193–201, 2016.
- [43] K. Kellens et al., “Environmental Impact of Additive Manufacturing Processes: Does AM Contribute to a More Sustainable Way of Part Manufacturing?,” *Procedia CIRP*, vol. 61, Section 3, pp. 582–587, 2017.
- [44] M. Baumers et al., “Energy inputs to additive manufacturing: Does capacity utilization matter?,” *Solid Free. Fabr. Symp.*, pp. 30–40, 2011.
- [45] M. Baumers, P. Dickens, C. Tuck, and R. Hague, “The cost of additive manufacturing: Machine productivity, economies of scale and technology-push,” *Technol. Forecast. Soc. Change*, vol. 102, pp. 193–201, 2016.
- [46] W. J. Hopp and M. L. Spearman, *Factory Physics*, Third. USA: Waveland Press, Inc, 2008.
- [47] A. Juriani, “Casting Defects Analysis in Foundry and Their Remedial Measures with Industrial Case Studies,” *IOSR J. Mech. Civ. Eng. Ver. I*, vol. 12, no. 6, pp. 2278–1684, 2015.
- [48] C. Silva, M. Ross, and T. Farias, “Analysis and simulation of ‘low-cost’ strategies to reduce fuel consumption and emissions in conventional gasoline light-duty vehicles,” *Energy Convers. Manag.*, vol. 50, no. 2, pp. 215–222, 2009.
- [49] G. Ziolkowski et al., “Application of X-ray CT method for discontinuity and porosity detection in 316L stainless steel parts produced with SLM technology,” *Arch. Civ. Mech. Eng.*, vol. 14, no. 4, pp. 608–614, 2014.

- [50] W. E. King et al., “Observation of keyhole-mode laser melting in laser powder-bed fusion additive manufacturing,” *J. Mater. Process. Technol.*, vol. 214, no. 12, pp. 2915–2925, 2014.
- [51] N. Raghavan et al., “Localized melt-scan strategy for site specific control of grain size and primary dendrite arm spacing in electron beam additive manufacturing,” *Acta Mater.*, vol. 140, pp. 375–387, 2017.
- [52] M. Thomas, G. J. Baxter, and I. Todd, “Normalised model-based processing diagrams for additive layer manufacture of engineering alloys,” *Acta Mater.*, vol. 108, pp. 26–35, 2016.
- [53] M. J. Donachie, “Superalloys: A Technical Guide, 2nd Edition,” *America (NY).*, pp. 1–409, 2002.
- [54] John DuPont, John Lippold, Samuel Kiser, *Welding Metallurgy and Weldability of Nickel-Base Superalloys*. Jon Wiley & Sons, Inc., 2009.
- [55] M. Zielińska et al., “Thermal properties of cast nickel based superalloys,” *Arch. Mater. Sci. Eng.*, vol. 44, no. 1, pp. 35–38, 2010.
- [56] J. L. Caron and J. W. Sowards, *Weldability of Nickel-Base Alloys*, vol. 6. Elsevier, 2014.
- [57] M. M. Attallah et al., “Additive manufacturing of Ni-based superalloys: The outstanding issues,” *MRS Bull.*, vol. 41, no. 10, pp. 758–764, 2016.
- [58] L. N. Carter, M. M. Attallah, and R. C. Reed, “Laser Powder Bed Fabrication of Nickel-Base Superalloys: Influence of Parameters; Characterisation, Quantification and Mitigation of Cracking,” *Superalloys 2012*, pp. 577–586, 2012.
- [59] J. Campbell, *Complete Casting Handbook*. Elsevier Ltd., 2015.
- [60] W. Kurz and D. Fisher, *Fundamentals of solidification*, 3rd ed. Trans Tech Publications Ltd, 1989.
- [61] W. Losert, B. Q. Shi, and H. Z. Cummins, “Evolution of dendritic patterns during alloy solidification: From the initial instability to the steady state.”

- Proc. Natl. Acad. Sci. U. S. A.*, vol. 95, no. 2, pp. 439–442, 1998.
- [62] W. Kurz and R. Trivedi, “Rapid solidification processing and microstructure formation,” *Mater. Sci. Eng. A*, vol. 179–180, no. PART 1, pp. 46–51, 1994.
- [63] W. Kurz and D. J. Fisher, “Dendrite growth at the limit of stability: tip radius and spacing,” *Acta Metall.*, vol. 29, no. 1, pp. 11–20, 1981.
- [64] R. Trivedi, “Interdendritic Spacing: Part II. A Comparison of Theory and Experiment,” P. B. T.-D. of C. F. Pelcé, Ed. San Diego: Academic Press, 1988, pp. 353–358.
- [65] R. W. Cahn and H. Jones, *Non-equilibrium processing of materials*, 1st Editio. 1999.
- [66] M. J. Aziz, “Model for solute redistribution during rapid solidification,” *J. Appl. Phys.*, vol. 53, no. 2, pp. 1158–1168, 1982.
- [67] W. Kurz, B. Giovanola, and R. Trivedi, “Theory of Microstructural Development During Rapid Solidification,” *Acta metall*, vol. 34, no. 5, pp. 823–830, 1986.
- [68] U. Scipioni Bertoli et al., “In-situ characterization of laser-powder interaction and cooling rates through high-speed imaging of powder bed fusion additive manufacturing,” *Mater. Des.*, vol. 135, pp. 385–396, 2017.
- [69] N. J. Harrison, I. Todd, and K. Mumtaz, “Reduction of micro-cracking in nickel superalloys processed by Selective Laser Melting: A fundamental alloy design approach,” *Acta Mater.*, vol. 94, pp. 59–68, 2015.
- [70] L. Wang, N. Wang, and N. Provatas, “Liquid channel segregation and morphology and their relation with hot cracking susceptibility during columnar growth in binary alloys,” *Acta Mater.*, vol. 126, pp. 302–312, 2017.
- [71] W. Trivedi, R. Kurz, “Dendritic growth,” *Inter. Mater. Rev*, vol. 39, no. 49, 1994.
- [72] J. D. Hunt, “Cellular and primary dendrite spacings,” *Solidif. Cast. Met.*, pp. 3–9, 1979.

- [73] G. F. Bolling and W. A. Tiller, "Growth from the melt. III. dendritic growth," *J. Appl. Phys.*, vol. 32, no. 12, pp. 2587–2605, 1961.
- [74] R. Trivedi and G. M. Pound, "Growth kinetics of plate-like precipitates," *J. Appl. Phys.*, vol. 40, no. 11, pp. 4293–4300, 1969.
- [75] J. S. Langer and H. Müller-Krumbhaar, "Theory of dendritic growth-I. Elements of a stability analysis," *Acta Metall.*, vol. 26, no. 11, pp. 1681–1687, 1978.
- [76] H. A. Davies, N. Shohoji, and D. H. Warrington, "The Structure of Rapidly Quenched Nickel-based Superalloy Ribbons Produced by Melt Spinning," in *Rapid Solidification Processing: Principles and Technologies II, Proceedings of the 2nd International Conference on Rapid Solidification Processing*, 1980, pp. 153–164.
- [77] H. Gong et al., "Influence of defects on mechanical properties of Ti-6Al-4V components produced by selective laser melting and electron beam melting," *Mater. Des.*, vol. 86, pp. 545–554, 2015.
- [78] P. Edwards, A. O'Conner, and M. Ramulu, "Electron Beam Additive Manufacturing of Titanium Components: Properties and Performance," *J. Manuf. Sci. Eng.*, vol. 135, no. 6, pp. 61016–61017, Nov. 2013.
- [79] J. A. Kanko, A. P. Sibley, and J. M. Fraser, "In situ morphology-based defect detection of selective laser melting through inline coherent imaging," *J. Mater. Process. Technol.*, vol. 231, pp. 488–500, 2016.
- [80] Y. Huang et al., "Finite element analysis of thermal behavior of metal powder during selective laser melting," *Int. J. Therm. Sci.*, vol. 104, pp. 146–157, 2016.
- [81] T. W. Eagar and N. S. Tsai, "Temperature fields produced by traveling distributed heat sources," *Weld. J.*, vol. 62, no. 12, pp. 346–355, 1983.
- [82] G. K. L. Ng et al., "Porosity formation and gas bubble retention in laser metal deposition," *Appl. Phys. A Mater. Sci. Process.*, vol. 97, no. 3, pp. 641–649, 2009.

- [83] E. Chauvet et al., “Hot cracking mechanism affecting a non-weldable Ni-based superalloy produced by Selective Electron Beam Melting,” *Acta Mater.*, vol. 142, pp. 82-94, 2017.
- [84] S. Tammam-Williams et al., “XCT analysis of the influence of melt strategies on defect population in Ti-6Al-4V components manufactured by Selective Electron Beam Melting,” *Mater. Charact.*, vol. 102, pp. 47–61, 2015.
- [85] C. Qiu et al., “On the role of melt flow into the surface structure and porosity development during selective laser melting,” *Acta Mater.*, vol. 96, pp. 72–79, 2015.
- [86] S. A. Khairallah et al., “Laser powder-bed fusion additive manufacturing: Physics of complex melt flow and formation mechanisms of pores, spatter, and denudation zones,” *Acta Mater.*, vol. 108, pp. 36–45, 2016.
- [87] M. J. Matthews et al., “Denudation of metal powder layers in laser powder bed fusion processes,” *Acta Mater.*, vol. 114, pp. 33–42, 2016.
- [88] K. Monroy, J. Delgado, and J. Ciurana, “Study of the pore formation on CoCrMo alloys by selective laser melting manufacturing process,” *Procedia Eng.*, vol. 63, pp. 361–369, 2013.
- [89] M. Cloots et al., “Microstructural characteristics of the nickel-based alloy IN738LC and the cobalt-based alloy Mar-M509 produced by selective laser melting,” *Mater. Sci. Eng. A*, vol. 658, pp. 68–76, 2016.
- [90] C. Panwisawas et al., “On the role of thermal fluid dynamics into the evolution of porosity during selective laser melting,” *Scr. Mater.*, vol. 105, pp. 14–17, 2015.
- [91] P. Mercelis and J.-P. Kruth, “Residual stresses in selective laser sintering and selective laser melting,” *Rapid Prototyp. J.*, vol. 12, no. 5, pp. 254–265, 2006.
- [92] D. Tomus et al., “Controlling the microstructure of Hastelloy-X components manufactured by Selective Laser Melting,” *Phys. Procedia*, vol. 41, pp. 823–827, 2013.

- [93] G. A. Young et al., “The mechanism of ductility dip cracking in nickel-chromium alloys,” *Suppl. to Weld. J.*, no. February, pp. 31–43, 2008.
- [94] A. J. Ramirez and J. C. Lippold, “High temperature behavior of Ni-base weld metal Part II - Insight into the mechanism for ductility dip cracking,” *Mater. Sci. Eng. A*, vol. 380, no. 1, pp. 245–258, 2004.
- [95] T. W. Clyne and G. J. Davies, “Comparison between experimental data and theoretical predictions relating to dependence of solidification cracking on composition.” 1977.
- [96] M. Rappaz, J. M. Drezet, and M. Gremaud, “A new hot-tearing criterion,” *Metall. Mater. Trans. A*, vol. 30, no. 2, pp. 449–455, 1999.
- [97] K. Kempen et al., “Producing crack-free, high density M2 HSS parts by selective laser melting: Pre-heating the baseplate,” *Proc. 24th Int. Solid Free. Fabrication Symp.*, pp. 131–139, 2013.
- [98] H. Ali et al., “In-situ residual stress reduction, martensitic decomposition and mechanical properties enhancement through high temperature powder bed pre-heating of Selective Laser Melted Ti6Al4V,” *Mater. Sci. Eng. A*, vol. 695, pp. 211–220, 2017.
- [99] L. N. Carter et al., “The influence of the laser scan strategy on grain structure and cracking behaviour in SLM powder-bed fabricated nickel superalloy,” *J. Alloys Compd.*, vol. 615, pp. 338–347, 2014.
- [100] S. Catchpole-Smith et al., “Fractal Scan Strategies for Selective Laser Melting of ‘Unweldable’ Nickel Superalloys,” *Addit. Manuf.*, vol. 15, pp.113-122, 2017.
- [101] E. A. Jäggle et al., “Precipitation Reactions in Age-Hardenable Alloys During Laser Additive Manufacturing,” *Journal of the Minerals Metals & Materials Society*, vol. 68, no. 3, pp. 943–949, 2016.
- [102] J. Grodzki et al., “Effect of B, Zr, and C on Hot Tearing of a Directionally Solidified Nickel-Based Superalloy,” *Metall. Mater. Trans. A Phys. Metall. Mater. Sci.*, vol. 47, no. 6, pp. 2914–2926, 2016.



- [103] J. C. Ion; H. R. Shercliff; M. F. Ashby., “Diagrams for laser materials processing,” *Acta. Met. Mater.*, vol. 40, no. 7, pp. 1539–1551, 1992.
- [104] M. Picasso and M. Rappaz, “Laser-Powder-Material Interactions in the Laser Cladding Process,” *J. Phys. Iv*, vol. 4, no. C4, pp. 27–33, 1994.
- [105] L. E. E. P. Breinan et al., “Surface Treatment of Superalloys by Laser Skin Melting,” *Superalloys*, 1976.
- [106] Y. M. Wang et al., “Additively manufactured hierarchical stainless steels with high strength and ductility,” *Nat. Mater.*, vol. 17, no. 1, pp. 63–70, 2018.
- [107] M. Baker, “Statisticians issue warning on P values,” *Nature*, vol. 531, p. 151, 2016.
- [108] D. Colquhoun, “An investigation of the false discovery rate and the misinterpretation of p -values Subject Areas : Author for correspondence :,” *R. Soc. Open Sci.*, vol. 1, no. 140216, 2014.
- [109] S. Carmignato, W. Dewulf, and R. Leach, *Industrial X-Ray Computed Tomography*. Springer International Publishing, 2017.
- [110] E. Maire and P. J. Withers, “Quantitative X-ray tomography,” *Int. Mater. Rev.*, vol. 59, no. 1, pp. 1–43, 2014.
- [111] E. W. Müller, “Field Ionization and Field Ion Microscopy,” vol. 13, L. Marton and C. Marton, Eds. Academic Press, pp. 83–179, 1960.
- [112] T. F. Kelly and M. K. Miller, “Invited review article: Atom probe tomography,” *Rev. Sci. Instrum.*, vol. 78, no. 3, 2007.
- [113] D. Blavette, E. Cadel, and B. Deconihout, “Role of the atom probe in the study of nickel-based superalloys,” *Mater. Charact.*, vol. 44, no. 1–2, pp. 133–157, 2000.
- [114] A. J. London et al., “Quantification of oxide particle composition in model oxide dispersion strengthened steel alloys,” *Ultramicroscopy*, vol. 159, pp. 360–367, 2015.
- [115] J. O. Andersson et al., “Thermo-Calc & DICTRA, computational tools for

- materials science,” *Calphad Comput. Coupling Phase Diagrams Thermochem.*, vol. 26, no. 2, pp. 273–312, 2002.
- [116] M. Hillert, *Phase Equilibria, Phase Diagrams and Phase Transformations - Their Thermodynamic Basics*, vol. 53, no. 9. 2008.
- [117] A. Kroupa, “Modelling of phase diagrams and thermodynamic properties using Calphad method - Development of thermodynamic databases,” *Comput. Mater. Sci.*, vol. 66, pp. 3–13, 2013.
- [118] Thermo-Calc Software AB, “TCNI8 : TCS Ni-based Superalloys Database.”
- [119] F. Freeman, “Thermal field modelling for pulsed selective laser melting process,” *Unpubl. manuscript, Univ. Sheffield, UK*, 2018.
- [120] C. A. Schneider, W. S. Rasband, and K. W. Eliceiri, “NIH Image to ImageJ: 25 years of image analysis,” *Nat. Methods*, vol. 9, no. 7, pp. 671–675, 2012.
- [121] J. H. Evans, “Dimensional analysis and the Buckingham Pi Theorem,” *Amer. J. Phys.*, vol. 40, May 2016, pp. 1815–1821, 1972.
- [122] “[https://ocw.mit.edu/courses/mechanical-engineering/2-25-advanced-fluid-mechanics-fall-2013/dimensional-analysis/MIT2\\_25F13\\_The\\_Buckingham.pdf](https://ocw.mit.edu/courses/mechanical-engineering/2-25-advanced-fluid-mechanics-fall-2013/dimensional-analysis/MIT2_25F13_The_Buckingham.pdf).” .
- [123] C. L. A. Leung et al., “In situ X-ray imaging of defect and molten pool dynamics in laser additive manufacturing,” *Nat. Commun.*, vol. 1355, pp. 1–9, 2018.
- [124] V. D. Divya et al., “Microstructure of selective laser melted CM247LC nickel-based superalloy and its evolution through heat treatment,” *Mater. Charact.*, vol. 114, pp. 62–74, 2016.
- [125] R. Hagedorn et al., “Processing of nickel based superalloy MAR M-247 by means of High Temperature - Selective Laser Melting (HT - SLM),” *High Value Manuf. Adv. Res. Virtual Rapid Prototyp. - Proc. 6th Int. Conf. Adv. Res. Rapid Prototyping, VR@P 2013*, pp. 291–295, 2014.
- [126] S. Tammis-Williams et al., “The Influence of Porosity on Fatigue Crack

- Initiation in Additively Manufactured Titanium Components,” *Sci. Rep.*, vol. 7, no. 7308, 2017.
- [127] J. Dawes, R. Bowerman, and R. Trepleton, “Introduction to the Additive Manufacturing Powder Metallurgy Supply Chain,” *Johnson Matthey Technol. Rev.*, vol. 59, no. 3, pp. 243–256, 2015.
- [128] M. Entezarian et al., *Plasma atomization: A new process for the production of fine, spherical powders*, vol. 48. 1996.
- [129] M. Gremaud, M. Carrard, and W. Kurz, “The microstructure of rapidly solidified AlFe alloys subjected to laser surface treatment,” *Acta Metall. Mater.*, vol. 38, no. 12, pp. 2587–2599, 1990.
- [130] D. Raabe et al., “Grain boundary segregation engineering in metallic alloys: A pathway to the design of interfaces,” *Curr. Opin. Solid State Mater. Sci.*, vol. 18, no. 4, pp. 253–261, 2014.
- [131] R. B. McLellan, “The diffusion of boron in nickel,” *Scr. Metall. Mater.*, vol. 33, no. 8, pp. 1265–1267, 1995.
- [132] J. W. Martin, R. D. Doherty, and B. Cantor, *Stability of microstructure in metallic systems*, Second edi. Cambridge University Press, 1997.
- [133] Y. Y. Chu, P. Ji, and T. Ko, “Diffusion of boron in alloys,” *Acta Met. Sin.*, vol. 27, 1991.
- [134] H. Farhangi, S. Norouzi, and M. Nili-Ahmadabadi, “Effects of casting process variables on the residual stress in Ni-base superalloys,” *J. Mater. Process. Technol.*, vol. 153–154, no. 1–3, pp. 209–212, 2004.
- [135] Y. Sato et al., “Viscosities of nickel base super alloys,” *17th Eur. Conf. Thermophys. Prop.*, pp. 1–5, 2005.
- [136] K. Eckler et al., “Evidence for a transition from diffusion-controlled to thermally controlled solidification in metallic alloys,” *Phys. Rev. B*, vol. 45, no. 9, pp. 5019–5022, 1992.
- [137] M. Schwarz et al., “Dendritic growth velocity and diffusive speed in

- solidification of undercooled dilute Ni-Zr melts,” *Materials Science and Engineering*, vol. 226–228, no. 1. pp. 420–424, 1997.
- [138] M. Lachowicz, W. Dudziński, and M. Podrez-Radziszewska, “TEM observation of the heat-affected zone in electron beam welded superalloy Inconel 713C,” *Mater. Charact.*, vol. 59, no. 5, pp. 560–566, 2008.
- [139] F. J. Humphreys and M. Hatherly, *Recrystallisation and Related Annealing Phenomena*, vol. 2. 1996.
- [140] R. Engeli et al., “Processability of different IN738LC powder batches by selective laser melting,” *J. Mater. Process. Technol.*, vol. 229, pp. 484–491, 2016.
- [141] Q. B. Nguyen et al. “Characteristics of Inconel Powders for Powder-Bed Additive Manufacturing,” *Engineering*, vol. 3, no. 5, pp. 695–700, 2017.
- [142] A. B. Spierings, N. Herres, and G. Levy, “Influence of the particle size distribution on surface quality and mechanical properties in AM steel parts,” *Rapid Prototyp. J.*, vol. 17, no. 3, pp. 195–202, Apr. 2011.
- [143] J. J. Dunkley, *Advances in atomisation techniques for the formation of metal powders*. Woodhead Publishing Limited, 2013.

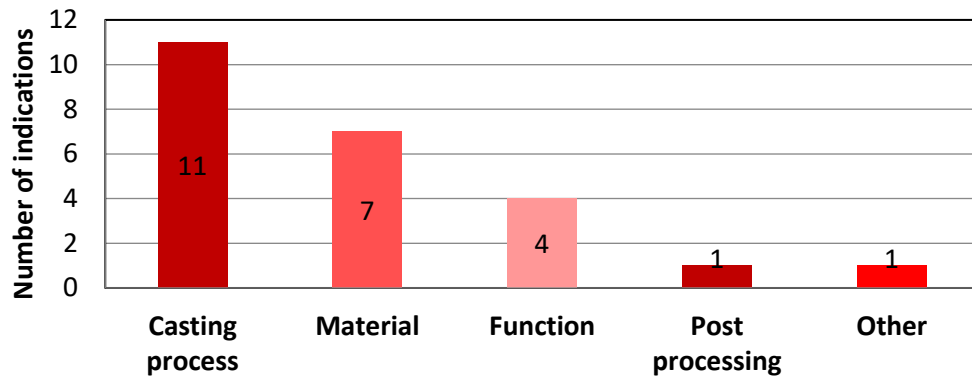
## Appendix 1: Initial “Voice of customer” questionnaire within Cummins

A “Voice of the Customer” (VOC) questionnaire was conducted at the outset of this project in order to assess the view of key stakeholders in terms of project requirements, attitude towards AM and appetite for R&D activities into the subject. 25 questionnaires were issued to key stakeholders from Materials, Advanced Engineering, Aerodynamics and Purchasing backgrounds. 11 responses were collected and used to refine the scope of the project.

The questions and responses are summarised below.

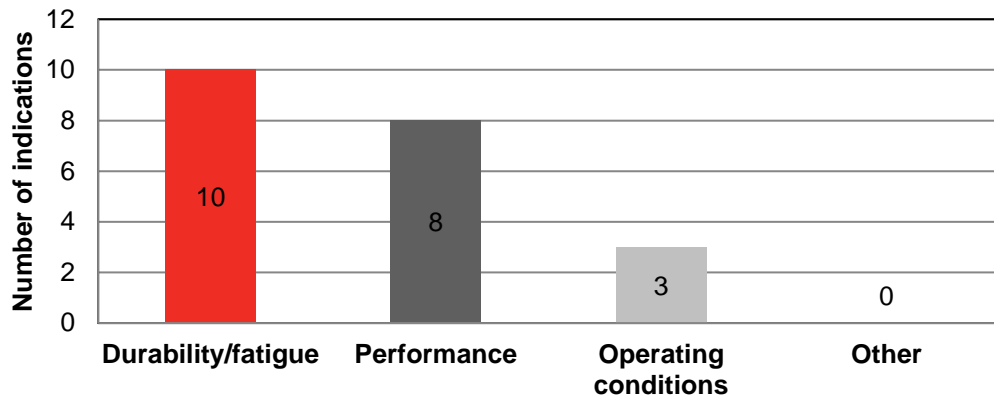
<b>1) In which areas of product development or manufacture could you see your department using additive manufacturing in the future?</b>
<b>Rapid prototyping and testing (8)</b>
Aerodynamic components (turbine/compressor wheels, nozzle) (7)
Performance/durability testing (3)
Casting tooling manufacture (2)
Housings (1)
Refining design suitability (1)
<b>Design benefits (3)</b>
Weight saving (3)
Wheels (1)
Aerodynamic performance (1)
Defect reduction (1)
Adding functionality (1)
<b>Low volume production (2)</b>
<b>Remanufacturing (1)</b>

2) What limits you in terms of design of the turbine wheel and why?



Limits blade thickness (4)	Limited maximum stresses (4)	Aerodynamics (1)	Inconsistencies (1)	Cost (1)
Geometry restrictions (5)	Mass and inertia issues (1)	Rotational / temperature effects (1)		
Limited grain structure control (3)		Nose / back face design limitations (1)		
Durability (2)				

3) What are the current functional limitations of cast turbine wheels?



Fatigue drives design / limits life (7)

Porosity / inclusions (3)

Variability of geometry and material (2)

Balancing efficiency and durability (2)

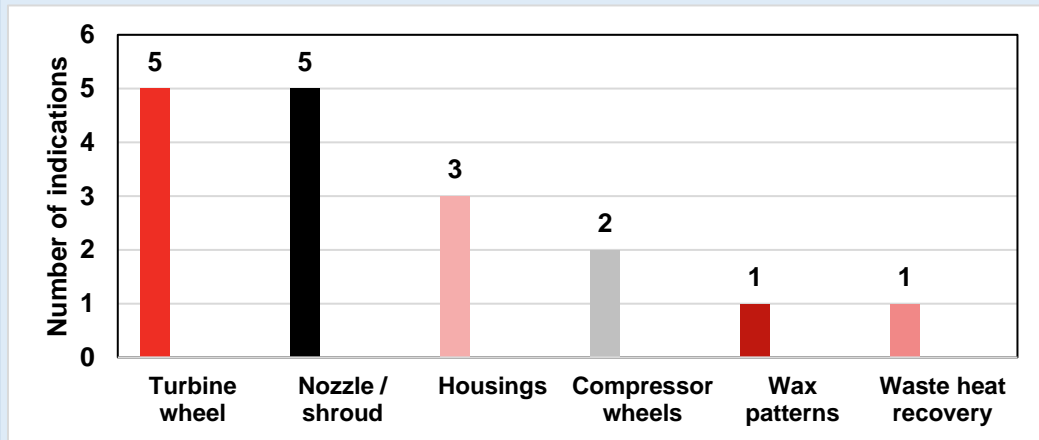
Surface conditioning (1)

Improve by changing blade shape (1)

Offsets between sources and tools – variation (1)

Current cast material less durable above 850°C (1)

4) Which components would you like to be investigated further with regards to additive manufacturing during this EngD?



5) Please explain the reasons for your answers to question 4 and provide a business priority for your choice of components.

1 <sup>st</sup> – Turbine wheel	2 <sup>nd</sup> - Nozzle
Very long design cycle (>3 months) – need rapid prototyping (2)	Difficult to manufacture conventionally (3)
Customer indications – currently lower performance than competitors (1)	Design to package more easily in VG assembly (2)
Limiting factor for durability (1)	Multi-material wear resistance (2)
	Long design cycle (3 months) (1)

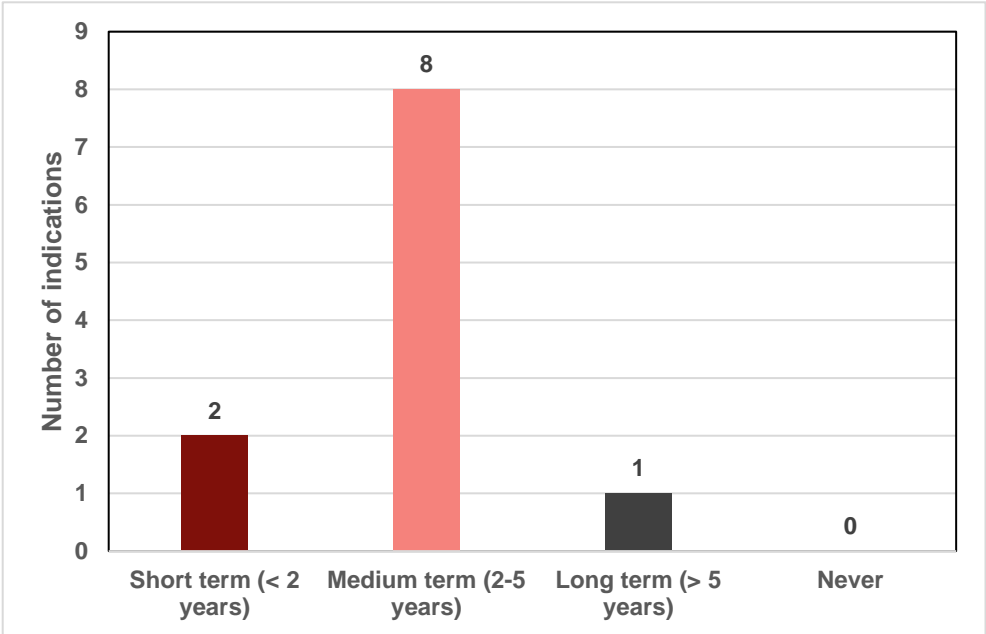
**VOC questionnaire common themes:**

- Rapid prototyping and testing for aerodynamic components.
- Turbine wheel design currently limited by casting process.
- Main functional limitation of turbine wheel is durability / fatigue.
- Nozzle is of second priority for investigation after turbine wheel.

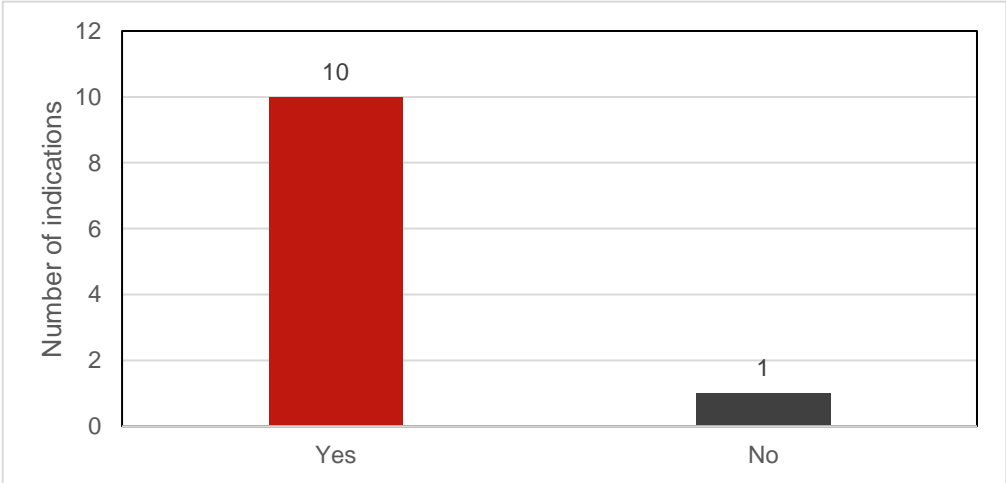


# Appendix 2: Project closing “Voice of customer” questionnaire within Cummins

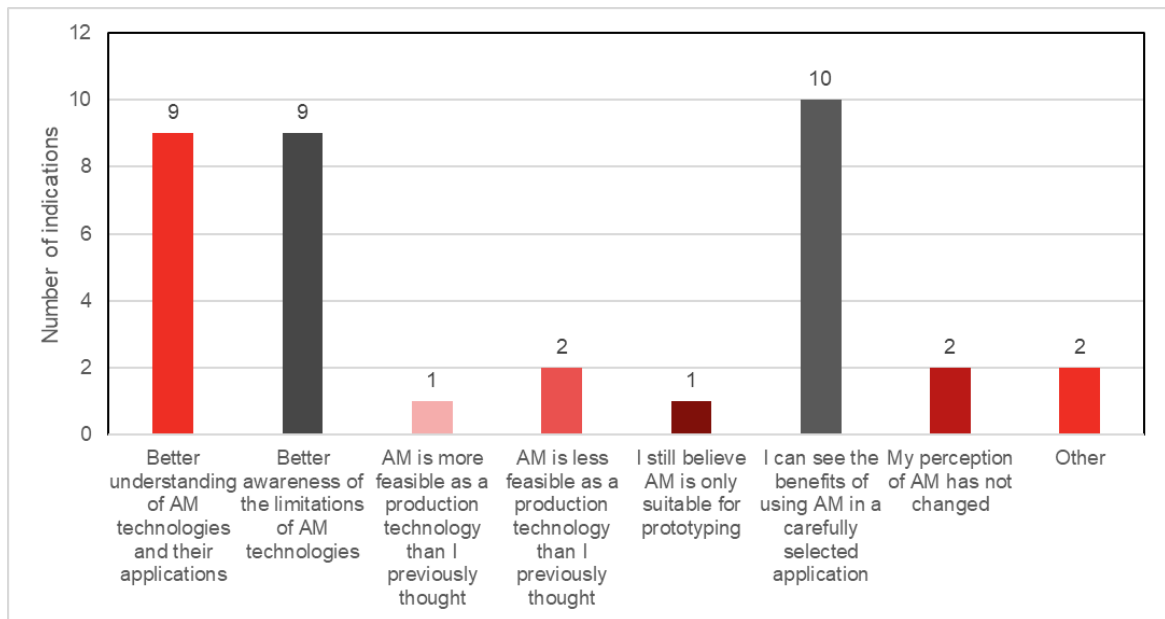
1) When do you envisage AM adoption to occur within the business?



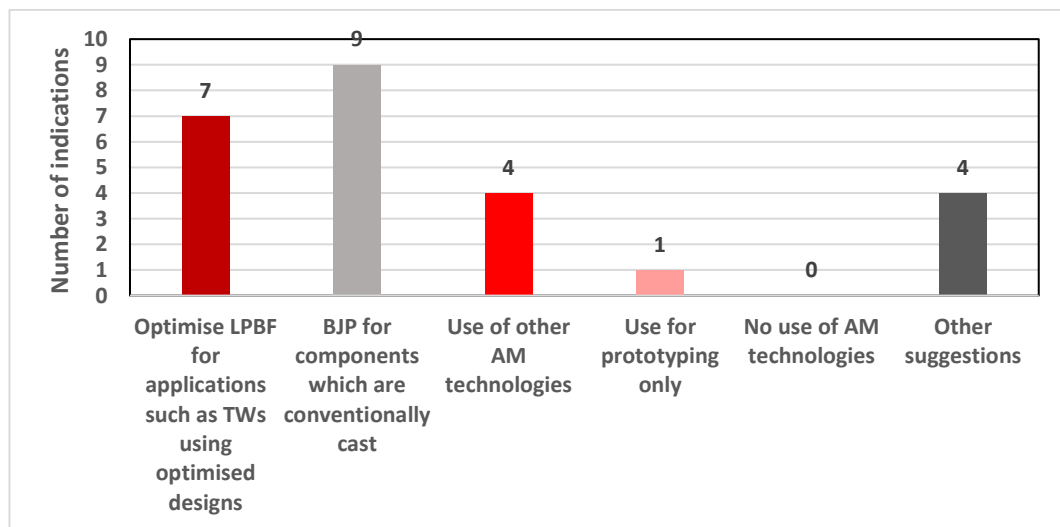
2) Has your perception of AM changed as a consequence of this project?



**3) How has your perception of AM changed as a consequence of this project?**



**4) What do you envisage the future business strategy for the use of AM to be?**




**Project closing VOC outcomes:**




- This EngD project has helped to changed perceived ideas of AM in terms of its use for carefully selected applications in production rather than only prototyping.
- 88% respondents envisage adoption of AM within the business within 2-5 years.
- Optimisation of LPBF for TW applications or BJP for cast components popular options for future business strategy.

## Appendix 3: SOP for Renishaw SLM125

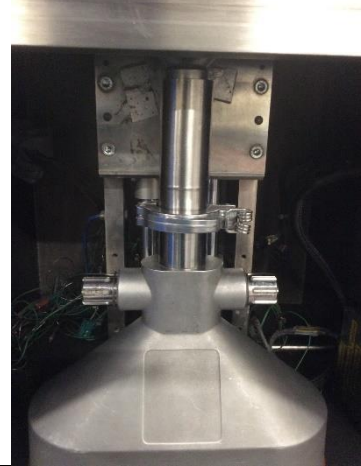



<p><b>Work Instruction</b></p> <p><b>Version 1.3 (17/10/2017)</b>  <b>Review due: October 2018</b>  <b>Prepared by: C Boig</b>  <b>Approved by: I Todd</b></p>	<p><b>Operation of:</b></p> <p><b>Renishaw SLM 125</b></p>
<p><b><u>Scope</u></b></p> <p>This work instruction covers the setup, operation and clean down procedures for the Renishaw SLM125 machine situated in Room C9, Quarrel Laboratory, Hadfield Building, University of Sheffield by trained personnel during working hours.</p> <p>This work instruction does not cover:</p> <ul style="list-style-type: none"> <li>• Out of hours operation</li> <li>• External powder handling</li> <li>• Use of volatile materials</li> <li>• Non-standard builds (e.g. melt tracks)</li> <li>• Use of heated bed</li> </ul> <p><b><u>Personnel qualifications</u></b></p> <p>Users must be trained by a designated Research Associate who will determine the new user's competency for independent operation of the Renishaw SLM125. All users must complete a COSHH assessment for their material before using the Renishaw SLM125. All users must read the risk assessment posted alongside the machine and sign the acknowledgement form prior to using the Renishaw SLM125</p> <p><b><u>Health and safety</u></b></p> <p style="text-align: center;"><b>WEAR CORRECT PPE</b>  <b>Face mask, Eye protection, Latex/Nitrile Gloves, Lab Coat, Safety Shoes</b>  <b>Volatile powders must be handled according to specific COSHH assessment – different safety procedures apply</b></p> <p><b><u>Cautions</u></b></p> <p>Failure to follow these instructions may result in serious health and safety implications and damage to the machine. In such instances permission to use this equipment will be revoked.</p>	


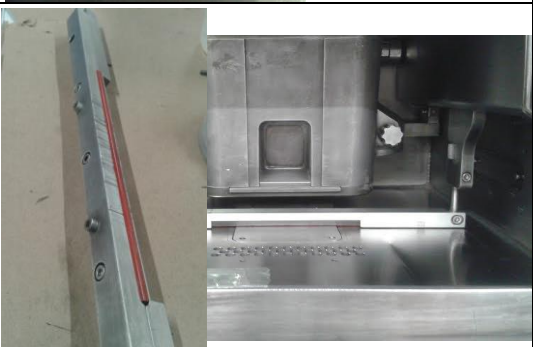

## The Application of AM to Ni-base Superalloys

Op. No.	Operation	Description / Photograph
<b>Set Up</b>		
010	Check all apparatus left as stipulated on smile card. Report any discrepancies using log system	
011	Check cleanliness of build chamber and SLM components by wiping with IPA and blue roll.	
012	Check safe change filter is isolated	 <p>Turn black knobs and blue handles to "off" position</p>
013	Log in to SLM machine	
014	Open door and insert interlock override key	Select "Open Door" then press and hold blue Reset button whilst opening door. Insert override key.




<p>015</p>	<p>Clear error message and press “FIND WIPER HOME”</p>	
<p>016</p>	<p>Attach funnel under receiving holes</p>	
<p>017</p>	<p>Slide neck tube over funnel</p>	

## The Application of AM to Ni-base Superalloys



018	Install powder receiver using O-ring and clip ensuring top of receiver is open		
019	Check dosing mechanism is working freely on hopper		Squeeze springs to check
020	Load powder hopper with powder		
021	Install powder hopper		

022	Install substrate and set height slightly above level of chamber floor	
023	Install wiper	
024	Set appropriate substrate / wiper heights and tighten wiper Allen screws	<p data-bbox="858 1099 1382 1272">Set substrate slightly raised from bottom of chamber. Use paper to check elevation of wiper. Raise/lower using screws on each arm. Should feel a slight, even resistance on paper.</p> 


## The Application of AM to Ni-base Superalloys



025	Clean lens using dedicated sticklers spray and lens wipes. Do not touch the lens with anything other than a moistened lens wipe.	
026	Fill screw holes and gap behind substrate with powder	This step prevents loss of powder when creating first few layers
027	Deposit some powder using "Dose" command. Send wiper to front and check quality of first layer	
028	Remove interlock override key and close door. Clear error message	To remove override key use open door procedure
029	Open safe change filter	
030	Upload build file	Copy file from memory stick to the build folder on the laptop or via the network



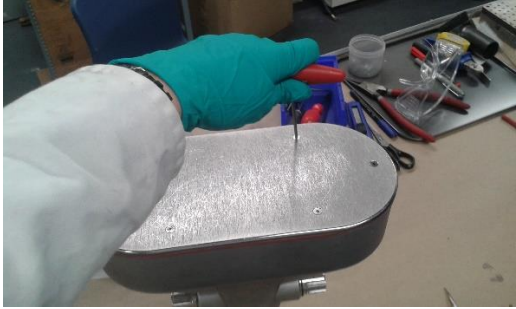

031	Select build file	
032	Press FIND WIPER HOME	
033	Press SET DATUM	
034	Check Argon level	
<b>Operation</b>		
035	Press start	
036	Check dosing level is appropriate	If powder fails to cover whole substrate, increase dosing
037	Monitor periodically throughout build	
<b>Clean Down</b>		
<b>WEAR CORRECT PPE</b> <b>Face mask, Eye protection, Latex/Nitrile Gloves, Lab Coat, Safety Shoes</b>		
038	Accept "Build Complete" message	
039	Log in	
040	Press emergency stop	

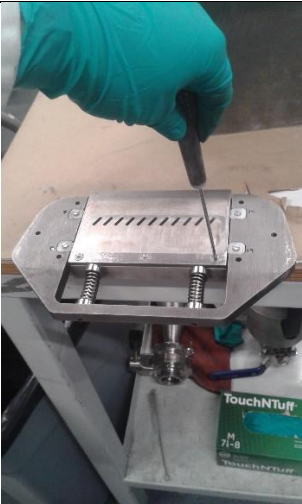

## The Application of AM to Ni-base Superalloys

041	Isolate safe change filter	
042	Open door and insert interlock over ride key	
043	Clear emergency stop error message	
044	Select “Wiper home”	
045	Vacuum burnt powder from edges	This saves time sieving. Burnt powder is darker in appearance. Take care not to vacuum too much re-usable powder.
046	Send wiper to forward position and remove wiper	
047	Remove powder hopper	
048	Use brush to sweep un-melted powder into receiver.	All brushes must be labelled with user name and material. Do not use someone else’s brush.
049	Vacuum remaining powder from substrate	Ensure powder has been vacuumed out of substrate screw holes.
050	Raise substrate	
051	Remove substrate	
052	Remove receiver and funnel	
053	Thoroughly vacuum chamber and inside of door	
054	Remove panels on sides of chamber, vacuum and wipe with blue roll and IPA	Two screws under each panel should be removed in order to remove side panels



055	Open glove compartment, unroll gloves, vacuum and wipe with blue roll and IPA		Use red key to unlock the glove compartment screws
056	Wipe all internal surfaces of chamber (excluding lens) with blue roll and IPA including walls and ceiling		
057	Wipe flange near funnel position several times – this is a hot spot for contamination		A “shelf” located as shown in picture holds a large amount of contamination. Clean it thoroughly.
058	Drop platform to bottom (press “go to 80 mm”), vacuum and wipe with blue roll and IPA then elevate to top. Repeat this AT LEAST three times.		Repetition of this step ensures any powder stuck below the platform is brought to the top and can be removed.
059	Clean lens with lens wipe and dedicated sticklers spray		
060	Roll up gloves and close glove compartment		Turn knobs quite tightly until they can no longer be unscrewed without the red key
061	Vacuum powder from external surfaces and Allen screw holes of all components that have been removed from the SLM		
062	Remove two screws from top of hopper and pour powder from hopper into a container		Handle powders according to the COSHH assessment for individual materials
063	Powder from receiver must be sieved before re-using. Do so according to COSHH assessment for specific material (all users		Handle powders according to the COSHH assessment for individual materials



## The Application of AM to Ni-base Superalloys

	should have one). Label sieve with name and material. Do not use anyone else's sieve.	
064	Label powder containers with material, user name and email address, date opened and COSHH number	
065	Store powder containers in yellow cupboard	
066	After sieving powder from receiver and soring it appropriately, remove base of receiver by removing six screws. Vacuum out the internal surfaces paying particular attention to the revolving "open / close" mechanism. Wipe the inside of the receiver with blue roll and IPA.	
067	Remove circlip on one end of the revolving open/close mechanism and pull out the revolving barrel. Vacuum and wipe with blue roll and IPA before re-assembling.	
068	Re-attach receiver base and set aside.	
069	Remove 5 screws on wiper to part the two halves. Vacuum and wipe. Rotate the silicon wiper blade so a fresh surface is showing and re-assemble. Set aside.	
070	Wipe funnel, tube, O-ring and clip with blue roll and IPA. Set aside.	


071	Remove base of powder hopper by removing six screws. Lift out the internal plate and remove white seals. Unscrew three small screws and remove this plate. Remove white seals. Vacuum (being careful not to suck up the seals) all surfaces and wipe with blue roll and IPA. Reassemble and set aside.	
	Store used and usable substrates in two separate piles in the cupboard. If fewer than two usable substrates remain after your session, arrange for the used substrates to be taken to the workshop.	
<b>Changing filter (all users must do so after their final build on the last day of their booking)</b>		
<b>WEAR CORRECT PPE</b> <b>Face mask, Eye protection, Latex/Nitrile Gloves, Lab Coat, Safety Shoes</b>		
072	Undo clips and lift out filter assembly	
073	Use a trolley to transport filter assembly to black barrels in workshop room	
074	Ensure bottom valves are tightly closed	

## The Application of AM to Ni-base Superalloys

075	Fill with water from hose	
076	Wait 5 mins for water to soak in	
077	Pour water into contaminated barrel (one without pump attached)	
078	Remove four large Allen screws	
079	Remove old filter and submerge in water in contaminated barrel	
080	Rinse out filter holder using hose	
081	Return to SLM room and wipe out holder with blue roll and IPA	
082	Leave on shelf under desk to dry	
083	Pick up the other filter holder (already clean and dry from last user)	
084	Get new filter from cupboard (If fewer than 10 filters remaining use the log system to request re-ordering)	

085	Put valve sealant on the seals at either end (comes in a sachet with the filter)	
086	Push filter into bottom half of holder	
087	Place top half of holder in position and tighten the four screws	
088	Slide the assembly into the machine and reattach pipes using O-rings and clips	
<b>Cleaning vacuum (all users must do this at end of their booking)</b>		
<b>WEAR CORRECT PPE</b>		
<b>Face mask, Eye protection, Latex/Nitrile Gloves, Lab Coat, Safety Shoes</b>		
089	Un plug vacuum	
090	Unlock chamber	
091	Slide chamber out of vacuum and place onto trolley. Take it to the black barrels in the workshop room	
092	Lift off the top filter, pull metal tube out and lift this section out. Rinse these two parts with hose over the contaminated water barrel	
093	Pour water from vacuum into contaminated water barrel and rinse out using hose	
094	Re-fill up to mark using pump on the clean water barrel	

## The Application of AM to Ni-base Superalloys

095	Reassemble the vacuum, remembering to lock the chamber in place	
<b>To finish</b>		
096	Ensure there is enough IPA, Argon, blue roll and gloves for the next person to complete at least one day's build.	
097	Ensure bench and apparatus left according to smile card layout with no missing or extra items on bench. Extra items should be stored tidily in blue cupboards	
9	Fill in check list form and store in allocated folder	



## **Appendix 4: Method for Glyceregia etching of IN713C LPBF samples to reveal melt traces and dendritic structure.**

Etching must be performed in a fume cupboard.

PPE: Lab coat, goggles, cotton lined long gloves

Samples must be polished to 1  $\mu\text{m}$  then re-polished using Alumina suspension immediately prior to etching in order to remove any oxide layer which may have formed on the surface.

Highly porous samples will etch more readily than fully dense samples due to their higher surface area, so the method may require adjustment according to individual sample characteristics.

### **Method**

- 30ml glycerol
- 20ml HCl
- 15ml HNO<sub>3</sub>

Add glycerol to HCl then add HNO<sub>3</sub>. Mix well and use immediately.

Glyceregia can be applied by swabbing or immersion. Swabbing may be beneficial for samples which are highly porous or in circumstances where only a light etch is required since this method is more easily controllable.

To swab: Hold the sample using tongs. Hold cotton wool using tongs. Soak cotton wool in glyceregia mixture and gently wipe the surface of the sample until the surface begins to appear dull. Immerse sample in water to cease etching.

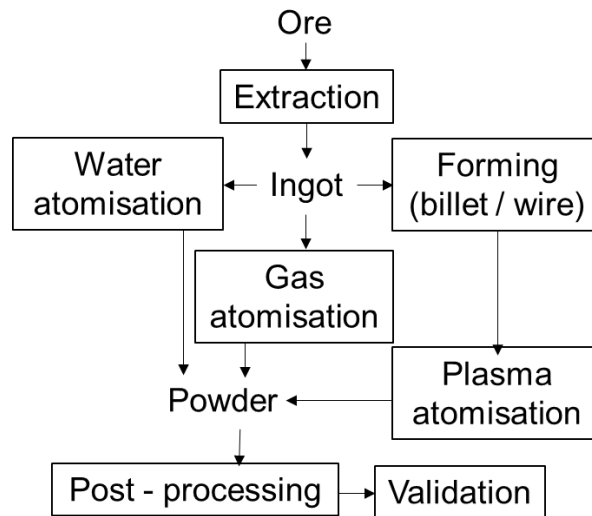
To immerse: Use tongs to immerse the sample in the glyceregia. Etching takes approximately 20 seconds for fully dense samples. Immerse sample in water to cease etching.

Dispose of waste etchant in labelled container.

## **Appendix 5: Characterisation of powdered feedstock**

The quality of the powdered feedstock has been shown to have a direct impact on the quality and consistency of LPBF parts [140]–[142] affecting the chemistry and defect populations through variation in powder morphology, flow characteristics, packing density, particle size distribution (PSD) and chemical changes or contamination. Furthermore, the powdered feedstock represents the greatest expenditure in AM processing over the lifetime of a laser PBF machine [127]. Hence, it is necessary to understand and control the quality of the feedstock in virgin and recycled powders. Since all laser PBF systems use a rake or wiper to create thin powder layers, the spreading and packing performance of the powder is essential for the formation of a homogeneous and continuous layer. Laser PBF uses powdered feedstock with a size range of 15-45  $\mu\text{m}$  and favours spherical particles to achieve the required layers. Flow characteristics are also important in systems which use a gravity fed dosing system, such as Renishaw SLM machines.

Atomisation is the usual method of production for metal powdered feedstock for AM processes and can be performed using water, gas or plasma atomisation processes depending on the alloy and the application [143]. Water atomisation, whereby water jets are aimed at a stream of molten metal atomising and solidifying it, produces highly irregular particle morphologies so is not well suited for laser PBF. Gas atomisation is more favourable since inert gasses are used to prevent oxidation and the particles take longer to solidify due to the lower heat capacity of the gas compared to water, resulting in high sphericity. For applications requiring highly spherical particles plasma atomisation is used whereby a wire or powdered feedstock is simultaneously melted and atomised by co-axial plasma torches and gas jets. The powder production methods are visualised in a flow chart in Figure A5.1. For this work, Hastelloy X powder of size range 20-53 $\mu\text{m}$  was sourced from commercial vendors LPW Technology Ltd. IN713C powder of 15-43 $\mu\text{m}$  was sourced from Sandvik Osprey Ltd. Both powders were produced via argon gas atomisation.



**Figure A5.1. Flow chart of powder production (after [127]).**

The powder was characterised prior to use through SEM, chemical analysis, image analysis and laser diffraction PSD analysis. The nominal chemical composition and composition measurements by LSM Analytical Services (now AMG Superalloys) are given in Table A3.1. Particle size distribution (PSD) measurements were made using laser diffraction on a Malvern Mastersizer 3000 machine with a dry powder dispersion module. The Hastelloy X powder had been recycled after SLM processing numerous times, whereas the IN713C powder was from virgin stock. Samples of powder were cold mounted in epoxy resin, then ground and polished to expose the inner structure of the particles. Optical micrographs were taken of the polished surfaces to look for porosity.

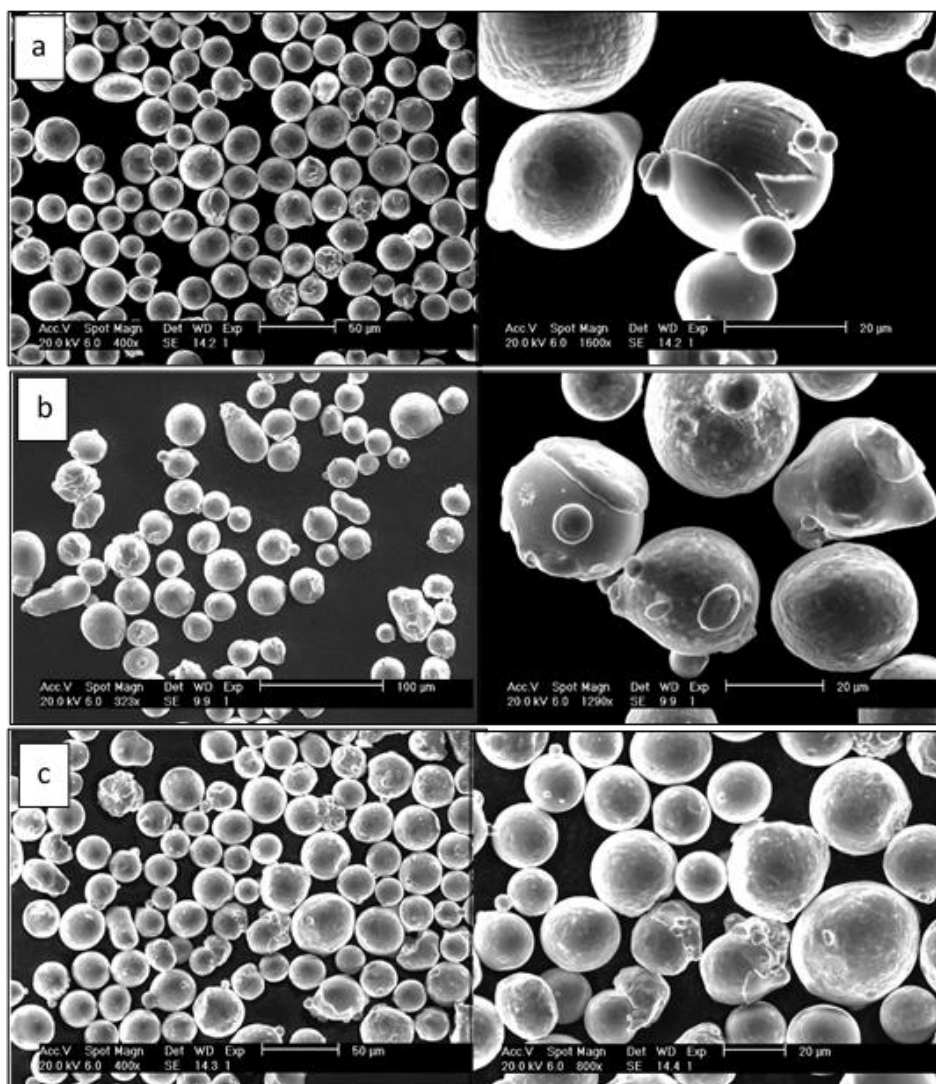
PSD measurements showed normal distributions with the average size of IN713C powder particles is smaller than that of the Hastelloy X powder (Table A5.1). The as received IN713C powder had poor flowability, resulting in avalanching of powder as it was deposited on the substrate causing problems with excessive inhomogeneity in the powder bed. The most likely cause for this behaviour is irregular shaped powder particles and satellite particles, more of which are seen in the as-received IN713C powder than the Hastelloy X powder (Figure A5.2). Some particles can be seen to contain porosity in both powders (Figure A5.3).

**Table A5.1. Nominal and measured compositions of Hastelloy X and IN713C powders.**

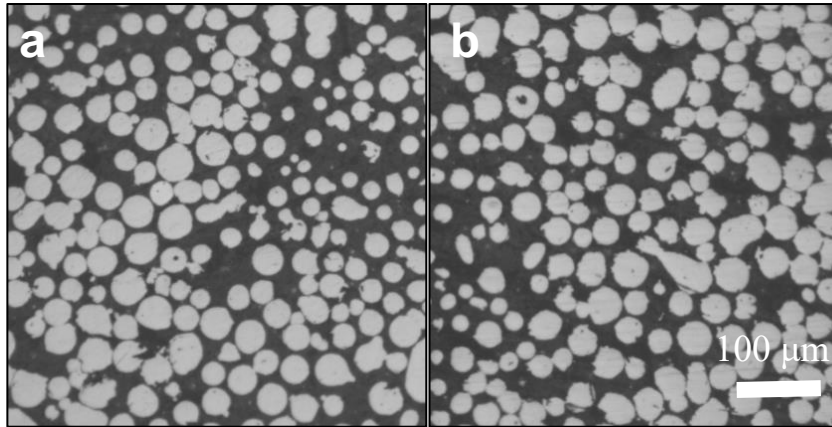
(wt %)	Element	Cr	Fe	Mo
Hastelloy X	Nominal	20.5-23.0	17.0-20.0	8.0-10.0
	Measured	21.3±0.19	19.5±0.17	9.0±0.12
IN713C	Nominal	12.0-14.0	0.0-2.5	3.8-5.2
	Measured	11.75	1.67	4.14
	<b>Element</b>	<b>Al</b>	<b>Ti</b>	<b>Zr</b>
Hastelloy X	Nominal	-	-	-
	Measured	-	-	-
IN713C	Nominal	5.5-6.5	0.5-1.0	0.05-0.15
	Measured	6.21	1.03	0.12
	<b>Element</b>	<b>Nb</b>	<b>Cu</b>	<b>B</b>
Hastelloy X	Nominal	-	-	-
	Measured	-	-	-
IN713C	Nominal	1.8-2.8	0.00-0.50	0.005-0.015
	Measured	2.19	<0.05	148 ppm
	<b>Element</b>	<b>Co</b>	<b>Mn</b>	<b>Si</b>
Hastelloy X	Nominal	1.5-2.5	0.2-1.0	0.00-0.10
	Measured	1.04±0.04	0.48±0.03	0.32±0.02
IN713C	Nominal	-	0.00-0.25	0.00-0.50
	Measured	<0.05	598 ppm	0.42
	<b>Element</b>	<b>W</b>	<b>C</b>	<b>Hf</b>
Hastelloy X	Nominal	0.6-1	0.05-0.15	-
	Measured	0.56±0.03	0.057±0.01	-
IN713C	Nominal	-	0.08-0.20	-
	Measured	<0.05	0.11	<0.05
	<b>Element</b>	<b>N</b>	<b>O</b>	<b>P</b>
Hastelloy X	Nominal	-	-	-
	Measured	-	-	-
IN713C	Nominal	-	-	-
	Measured	0.03	0.02	<0.005
	<b>Element</b>	<b>Ta</b>	<b>S</b>	<b>Pb</b>
Hastelloy X	Nominal	-	-	-
	Measured	-	-	<0.05
IN713C	Nominal	-	0.000-0.015	-
	Measured	<0.05	31 ppm	<0.005
<b>Ni balance</b>				

**Table A5.2. PSD measurements on multiple use Hastelloy X powder and sieved, virgin IN713C powder.**

PSD Measurement ( $\mu\text{m}$ )	Hastelloy X	IN713C
D [3,2]	34.1	32.4
D [4,3]	37.1	34.9
Dv (10)	24.1	23.3
Dv (50)	35.7	33.7
Dv (90)	52.5	48.6



**Figure A5.2. SEM micrographs of Hastelloy X (a) as-received IN713C (b) and sieved IN713C (c) powder particles.**



**Figure A5.3. Sectioned powder particles a) Hastelloy X b) IN713C.**

## Appendix 6: Analytical melt pool model

This model was developed by Felicity Freeman at the University of Sheffield.

```

%% Eager Moving Gaussian Beam
%Assumes no heat loss from top surface
%Scaling in Y and Z only
warning('off','MATLAB:integral2:maxFunEvalsPass')

%%List input parameters
Plist = []; %Point spacing (m)
Hlist = []; %Hatch spacing (m)
Elist = []; %Laser ON time (s) pulse exposure
Qlist = []; %Laser power (W)

for aa=1:length(Qlist)

%Main laser parameters - controlled above
Qmax=Qlist(aa); %Laser power (W)
point=Plist(aa); %Point spacing (m)
hatch=Hlist(aa); %Hatch spacing (m)
tau=Elist(aa); %Laser ON time (s) pulse exposure
layer=0.000020; %Layer thickness (m)

%Simulation size
Samplesize=0.01; %Sample size in beam travel direction (m)
step=0.000020; %Step size for simulation (m)
x=round((-0.004000):step:(0.000200),6); %Horizontal extent for
simulation - travel direction
y=round((-0.000400):step:(0.000200),6); %Horizontal extent for
simulation - across width
z=round((-0.000400):step:0,6); %Vertical extent for simulation -
depth
[X,Y,Z]=meshgrid(x,y,z);
dtmax=1; %Limiting temperature change for points in simulation

%Other laser parameters
c=4.1; %Laser travel speed between points (m/s)
n_abs=0.4; %Absorbitivity factor
sigma=0.000035; %Spot radius at half maximum (m)
v=(point)./(tau+(point./c)); %Apparent speed
nabla=(200./0.000013); %Gradient of ramp up to maximum
laser power, determined experimentally by Alistair Lyle
tau_ramp=(Qmax./nabla); %Time to reach maximum power
Q=@(t) ((nabla.*t).*(t<=tau_ramp))+(Qmax.*(t>tau_ramp)); %Time
dependent power
VBoil_Limit_Low=5E-14; %Threshold for keyhole melting
(m3)
VBoil_Limit_High=45E-14; %Threshold for keyhole melting
(m3)

%Material properties
T0=(25+273); %Initial temperature (K)
Tliq=(1602); %Liquidus Temperature (K)
Tsol=(1367); %Solidus Temperature (K)

```

## The Application of AM to Ni-base Superalloys

```

Tboil=3073; %Boiling Temperature (K)- Assume
same as Ni
rho=7910; %Density (kg/m3)
cp_sol=444; %Specific Heat by mass for solid
IN713C (J/kgK)
cp_liq=(cp_sol).*(0.2/0.17); %Specific Heat for liquid IN713C
(J/kgK)
k=9.823; %Thermal Conductivity (W/mK)
LHm=297000; %Latent Heat of melting
(J/kg)Assuming same as Ni
a_sol=(k)/(rho.*cp_sol); %Thermal Diffusivity of Solid
(m2/s)
a_liq=(k)/(rho.*cp_liq); %Thermal Diffusivity of Liquid
(m2/s)
cp_v_sol=(cp_sol*rho); %Specific Heat by volume for solid
IN713C (J/m3K)
THAZ=(0.5).*Tsol; %Heat affected zone temperature
(K)
R=8.314; %Gas constant (J/mol K)

if abs(max(x)-min(x))>Samplesize
    disp('***ERROR: Please adjust x extent of sample size***')
    return
else
    if abs(max(y)-min(y))>Samplesize
        disp('***ERROR: Please adjust y extent of sample size***')
        return
    end
end

%Scaling parameters - uses normalised energy density
scaling=1;

%Steady state temperature calculation
for count=1:2
    T=(X.*0)+T0;

    %Hatch 1 - beam centreline
    for i1=0:round((-1)*((Samplesize./(-2))./point),0)
        if i1==0
            tmax=(tau);
            F=@(t)
            ((Q(t).*n_abs)/(pi.*rho.*cp_sol.*((4.*pi.*a_sol).^1/2))).*((t.^
            (-1/2))./(2.*a_sol.*t)+(sigma.*sigma))...
            .* (exp((( -
            1).*((X.^2)+(Y.^2))./(4.*a_sol.*t)+(2.*(sigma.*sigma)))))...
            -(((Z./scaling).^2)/(4.*a_sol.*t)));
            dT=integral(F,0,tau,'ArrayValued',true);
        else
            tmax=(tau)+(i1.*(tau+(point./c)));
            i2=(i1*(-1));
            F=@(t)
            ((Q(t).*n_abs)/(pi.*rho.*cp_sol.*((4.*pi.*a_sol).^1/2))).*((t-
            tmax+(t-tau)).^(-1/2))./(2.*a_sol.*(tmax+(t-
            tau)))+(sigma.*sigma))...
            .* (exp((( -1).*((X-
            (i2.*point).^2)+(Y.^2))./(4.*a_sol.*(tmax+(t-
            tau)))+(2.*(sigma.*sigma)))))...

```



```

        -(((Z./scaling).^2)/(4.*a_sol.*(tmax+(t-tau)))));
    dT=integral(F,0,tau,'ArrayValued',true);
    end
    T=T+dT;
end

%Previous Hatches
for j1=1:round((-1)*((SampleSize./(-2))./hatch),0)
    for i2=(-1)*i1:i1
        if mod(j1,2)==0
            i3=i2*(-1);
        else
            i3=i2;
        end
    end

    tmax=(tau)+((SampleSize./v).*j1)+((i3+j1)*(tau+(point./c)));
    F=@(t)
        ((Q(t).*n_abs)./(pi.*rho.*cp_sol.*((4.*pi.*a_sol).^ (1/2)))).*(((tmax+(t-tau)).^(-1/2))./((2.*a_sol.*(tmax+(t-tau)))+(sigma.*sigma))))...
        .* (exp((-1).*(((X-(i2.*point)).^2)+(Y+(j1.*hatch)).^2))./((4.*a_sol.*(tmax+(t-tau)))+(2.*(sigma.*sigma)))))...
        -(((Z./scaling).^2)/(4.*a_sol.*(tmax+(t-tau)))));
    dT=integral(F,0,tau,'ArrayValued',true);
    T=T+dT;
    if i2==0
        maxdT=max(max(max(dT)))
    end
end
if maxdT<dtmax
    break
end
end

%Size above boiling point
Qsol=(rho.*cp_sol.*(Tsol-T0).*(step.^3));
%Heat input for a cell to reach solidus
Qmelt=(rho.*(step.^3)).*LHm;
%Heat input for a cell to melt
Qboil=(rho.*cp_liq.*(Tboil-Tsol).*(step.^3));
%Heat input for a cell to reach boiling point
Qsum=Qsol+Qmelt+Qboil;
%Total heat for a cell to get from T0 to boiling point

DeltaT=T-T0;
DeltaQ=(rho.*cp_sol.*DeltaT.*(step.^3));
%Heat input to each cell, model assumes no phase change so use cp_sol
maxDQ=max(max(max(DeltaQ)));

if max(max(max(DeltaQ)))>Qsum
    DeltaQ_side=transpose(squeeze(DeltaQ(find(~y),:,:)));
    [C1,~]=contour(x,z,DeltaQ_side,[Qsum,Qsum]);
%Contour where heat in cell sufficient to reach boiling point
[~,
Aboil]=convhull(transpose(C1(1,2:end)),transpose(C1(2,2:end)));

```

## The Application of AM to Ni-base Superalloys

```

        A6_VBoil(aa)=(2/3)*pi()*((2.*Aboil./pi())^(0.5))^3);
%Volume of melt pool at or above boiling point
    else
        A6_VBoil(aa)=0;
    end

    if count==1
        if A6_VBoil(aa)<VBoil_Limit_Low
            break
        else
            if A6_VBoil(aa)<VBoil_Limit_High
                scaling=(2E12 * A6_VBoil(aa))+1;
            else
                scaling=2;
            end
        end
    else
        break
    end
end

% melt length, depth & side view
figure(1)
T_side=transpose(squeeze(T(find(~y),:,:)));
[C4,~]=contour(x,z,T_side,[Tsol,Tsol]);
A1_MeltLength(aa)=(C4(1,end)-(C4(1,2)));
A2_MeltDepth(aa)=((-1)*min(C4(2,2:end)));
clf
hold on
contourf(x,z,T_side,[T0,THAZ,(0.6).*Tsol,(0.7).*Tsol,(0.8).*Tsol,(0.9).*Tsol,Tsol,Tliq]);
axis image
colormap jet;
h = colorbar;
ylabel(h, 'Temperature (K)')
axis([min(x) max(x) min(z) max(z)])
%line('XData', [min(x) max(x)], 'YData', [(-1*layer) (-1*layer)],
'LineStyle', '- -', 'Color', 'w', 'LineWidth', 0.5);
set(gca, 'XAxisLocation', 'bottom');
set(gca, 'YAxisLocation', 'left');
title('Melt Pool Profile - Side');
xlabel('Length (m)');
ylabel('Depth (m)');

[~, vol]=convhull(transpose(C4(1,2:end)),transpose(C4(2,2:end)));
radius=(2.*vol./pi())^(0.5);
A5_MeltPoolVolume(aa)=(2/3)*pi()* (radius^3)*1000000*1000000*100000
0;

% melt width & top view
figure(2)
T_top=(T(:, :, end));
[C5,~]=contour(x,y,T_top,[Tsol,Tsol]);
A3_MeltWidth(aa)=(max(C5(2,2:end)))-(min(C5(2,2:end)));
clf
hold on
contourf(x,y,T_top,[T0,THAZ,(0.6).*Tsol,(0.7).*Tsol,(0.8).*Tsol,(0.9).*Tsol,Tsol]);

```

```

axis image
colormap jet;
h = colorbar;
ylabel(h, 'Temperature (K)')
axis([min(x) max(x) min(y) max(y)])
line('XData', [min(x) max(x)], 'YData', [(0) (0)], 'LineStyle', '-
-', 'Color', 'w', 'LineWidth', 0.5);
line('XData', [min(x) max(x)], 'YData', [(-1*hatch) (-1*hatch)],
'LineStyle', '- -', 'Color', 'w', 'LineWidth', 0.5);
line('XData', [min(x) max(x)], 'YData', [(-2*hatch) (-2*hatch)],
'LineStyle', '- -', 'Color', 'w', 'LineWidth', 0.5);
set(gca, 'XAxisLocation', 'bottom');
set(gca, 'YAxisLocation', 'left');
title('Melt Pool Profile - Top');
xlabel('Length (m)');
ylabel('Width (m)');

%front view
profile1=0;
f=find(~x);
for g=0:f
    T1=squeeze(T(:, (f-g), :));
    T1(T1<Tsol)=0;
    T1(T1>=Tsol)=1;
    profile2=sum(sum(T1));
    if profile2>profile1
        profile1=profile2;
    else
        g=(g-1);
        break
    end
end
T_front=transpose(squeeze(T(:, (f-g-1), :)));
figure(3)
clf
hold on
contourf(y, z, T_front, [T0, THAZ, (0.6).*Tsol, (0.7).*Tsol, (0.8).*Tsol,
(0.9).*Tsol, Tsol]);
axis image
colormap jet;
h = colorbar;
ylabel(h, 'Temperature (K)')
axis([min(y) max(y) min(z) max(z)])
set(gca, 'XAxisLocation', 'bottom');
set(gca, 'YAxisLocation', 'left');
title('Melt Pool Profile - Front');
xlabel('Width (m)');
ylabel('Depth (m)');

%Create solidus contour for cooling rate calculation
figure(6)
clf
T_side=transpose(squeeze(T(find(~y), :, :)));
[C6, ~]=contour(x, z, T_side, [Tsol, Tsol]);

%adjust temperatures within melt pool for latent heat of melting
Qmelt=(rho.*(step.^3)).*LHm; %Latent heat of
melting for a cell

```

## The Application of AM to Ni-base Superalloys

```

T1=T;
T1(T1<Tsol)=0; %Identify cells above
the solidus
T1(T1>=Tsol)=(T1(T1>=Tsol)-T0); %Delta T for cells
above solidus
Q2=(rho.*cp_sol.*T1).*(step.^3); %Heat input from laser
to each cell
QSol=(rho.*cp_sol.*(Tsol-T0).*(step.^3)); %Heat required for a
cell to reach solidus
Q2(Q2>0)=(Q2(Q2>0))-(QSol); %Excess heat after
reaching solidus
Q2(Q2<Qmelt)=0; %If excess heat less
than latent heat of melting set to zero
Q2(Q2>=Qmelt)=(Q2(Q2>=Qmelt))-Qmelt; %Excess heat after
reaching solidus
T1=(Q2)./(rho.*cp_liq.*(step.^3)); %Recalculate delta T
from adjusted heat using liquid specific heat capacity
T(T>=Tsol)=(Tsol); %Clear additional
temperature from cells above solidus in main temperature matrix
T=(T+T1); %Add back in to main
temperature matrix
T_check=T(:, :, end);

%cooling rate plot
T1=(squeeze(T(find(~y), :, end)));
plot(x, T1);
title('Surface Temperature Profile with Solidus and Liquidus');
axis([min(x) 0 T0 2000])
set(gca, 'XAxisLocation', 'bottom');
set(gca, 'YAxisLocation', 'left');
xlabel('Length (m)');
ylabel('Temperature (K)');
line('XData', [min(x) max(x)], 'YData', [Tliq Tliq], 'LineStyle',
'- -', 'LineWidth', 1);
line('XData', [min(x) max(x)], 'YData', [Tsol Tsol], 'LineStyle',
'- -', 'LineWidth', 1);

%Create liquidus contour for cooling rate calculation
T_side=transpose(squeeze(T(find(~y), :, :)));
[C7, ~]=contour(x, z, T_side, [Tliq, Tliq]);
A4_CoolingRate(aa)=(Tliq-Tsol)./((C7(1,2))-(C6(1,2))).*v;

%output individual results
Results=[A1_MeltLength(aa), A2_MeltDepth(aa), A3_MeltWidth(aa), A4_Co
olingRate(aa), A5_MeltPoolVolume(aa), A6_VBoil(aa)];

close all

end

save('results.txt', 'A1_MeltLength', 'A2_MeltDepth', 'A3_MeltWidth', '
A4_CoolingRate', 'A5_MeltPoolVolume', 'A6_VBoil', '-ascii')

```

## Appendix 7: Matlab code for numerical integration involved in calculations of HCS

```

% This tool uses the RDG model to calculate cavitation pressure
drop the equation is found in https://doi.org/10.1007/s11661-999-
0334-z (Equation 12) for a set of LPBF process parameter
combinations

% The constants are defined as follows
% Tm = melting temperature of the matrix metal
% L = DAS
% u = viscosity
%sf = shrinkage factor
%Tl = liquidus temperature
%Tcg = grain coalescence temperature
%G = thermal gradient
%strain = strain
%vt = velocity of the isotherms

%Input factors:
Tm=1728
u=4.50E-03
sf=9.1034483E-02
Tl=1602.52
Tcg=1367.59

%Process factors - list
Glist = [];
vtlist = [];
strainlist = [];
Llist = [];

for ii=1:length(Glist)

G=Glist(ii);
strain=strainlist(ii);
vt=vtlist(ii);
L=Llist(ii);

PreA=(180/(L^2))*(((1+sf)*u)/G);
PreB=(180/(L)^2)*((vt*sf*u)/G);

% T is defined as a symbol for ease of integration
syms T;
fs=(1-(((Tm-T)./(Tm-Tl)).^(-1.1)));
FS=int(1-(((Tm-T)./(Tm-Tl)).^(-1.1)));
FS2=fs.^2;
ET= (strain/G).*int(fs);
FS3=((1-fs).^3);
FS4=((1-fs).^2);
a= ((ET*(fs.^2))/(((1-fs).^3)));
b=(((fs.^2)/(((1-fs).^2))));
A= int(a);

```

## The Application of AM to Ni-base Superalloys

```
B=int(b);
A=matlabFunction(int(a));
B=matlabFunction(int(b));
MaxA=A(Tl);
MinA=A(Tcg);
MaxB=B(Tl);
MinB=B(Tcg);
TotalA(ii)=MaxA-MinA;
TotalB(ii)=MaxB-MinB;
Pmech(ii)=PreA*(A(Tl)-A(Tcg));
Pshrink(ii)=PreB*(B(Tl)-B(Tcg));
Total(ii)=PreA*(A(Tl)-A(Tcg))+PreB*(B(Tl)-B(Tcg));

Results=[TotalA(ii),TotalB(ii),Pmech(ii),Pshrink(ii),Total(ii)];

end

save('RDGtestResult.txt','TotalA','TotalB','Pmech','Pshrink','Total', '-ascii')
```